

**Mixed-conducting (Ba,Sr)(Co,Fe,Zn)O_{3-δ}
as cathode material for proton-conducting
ceramic fuel cells:
Defect chemistry and oxygen reduction
mechanism**

Von der Fakultät Chemie der Universität Stuttgart
zur Erlangung der Würde eines Doktors der
Naturwissenschaften (Dr. rer. nat.)
genehmigte Abhandlung

vorgelegt von
Daniel Pöttsch
aus Dresden

Hauptberichter: Prof. Dr. J. Maier
Mitberichter: Prof. Dr. J. van Slageren
Prüfungsvorsitzender: Prof. Dr. R. Niewa

Tag der Einreichung: 09. Mai 2014
Tag der mündlichen Prüfung: 14. Juli 2014

Max-Planck-Institut für Festkörperforschung
Stuttgart
2014

Dad
1965 – 2014

Erklärung über die Eigenständigkeit der Dissertation

Ich versichere, dass ich die vorliegende Arbeit mit dem Titel

“Mixed-conducting (Ba,Sr)(Co,Fe,Zn)O_{3-δ} as cathode material for proton-conducting ceramic fuel cells: Defect chemistry and oxygen reduction mechanism”

selbständig verfasst und keine anderen als die angegebenen Quellen und Hilfsmittel benutzt habe; aus fremden Quellen entnommene Passagen und Gedanken sind als solche kenntlich gemacht.

Stuttgart, 09. Mai 2014

Daniel Pöttsch

Declaration of Authorship

I hereby certify that the dissertation entitled

“Mixed-conducting (Ba,Sr)(Co,Fe,Zn)O_{3-δ} as cathode material for proton-conducting ceramic fuel cells: Defect chemistry and oxygen reduction mechanism”

is entirely my own work except where otherwise indicated. Passages and ideas from other sources have been clearly indicated.

Stuttgart, 09. Mai 2014

Daniel Pöttsch

Contents

Zusammenfassung	VII
Abstract	XI
Abbreviations and Symbols	XV
1 Introduction	1
2 Systems with three mobile charge carriers	5
2.1 Bulk thermodynamics	5
2.2 Bulk diffusion	10
2.2.1 General equations and bipolar diffusion	10
2.2.2 Chemical diffusion for three mobile carriers	12
2.3 Surface oxygen exchange kinetics	16
2.3.1 Thin-film electrodes on YSZ electrolytes	18
2.3.2 Porous electrodes on proton-conducting electrolytes	20
3 Experimental	23
3.1 Sample preparation	23
3.1.1 Powder preparation	23
3.1.2 Pellet preparation	24
3.1.3 Characterization - XRD	25
3.2 Characterization of the defect chemistry	26
3.2.1 Determination of the oxygen nonstoichiometry	26
3.2.2 Ex-situ determination of the water content	26
3.2.3 In-situ determination of the mass relaxation upon $\Delta p_{\text{H}_2\text{O}}$	27
3.2.4 Conductivity relaxation - DC	29
3.2.5 Tracer diffusion - SIMS	29
3.3 Dense thin-film microelectrodes	30
3.3.1 Sample preparation	30
3.3.2 Impedance spectroscopy	30
4 Results and Discussion	33
4.1 Sample characterization	33
4.2 Thermodynamic analysis	36
4.2.1 Dry atmosphere	37
4.2.2 Humid atmosphere	40
4.3 Simulation of the diffusion model	50
4.3.1 Simulation details	51

4.3.2	Varying the hole concentrations	53
4.3.3	Varying the ratio of $D_{\text{OH}\cdot}$ to $D_{\text{V}\cdot\cdot}$	57
4.3.4	Varying the contribution of hydrogen uptake to the total proton uptake	59
4.3.5	Effect on mass and conductivity relaxations	61
4.3.6	Increasing the hole concentration with $p_{\text{O}_2}^{1/2} K_{\text{ox}}$ at fixed $p_{\text{H}_2\text{O}} K_{\text{hydrat}}$. .	62
4.4	Diffusion - Single-fold vs. two-fold	66
4.4.1	Thermogravimetric relaxation	66
4.4.2	SIMS and DC relaxation	73
4.5	Effect of electronic conductivity in BZY on the impedance	77
4.5.1	Influence on the impedance spectra	82
4.5.2	Influence on the exponents of the parameter dependencies	85
4.5.3	Influence on the DC bias dependence	88
4.5.4	Strategies to diminish the influence of R_{eon}	89
4.6	Oxygen reduction mechanism	92
4.6.1	Diameter dependence	92
4.6.2	Partial pressure dependencies of R'_{g}	92
4.6.3	Partial pressure dependencies of $C^{\delta'}$	97
4.6.4	Temperature dependence and comparison of the catalytic activities . .	100
5	Summary and Conclusions	101
A	MATLAB scripts	105
A.1	Defect concentrations from $p_{\text{O}_2}^{1/2} K_{\text{ox}}$ and $p_{\text{H}_2\text{O}} K_{\text{hydrat}}$	105
A.2	Defect concentrations from Δm upon $\Delta p_{\text{H}_2\text{O}}$ for BSFZ	107
B	Input data for diffusion simulations	109
C	Conductivity measurements vertical & parallel to diffusion direction	113
	Bibliography	115
	Acknowledgments	121
	Curriculum Vitae	123

Zusammenfassung

In der vorliegenden Arbeit werden gemischt leitende Festoxide mit Perowskit-Struktur bezüglich ihrer Anwendbarkeit als Sauerstoffelektrode (Kathode) in Festoxid-Brennstoffzellen untersucht, die auf Protonen leitenden Elektrolytmembranen basieren (H^+ -SOFC). Diese Art von Hochtemperatur-Brennstoffzellen ist vielversprechend, da sie es ermöglicht die Betriebstemperatur von typischerweise $\geq 800\text{ }^\circ\text{C}$ für SOFCs basierend auf Oxidionen leitenden Membranen (O^{2-} -SOFC) auf $\leq 700\text{ }^\circ\text{C}$ zu senken. Solch eine Temperaturabsenkung bringt eine Reihe von Vorteilen mit sich wie verringerte Degradation, längere Laufzeiten, kürzer Anlaufzeiten und geringere Kosten. Ein weiterer Vorteil ist, dass Wasser an der Kathode gebildet wird ohne den Brennstoff zu verdünnen, was den praktischen Betrieb vereinfacht. Unter reduzierter Temperatur dominiert die Überspannung an der Kathode (hohe Aktivierungsenergie) über alle anderen Verluste in der Brennstoffzelle.

Daher ist es zwingend erforderlich die katalytische Aktivität der Kathode systematisch und zielgerichtet zu verbessern, wofür ein grundlegendes Verständnis der elektrochemischen Eigenschaften der Materialien entscheidend ist. Diese Eigenschaften werden unter anderem von der Defektchemie der beweglichen Ladungsträger des Materials bestimmt. In feuchter, oxidierender Atmosphäre bei erhöhter Temperatur müssen drei Defekte in Betracht gezogen werden: Sauerstoffleerstellen, im Zwischengitter sitzende protonische Defekte verknüpft mit einem regulären Gittersauerstoff, und Elektronenlöcher. Diese Kombination aus ionischen (Sauerstoffleerstellen und Protonen) und elektronischen (Löcher) Ladungsträgern führt zum gemischt leitenden Verhalten dieser Materialklasse. In einer H^+ -SOFC ist eine gemischte Protonen/Löcherleitfähigkeit in der Kathode in hohem Maße erwünscht, da sie die gesamte Elektrodenoberfläche für die Wasserbildung katalytisch aktivieren würde. Dies würde die Leistung der Kathode erheblich verbessern, da ihre Oberfläche normalerweise viel größer ist als die Länge der Dreiphasengrenze, auf welche demgegenüber der katalytisch aktive Bereich beschränkt wäre, wenn die Elektrode für Protonen isolierend ist.

Die Volumen-Thermodynamik und Transporteigenschaften mit drei beweglichen Ladungsträgern sind erheblich komplizierter als in einem System mit „nur“ zwei beweglichen Defekten. In letzterem ist über die Elektroneutralitätsbedingung eine eindeutige Beziehung zwischen beiden Ladungsträgerkonzentrationen gegeben. Dagegen gibt es im System mit drei Ladungsträgern für einen gegebenen Defekt mehr Freiheitsgrade. Dadurch sind numerische Simulationen notwendig um die thermodynamischen und Volumentransporteigenschaften zu beschreiben und zu verstehen.

Die Protonenkonzentration von gemischt leitenden Perowskiten wurde ex-situ durch Karl-Fischer Titration und Thermogravimetrie unter Auswertung des Massenspektrometersignals und in-situ durch dynamische, thermogravimetrische Relaxationsexperimente bei stufenweiser Änderung des Wasserpartialdrucks bestimmt. Vier verschiedene Materialien, welche in der Li-

teratur als Kathodenmaterial vorgeschlagen werden, wurden ausgewählt: $\text{La}_{0.6}\text{Sr}_{0.4}\text{Co}_{0.8}\text{Fe}_{0.2}\text{O}_{3-\delta}$ (LSCF), $\text{Ba}_{0.6}\text{Sr}_{0.4}\text{Co}_{0.9}\text{Nb}_{0.1}\text{O}_{3-\delta}$ (BSCN), $\text{Ba}_{0.5}\text{Sr}_{0.5}\text{Co}_{0.8}\text{Fe}_{0.2}\text{O}_{3-\delta}$ (BSCF) und $\text{Ba}_{0.5}\text{Sr}_{0.5}\text{Fe}_{0.8}\text{Zn}_{0.2}\text{O}_{3-\delta}$ (BSFZ). Nachdem ihr Potential als gemischter Protonen/Löcherleiter durch Bestimmung der maximalen Protonenkonzentration über auf Raumtemperatur hydratisierte Proben untersucht wurde (steigt von ≈ 0.1 auf 20 mol% in der gegebenen Reihenfolge), wurde BSFZ als vielversprechendster Kandidat identifiziert und für weitere Untersuchungen ausgewählt. Aus thermodynamischer Sicht sind zwei Grenzfälle in der Protonenaufnahme bekannt: Aufnahme eines Wassermoleküls, welches eine Sauerstoffleerstelle besetzt und zwei protonische Defekte bildet (Säure-Base-Thermodynamik), und Aufnahme von Wasser unter gleichzeitiger Freisetzung von Sauerstoff, was formal gleichbedeutend mit reiner Wasserstoffaufnahme ist (Redoxthermodynamik). In Abhängigkeit der Temperatur, des Sauerstoff- und Wasserpartialdrucks ist jede Kombination aus beiden Mechanismen möglich. Dies führt zu einer wesentlichen Verkomplizierung in der experimentellen in-situ Auswertung, da die Protonenkonzentration nicht direkt aus der Massenänderung berechnet werden kann. Mit Hilfe der numerischen Simulationen des Transportverhaltens unter verschiedenen Bedingungen, Messung der Massenrelaxation aufgrund der Wasserpartialdruckänderungen unter zwei verschiedenen Sauerstoffpartialdrücken und durch Bestimmung der thermodynamischen Eigenschaften in trockenen Bedingungen konnte die Protonenkonzentration unter Anwendung des thermodynamischen Modells berechnet werden. Die erhaltenen Werte reichen von 0.32 bis 1.5 mol% zwischen 600 und 350 °C bei 20 mbar $p_{\text{H}_2\text{O}}$, und sind – in Übereinstimmung mit dem thermodynamischen Modell und Literaturdaten bzgl. BSCF – fast p_{O_2} unabhängig.

Für BSFZ wurden die Transienten Massenrelaxation nach $p_{\text{H}_2\text{O}}$ -Wechsel für zwei verschiedene p_{O_2} -Werte gemessen. Interessanterweise ändert sich der Mechanismus der Protonenaufnahme von vorwiegend Säure-Base-Wasseraufnahme bei 10 mbar (hohe Relaxationszeiten und Massenzunahmen) zu vorwiegend Wasserstoffaufnahme bei 1 bar p_{O_2} (schnelle und geringe Massenzunahme). Dieser Übergang ist mit dem thermodynamischen Modell vereinbar. Die Transienten konnten mit der bekannten Lösung des zweiten Fick'schen Gesetzes für eindimensionale Diffusion in der Ebene (mit hinreichend schneller Oberflächenreaktion) angepasst werden, wodurch chemische Diffusivitäten erhalten wurden. In einem Material mit drei beweglichen Ladungsträgern kann der Wassertransport komplizierter sein als in einem Medium mit zwei Ladungsträgern, in dem Protonen- und Sauerstoffleerstelldiffusion trivialerweise aneinander gekoppelt sind. In Perowskiten sind die Löcher normalerweise die schnellste Spezies. Für hinreichend hohe Löcherkonzentrationen kann sich die Protonenwanderung in die Probe von den normalerweise langsameren Sauerstoffleerstellen entkoppeln und stattdessen an die Löcher gekoppelt wandern, welche in die entgegengesetzte Richtung fließen (chemische Diffusion von Wasserstoff). Um das thermodynamische Gleichgewicht zu erreichen, d.h. um Wasser in Gänze aufzunehmen, wird dann Sauerstoff in einem langsameren Prozess in die Probe transportiert (Gegendiffusion von Sauerstoffleerstellen, welche die Probe verlassen und an Löcher gekoppelt sind, welche zurück in die Probe eingebracht werden). Dieser Transportmechanismus führt zu einer sogenannten "two-fold" Relaxation, welche eine nichtmonotone Relaxation der Löcherkonzentration aufweist. Allerdings konnte die Massentransiente aufgrund der kleinen Signalintensität der Wasserstoffaufnahme zur Gesamtrelaxation in 10 mbar p_{O_2} nicht verlässlich mit dem "two-fold" Modell angepasst werden. Es wurde stattdessen mit einem einzelnen, effektiven Diffusionskoeffizient angepasst. Basierend auf numerischen Simulationen können diese Werte als Untergrenze für die Protonendiffusivität betrachtet werden.

Unter 1 bar p_{O_2} wird nur Wasserstoff aufgenommen, was in einer ambipolaren Diffusion von Protonen und Löchern resultiert und eine monotone “single-fold” Relaxation mit einem chemischen Diffusionskoeffizienten von Wasserstoff darstellt. Da der Hydrierungsgrad in BSFZ unter den untersuchten Bedingungen niedrig ist, können die angepassten Werte grob der Defektdiffusivität des Protons gleichgesetzt werden.

Die Protonenleitfähigkeit wird aus der Konzentration und Diffusivität, welche aus den Massenrelaxationsexperimenten erhalten wurden, berechnet. Die Anpassung mit nur einem Parameter in 10 mbar p_{O_2} , welche eine Untergrenze für die Protonendiffusivität darstellt, ergibt eine vorsichtige Abschätzung für die Protonenleitfähigkeit. Die erhaltenen Werte reichen von $\approx 9 \times 10^{-5}$ in der zurückhaltenden bis $2 \times 10^{-3} \text{ Scm}^{-1}$ in der realistischen Abschätzung. Sie sind anderthalb Größenordnung unter der Protonenleitfähigkeit von 15% Y-dotiertem BaZrO_3 , welches einer der besten Hochtemperatur-Protonenleiter ist. Nichtsdestotrotz liegt sogar die abgeschätzte Untergrenze der Protonenleitfähigkeit in BSFZ mehrere Größenordnungen über einem benötigten Minimum von etwa $3 \times 10^{-8} \text{ Scm}^{-1}$ (Grenze zwischen Oberflächen- und Volumenpfad für dichte $(\text{La,Sr})\text{MnO}_{3\pm\delta}$ Elektrode auf YSZ), um die gesamte Elektrodenoberfläche katalytisch zu aktivieren. Meines Wissens nach ist dies die erste Untersuchung, welche quantitative Werte für die Protonenleitfähigkeit in den gemischt leitenden Perowskiten liefert, welche typischerweise als Kathodenmaterialien in Festoxidbrennstoffzellen eingesetzt werden.

Die elektrochemische Aktivität von BSFZ und BSCF wurde durch Impedanzspektroskopie untersucht. Dünnfilm-Mikroelektroden wurden über Puls-Laser-Abscheidung (PLD) auf polierten Y-dotierten BaZrO_3 Substraten und Photolithographie (mit Ionenstrahlätzen) hergestellt. Für diese Mikroelektroden dominiert der Niederfrequenzbeitrag normalerweise die Gesamtimpedanz, und sein Widerstand ist umgekehrt proportional zum ratenbestimmenden Schritt der Sauerstoffreduktion zu Wasser. Die umgekehrte Proportionalität des Oberflächenreaktionswiderstandes zur Fläche der Mikroelektroden bestätigt, dass die gesamte Elektrodenoberfläche katalytisch aktiv ist. Seine Abhängigkeit vom Sauerstoff- und Wasserpartialdruck liefert wichtige Informationen über den Sauerstoffreduktionsmechanismus. Der Exponent der Sauerstoff- und Wasserpartialdruckabhängigkeit weist darauf hin, dass molekularer Sauerstoff und Sauerstoffleerstellen am ratenbestimmenden Schritt der Sauerstoffreduktionsreaktion teilnehmen. Dies ist mit Ergebnissen von gemischt leitenden Dünnfilmelektroden auf YSZ identisch, in denen die Wanderung einer Sauerstoffleerstelle zu einem oberflächenadsorbierten Superoxid ratenbestimmend ist. Während der Impedanzmessungen wurde gezeigt, dass die bekannte, nicht vernachlässigbare elektronische Leitfähigkeit von Y-dotierten BaZrO_3 zu einem elektronischen Leckstrom in gas-symmetrischen Zellen führt, welcher die Auswertung der gemessenen Spektren (insbesondere in porenfreien Elektroden) empfindlich stören kann. Diese Störung wurde dadurch verringert, dass zu BaZrO_3 mit nur 1% Y-Gehalt übergegangen wurde und sie in die Auswertung mit einbezogen wurde. Im Gegensatz dazu wird dieser Aspekt in keiner veröffentlichten Untersuchung zur Sauerstoffreduktion in H^+ -SOFCs berücksichtigt, was zu Fehlinterpretationen bezüglich des Mechanismus führen kann.

Zusammenfassend ist zu sagen, dass die Protonenkonzentration und Leitfähigkeit für BSFZ bestimmt werden konnte. Es wurde für BSFZ und BSCF Mikroelektroden bestätigt, dass wie zu erwarten die gesamte Elektrodenoberfläche katalytisch aktiv ist. Diese Ergebnisse lie-

fern einen Ansatz für eine wissensbasierte Verbesserung der Kathodenleistung in Protonen leitenden Festoxidbrennstoffzellen.

Abstract

In the present study mixed-conducting solid oxides with perovskite structure are investigated regarding their applicability as oxygen electrode (cathode) in solid oxide fuel cells based on proton-conducting electrolyte membranes (H^+ -SOFC). This type of high temperature fuel cells is a promising device as it may allow one to decrease the operating temperature from $\geq 800^\circ\text{C}$, typically necessary for SOFCs using oxide-ion conducting membranes (O^{2-} -SOFC), to $\leq 700^\circ\text{C}$. Such a temperature reduction would bring about a variety of advantages such as less degradation, longer lifetime, shorter start-up times and lower costs. A further advantage is the formation of water at the cathode without diluting the fuel at the anode simplifying the stack operation. At reduced temperatures the overpotential of the cathode (high activation energy) dominates over all contributions to the performance of the fuel cell.

Hence, it is mandatory to systematically and purposefully enhance the catalytic activity of the cathode, for which a fundamental understanding of the electrochemical properties of the materials is key. These properties are inter alia determined by the defect chemistry of the material's mobile charge carriers. In humid, oxidizing atmosphere at elevated temperature three defects have to be considered: Oxygen vacancies, interstitial protonic defects associated with a regular oxygen site and electron holes. This combination of ionic (oxygen vacancies and protons) and electronic (holes) charge carriers provides the mixed-conducting characteristics of these class of materials. In a H^+ -SOFC a mixed proton/hole conductivity in the cathode is highly desired as to make the whole electrode surface catalytically active for water formation. This would severely enhance the performance of the cathode as its surface is typically much larger than the length of the triple-phase-boundary to which, in contrast, the catalytically active zone would be limited if the electrode is insulating for protons.

The bulk thermodynamic and transport behavior regarding three mobile charge carriers are significantly more complex than for systems with "only" two mobile defects. In the latter an unambiguous correlation between both charge carriers is given through the local electroneutrality condition. For the situation having three charge carriers this correlation is, in contrast, a priori less restrictive for a given carrier, and numerical simulations are necessary to describe and understand the bulk thermodynamic and transport properties.

The proton concentration of mixed-conducting perovskites was ex-situ determined by Karl-Fischer titration and thermogravimetry analyzing the mass spectrometer signal, and in-situ by dynamic, thermogravimetric relaxation experiments upon step-wise changes in the water partial pressure. Four different materials proposed as cathode for solid oxide fuel cells in the literature are chosen: $\text{La}_{0.6}\text{Sr}_{0.4}\text{Co}_{0.8}\text{Fe}_{0.2}\text{O}_{3-\delta}$ (LSCF), $\text{Ba}_{0.6}\text{Sr}_{0.4}\text{Co}_{0.9}\text{Nb}_{0.1}\text{O}_{3-\delta}$ (BSCN), $\text{Ba}_{0.5}\text{Sr}_{0.5}\text{Co}_{0.8}\text{Fe}_{0.2}\text{O}_{3-\delta}$ (BSCF) and $\text{Ba}_{0.5}\text{Sr}_{0.5}\text{Fe}_{0.8}\text{Zn}_{0.2}\text{O}_{3-\delta}$ (BSFZ). After exploring the capability as mixed proton/hole conductor by determining the maximum proton concentration of to room temperature hydrated samples (increases from ≈ 0.1 to 20 mol% in the given se-

ries), BSFZ was found to be the most promising candidate of the four and, therefore, selected for further investigations. From a thermodynamic point of view two limiting possibilities incorporating protons are identified: Incorporating a water molecule occupying an oxygen vacancy and forming two protonic defects (acid-base thermodynamics) and taking up water releasing simultaneously oxygen, i.e. hydration-deoxygenation, formally equivalent to pure hydrogen incorporation (redox thermodynamics). Depending on temperature, oxygen and water partial pressure any combination of both mechanisms is possible. This leads to a substantial complexity in the experimental in-situ analysis as the proton concentration cannot directly be calculated from the mass changes. With the help of numerically simulating the transport behavior at different conditions, measuring the mass relaxation upon water partial pressure changes at two different oxygen partial pressures and determining the thermodynamic properties in dry conditions, the proton concentration could be calculated applying the thermodynamic model. The obtained proton concentrations range from 0.32 to 1.5 mol% between 600 and 350 °C at 20 mbar $p_{\text{H}_2\text{O}}$, being almost p_{O_2} independent, in agreement with the thermodynamic model and literature data for BSCF.

For BSFZ the mass relaxation transients upon $\Delta p_{\text{H}_2\text{O}}$ were measured for two different p_{O_2} values. Interestingly, the mechanism of proton uptake was found to change from predominantly acid-base water uptake at 10 mbar (large relaxation times and mass increase) to predominantly redox hydrogen uptake at 1 bar p_{O_2} (fast and small mass gain). This transition is in agreement with the thermodynamic model. The transients could be fitted through the known solution of Fick's second law of one-dimensional diffusion into a plane sheet (with sufficiently fast surface equilibration) obtaining chemical diffusivities. In a material with three mobile carriers water transport can be more complex than in a two carrier medium where proton and oxygen vacancy diffusion are coupled to each other in a simple way. In perovskites the holes are typically the fastest species. For sufficiently high hole concentrations the protons migrating into the sample can decouple from the typically slower oxygen vacancies and, instead, migrate coupled to the holes which diffuse in the opposite direction (chemical diffusion of hydrogen). To obtain the thermodynamic equilibrium, i.e. to take up water in total, oxygen is transported into the sample in a slower process (counter-diffusion of oxygen vacancies leaving the sample, and coupled to holes which are incorporated back into the sample). This transport mechanism leads to a so called two-fold relaxation exhibiting a non-monotonic relaxation in the hole concentration. However, owing to the low signal intensity of the hydrogen uptake in the mass relaxation at 10 mbar p_{O_2} , the mass transients could not reliably fitted to the two-fold relaxation model. It was, instead, fitted to a single effective diffusion coefficient. Based on numerical simulations these fit values are taken as lower bound for the proton diffusivity. At 1 bar p_{O_2} only hydrogen is taken up resulting in an ambipolar diffusion of protons and holes, representing a monotonic single-fold relaxation with a single chemical diffusion coefficient of hydrogen. As the degree of hydrogenation is low for BSFZ in the investigated temperature range, these fit values can roughly be equaled to the proton defect diffusivity.

The proton conductivity is calculated using its concentration and diffusivity obtained from the mass relaxation experiments. The one-parameter fit from transients in 10 mbar p_{O_2} – being a lower bound for the proton diffusivity – yields a conservative estimate for the proton conductivity. The obtained values range from $\approx 9 \times 10^{-5}$ in the conservative to $2 \times 10^{-3} \text{ Scm}^{-1}$ in the realistic estimation. They are up to one and a half orders of magnitude below the proton

conductivity of 15% Y-doped BaZrO₃ being one of the best known high temperature proton conductors. Nevertheless, even the estimate of the lower limit of proton conductivity in BSFZ is orders of magnitude larger than a required minimum of about $3 \times 10^{-8} \text{ Scm}^{-1}$ (found as border between surface and bulk path for dense (La,Sr)MnO_{3±δ} electrodes on YSZ) to make the whole electrode surface catalytically active. This is to the best of my knowledge the first study providing quantitative values for the proton conductivity in those mixed-conducting perovskites typically used as cathode material in solid oxide fuel cells.

The electrochemical activity of BSFZ and BSCF was investigated by impedance spectroscopy. Thin-film microelectrodes were prepared by pulse laser deposition on polished Y-doped BaZrO₃ substrates and photolithography (ion beam etching). For these microelectrodes the low frequency contribution typically dominates the overall impedance, and its resistance is inversely proportional to the reaction rate determining the overall oxygen to water reaction. The inverse dependence of the surface reaction resistance to the area of the microelectrode confirms that the whole electrode surface is catalytically active. Its dependency on oxygen and water partial pressure provides important information about the oxygen reduction mechanism. The exponents of the oxygen and water partial pressure dependency indicate that molecular oxygen and oxygen vacancies are participating in the rate determining step of the oxygen reduction reaction. This is identical to results obtained for mixed-conducting thin-film electrodes on YSZ where it was found that the migration of an oxygen vacancy at the surface to adsorbed superoxide species is rate determining. In the course of the impedance measurements it was shown that the known non-zero electronic conductivity of Y-doped BaZrO₃, leading to an electronic leakage current in gas-symmetrical cells, can severely disturb the interpretation of the measured spectra (in particular for pore-free electrodes). This disturbance was diminished by switching to BaZrO₃ with only 1% Y-dopant concentration and had to be taken into the analysis. In contrast, this aspect is not considered by any published study investigating the oxygen reduction reaction in H⁺-SOFC which could lead to misinterpretations on the mechanism.

To summarize, proton concentration and conductivity could be determined for BSFZ. The expected whole electrode surface being catalytically active for the oxygen reduction could be confirmed for BSFZ and BSCF microelectrodes. These findings now serve a starting point for a knowledge-based improvement of the cathode performance in proton-conducting solid oxide fuel cells.

Abbreviations and Symbols

List of Abbreviations

Abbreviation	Description
A'	acceptor dopant
AC	alternating current
ASR	area specific resistance
BCY	Yttrium doped barium cerate $\text{Ba}(\text{Ce},\text{Y})\text{O}_{3-\delta}$
BSCF	$\text{Ba}_{0.5}\text{Sr}_{0.5}\text{Co}_{0.8}\text{Fe}_{0.2}\text{O}_{3-\delta}$
BSCN	$\text{Ba}_{0.6}\text{Sr}_{0.4}\text{Co}_{0.9}\text{Nb}_{0.1}\text{O}_{3-\delta}$
BSF	$(\text{Ba},\text{Sr})\text{FeO}_{3-\delta}$
BSFZ	$\text{Ba}_{0.5}\text{Sr}_{0.5}\text{Fe}_{0.8}\text{Zn}_{0.2}\text{O}_{3-\delta}$
BSFZ10	$\text{Ba}_{0.5}\text{Sr}_{0.5}\text{Fe}_{0.9}\text{Zn}_{0.1}\text{O}_{3-\delta}$
BSFZ30	$\text{Ba}_{0.5}\text{Sr}_{0.5}\text{Fe}_{0.7}\text{Zn}_{0.3}\text{O}_{3-\delta}$
BZY	Yttrium doped barium zirconate $\text{Ba}(\text{Zr},\text{Y})\text{O}_{3-\delta}$
BZY x	barium zirconate with $x\%$ Y dopant concentration $\text{BaZr}_{1-x}\text{Y}_x\text{O}_{3-\delta}$
CE	counter electrode
DC	direct current
DFT	density functional theory
e'	electronic defect
FC	flow controller
h^\bullet	electronic hole defect
H ⁺ -SOFC	proton conducting solid oxide fuel cell
HF	high frequency
H_i^\bullet	protonic defect written as interstitial defect
ICP-OES	inductively coupled plasma optical emission spectrometry
KFT	Karl-Fischer titration
LF	low frequency
LSCF	$\text{La}_{0.6}\text{Sr}_{0.4}\text{Co}_{0.8}\text{Fe}_{0.2}\text{O}_{3-\delta}$
LSCF	$(\text{La},\text{Sr})\text{CoO}_{3-\delta}$
LSM	$(\text{La},\text{Sr})\text{MnO}_{3\pm\delta}$
MF	medium frequency
MS	mass spectrometry
O ²⁻ -SOFC	oxide ion conducting solid oxide fuel cell
OD_O^\bullet	deuteronic defect written as lattice defect
OH_O^\bullet	protonic defect written as lattice defect
O_O^\times	regular lattice oxygen
ORR	oxygen reduction reaction

PLD	pulse laser deposition
SEM	secondary electron microscopy
SIMS	secondary ion mass spectrometry
SOFC	solid oxide fuel cell
SPS	spark plasma sintering
TPB	triple phase boundary
TG	thermogravimetry
$V_{\text{O}}^{\bullet\bullet}$	oxygen vacancy
WE	working electrode
XRD	X-ray diffraction
YSZ	Yttrium stabilized zirconia

List of Symbols

Symbol	Unit	Description
a		activity
a	pm	lattice constant
α	-	normalized diffusivity ratio
β	-	normalized transient reduction
c	-	concentration/molar fraction
C	F	capacitance
c	pm	lattice constant
c^*	-	tracer concentration
C^δ	F	chemical capacitance
D	cm^2s^{-1}	diffusivity
D^*	cm^2s^{-1}	tracer diffusivity
D^{eff}	cm^2s^{-1}	effective diffusivity
D^δ	cm^2s^{-1}	chemical diffusivity
δ	-	oxygen vacancy concentration (non-stoichiometry)
Δ		difference
E	eV	energy
e	$1.602\,176 \times 10^{-19}$ C	unit charge
E_a	eV	activation energy
ϵ_r	-	dielectric constant
F	$96\,485$ Cmol ⁻¹	Faraday constant
ΔG^0	kJmol^{-1}	standard Gibbs free energy
γ	-	normalized transient reduction minus redox fraction
ΔH^0	kJmol^{-1}	standard enthalpy
J	$\text{molcm}^{-1}\text{s}^{-1}$	flux
j	$\text{mlmin}^{-1}\text{cm}^{-2}$	flux (in gas permeation membranes)
K	-	equilibrium constant
\overrightarrow{k}	s^{-1}	forward rate constant
\overleftarrow{k}	s^{-1}	backward rate constant
k^{q}	cms^{-1}	effective rate constant

k^δ	cm s^{-1}	chemical effective rate constant
K_{hydrat}	-	equilibrium constant for acid-base hydration
K_{ox}	-	equilibrium constant for oxygen exchange
K_{hydrogen}	-	equilibrium constant for redox hydrogenation
L	m	sample thickness
l	cm	diffusion length
m	g	mass
M	g mol^{-1}	molar mass
m	$\text{s}^{-1/2}$	slope of plot $\text{time}^{1/2}$ vs. normalized concentration
m	-	parameter of the p_{O_2} dependence
μ	kJ mol^{-1}	chemical potential
$\tilde{\mu}$	kJ mol^{-1}	electrochemical potential
n	mol	equivalent
n	-	parameter of the $p_{\text{H}_2\text{O}}$ dependence
N_{A}	$6.0221 \times 10^{23} \text{ mol}^{-1}$	Avogadro's number
∇		gradient
ω	Hz	frequency
p	bar	pressure
$p_{\text{D}_2\text{O}}$	bar	heavy water partial pressure
ϕ	V	electrical potential
$p_{\text{H}_2\text{O}}$	bar	water partial pressure
p_{O_2}	bar	oxygen partial pressure
Q		constant phase element
R	$8.31447 \text{ J K}^{-1} \text{ mol}^{-1}$	universal gas constant
R	Ω	resistance
r	pm	radius (of an ion)
R_{b}	Ω	bulk resistance
\mathfrak{R}	s^{-1}	reaction rate
\mathfrak{R}_0	s^{-1}	equilibrium exchange rate
$\overrightarrow{\mathfrak{R}}$	s^{-1}	forward reaction rate
$\overleftarrow{\mathfrak{R}}$	s^{-1}	backward reaction rate
R_{eon}	Ω	electronic resistance
R_{i}	Ω	interface resistance
R_{ion}	Ω	ionic resistance
R_{s}	Ω	surface reaction resistance
ΔS^0	$\text{J mol}^{-1} \text{ K}^{-1}$	standard entropy
σ	S cm^{-1}	conductivity
T	K or $^\circ\text{C}$	temperature
t	-	Goldschmidt tolerance factor
t	-	transference number
t	s	time
u	$\text{cm}^2 \text{ V}^{-1} \text{ s}^{-1}$	mobility
V_{m}	$\text{cm}^3 \text{ mol}^{-1}$	molar volume
X	-	degree of hydration
X'	-	degree of hydrogenation

X''	-	degree of protonation
x	cm	space coordinate
x	-	parameter of the diameter dependence
z	-	charge
Z	Ω	impedance (complex resistance)
z	-	degree of depression in the constant phase element
Z_{img}	Ω	imaginary part of the impedance
Z_{real}	Ω	real part of the impedance

1 Introduction

Owing to finite resources of crude oil, limited acceptance of nuclear power sources (at least, in Germany and Japan) and an increasing environmental awareness in society and politics, alternative and renewable energy sources are mandatory. Amongst wind, solar and biomass (probably competing with food production), fuel cells and batteries are promising technologies in order to supply energy in a sustainable way. In this thesis, the focus is set to fuel cells. They are environmentally friendly as they are (i) not limited by Carnot's law, i.e. higher efficiencies with less consumption of primary energy resources are achievable with good scalability to smaller units. (ii) Using hydrogen as fuel they are, in principle, CO₂ neutral and renewable (depends on the source of hydrogen) as the only exhaust is water. A large variety of fuel cell types is available classified by the electrolyte used and operating temperature suited for different applications, such as low temperature fuel cells mostly for mobile applications (polymer membranes, aqueous alkaline solutions or phosphoric acid as electrolyte – 50 – 200 °C), intermediate temperature fuel cells (molten carbonates as electrolyte – 600 – 700 °C) and, last but not least, high temperature fuel cells mostly for stationary applications (solid oxides as electrolytes – ≥ 800 °C).^[1]

Amongst the solid oxide fuel cells (SOFC) two types can be identified: SOFCs using oxide-ion conducting electrolytes such as Yttrium stabilized zirconia ((Zr,Y)O_{2- δ} , YSZ) – O²⁻-SOFC, and SOFCs using proton-conducting electrolytes such as Yttrium or Scandium doped barium zirconates or cerates (Ba(Zr,Ce,Y,Sc)O_{3- δ}) – H⁺-SOFC. While the first one typically needs to be operated at temperatures above 800 °C (electrolyte exhibits high enough ionic conductivity; however, efforts on lowering the temperature are made^[2-6]), the latter can be operated at lower temperatures below 700 °C, i.e. the intermediate temperature range, as the electrolyte still shows sufficiently high bulk proton conductivity. The reduced operating temperatures enable advantages such as lower costs owing to less demands regarding sealing and materials, shorter start-up times, longer life-time (stability) and formation of water at the cathode (oxygen electrode) instead of the anode (fuel electrode) without diluting the fuel.^[7] However, the reduced temperature increases mostly the overpotential of the cathode as the oxygen reduction typically has the highest activation energy (above 1 eV,^[8] bulk proton conductivity ≈ 0.4 eV^[9;10]) making it the limiting part of the fuel cell performance. Hence, it is highly desirable to understand the bulk diffusion and surface reaction properties of the mixed conducting electrode materials to purposefully improve the parameters. Commonly, the same mixed-conducting oxides used for the O²⁻-SOFC with perovskite structure are taken as cathode in H⁺-SOFC. To achieve a high cell performance, it is advantageous to have a mixed-conducting electrode to extend the reactive zone (where typically the oxygen reduction/dissociation takes place) beyond the limited triple-phase-boundary length (where electrode, electrolyte and gas phase are in contact) ideally to the whole electrode surface.^[11] This is easily achieved for O²⁻-SOFC as most doped perovskite electrode materials exhibit sufficiently high oxide ionic and electronic conductivity (even for (La,Sr)MnO_{3 \pm δ} (LSM) thin-films

with a very low ionic conductivity of $3 \times 10^{-8} \text{ Scm}^{-1}$ at 800°C on YSZ the whole electrode surface is catalytically active^[12]). The oxygen reduction mechanism has been investigated and is understood in great detail for several cathode materials on YSZ using dense thin-film electrodes with well-defined morphology. This indicates, in principle, another advantage for H^+ -SOFCs. For the oxygen reduction mechanism at mixed-conducting perovskite electrodes on YSZ it was found that incorporation of molecular oxygen chemisorbed at the electrode surface into an oxygen vacancy is the rate determining step, i.e. the elementary reaction which is limiting the cathode performance. In contrast, forming water at the electrode surface of a H^+ -SOFC does not necessarily require this step, and reduction and dissociation of oxygen could directly occur at the electrode surface.

In contrast, the oxygen reduction for H^+ -SOFCs was so far typically investigated on porous electrodes (single-phase electrodes or composite mixtures of electrode and electrolyte) which, indeed, are on the one hand closely related to applications, but on the other hand exhibit a complex, poorly defined and less reproducible morphology which makes it very difficult to draw mechanistic conclusion and compare different materials and setups.^[13] In this thesis, dense, thin-film microelectrodes known from investigations of the O^{2-} -SOFC type are used to study the oxygen reduction mechanism in H^+ -SOFCs.^[11;14;15] Proton-conducting Y-doped BaZrO_3 – a promising candidate with high bulk conductivity and thermal stability – was used as electrolyte.^[16] Moreover, to enable the whole electrode surface to be catalytically active it is necessary to have a mixed proton/electron conducting material. However, there is some skepticism in the H^+ -SOFC community whether the mixed-conducting perovskites are conductive for protons, at all.^[17–23] Few publications trying to determine the proton concentration are found.^[24–27] In contrast, the proton conductivity of typical mixed-conducting cathode materials is so far not quantified. To the best of my knowledge selectively proton-conducting, well-defined electrodes are not available to perform Wagner-Hebb polarization experiments typically used to determine the oxide ion conductivity in these mixed conductors, which makes it more difficult to determine the minor proton conductivity in a predominantly electronic-conducting material.^[28;29]

In this thesis, the bulk thermodynamic and diffusion properties as well as the surface kinetics are investigated and discussed taking all three mobile charge carriers into account which makes the physical analysis very complex.^[30–33] Numerical calculations and simulations are performed and found necessary to understand the bulk thermodynamic and diffusion behavior in this three charge carrier situation. Amongst the huge variety of mixed-conducting perovskites offered in the literature four materials are chosen. (i) $\text{Ba}_{0.5}\text{Sr}_{0.5}\text{Co}_{0.8}\text{Fe}_{0.2}\text{O}_{3-\delta}$ (BSCF) as a promising candidate for O^{2-} -SOFC with high catalytic activity, high oxygen vacancy concentration (probably a criterion for a high proton concentration) with fast diffusion and sufficient hole conductivity showing a high power density in H^+ -SOFCs, too.^[2;34–38] (ii) $\text{Ba}_{0.5}\text{Sr}_{0.5}\text{Fe}_{0.8}\text{Zn}_{0.2}\text{O}_{3-\delta}$ (BSFZ) as cobalt free counterpart of BSCF with high oxygen vacancy concentration, as well, lower hole conductivity and catalytic activity (cobalt free perovskite electrodes tend to appear less active^[8;39]), but still exhibiting a good performance in oxygen permeation membrane and fuel cell tests.^[40–42] (iii) $\text{Ba}_{0.6}\text{Sr}_{0.4}\text{Co}_{0.9}\text{Nb}_{0.1}\text{O}_{3-\delta}$ (BSCN) as iron free complement exhibiting a fuel cell performance comparable to BSCF.^[6;43] (iv) $\text{La}_{0.6}\text{Sr}_{0.4}\text{Co}_{0.8}\text{Fe}_{0.2}\text{O}_{3-\delta}$ (LSCF) as state-of-the-art mixed-conducting electrode studied in detail for O^{2-} -SOFC over a long period.^[44–47] After first proton concentration measurements,

BSFZ and BSCF are selected for further examination as promising candidates for mixed protonic/electronic conductors. The hydration and oxygen reduction kinetic behavior of BSFZ showing the highest proton concentration of the four materials is intensively studied by thermogravimetric and conductivity relaxation, tracer exchange experiments and impedance spectroscopy. As comparison, the oxygen reduction at BSCF on BZY is investigated, as well. In addition, the electronic leakage of the proton-conducting electrolyte appearing in oxidizing atmosphere at elevated temperatures which severely disturbs the electrochemical analysis had to be analyzed and means are developed to minimize it. This effect can lead to misinterpretations, and is, in contrast to all literature data, properly taken into account in this thesis.^[48]

2 Systems with three mobile charge carriers

2.1 Bulk thermodynamics

The electrochemical properties of solid oxides are determined by the chemistry and physics of their mobile defects. In this work only point defects - defects of zero dimension - are discussed, grouped into electronic and ionic defects. The defects are denominated using Kröger-Vink notation: X_a^b with X denoting the defect (V for vacancy, h for electronic hole and e for electron), subscript a as the lattice site where the defects sits (i for interstitial site) and superscript b for the charge relative to the ideal lattice (\bullet for positive, \prime for negative and \times for neutral charges).^[49] In solid oxides the electronic defects are holes h^\bullet and electrons e' , the ionic defects oxygen vacancies $V_O^{\bullet\bullet}$ and protonic defects. As referred to below, these protons are associated with the lattice oxygen O^{2-} forming an OH^- on a O^{2-} site, corresponding to an effectively positively charged OH_O^\bullet defect. Phenomenologically, this may also considered as an interstitial proton H_i^\bullet if it is tacitly understood that one interstitial site (i) is associated with a regular oxygen. However, this does not mean that the protons occupy crystallographic interstitial sites. The electronic defects enable electronic properties such as p- or n-type conductivity. In general, they are present in high concentrations in oxides with redox-active transition metals which easily change their valence state. Dependent on material, temperature and oxygen partial pressure, in oxides with perovskite structure localized (at the transition metal) and delocalized (metallic behavior such as in $(La,Sr)CoO_{3-\delta}$ (LSC)) electronic defects are found.^[50] However, at high temperatures combined with high/low oxygen partial pressure electronic defects also gain importance for actual redox-inactive oxides, i.e. proton-conducting electrolytes. Consequences for the interpretation of electrochemical measurements using these electrolytic oxides are discussed in section 4.5.

While point defects are present even in pure crystals at $T > 0$ K, they are most frequently introduced on purpose by systematic aliovalent cation doping - i.e. by exchanging a regular lattice cation with a cation of different charge. Dopants with lower charge are (formally) negatively charged acceptors; dopants with higher charge are (formally) positively charged donors. To preserve electroneutrality the doping has to be compensated by simultaneously generated defects of opposite charge. This work deals only with acceptor-doped oxides with perovskite structure in oxidizing atmosphere. The introduced acceptors A' (or A'' and more) are compensated by oxygen vacancies $V_O^{\bullet\bullet}$ (release of oxygen) and (or) electronic holes h^\bullet (oxidation of a cation and/or oxide ion).

Additionally, the defects interact with the atmosphere and react upon changes in temperature and gas composition. As in perovskites acceptor dopants are immobile at moderate

temperatures, only the mobile point defects $V_{\text{O}}^{\bullet\bullet}$, h^{\bullet} and $\text{OH}_{\text{O}}^{\bullet}$ are discussed.^a Furthermore, with respect to the examination of the oxygen reduction mechanism in humid, oxidizing atmosphere only gas compositions with different p_{O_2} and $p_{\text{H}_2\text{O}}$ are considered. The external thermodynamic behavior can be described by the following equilibria.^[53–56]

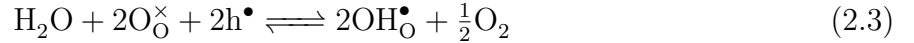
Gaseous oxygen from the atmosphere can occupy oxygen vacancies by generating holes - eq. 2.1.



In humid atmosphere oxygen vacancies can also be filled by water - eq. 2.2. Water splits up into an hydroxide ion which occupies the vacancy and a proton which attaches to a regular lattice oxygen, thus, generating two equal protonic defects $\text{OH}_{\text{O}}^{\bullet}$.



Finally, protonic defects can equilibrate with water without involving oxygen vacancies^b leaving oxygen in the gas phase and reducing the sample - eq. 2.3. Then, the hydration is coupled to a deoxygenation and only hydrogen is taken up (formally hydrogenated).



It has to be noted that the shown three equilibria are not independent, i.e. one of them is redundant. Each of the three mass action constants can be expressed by the two other ones - cf. eq. 2.4 to 2.6. To describe the thermodynamic defect chemistry, only two equilibria are necessary.

Using mass action laws the three thermodynamic equilibria are expressed by their corresponding mass action constants: K_{ox} for the oxygenation equilibrium eq. 2.1

$$K_{\text{ox}} = \frac{[\text{O}_{\text{O}}^{\times}][h^{\bullet}]^2}{p_{\text{O}_2}^{1/2}[V_{\text{O}}^{\bullet\bullet}]} = \frac{K_{\text{hydrat}}}{K_{\text{hydrogen}}} \quad (2.4)$$

K_{hydrat} for the hydration with water (eq. 2.2)

$$K_{\text{hydrat}} = \frac{[\text{OH}_{\text{O}}^{\bullet}]^2}{p_{\text{H}_2\text{O}}[V_{\text{O}}^{\bullet\bullet}][\text{O}_{\text{O}}^{\times}]} = K_{\text{ox}}K_{\text{hydrogen}} \quad (2.5)$$

and K_{hydrogen} for the hydrogenation (hydration - deoxygenation) reaction (eq. 2.3)

$$K_{\text{hydrogen}} = \frac{[\text{OH}_{\text{O}}^{\bullet}]^2 p_{\text{O}_2}^{1/2}}{p_{\text{H}_2\text{O}}[h^{\bullet}]^2[\text{O}_{\text{O}}^{\times}]^2} = \frac{K_{\text{hydrat}}}{K_{\text{ox}}} \quad (2.6)$$

Defect concentrations (per unit cell, i.e. molar fractions) and partial pressures (normalized by 1 bar) are introduced instead of their respective activities, i.e. the activity coefficients are

^aNote that $\text{OH}_{\text{O}}^{\bullet}$ is not mobile in toto rather the proton moves from one O^{2-} to a neighboring one (interstitial hopping); that is why also kinetically it will equally be referred to H_i^{\bullet} .^[51;52]

^bOxygen vacancies are not involved in the thermodynamic equilibrium. They can of course participate in the surface reaction kinetics.

set to unity. Although this is only valid for dilute systems and ideal gases, it is a reasonable approach but has to be kept in mind as an approximation which may lead to quantitative differences between theory and experiment. Note that taking account of variable $[O_O^\times]$, one includes exhaustibility effects. Two further constraints are the electroneutrality condition

$$[A'] = 2\delta + [OH_O^\bullet] + [h^\bullet] \quad (2.7)$$

with $[A']$ being the acceptor dopant concentration, and the site balance of the perovskite structure:

$$[O_O^\times] = 3 - \delta - [OH_O^\bullet] \quad (2.8)$$

Here, the oxygen vacancy concentration $[V_O^{\bullet\bullet}]$ is denoted by the shorter term δ also used in the chemical formula $ABO_{3-\delta}$.

The choice of two of the three thermodynamic equilibria to describe the defect chemistry is arbitrary. Coming from the situation in O^{2-} -SOFC in which only two carriers $V_O^{\bullet\bullet}$ and h^\bullet are relevant (equilibrium 2.1) and the background of H^+ -conducting electrolytes where only OH_O^\bullet and $V_O^{\bullet\bullet}$ have to be discussed (equilibrium 2.2, however, as mentioned earlier in oxidizing atmosphere and high temperature, eq. 2.1 cannot be neglected - cf. chapter 4.5), those two equilibria are chosen. Taking account of eqs. 2.7 and 2.8 their equilibrium constants are rewritten as

$$p_{O_2}^{1/2} K_{ox} = \frac{(3 - \delta - [OH_O^\bullet])([A'] - 2\delta - [OH_O^\bullet])^2}{\delta} \quad (2.9)$$

and

$$p_{H_2O} K_{hydrat} = \frac{[OH_O^\bullet]^2}{\delta(3 - \delta - [OH_O^\bullet])} \quad (2.10)$$

showing that besides the doping content $p_{O_2}^{1/2} K_{ox}$ and $p_{H_2O} K_{hydrat}$ are the control parameters for tuning the defect concentrations (within the stability limits of the material). The equilibrium constants are temperature dependent thermodynamic material properties related to the Standard Gibbs free reaction energy

$$\Delta G^0 = \Delta H^0 - T\Delta S^0 = -RT \ln K \quad (2.11)$$

with ΔH^0 as standard enthalpy, ΔS^0 as standard entropy, T as absolute temperature and R as universal gas constant. Knowing the thermodynamic constants, the gas partial pressures and the acceptor dopant concentration the defect concentrations can be calculated using eqs. 2.9, 2.10 and 2.7.

In figure 2.1 the normalized concentrations (mole fractions) of the three charge carriers are plotted linearly (left) and logarithmic (right) for a large range of $p_{O_2}^{1/2} K_{ox}$ and $p_{H_2O} K_{hydrat}$ with $[A'] = 1$. Four types of perovskite materials can be identified in this plot: Predominantly $V_O^{\bullet\bullet}$ conducting electrolytes such as (La,Sr)(Ga,Mg)O_{3-δ} (LSGM^[57]) ($p_{O_2}^{1/2} K_{ox} \ll 1$ and $p_{H_2O} K_{hydrat} \ll 1$), predominantly OH_O^\bullet conducting electrolytes such as BZY ($p_{O_2}^{1/2} K_{ox} \ll 1$ and $p_{H_2O} K_{hydrat} > 1$), mixed $V_O^{\bullet\bullet}/h^\bullet$ conducting electrodes such as LSCF ($p_{O_2}^{1/2} K_{ox} > 1$ and $p_{H_2O} K_{hydrat} \ll 1$) and, finally, the desired mixed OH_O^\bullet/h^\bullet conducting electrodes, possibly the same mixed-conducting perovskites that in the dry state are used for O^{2-} -SOFCs, ($p_{O_2}^{1/2} K_{ox} > 1$

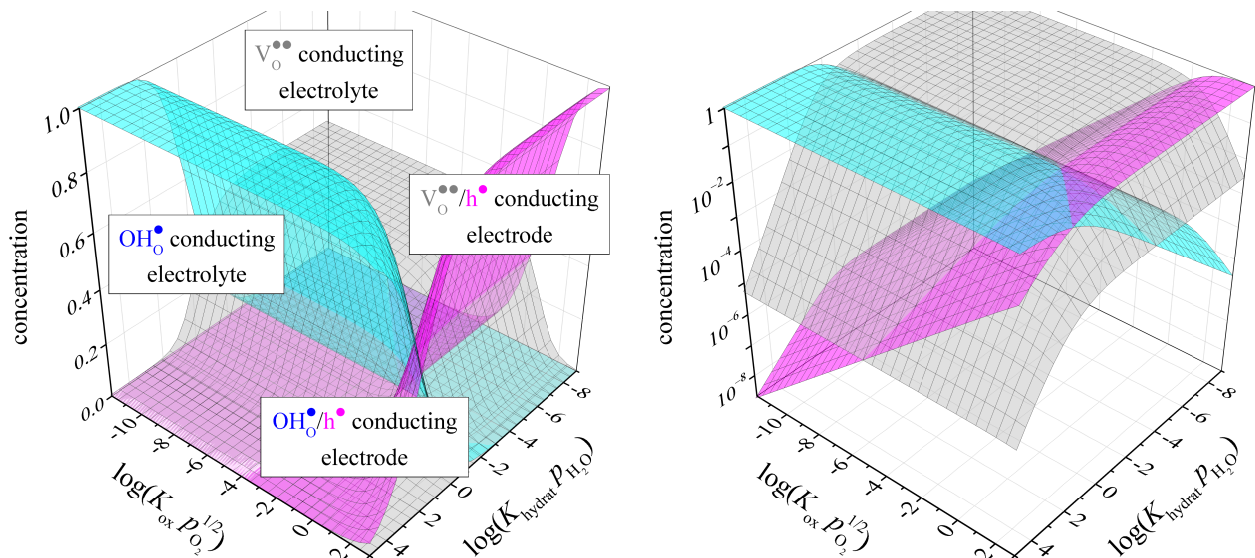


Figure 2.1: Defect concentrations of oxygen vacancies $V_{\text{O}}^{\bullet\bullet}$ (gray), protons $\text{OH}_{\text{O}}^{\bullet}$ (blue) and holes h^{\bullet} (magenta) obtained by numerical solution using MATLAB (script A.1 in appendix) based on the defect model with $[A'] = 1$.

and $p_{\text{H}_2\text{O}}K_{\text{hydrat}} > 1$). The proton concentration which is of most interest in this work can be normalized to thermodynamically maximum possible states which is useful to classify different thermodynamic and diffusion kinetic regimes (e.g. influence of the “degree of hydration” on the decoupling in the water diffusion – cf. simulations in chapter 4.3). Referring to Kreuer^[10;16] the *degree of hydration* X normalizes the proton concentration with respect to pure acid-base thermodynamics, i.e. the maximum theoretically possible proton concentration is limited by the $V_{\text{O}}^{\bullet\bullet}$ concentration in dry conditions.

$$X = \frac{[\text{OH}_{\text{O}}^{\bullet}]}{2[V_{\text{O}}^{\bullet\bullet}]_{p_{\text{H}_2\text{O}}=0}} = \frac{[\text{OH}_{\text{O}}^{\bullet}]}{2[V_{\text{O}}^{\bullet\bullet}] + [\text{OH}_{\text{O}}^{\bullet}]} \quad (2.12)$$

For pure hydrogenation (hydration and deoxygenation) thermodynamics it is feasible to define the analogous *degree of hydrogenation* X' (denominated as “degree of protonation” by Sanders and O’Hayre^[58]).

$$X' = \frac{[\text{OH}_{\text{O}}^{\bullet}]}{[h^{\bullet}]_{p_{\text{H}_2\text{O}}=0}} = \frac{[\text{OH}_{\text{O}}^{\bullet}]}{[h^{\bullet}] + [\text{OH}_{\text{O}}^{\bullet}]} \quad (2.13)$$

The general definition including mixed cases (simultaneous protonation by acid-base and redox reaction) is instead denoted as *degree of protonation* X'' .

$$X'' = \frac{[\text{OH}_{\text{O}}^{\bullet}]}{[A']} \quad (2.14)$$

For $[h^{\bullet}] = 0$, respectively, $[V_{\text{O}}^{\bullet\bullet}] = 0$ the last definition equals the respective previous ones.

The chemical capacitance C^{δ} is a parameter indicating how strong the defect concentrations change on changes in component activity. Quantitatively it is proportional to change of the

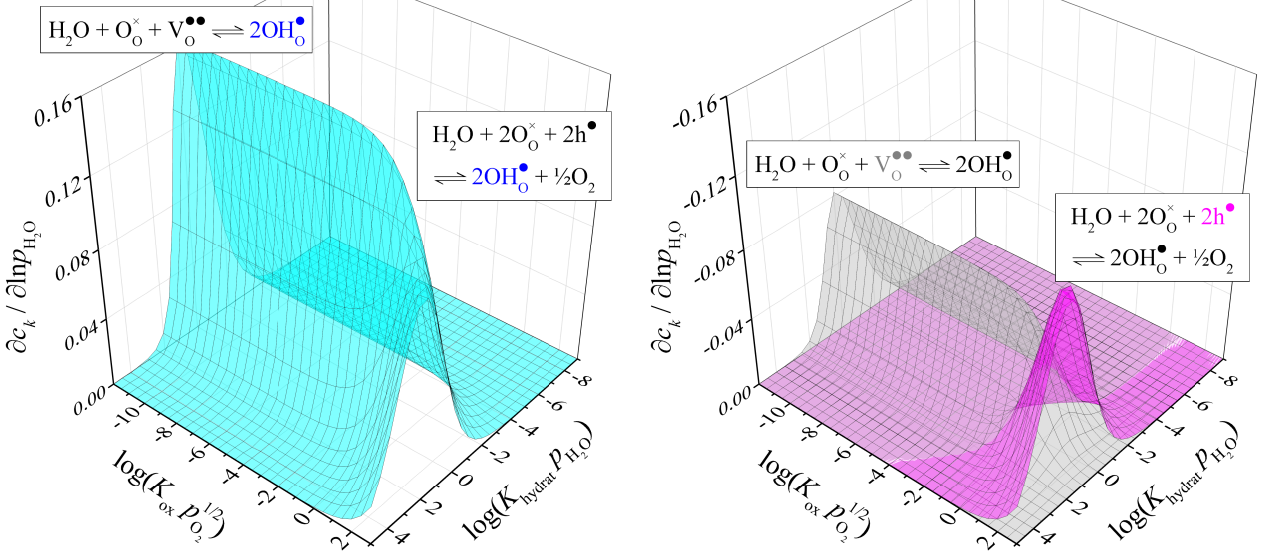


Figure 2.2: Response of the defect concentrations to changes in $p_{\text{H}_2\text{O}}$. The finite change in the concentrations Δc are numerically obtained for a finite change in $p_{\text{H}_2\text{O}}$ with $p_1 = 1$ and $p_2 = 0.9$. Note that the absolute scale of both z-axes are identical but that the right z-axis is negative.

defect concentration c with the change of the chemical potential μ , i.e. explicitly to $\ln p_{\text{H}_2\text{O}}$ or $\ln p_{\text{O}_2}$

$$C_k^\delta = z^2 F^2 L \frac{\partial c_k}{\partial \mu_k} \propto \frac{\partial c_k}{\partial \ln p_k} \quad (2.15)$$

with $z =$ charge of species k , $F =$ Faraday constant and $L =$ sample thickness parallel to the measurement direction. This is a further method to visualize the acid-base and redox-active regime. For low $p_{\text{O}_2} K_{\text{ox}}$ values, i.e. low $[\text{h}^\bullet]$, protons are taken up/released by acid-base reaction resulting in $\partial c_{\text{OH}_\text{O}^\bullet} / \partial \ln p_{\text{H}_2\text{O}} = -2 \partial c_{\text{V}_\text{O}^{\bullet\bullet}} / \partial \ln p_{\text{H}_2\text{O}}$ (figure 2.2 left). In this regime, $\text{OH}_\text{O}^\bullet$ and $\text{V}_\text{O}^{\bullet\bullet}$ change little with p_{O_2} (figure 2.3 left). $\partial c_{\text{V}_\text{O}^{\bullet\bullet}} / \partial \ln p_{\text{H}_2\text{O}}$ decreases and $\partial c_{\text{h}^\bullet} / \partial \ln p_{\text{H}_2\text{O}}$ increases with increasing $p_{\text{O}_2}^{1/2} K_{\text{ox}}$ (mixed regime) until protons are exclusively taken up by redox reaction, i.e. $\partial c_{\text{OH}_\text{O}^\bullet} / \partial \ln p_{\text{H}_2\text{O}} = -\partial c_{\text{h}^\bullet} / \partial \ln p_{\text{H}_2\text{O}}$. Here, $\text{OH}_\text{O}^\bullet$ and, consequently, h^\bullet respond strongly to changes in p_{O_2} and $p_{\text{H}_2\text{O}}$ (figure 2.3).

Last but not least, two general points visible in figure 2.1 and 2.2 are mentioned. (i) To obtain the same concentration of protons in the redox-active as in the acid-base active regime, higher $p_{\text{H}_2\text{O}} K_{\text{hydrat}}$ values are necessary, i.e. higher $p_{\text{H}_2\text{O}}$, lower temperature or a more easily hydratable material. This highlights the fact that it is obviously more difficult for redox-active materials to take up protons. There is a competition between protons and holes (expressed by equilibrium 2.3 and the electroneutrality condition 2.7). On introducing redox-active cations, $\Delta_{\text{ox}} H^0$ becomes more and $\Delta_{\text{hydrat}} H^0$ less negative favoring decreased proton concentration.^[59–61] Qualitatively the less negative $\Delta_{\text{hydrat}} H^0$ can be explained by the typically more covalent transition metal-oxide (TM-O) bonds with redox-active cations decreasing the basicity of the oxide ions (cf. Han et al. who found that the water content in $(\text{La}, \text{Sr})(\text{Sc}, \text{Fe})\text{O}_{3-\delta}$ suddenly drops with the introduction of a small amount of iron^[24]). Hence, finding a material with high proton as well as hole concentration seems to be a chal-

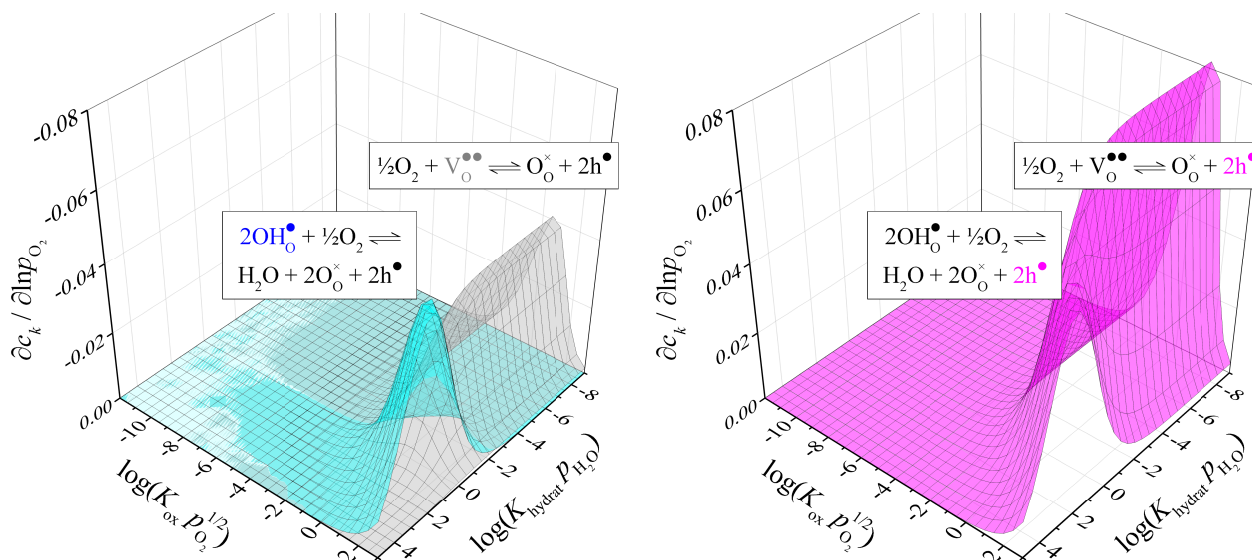


Figure 2.3: Response of the defect concentrations to changes in p_{O_2} . The finite change in the concentrations Δc are numerically obtained at finite change in p_{O_2} with $p_1 = 1$ and $p_2 = 0.9$. Note that the absolute scale of both z-axes are identical but that the right z-axis is negative.

lenge. (ii) For an ideal defect system with activity coefficients of unity the border between predominant acid-base water and redox hydrogen uptake can be identified by the cross section where $[V_O^{\bullet\bullet}] = [h^{\bullet}]$ (cf. cross section between gray and magenta contour in figures 2.1 and 2.2). Thus, for $[V_O^{\bullet\bullet}] > [h^{\bullet}]$ predominantly acid-base and for $[V_O^{\bullet\bullet}] < [h^{\bullet}]$ predominantly redox thermodynamics are expected. For a real, non-dilute situation the concentrations have to be replaced by their activities, the border is then still the cross section where the activities of $V_O^{\bullet\bullet}$ and h^{\bullet} equal. However, this does not necessarily mean that their concentrations are the same as their activity coefficients might differ, i.e. different activity coefficients shift the criterion with respect to the concentration. It will be seen later that this is obviously the case for BSFZ.

2.2 Bulk diffusion

2.2.1 General equations and bipolar diffusion

Understanding the bulk transport of the mobile charge carriers in a mixed electronically/ionically conducting material is crucial for application. It is also important for the analysis of diffusion data generally. Different measurement techniques lead to different, phenomenological diffusion coefficients D (and oxygen/water surface exchange rate constants k – chapter 2.3), dependent on the applied driving force. In this chapter only diffusion processes are discussed, i.e. the transport process through the bulk is limiting and the surface reaction is much faster. An experimental criterion for this is the so called critical thickness $L_{crit} = 2D/k$. If the sample is much thicker than L_{crit} the process is diffusion controlled (D -determined), and conversely if the sample is thinner it is surface exchange reaction controlled (k -determined).^[62;63] Finally,

simultaneous Dk -determination can also occur.

Considering charged species as mobile carrier the driving force for its transport (and reaction) is the gradient of its electrochemical potential

$$\nabla\tilde{\mu} = \nabla\mu + zF\nabla\phi \quad (2.16)$$

with $\nabla\mu =$ gradient in the chemical potential and $\nabla\phi =$ gradient in the electrical potential ($z =$ the charge number of the species and $F =$ the Faraday constant). For small driving forces, i.e. linear irreversible thermodynamics, the flux J is given by

$$J = -\frac{\sigma}{z^2F^2}\nabla\tilde{\mu} \quad (2.17)$$

($\sigma =$ conductivity of the species). The conductivity is connected with the mobility u and the concentration c by

$$\sigma = zFcu \quad (2.18)$$

Inserting the relation between mobility and diffusivity $D = uRT/zF$ into eq. 2.18 yields the Nernst-Einstein relation.

$$\sigma = \frac{z^2F^2cD}{RT} \quad (2.19)$$

The various measurement techniques do not directly give the microscopic diffusion coefficient, rather they lead to different phenomenological diffusivities in the first place denoted with respective superscripts: (i) External voltage/current denoted with q . This is done e.g. in electrochemical impedance spectroscopy as discussed in the oxygen reduction mechanism chapter 2.3. (ii) Tracer-diffusion denoted with $*$, i.e. changing a species in the gas phase with a suited isotope ($^{16}\text{O}/^{18}\text{O}$ or $^1\text{H}/^2\text{H}=\text{D}$). (iii) Chemical diffusion denoted with δ , i.e. changing the activity of typically one component, e.g. oxygen. For the two charge carrier situation in mixed oxide ion/hole conductors without association between ionic and electronic defects (no trapping) they are given as

$$D_{\text{O}}^q \approx D_{\text{O}}^* = \frac{[\text{V}_{\text{O}}^{\bullet\bullet}]}{c_{\text{O}}} D_{\text{V}_{\text{O}}^{\bullet\bullet}} \quad (2.20)$$

and

$$D_{\text{O}}^{\delta} = \frac{[\text{V}_{\text{O}}^{\bullet\bullet}]}{RT} \frac{\partial\mu_{\text{O}}}{\partial c_{\text{O}}} D_{\text{V}_{\text{O}}^{\bullet\bullet}} = t_{\text{V}_{\text{O}}^{\bullet\bullet}} D_{\text{h}^{\bullet}} + t_{\text{h}^{\bullet}} D_{\text{V}_{\text{O}}^{\bullet\bullet}} \quad (2.21)$$

with c_{O} the total concentration of oxygen, t_k the transference numbers and D_k the defect diffusivities of species k . The derivative in eq. 2.21 is an inverse chemical capacitance (eq. 2.15) and proportional to the so called thermodynamic factor.^[64;65]

For interstitial migration (overall availability of jump partners) the tracer diffusion coefficient D^* equals the defect diffusion coefficient of the tracer which is the case proton/deuterium diffusion in perovskites, i.e. $D_{\text{OD}_{\text{O}}}^* = D_{\text{OD}_{\text{O}}} \approx D_{\text{OH}_{\text{O}}}$. In contrast, for diffusion through vacancies a correction factor is needed which is between 0.5 and 0.78 depending on the crystal structure.^[64] For heavier isotopes than the couple H/D (less mass relative mass difference, negligible isotope effect) this tracer defect diffusivity equals the diffusivity of the regular defect. Owing to the large difference in mass between H and D an isotope effect is expected, therefore, $D_{\text{OD}_{\text{O}}}$ is slightly smaller than $D_{\text{OH}_{\text{O}}}$.

2.2.2 Chemical diffusion for three mobile carriers

For the three charge carrier situation three fluxes of $\text{OH}_\text{O}^\bullet$, $\text{V}_\text{O}^{\bullet\bullet}$ and h^\bullet have to be considered. The flux of protons will be called $J_{\text{H}_i^\bullet}$ instead of $J_{\text{OH}_\text{O}^\bullet}$ to make clear that the proton is the mobile species, not the hydroxide ion. Nonetheless, $\text{OH}_\text{O}^\bullet$ is still used as subscript for the thermodynamic data. Based on eq 2.17 of the preceding chapter the defect fluxes are written as

$$\begin{pmatrix} J_{\text{V}_\text{O}^{\bullet\bullet}} \\ J_{\text{H}_i^\bullet} \\ J_{\text{h}^\bullet} \end{pmatrix} = -\frac{1}{F^2} \begin{pmatrix} \sigma_{\text{V}_\text{O}^{\bullet\bullet}}/4 & 0 & 0 \\ 0 & \sigma_{\text{OH}_\text{O}^\bullet} & 0 \\ 0 & 0 & \sigma_{\text{h}^\bullet} \end{pmatrix} \begin{pmatrix} \nabla \tilde{\mu}_{\text{V}_\text{O}^{\bullet\bullet}} \\ \nabla \tilde{\mu}_{\text{OH}_\text{O}^\bullet} \\ \nabla \tilde{\mu}_{\text{h}^\bullet} \end{pmatrix} \quad (2.22)$$

The chemical potentials of the respective neutral species O for oxygen and H for hydrogen are expressed via local thermodynamic equilibrium (cf. eqs. 2.1, 2.2 and 2.3) by

$$\begin{pmatrix} \nabla \mu_\text{O} \\ \nabla \mu_\text{H} \end{pmatrix} = \begin{pmatrix} -1 & 0 & 2 \\ 0 & 1 & -1 \end{pmatrix} \begin{pmatrix} \nabla \tilde{\mu}_{\text{V}_\text{O}^{\bullet\bullet}} \\ \nabla \tilde{\mu}_{\text{OH}_\text{O}^\bullet} \\ \nabla \tilde{\mu}_{\text{h}^\bullet} \end{pmatrix} \quad (2.23)$$

Owing to electroneutrality the sum of the fluxes in eq. 2.22 multiplied with the charge number of the respective carrier needs to be zero.

$$\sum z_k J_k = 2J_{\text{V}_\text{O}^{\bullet\bullet}} + J_{\text{H}_i^\bullet} + J_{\text{h}^\bullet} = 0 \quad (2.24)$$

Inserting eq. 2.23 into 2.22 and the result into 2.24 the electrochemical potential of the holes is rewritten as

$$\nabla \tilde{\mu}_{\text{h}^\bullet} = \frac{t_{\text{V}_\text{O}^{\bullet\bullet}}}{2} \nabla \mu_\text{O} - t_{\text{OH}_\text{O}^\bullet} \nabla \mu_\text{H} \quad (2.25)$$

where $t_k = \sigma_k / \sigma_{\text{total}}$ is the transference number t of species k . Finally, $\nabla \tilde{\mu}_{\text{h}^\bullet}$ can be substituted back into eq. 2.22 and 2.23 and the fluxes of the charge carriers $\text{V}_\text{O}^{\bullet\bullet}$ and $\text{OH}_\text{O}^\bullet$ are written as function of gradients in the chemical potential of oxygen and hydrogen.

$$-J_\text{O} = J_{\text{V}_\text{O}^{\bullet\bullet}} = \frac{\sigma_{\text{V}_\text{O}^{\bullet\bullet}}(1 - t_{\text{V}_\text{O}^{\bullet\bullet}})}{4F^2} \nabla \mu_\text{O} + \frac{\sigma_{\text{V}_\text{O}^{\bullet\bullet}} t_{\text{OH}_\text{O}^\bullet}}{2F^2} \nabla \mu_\text{H} \quad (2.26)$$

$$J_\text{H} = J_{\text{H}_i^\bullet} = -\frac{\sigma_{\text{OH}_\text{O}^\bullet}(1 - t_{\text{OH}_\text{O}^\bullet})}{F^2} \nabla \mu_\text{H} - \frac{\sigma_{\text{OH}_\text{O}^\bullet} t_{\text{V}_\text{O}^{\bullet\bullet}}}{2F^2} \nabla \mu_\text{O} \quad (2.27)$$

Using $\nabla \mu_{\text{H}_2\text{O}} = 2\nabla \mu_\text{H} + \nabla \mu_\text{O}$ eq. 2.26 and 2.27 equal eq. (11a) and (11b)^c given by Kim and Yoo.^[33] However, it is more feasible to express the fluxes as a functions of the defect gradients $\nabla \mu_k$. Hence, eq. 2.23 is substituted back in eq. 2.26 and 2.27.

$$J_{\text{V}_\text{O}^{\bullet\bullet}} = -\frac{\sigma_{\text{V}_\text{O}^{\bullet\bullet}}(1 - t_{\text{V}_\text{O}^{\bullet\bullet}})}{4F^2} \nabla \mu_{\text{V}_\text{O}^{\bullet\bullet}} + \frac{\sigma_{\text{V}_\text{O}^{\bullet\bullet}} t_{\text{OH}_\text{O}^\bullet}}{2F^2} \nabla \mu_{\text{OH}_\text{O}^\bullet} + \frac{\sigma_{\text{V}_\text{O}^{\bullet\bullet}} t_{\text{h}^\bullet}}{2F^2} \nabla \mu_{\text{h}^\bullet} \quad (2.28)$$

$$J_{\text{H}_i^\bullet} = -\frac{\sigma_{\text{OH}_\text{O}^\bullet}(1 - t_{\text{OH}_\text{O}^\bullet})}{F^2} \nabla \mu_{\text{OH}_\text{O}^\bullet} + \frac{\sigma_{\text{OH}_\text{O}^\bullet} t_{\text{V}_\text{O}^{\bullet\bullet}}}{2F^2} \nabla \mu_{\text{V}_\text{O}^{\bullet\bullet}} + \frac{\sigma_{\text{OH}_\text{O}^\bullet} t_{\text{h}^\bullet}}{F^2} \nabla \mu_{\text{h}^\bullet} \quad (2.29)$$

^cIn ref. [33] the first sign in (11b) is incorrect, without, however, further consequences for the discussion there.

The gradients in the electrical potential $\nabla\phi$ in eq. 2.16 disappear in eqs. 2.28 and 2.29 as they sum up to zero (e.g. $\nabla\mu_{\text{H}} = \nabla\mu_{\text{OH}\bullet} + F\nabla\phi - \nabla\mu_{\text{h}\bullet} - F\nabla\phi$). They can further be expressed for each charge carrier k with

$$\nabla\mu_k = \frac{\partial\mu_k}{\partial c_k} \nabla c_k \quad (2.30)$$

This shows the advantage to have moved to the chemical potential gradients of the carriers. Unlike $\nabla\mu_{\text{H}}$ and $\nabla\mu_{\text{O}}$, the $\nabla\mu_k$ are unique functions of c_k allowing for a clear derivation of diffusion coefficients. With $\mu_k = \mu_k^0 + RT \ln a_k$ and $\partial \ln c_k / \partial c_k = 1/c_k$ eq. 2.30 reads

$$\nabla\mu_k = \frac{1}{c_k} \frac{\partial \ln a_k}{\partial \ln c_k} \nabla c_k = \frac{1}{c_k} \nabla c_k \quad (2.31)$$

In the case of weak disorder (dilute ideal solution) the thermodynamic factors for the defects (partial derivative in eq. 2.31) are unity. Inserting eq. 2.31 into 2.28 and 2.29 the fluxes are expressed as

$$J_{\text{V}\bullet\bullet} = -\frac{RT}{4F^2} \frac{\sigma_{\text{V}\bullet\bullet}(1 - t_{\text{V}\bullet\bullet})}{c_{\text{V}\bullet\bullet}} \nabla c_{\text{V}\bullet\bullet} + \frac{RT}{2F^2} \frac{\sigma_{\text{V}\bullet\bullet} t_{\text{OH}\bullet}}{c_{\text{OH}\bullet}} \nabla c_{\text{OH}\bullet} + \frac{RT}{2F^2} \frac{\sigma_{\text{V}\bullet\bullet} t_{\text{h}\bullet}}{c_{\text{h}\bullet}} \nabla c_{\text{h}\bullet} \quad (2.32)$$

and

$$J_{\text{H}\bullet} = -\frac{RT}{F^2} \frac{\sigma_{\text{OH}\bullet}(1 - t_{\text{OH}\bullet})}{c_{\text{OH}\bullet}} \nabla c_{\text{OH}\bullet} + \frac{RT}{2F^2} \frac{\sigma_{\text{OH}\bullet} t_{\text{V}\bullet\bullet}}{c_{\text{V}\bullet\bullet}} \nabla c_{\text{V}\bullet\bullet} + \frac{RT}{F^2} \frac{\sigma_{\text{OH}\bullet} t_{\text{h}\bullet}}{c_{\text{h}\bullet}} \nabla c_{\text{h}\bullet} \quad (2.33)$$

Using Nernst-Einstein relation (eq 2.19) leads to

$$J_{\text{V}\bullet\bullet} = -D_{\text{V}\bullet\bullet}(1 - t_{\text{V}\bullet\bullet}) \nabla c_{\text{V}\bullet\bullet} + 0.5 D_{\text{OH}\bullet} t_{\text{V}\bullet\bullet} \nabla c_{\text{OH}\bullet} + 0.5 D_{\text{h}\bullet} t_{\text{V}\bullet\bullet} \nabla c_{\text{h}\bullet} \quad (2.34)$$

and

$$J_{\text{H}\bullet} = -D_{\text{OH}\bullet}(1 - t_{\text{OH}\bullet}) \nabla c_{\text{OH}\bullet} + 2D_{\text{V}\bullet\bullet} t_{\text{OH}\bullet} \nabla c_{\text{V}\bullet\bullet} + D_{\text{h}\bullet} t_{\text{OH}\bullet} \nabla c_{\text{h}\bullet} \quad (2.35)$$

Note that these equations are equal to the transport equations (18) found in Liu et al..^[66]

The defect concentration gradients are not independent and are linked to each other by electroneutrality ($\nabla c_{\text{OH}\bullet} + 2\nabla c_{\text{V}\bullet\bullet} + \nabla c_{\text{h}\bullet} = 0$). Hence, one gradient can be substituted and both fluxes can be written as a function of two defect gradients and the respective prefactor. Which gradient is substituted is arbitrary in all cases, the fluxes read in a very general way

$$J_{\text{V}\bullet\bullet} = -D_{\nabla k(l)}^{\text{V}} \nabla c_k - D_{\nabla l(k)}^{\text{V}} \nabla c_l \quad (2.36)$$

and

$$J_{\text{H}\bullet} = -D_{\nabla k(l)}^{\text{H}} \nabla c_k - D_{\nabla l(k)}^{\text{H}} \nabla c_l \quad (2.37)$$

The prefactors can be regarded as chemical diffusion coefficients. The following nomenclature is used for them: The superscript labels the transported charge carriers (V for $\text{V}\bullet\bullet$, H for $\text{OH}\bullet$ and h for $\text{h}\bullet$), the two subscript labels refer to the driving forces chosen, whereby the first refers to the respective driving gradient and the second in brackets to the remaining gradient of the substitution procedure. Note that this does not necessarily mean that the third substituted gradient is zero. The three possibilities of substituting one gradient result

in three flux equations for each ionic defect. For the sake of completeness and as for the later discussion one or another substitution might be better suited to explain an observation, all flux equations are shown in the following.

Expressing the fluxes with $\nabla c_{V_{\bullet\bullet}}^{\circ}$ and $\nabla c_{OH_{\bullet}^{\circ}}$ as driving forces:

$$\begin{aligned}
 J_{V_{\bullet\bullet}}^{\circ} &= -D_{\nabla V(H)}^V \nabla c_{V_{\bullet\bullet}}^{\circ} - D_{\nabla H(V)}^V \nabla c_{OH_{\bullet}^{\circ}} \text{ with:} \\
 D_{\nabla V(H)}^V &= D_{V_{\bullet\bullet}}^{\circ} + t_{V_{\bullet\bullet}}^{\circ} (D_{h_{\bullet}} - D_{V_{\bullet\bullet}}^{\circ}) \\
 D_{\nabla H(V)}^V &= 0.5 t_{V_{\bullet\bullet}}^{\circ} (D_{h_{\bullet}} - D_{OH_{\bullet}^{\circ}}) \\
 J_{H_i^{\bullet}} &= -D_{\nabla H(V)}^H \nabla c_{OH_{\bullet}^{\circ}} - D_{\nabla V(H)}^H \nabla c_{V_{\bullet\bullet}}^{\circ} \text{ with:} \\
 D_{\nabla H(V)}^H &= D_{OH_{\bullet}^{\circ}} + t_{OH_{\bullet}^{\circ}} (D_{h_{\bullet}} - D_{OH_{\bullet}^{\circ}}) \\
 D_{\nabla V(H)}^H &= 2 t_{OH_{\bullet}^{\circ}} (D_{h_{\bullet}} - D_{V_{\bullet\bullet}}^{\circ})
 \end{aligned} \tag{2.38}$$

Expressing the fluxes with $\nabla c_{V_{\bullet\bullet}}^{\circ}$ and $\nabla c_{h_{\bullet}}$ as driving forces:

$$\begin{aligned}
 J_{V_{\bullet\bullet}}^{\circ} &= -D_{\nabla V(h)}^V \nabla c_{V_{\bullet\bullet}}^{\circ} - D_{\nabla h(V)}^V \nabla c_{h_{\bullet}} \text{ with:} \\
 D_{\nabla V(h)}^V &= D_{V_{\bullet\bullet}}^{\circ} + t_{V_{\bullet\bullet}}^{\circ} (D_{OH_{\bullet}^{\circ}} - D_{V_{\bullet\bullet}}^{\circ}) \\
 D_{\nabla h(V)}^V &= 0.5 t_{V_{\bullet\bullet}}^{\circ} (D_{OH_{\bullet}^{\circ}} - D_{h_{\bullet}}) \\
 J_{H_i^{\bullet}} &= -D_{\nabla V(h)}^H \nabla c_{V_{\bullet\bullet}}^{\circ} - D_{\nabla h(V)}^H \nabla c_{h_{\bullet}} \text{ with:} \\
 D_{\nabla V(h)}^H &= -2(D_{OH_{\bullet}^{\circ}} + t_{OH_{\bullet}^{\circ}} (D_{V_{\bullet\bullet}}^{\circ} - D_{OH_{\bullet}^{\circ}})) \\
 D_{\nabla h(V)}^H &= -(D_{OH_{\bullet}^{\circ}} + t_{OH_{\bullet}^{\circ}} (D_{h_{\bullet}} - D_{OH_{\bullet}^{\circ}}))
 \end{aligned} \tag{2.39}$$

Expressing the fluxes with $\nabla c_{h_{\bullet}}$ and $\nabla c_{OH_{\bullet}^{\circ}}$ as driving forces:

$$\begin{aligned}
 J_{V_{\bullet\bullet}}^{\circ} &= -D_{\nabla H(h)}^V \nabla c_{OH_{\bullet}^{\circ}} - D_{\nabla h(H)}^V \nabla c_{h_{\bullet}} \text{ with:} \\
 D_{\nabla H(h)}^V &= -0.5(D_{V_{\bullet\bullet}}^{\circ} + t_{V_{\bullet\bullet}}^{\circ} (D_{OH_{\bullet}^{\circ}} - D_{V_{\bullet\bullet}}^{\circ})) \\
 D_{\nabla h(H)}^V &= -0.5(D_{V_{\bullet\bullet}}^{\circ} + t_{V_{\bullet\bullet}}^{\circ} (D_{h_{\bullet}} - D_{V_{\bullet\bullet}}^{\circ})) \\
 J_{H_i^{\bullet}} &= -D_{\nabla H(h)}^H \nabla c_{H_i^{\bullet}} - D_{\nabla h(H)}^H \nabla c_{h_{\bullet}} \text{ with:} \\
 D_{\nabla H(h)}^H &= D_{OH_{\bullet}^{\circ}} + t_{OH_{\bullet}^{\circ}} (D_{V_{\bullet\bullet}}^{\circ} - D_{OH_{\bullet}^{\circ}}) \\
 D_{\nabla h(H)}^H &= -t_{OH_{\bullet}^{\circ}} (D_{h_{\bullet}} - D_{V_{\bullet\bullet}}^{\circ})
 \end{aligned} \tag{2.40}$$

Note that all three flux equations each defect represent the same physical processes and are just different ways to formally describe them. The flux of the holes is calculated via local electroneutrality (cf. eq. 2.24).

$$J_{h_{\bullet}} = -2J_{V_{\bullet\bullet}}^{\circ} - J_{H_i^{\bullet}} \tag{2.41}$$

Comparing the chemical diffusion coefficients, they are not independent on each other and the following linear relations among them are found.

$$\begin{aligned}
D_{\nabla H(V)}^H &= -D_{\nabla h(V)}^H \\
D_{\nabla V(H)}^H &= -2D_{\nabla h(H)}^H \\
D_{\nabla V(H)}^V &= -2D_{\nabla h(H)}^V \\
D_{\nabla H(V)}^V &= -D_{\nabla h(V)}^V \\
D_{\nabla V(h)}^V &= -2D_{\nabla H(h)}^V \\
D_{\nabla V(h)}^H &= -2D_{\nabla H(h)}^H \\
D_{\nabla V(h)}^V &= D_{\nabla V(H)}^V - 2D_{\nabla H(V)}^V \\
D_{\nabla H(h)}^H &= D_{\nabla H(V)}^H - 0.5D_{\nabla V(H)}^H
\end{aligned} \tag{2.42}$$

These relations arise from the different charge and sign of the defect concentration gradients (i.e. from the substitution process through electroneutrality). All in all, the twelve chemical diffusion coefficients given in eq. 2.38 to 2.40 are reduced to four independent ones necessary to describe the fluxes of $V_{\text{O}}^{\bullet\bullet}$, $\text{OH}_{\text{O}}^{\bullet}$ and h^{\bullet} . The complexity of the three compared to the two charge carrier situation arises from the fact that each charged diffusing species can simultaneously be coupled to two instead of only one other species (to preserve local electroneutrality); hence, it can be seen as tripolar diffusion.^[58] The strength of the coupling between the individual charge carriers (How much of the flux of species 1 is compensated by species 2 and 3?) depends on their concentrations and mobilities. As the time and space development of the concentration gradients cannot analytically be solved, numerical simulations are necessary to analyze and understand the “tripolar diffusion” in detail. As phenomenological consequence a flux of species k can occur without a driving force in its own gradient ∇c_k . Of course, for non steady-state situations as soon as the flux J_k starts a gradient in c_k develops.

This is e.g. found in the diffusion of water sketched in figure 2.4. Two limiting cases of transport are identified.^[30;33] Taking up water in a medium with only ionic carriers $V_{\text{O}}^{\bullet\bullet}$ and $\text{OH}_{\text{O}}^{\bullet}$ necessitates that both are directly coupled resulting in a so called single-fold chemical diffusion of water - figure 2.4a.^[33;54] In a medium with an additional fast third charge carrier, e.g. holes, the protons can migrate decoupled from oxygen vacancies by coupling to holes resulting in a fast chemical diffusion of hydrogen followed by a slower diffusion of oxygen (oxygen vacancy/hole couple) to incorporate water in total – figure 2.4b.^[30;33] Note that as derived from the above flux equations those two chemical fluxes cannot completely be described by two independent chemical diffusion coefficients as proposed by Kim and Yoo.^[33] A transient hole flux occurs although initially only a gradient in protons and oxygen vacancies is present (cf. simulations chapter 4.3 and experimental results chapter 4.4). Furthermore, even a so called “uphill” diffusion (i.e. flux of k against its own gradient, thus, uphill in terms of concentration gradient, but still downhill in terms of a gradient in electrochemical potential) found in permeation membranes can occur.^[67;68]

To cross-check the correctness of the flux equations the limiting two charge carrier situations are analyzed. For the chemical, ambipolar diffusion of water, i.e. in the absence of holes, i.e. $c_{h^{\bullet}} = 0$, hence, $t_{V_{\text{O}}^{\bullet\bullet}} + t_{\text{OH}_{\text{O}}^{\bullet}} = 1$, $0.5\nabla c_{\text{OH}_{\text{O}}^{\bullet}} = -\nabla c_{V_{\text{O}}^{\bullet\bullet}} = \nabla c_{\text{H}_2\text{O}}$ (electroneutrality) and

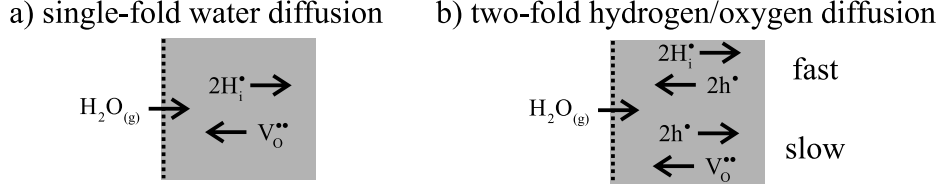


Figure 2.4: Sketch of a) single-fold diffusion of water in a medium (gray) with two mobile ionic charge carriers and b) two-fold diffusion of water in a medium with additional electronic mobile charge carriers. ^[30;33;54]

$0.5J_{H_i^*} = -J_{V_O^{**}} = J_{H_2O}$ eq. 2.39 (arbitrary chosen) simplifies to

$$J_{H_2O} = -(t_{OH_O^*}D_{V_O^{**}} + t_{V_O^{**}}D_{OH_O^*})\nabla c_{H_2O} = -D_{H_2O}^\delta \nabla c_{H_2O} \quad (2.43)$$

which equals the analytical solution. $D_{H_2O}^\delta$ can also be written in terms of the degree of hydration X . ^[69]

$$D_{H_2O}^\delta = \frac{(2 - X)D_{OH_O^*}D_{V_O^{**}}}{XD_{OH_O^*} + 2(1 - X)D_{V_O^{**}}} \quad (2.44)$$

For the chemical diffusion of hydrogen (absence of oxygen vacancies), $c_{V_O^{**}} = 0$, hence, $t_{h^*} + t_{OH_O^*} = 1$, $\nabla c_{OH_O^*} = -\nabla c_{h^*} = \nabla c_H$ and $J_{H_i^*} = -J_{h^*} = J_H$ eq. 2.39 simplifies to

$$J_H = -(t_{OH_O^*}D_{h^*} + t_{h^*}D_{OH_O^*})\nabla c_H = -D_H^\delta \nabla c_H \quad (2.45)$$

being the analytical solution for the respective system. For the ambipolar diffusion of V_O^{**} and h^* the correct result is obtained as well, cf. eq. 2.21.

2.3 Surface oxygen exchange kinetics

The oxygen reaction mechanism, i.e. reduction/dissociation of an oxide molecule is a complex process with several steps. The single steps itself depend on the material class of electrode (pure electronic or mixed conductor) and electrolyte (proton or oxide ion conducting). Typically, one of these steps is specifically much slower compared to the others, i.e. this step is rate determining and the other steps are in a quasi-equilibrium. Depending on the mobile defects in the cathode and electrolyte material, two principle mechanisms are outlined. The electrolyte considered in this work is a proton conductor with mobile protonic and V_O^{**} defects where at intermediate temperature and humid atmosphere the proton conductivity usually dominates over the V_O^{**} conductivity. The overall reaction at the cathode is given in eq. 2.46 highlighting that water is formed there, and that protonic and hole defects are involved.



As shown in the defect thermodynamics chapter 2.1 three different types of electrode material exist: Electrodes conductive for (i) protons and holes, (ii) oxygen vacancies and holes and (iii) only holes (or electrons). With respect to the two general mechanisms expected for proton-conducting electrolytes, the two latter are put together as they both are insulating for protons.

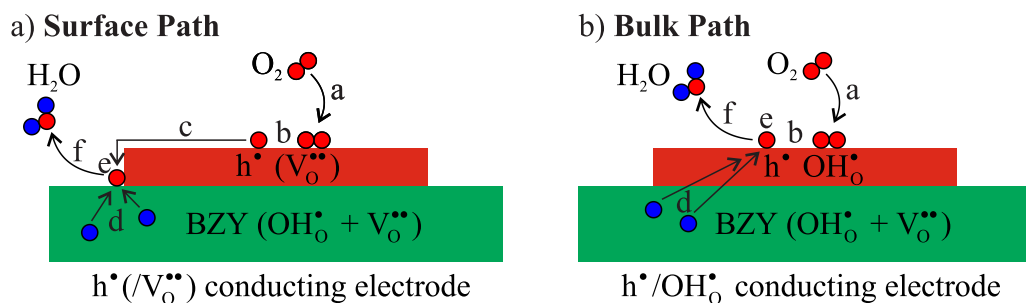


Figure 2.5: Sketch of the general deviation between surface and bulk path depending on the nature of the electrode material (red).

In figure 2.5 both mechanisms are sketched. Electrode materials of class (ii) (mixed-conducting perovskite such as BSCF, BSFZ, BSCN, LSCF, etc. under the assumption of not being proton-conductive) and (iii) (LSM, Pt) are insulating for protons, i.e. the water formation is limited to the triple-phase-boundary (TPB) length. The individual steps for the oxygen reduction in figure 2.5a are: a) Gas diffusion of the oxygen molecule. This can be rate-limiting for porous electrodes (small pores, large diffusion length) but can be ruled out as rate determining step (rds) for thin-film electrodes. b) Surface physi-sorption, transfer of 1 – 2 electrons (reduction, chemi-sorption) and dissociation and c) surface diffusion to the TPB (therefore, this mechanism is called “Surface Path”). After physi-sorption reduction/dissociation/surface migration do not necessarily occur in this order, i.e. one or several reduction steps can take place before, after or during the surface migration. d) Proton diffusion from the electrolyte to the TPB where e) water is formed and f) desorbed.

For electrode materials being conductive for protons and holes (or electrons) the protons from the electrolyte can migrate through the bulk of the electrode to the whole surface where then water is formed. Therefore, this mechanism is called “Bulk Path”, sketched in figure 2.5b. Steps a) (gas diffusion) and b) (adsorption, electron transfer and dissociation) are similar to the surface path, but, additionally, protonated intermediate species can occur which is possibly helpful for these steps (also for the surface path). Here, the protons directly migrate to the surface adsorbed oxygen species (d), water is formed there (e) and released to the gas phase (f). The sequence of the single steps does not necessarily follow this order and the protonation of the adsorbed oxygen species can occur at any step. This and the surface water formation has consequences compared to mixed-conducting electrodes on oxide-conducting electrolytes (e.g. YSZ, for which the mechanism is well understood). For such systems with V_O^{••} conducting electrolyte, the oxide ions formed by the reduction/dissociation must be incorporated into the cathode material (for the bulk path), and this step was found to be limiting based on impedance and DFT results.^[39;70;71] In contrast, having a mixed proton/hole conducting electrode on a proton-conducting electrolyte, this limiting step is not necessarily required and a different, maybe faster mechanism can be expected.

The most important measurement technique for an electrochemical scientist is impedance spectroscopy, i.e. measurement of complex AC resistances over an extended frequency range. The fundamental principle is that with impedance spectroscopy processes of different time scales can be separately extracted. The standard plot of an impedance spectrum, e.g. fig-

ure 2.6, is the real part Z_{real} of the complex impedance Z (in principle, the omic part) versus the imaginary part Z_{img} resulting from the phase shift between the input AC voltage and the output AC (capacitive contributions). The physical properties of an electrochemical cell can be represented with equivalent elements from electrical engineering, i.e. resistances, capacitances, inductances, etc. The most frequently used circuit is a resistance in parallel to a capacitor. For the Cole-Cole plot (real versus imaginary part of the complex impedance) a semicircle is measured for such a RC element and the frequency ω of the maximum of this semicircle is related to the time constant of this RC element by $\omega = (RC)^{-1}$. The physical meaning of these elements are discussed in detail in the next section. In the investigation of the oxygen reduction reaction (ORR), the most important element is the so called “surface reaction resistance” R_s . As already seen in the exemplary spectrum figure 2.6, this resistance dominates the overall impedance and can be related to the ORR at the electrode. This property is important as it is inversely proportional to the effective rate constant k^q of the rate limiting step which itself is proportional to the equilibrium exchange rate \mathfrak{R}_0 which equals because of microscopic reversibility the forward and backward reaction rates $\overrightarrow{\mathfrak{R}}$ and $\overleftarrow{\mathfrak{R}}$ - cf. eq. 2.47 (\overrightarrow{k} and \overleftarrow{k} respective rate constants and $[A]^a \dots$ equilibrium concentrations of the involved species A, B, ... with its respective reaction orders a, b, \dots).^[65;72] The required small disturbance keeps the system close to thermodynamic equilibrium (necessary to have a linear relation between input and output), forward and backward rates are equal. The superscript q denotes the origin of the disturbance owing to the measurement technique, here, an externally applied voltage.

$$\frac{1}{R_s} \propto k^q \propto \mathfrak{R}_0 = \sqrt{\overrightarrow{\mathfrak{R}} \overleftarrow{\mathfrak{R}}} = \overrightarrow{\mathfrak{R}} = \overleftarrow{\mathfrak{R}} = \sqrt{\overrightarrow{k} [A]^a [B]^b \dots \overleftarrow{k} [U]^u [V]^v \dots} \quad (2.47)$$

By measuring the dependence of R_s on different parameters such as geometry of the electrode, temperature and gas composition, mechanistic information about the rate determining step can be collected such as bulk or surface path (does R_s scale with electrode surface or TPB length), reaction order with respect to p_{O_2} and $p_{\text{H}_2\text{O}}$ and activation energy E_a (temperature dependence; note that E_a contains ΔH of preceding/succeeding quasi-equilibrium, thus, it is a weak parameter). In the next section a brief summary is given about the oxygen reduction mechanism for mixed-conducting electrodes on oxide-conducting electrolytes to give an impression what can qualitatively be expected for the same material on proton-conducting electrolytes.

2.3.1 Thin-film electrodes on YSZ electrolytes

In this section a summary of the results of BSCF thin-film electrodes on YSZ, collected by Lei Wang^[73], is shown as on the one hand BSCF microelectrodes were investigated on BZY and on the other hand BSCF is closely related to the here in detail investigated BSFZ (same structure with similar lattice constants and defect concentrations). Nonetheless, the results are expected to be transferable to other mixed-conducting electrode materials of perovskite type.

A typical impedance spectrum of a BSCF microelectrode on YSZ is shown in figure 2.6a. Three contributions to the total impedance are found which are highlighted in different colors and sketches in c). (1) An intercept in the high-frequency (HF) domain which is assigned to

the ionic bulk resistance R_b of the YSZ single crystal (orange, subscript b for bulk to separate it from grain-boundary contributions R_{gb} detectable in poly-crystalline electrolytes). The bulk capacitance (dielectric relaxation) is normally small (in the range of $10^{-12} \text{ Fcm}^{-2}$) and, therefore, outside the measurement range (high $\omega = (RC)^{-1}$). (2) A small medium-frequency (MF) contribution from the interface transfer of ions between electrode and electrolyte R_i (blue) in parallel to a respective interface capacitance C_i (in the range of 10^{-4} Fcm^{-2}), and (3) the dominating low-frequency (LF) contribution R_s (red) from the electrode accompanied with a large chemical capacitance C^δ (in the range of 10^{-2} Fcm^{-2} , respectively, 10^3 Fcm^{-3}) caused by stoichiometry change in the defect concentrations (the AC voltage changes the chemical potential of oxygen).^[65;74] The large porous silver counter electrode with its very small surface reaction resistance does not contribute to the impedance and is, therefore, not considered.^[13] The three contributions are fitted by the equivalent circuit shown in the bottom part of figure 2.6b. The physically correct equivalent circuit for the surface reaction resistance contributing to the electrode response (i.e. bulk instead of surface path) is given in the top part of figure 2.6b.^[13;74] For $C^\delta \gg C_i$ this model is mathematically equivalent to the circuit shown in the bottom part of the figure which can be regarded as a phenomenological equivalent circuit as it is a priori not known which path takes place. To be generally applicable (not fitting with a specific mechanism in mind, i.e. bulk path), the phenomenological equivalent circuit is used to fit all impedance spectra.^d However, the result does not differ from using the physically correct one. Besides the importance of R_s , the values of the capacitive contributions help to identify the respective process.

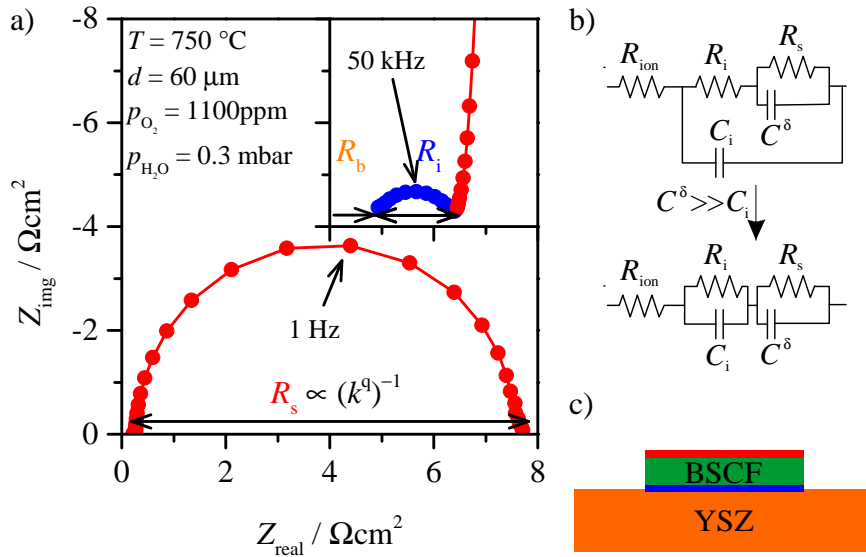


Figure 2.6: a) Typical impedance spectrum for a dense BSCF microelectrode (100 nm thin) on single-crystalline YSZ. The three contributions are colored the same way as in the scheme c). b) The physically correct equivalent circuit (top) derived from the generalized model which is mathematical equivalent to the bottom phenomenological equivalent circuit for $C^\delta \gg C_i$.^[13;74] The latter is used to fit the impedance spectra.

^dThe influence of an electronic short-circuit through the BZY electrolyte (section 4.5) further complicates deriving a physically exact equivalent circuit from the generalized model.^[74]

For BSCF on YSZ R_s scales inversely with the square of the microelectrode diameter, hence, oxygen reduction occurs via the bulk path. The activation energy is 1.6 ± 0.1 eV and the exponent of the p_{O_2} dependence is -0.73 ± 0.04 indicating that molecular oxygen is involved in the rds (explained in detail in chapter 4.6). A linear correlation between k^q and the product $D_{V_{\bullet\bullet}O}[V_{\bullet\bullet}O]$ suggest that actually the surface diffusion of an oxygen vacancy to the adsorbed oxygen species is rate limiting.^[70] The contribution of $V_{\bullet\bullet}O$ migration in the rds is confirmed by DFT calculations at least for LSM.^[71] The oxygen reduction mechanism for a variety of thin-film mixed-conducting perovskite electrodes on YSZ is inter alia discussed in references [8;70;71;75–78], see overview article by Wang et al.^[39] for more examples.

2.3.2 Porous electrodes on proton-conducting electrolytes

The performance and oxygen reduction kinetics of SOFCs using proton-conducting electrolytes (H^+ -SOFC) was studied for porous cathodes, partly composite (mixture of cathode and electrolyte material to enhance the TPB length and adjust thermochemical expansion), either for symmetric cells or real fuel cell setups. General qualitative statements across the literature data are given, details especially with respect to mechanistic conclusions need to be taken with care (because of electronic short-circuit through proton-conducting electrolytes^[48] – cf. next section 4.5) and cannot be transferred to dense thin-film electrodes, anyway. In general, using the same mixed-conducting electrode materials as for O^{2-} -SOFCs the formation of water at the triple-phase-boundary is expected by various authors, i.e. published mechanisms show single steps for the ORR where the water formation at the TPB is presumed.^[79–81] This includes the assumption that there is either very little or no proton-conductivity in these materials to enable the bulk path or at least to enhance the reactive zone close to the TPB. In contrast, Grimaud et al. give a mechanism where water is formed at the electrode surface and, in addition, suggest the necessity of incorporating the adsorbed oxygen atom species into an oxygen vacancy of the electrode (the rds for mixed conductors on YSZ), thus, assuming a mixed proton/electron conduction in the electrode material.^[25] The exponents of the p_{O_2} and p_{H_2O} dependency (dependency parameters) vary largely, even within a single publication for one composition but different morphologies. Published activation energies scatter less and are slightly above 1 eV, however, this information is not very helpful for the identification of the rds. A selection of p_{O_2} and p_{H_2O} dependencies of the surface reaction resistance (for porous electrodes typically denoted as polarization resistance) for different electrode materials on proton-conducting electrolytes is collected in table 2.1. All p_{O_2} dependencies are negative and are commonly around $-1/4$ ^[79;82]. A larger variation is found for p_{H_2O} dependencies as they even differ in sign. E.g. Grimaud et al. published a change from -0.96 to $+0.15$ for $PrBaCo_2O_{5+\delta}$ by changing the morphology from porous to “dense” (in the paper it is called “dense” but SEM images show that these electrodes are not as dense as thin-film electrodes are, they are just less porous).^[25]

Another influence on the impedance data measured in symmetrical cells (cathode material in the same oxidizing atmosphere on both sides of the electrolyte) is caused by the non-negligible electronic leakage in proton-conducting electrolytes in oxidizing atmosphere at moderate and high temperatures and has always be kept in mind. The data in this study suffer from this disturbance, but it is considered in the discussion. In contrast, this effect is not taken into account reading through literature data. It is e.g. an alternative explanation for change of

Table 2.1: Reported p_{O_2} and $p_{\text{H}_2\text{O}}$ dependency values for porous mixed-conducting cathodes on proton-conducting electrolytes.

Electrode	Electrolyte	m in $p_{\text{O}_2}^{-m}$	n in $p_{\text{H}_2\text{O}}^{-n}$	T range	ref.
$\text{Ba}_{0.5}\text{Sr}_{0.5}\text{Fe}_{0.8}\text{Cu}_{0.2}\text{O}_{3-\delta}$	$\text{Ba}(\text{Zr,Ce,Y})\text{O}_{3-\delta}$	0.25	0	600 – 700 °C	[82]
$\text{LaCoO}_3/\text{BCZY}$	$\text{Ba}(\text{Ce,Zr,Y})\text{O}_{3-\delta}$	0.1		500 – 600 °C	[81]
$\text{Sm}_{0.5}\text{Sr}_{0.5}\text{CoO}_{3-\delta}$	$\text{Ba}(\text{Ce,Sm})\text{O}_{3-\delta}$	0.19	0	400 – 700 °C	[79]
$\text{La}_{0.6}\text{Sr}_{0.4}\text{Fe}_{0.8}\text{Co}_{0.2}\text{O}_{3-\delta}$	$\text{Ba}(\text{Ce,Y})\text{O}_{3-\delta}$		0.01	600 °C	[25]
BSCF	$\text{Ba}(\text{Ce,Y})\text{O}_{3-\delta}$		0.12 to 0.6	600 °C	[25]
$\text{PrBaCo}_2\text{O}_{5+\delta}$	$\text{Ba}(\text{Ce,Y})\text{O}_{3-\delta}$		-0.15 to 0.96	600 °C	[25]

the sign in the $p_{\text{H}_2\text{O}}$ dependence reported by Grimaud et al..^[25] The influence is outlined in detail in chapter 4.5.

3 Experimental

3.1 Sample preparation

3.1.1 Powder preparation

$\text{BaZr}_{1-x}\text{Y}_x\text{O}_{3-\delta}$ – Powders of $\text{BaZr}_{1-x}\text{Y}_x\text{O}_{3-\delta}$ (BZY x) were synthesized by classical solid state reaction. Stoichiometric amounts of BaCO_3 (Fluka, $\geq 98.5\%$, Germany) and $\text{Zr}_{1-x}\text{Y}_x\text{O}_{2-\delta}$ (Tosoh, TZ-0Y, TZ-3Y, TZ-8Y, Japan) were mixed in an agar mortar and calcined at 1100°C for 8 h. The mixture was ball-milled for 2 h and subsequently annealed at 1300°C two times. The different compositions are listed in table 3.1.

Table 3.1: Net weights for the BaZrO_3 samples with different Y content for the solid state reaction to yield ≈ 60 g of final powder.

Composition	BaCO_3 <i>m/g</i>	TZ – 0Y <i>m/g</i>	TZ – 3Y <i>m/g</i>	TZ – 8Y <i>m/g</i>
BZY15	39.4740			24.3400
BZY6	39.4740		24.5200	
BZY4	39.4740	8.2147	16.3880	
BZY1	39.4740	20.5367	4.0867	

$\text{Ba}_{0.5}\text{Sr}_{0.5}\text{Fe}_{1-y}\text{Zn}_y\text{O}_{3-\delta}$ – Aqueous solutions of Fe (Sigma, $\geq 98\%$, USA) and Zn (Sigma, $\geq 99\%$, USA) nitrates (≈ 1 M, quantified by ICP-OES), and powders of $\text{Ba}(\text{NO}_3)_2$ (Fluka, $\geq 99\%$, Germany) and $\text{Sr}(\text{NO}_3)_2$ (Aldrich, $\geq 99\%$, USA) were used as starting materials (Ba and Sr nitrates contain no crystal water and can be weighted directly; Fe and Zn nitrates contain a variable amount, thus preparing stock solutions is more efficient). Stoichiometric amounts of Ba and Sr nitrates and Fe and Zn solutions were mixed with some bi-distilled water in a big beaker (11 for ≤ 15 g final powder). Ethylenediaminetetraacetic acid (EDTA) and citric acid (CA) were added with a molar ratio of $\sum n_{\text{cations}} : n_{\text{EDTA}} : n_{\text{CA}} = 2 : 2 : 3$ and the pH value was adjusted to 9 using 28% aqueous ammonia solution. The deep violet solution was subsequently heated under stirring. At 200°C the magnetic stir bar was removed and the temperature was further increased to ensure mixing the solution by boiling it. The solution polymerized to a black gel-like foam and finally ignited slowly to a brown ash at 500°C . The ash was ground in an agar mortar and put back into the beaker at 500°C to burn as much organic material as possible^a. The brown powder was ground again and calcinated in an alumina crucible for 10 h at 1100°C in air.^[40]

^aLeaving out this step can cause Zn organyls to evaporate during calcination.

$\text{Ba}_{0.5}\text{Sr}_{0.5}\text{Co}_{0.8}\text{Fe}_{0.2}\text{O}_{3-\delta}$ – Remaining powder of BSCF prepared by Lei Wang via wet chemical glycine nitrate method was used.^[83]

$\text{Ba}_{0.6}\text{Sr}_{0.4}\text{Co}_{0.9}\text{Nb}_{0.1}\text{O}_{3-\delta}$ – Donor-doped BSCN was synthesized by solid-state reaction. Stoichiometric amounts of BaCO_3 (Fluka, $\geq 98.5\%$, Germany), SrCO_3 (Aldrich, $\geq 99.9\%$, USA), Nb_2O_5 (Aldrich, $\geq 99.99\%$, USA) and Co_3O_4 (Alfa Aesar, $\geq 99.7\%$, USA) were mixed 1 h in a ball-mill, calcined 10 h at 950°C in air, ball-milled for another hour and finally annealed 5 h at 1100°C in air.^[6]

$\text{La}_{0.6}\text{Sr}_{0.4}\text{Co}_{0.8}\text{Fe}_{0.2}\text{O}_{3-\delta}$ – Powder of LSCF was purchased from HITEC Materials, USA.

3.1.2 Pellet preparation

BZY x – Dense, polycrystalline pellets were obtained by spark plasma sintering (SPS, FCT-Systeme, Germany). About 4 to 6 g of ball-milled powder was put into a graphite mold (20 mm diameter) and sintered in argon heating to $1500 - 1600^\circ\text{C}$ with 100Kmin^{-1} (measured with a pyrometer) and 15 kN pressure with 0.5kNmin^{-1} . The pellet was cooled without a defined ramp by switching off the current. The sintered pellet was post-annealed at 1700°C for 20 h in air. Pellets with up to 100% of theoretical density (occasionally, the substrates are even transparent, cf. SEM image figure 3.1a where the grains perfectly fit to each other and no pores are visible) are obtained.

Cathode materials – *Classical sintered*: About 1.5 g of ball-milled powder was isostatically pressed in a rubber mold (13 mm diameter) at 350 kN. The grain pellet was sintered in pure, dry oxygen. Sintering time and temperature for the different compositions are collected in table 3.2. The maximum achievable density was $\approx 96\%$ of the theoretical value. *SPS sintered*: 4 g of ball-milled powder were sintered at 1050°C heating with 300Kmin^{-1} (measured by a thermocouple) at 15 kN pressure. The pellet was cooled without a defined ramp by switching off the current. The density of the pellets was between 96 and $\approx 100\%$. Compare the SEM images of classical (figure 3.1b) and SPS (3.1c) sintered pellets where in the latter less pores are visible (both images in same scale).

Table 3.2: Temperatures and times for classical sintering in pure oxygen for different cathode materials.

Abbreviation	Nominal composition	$T / ^\circ\text{C}$	t / h
BSFZ	$\text{Ba}_{0.5}\text{Sr}_{0.5}\text{Fe}_{0.8}\text{Zn}_{0.2}\text{O}_{3-\delta}$	1200	8
BSCF	$\text{Ba}_{0.5}\text{Sr}_{0.5}\text{Co}_{0.8}\text{Fe}_{0.2}\text{O}_{3-\delta}$	1200	8
BSCN	$\text{Ba}_{0.5}\text{Sr}_{0.5}\text{Co}_{0.9}\text{Nb}_{0.1}\text{O}_{3-\delta}$	1200	5
LSCF	$\text{La}_{0.6}\text{Sr}_{0.4}\text{Co}_{0.8}\text{Fe}_{0.2}\text{O}_{3-\delta}$	1285	10

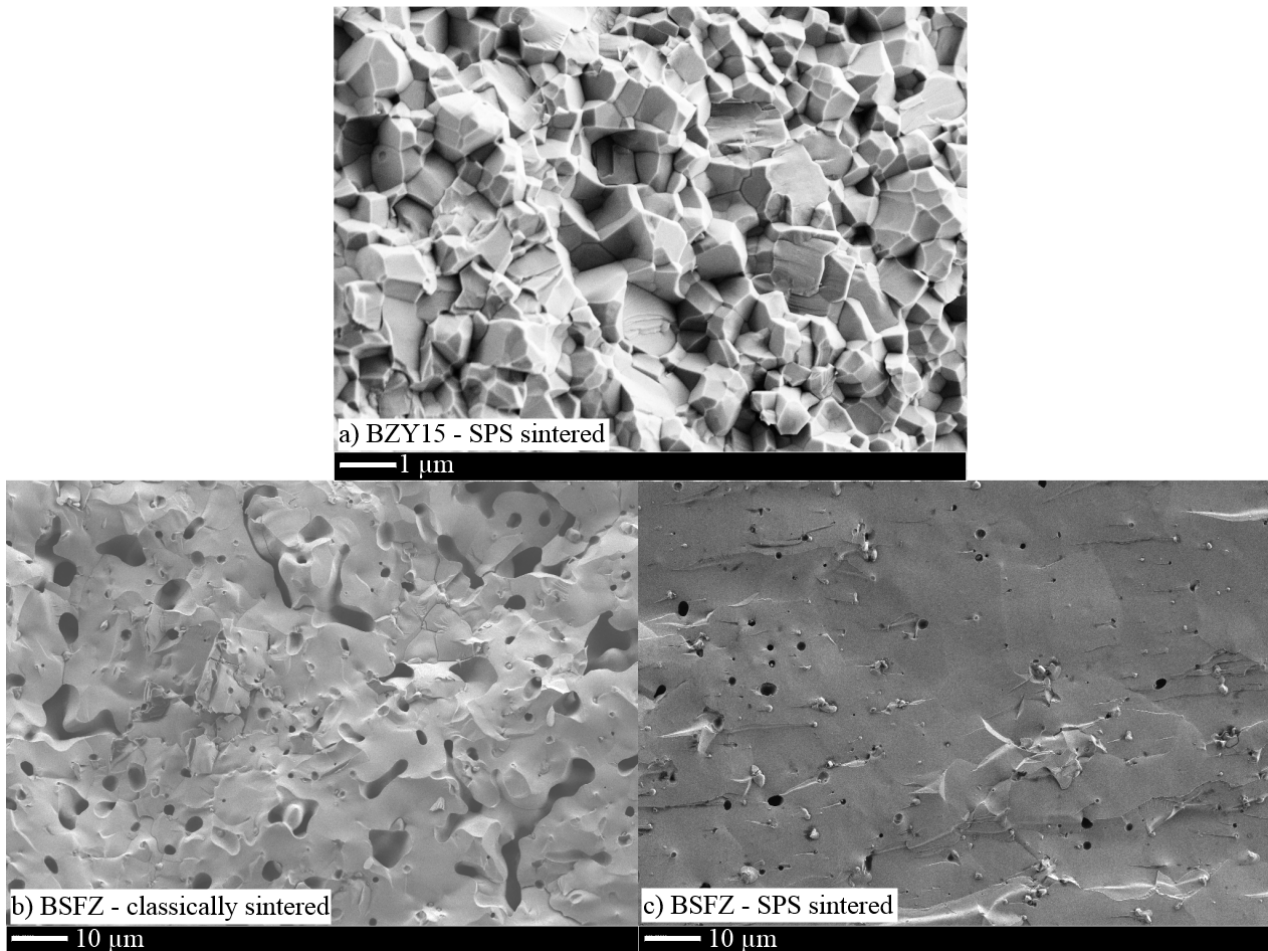


Figure 3.1: Scanning electron microscope (SEM) images of a) a SPS sintered, transparent BZY15 pellet, b) a classical and c) a SPS sintered BSFZ pellet.

3.1.3 Characterization - XRD

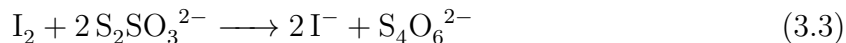
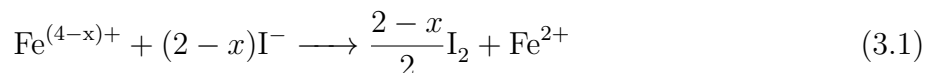
Room temperature powder diffraction patterns were recorded on a Philips PW 3710 X-ray diffractometer using $\text{Cu K}\alpha$ radiation in Bragg-Brentano geometry. Lattice parameters were refined using Topas-Software.

3.2 Characterization of the defect chemistry

3.2.1 Determination of the oxygen nonstoichiometry

The oxygen nonstoichiometry in dry, oxygen containing atmosphere was measured by thermogravimetry. A powder sample was equilibrated between 300 and 950 °C in 50 K (between 300 and 650 °C) and 100 K (between 650 and 950 °C) steps for 1 h (950 – 450 °C), respectively, 2 h (400 – 300 °C) both in 1% and 100% oxygen content. The oxygen concentration change between 1% and 100% was recorded at 950 °C.

An absolute value of the oxygen nonstoichiometry was determined by iodometric titration. A powder sample was equilibrated 3.5 h at 350 °C in 1% oxygen content and cooled to room temperature with 5 Kmin⁻¹. The mass increasing during cooling was recorded and corrected for buoyancy with an empty crucible measurement. About 30 mg BSFZ and 300 mg KI were added to a 500 ml Schlenk flask flushed with argon. 30 ml of bidistilled water and 10 pipettes of diluted hydrochloric acid (both liquids flushed with argon) were added to dissolve the powder with the help of an ultrasonic bath. Fe⁴⁺ and Fe³⁺ are reduced by I⁻ to Fe²⁺ and I₂ (equ. 3.1) which is kept dissolved by forming the tricomplex I₃⁻ (equ. 3.2). The formed I₂ is titrated using a 0.01 M sodium thiosulfate solution (Fixanal, Fluka Analytical, Germany). When the brown solution is titrated to light yellow some droplets of a starch solution was added resulting in a deep blue color. The solution was titrated to colorless.



3.2.2 Ex-situ determination of the water content

The absolute amount of water was determined by Karl-Fischer titration (KFT) and thermogravimetric analysis coupled with a mass spectrometer (TG-MS).

Room temperature – Classical sintered pellets were crushed carefully and sieved into smaller particles between 100 and 250 μm grain size. This was done to obtain an acceptable ratio between surface and volume to avoid too much error from adsorbed water at the surface and moderate hydration times. The grains were heated with 5 – 10 Kmin⁻¹ to 800 °C in humid nitrogen ($p_{\text{H}_2\text{O}} = 20$ mbar, $p_{\text{O}_2} \approx 10$ ppm) and step-wise cooled down to room temperature with 10 Kmin⁻¹ and equilibration times of 4 (highest T) to 24 h (200 °C).

High temperature – Water contents at fuel cell operating conditions were measured on the SPS sintered pellets used in the in-situ TG determination before (cf. next section). The pellets were equilibrated at constant temperature between 350 and 600 °C in 50 K steps, p_{O_2} (10 mbar and 1 bar) and $p_{\text{H}_2\text{O}} = 20$ mbar (17 °C thermostat temperature) and rapidly quenched within 1 min by cooling the quartz glass tube in ice water. A crucible made of gold foil was used to ensure good heat conduction.

Karl-Fischer titration – The absolute water content of hydrated grains/pellets was measured using a 831 KF-Coulometer (Metrohm, Germany). The setup is sketched in figure 3.2. Before the measurement the specimens were kept 1 h in an exsiccator with constant humidity (saturated $\text{Ca}(\text{NO}_3)_2$ aqueous solution) and temperature (air-conditioned laboratory) to ensure a reproducible fraction of surface water. About 500 mg of sample put into a quartz glass crucible were added into the cold zone of the mobile quartz glass tube and dry argon was flushed with $\approx 4 \text{ l h}^{-1}$ through the tube into the Karl-Fischer titration cell. After the drift in the cell decreased below $10 \mu\text{g min}^{-1}$ the tube was shifted so that the sample was in the hot zone of the tube furnace kept at 600°C to release the water. Data was recorded with a resolution of 2 s or 3 s until the initial drift was reached. The drift was subtracted from the total water content. The procedure was repeated with dry samples which were also kept in the exsiccator before to determine the amount of surface water.^[24] The reproducibility and reliability of the setup were cross-checked with $\text{CuSO}_4 \times 5 \text{ H}_2\text{O}$ powders (water content known from TG) of different weight.

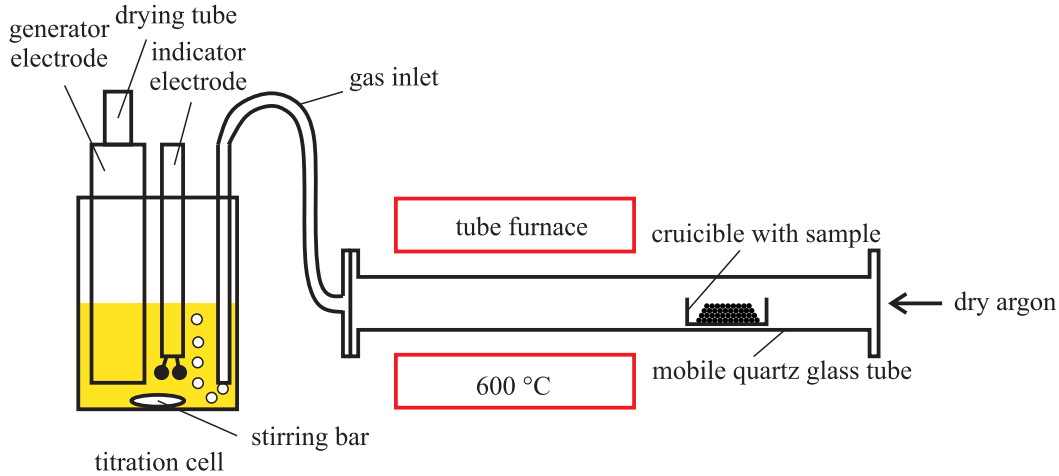


Figure 3.2: Setup of Karl-Fischer titration.^[24]

TG-MS – The hydrated grains were additionally analyzed by thermogravimetry coupled with a mass spectrometer. They were put into a STA449C Jupiter TG (Netzsch, Germany) and heated in dry nitrogen (flow rate = 30 ml min^{-1}) up to 800°C with 10 K min^{-1} to release the water. The gas outlet was analyzed with a mass spectrometer. The area of the mass signals related to water (18 and 17) were used to determine the absolute amount of water. Three different amounts of $\text{CuSO}_4 \times 5 \text{ H}_2\text{O}$ with known water content (from weight loss) were analyzed the same way to obtain a calibration line. An empty crucible was measured as well to be able to subtract the buoyancy effect.

3.2.3 In-situ determination of the mass relaxation upon $\Delta p_{\text{H}_2\text{O}}$

About 4 g of dense, SPS sintered BSFZ pellets were put in an alumina crucible into the STA449C Jupiter TG (Netzsch, Germany) used previously for the TG-MS water determination. The flow chart of the setup is shown in figure 3.3: Dry gas lines are colored black, H_2O humidified ones blue and D_2O humidified red. All gas inputs were fed with the same O_2/N_2 mixture from a gas bottle. The balance of the TG was flushed with 10 ml min^{-1} dry

gas through FC1 (protective gas) to keep the balance part (large volume) at constant gas composition. Both water and heavy water humidifiers were kept in the same thermostat. For D_2O the respective partial pressure was defined by the thermostat temperature and the flow rates between FC1 and FC4 which was kept constant at 50 mlmin^{-1} , i.e. the total flux through the sample was 60 mlmin^{-1} . The partial pressures of water and heavy water differ at same temperature (cf. tables in^[84] and $p_{D_2O} < p_{H_2O}$). To ensure same partial pressures at the same thermostat temperature (e.g. important for the SIMS analysis), the humid gas flux through FC3 is diluted with dry gas from FC2 in an appropriate ratio. The dry protective gas and humidified purge gas were mixed in the TG before entering the heated sample. The partial pressure of water or heavy water was calculated through the partial pressure in the humidifier defined by the thermostat's temperature and the flow rates of FC1 to FC4. A small amount of the gas output was introduced into a mass spectrometer through a quartz capillary heated to 200°C to prevent condensation. For the analysis upon Δp_{H_2O} (and Δp_{D_2O}) the temperature of the thermostat was abruptly changed from 5 to 12 to 18°C . However, it took ≈ 5 min until the final new partial pressure was reached at the sample.

An empty crucible was measured to check the necessity of a buoyancy correction which was found to be negligible upon Δp_{H_2O} and Δp_{D_2O} . Occasionally, the oxygen and water partial pressures were successfully cross-checked with a lambda sensor ZR5 (Zirox, Germany) and humidity sensor HygroClip (rotronic, Germany). The resolution of the Netzsch thermobalance is given with $1 \mu\text{g}$, its reproducibility and relative precision (checked with a calibrated laboratory balance (Sartorius, Germany)) was found to be $\pm 2 \mu\text{g}$ and 7×10^{-5} , respectively.^[85]

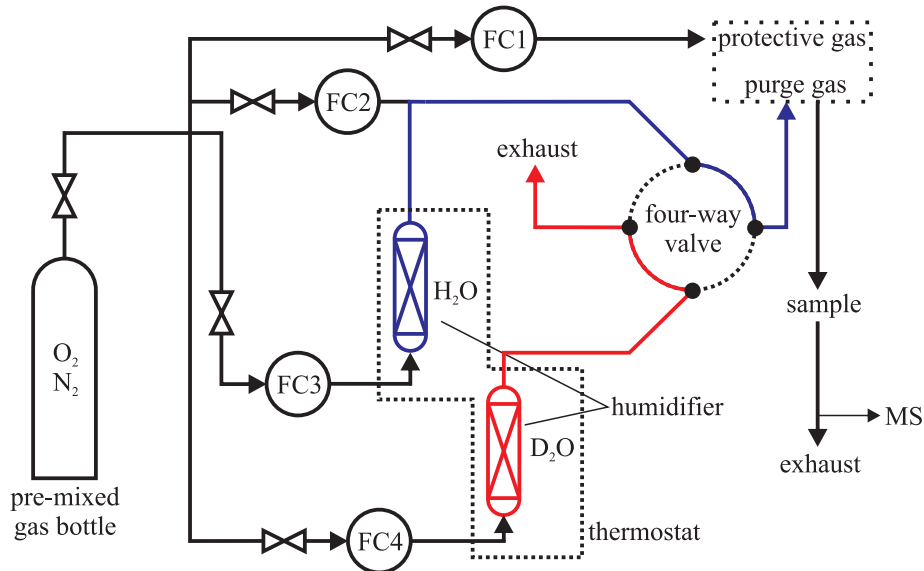


Figure 3.3: Flow chart of the thermogravimetric setup to analyze the mass transients upon Δp_{H_2O} , Δp_{D_2O} and to perform H/D exchange for the SIMS analysis. Dry gas lines are colored in black, H_2O humidified in blue and D_2O humidified in red.

3.2.4 Conductivity relaxation - DC

Conductivity relaxation experiments upon $\Delta p_{\text{H}_2\text{O}}$ were performed on dense thin-films.^[86] The setup is sketched in figure 3.4. A 300 nm thick, 2 mm wide and 5 mm long film of BSFZ was applied on a $5 \times 5 \times 0.5 \text{ mm}^3$ one-side polished MgO substrate with (100) orientation by PLD (substrate temperature = 770°C , $p_{\text{O}_2} = 0.4 \text{ mbar}$, laser pulse frequency = 5 Hz , pulse energy = 660 mJ , 30 min annealing at 650°C after deposition). A 2 mm broad stripe of the film was gas tightly covered by a 300 nm thin alumina layer applied by electron beam physical vapor deposition (PLD and EBPVD done by the Technology Group, MPI for Solid State Research, Stuttgart). Two electrical contacts were applied close to the Al_2O_3 /BSFZ interface by thin sputtered 400 nm Pt bars to the ends of which Pt wires were glued with silver paste (Demetron, Germany). Two additional Pt wires were glued to the very end of the BSFZ stripe. A four-point galvanostatic DC measurement was performed using a 2400 Digital Sourcemeter (Keithley, USA) and an in-house written software by Uwe Traub. The two outer contacts act as source where a constant current of $3 \mu\text{A}$ was applied and the voltage drop across the covered part of the thin-film was recored through the two inner contacts (Pt bars). The whole setup was put into a glass tube and a tube furnace. The gas composition was mixed through N_2 , O_2 and a 1% O_2/N_2 mixture and checked with a oxygen gas sensor ZR5 (Zirox, Germany). The water partial pressure was controlled with a humidifier kept at constant temperature in a thermostat. The thermostat temperature was changed between 2 and 17°C .

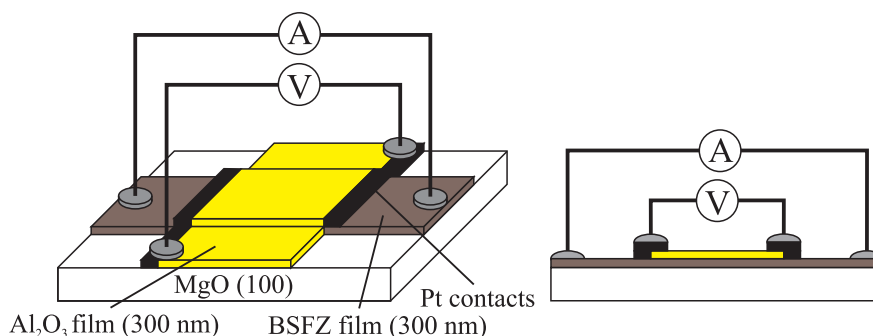


Figure 3.4: Four-point DC conductivity measurement setup on a dense thin-film sample.^[86]

3.2.5 Tracer diffusion - SIMS

Tracer profiles of deuterium were analyzed using time-of-flight secondary ion mass spectroscopy (ToF-SIMS). Dense, SPS sintered pellets of BSFZ were equilibrated in the Netzsch TG with the same setup used for in-situ mass relaxation experiments at constant temperature, p_{O_2} and $p_{\text{H}_2\text{O}}$. The gas composition was suddenly changed to D_2O . The partial pressures of H_2O and D_2O were chosen in a way to exclude chemical diffusion during the H/D exchange. For this purpose the proton and deuteron concentrations resulting from the thermodynamic mass relaxation analysis were used to calculate both partial pressures where the condition $[\text{OH}_\bullet] = [\text{OD}_\bullet]$ is fulfilled (owing to the isotope effect the concentration of deuterons is slightly lower than of protons at the same conditions). After one hour of H/D exchange the heating was stopped and the sample was left allowed to cool for about 20 min until it could be

removed from the TG (one has to wait until the temperature is low enough to avoid damage to the TG). During this time chemical diffusion could not be avoided and was considered in the analysis. After removing the pellets they were continuously cooled with dry ice to avoid a drift of the profile. The pellets were cast into a cold-curing conductive resin (Technovit 5000, Heraeus Kulzer, Germany) cooled with ice (less than 30 min). They were cut into two pieces and polished under cooling with dry ice (crystal preparation group, MPI for Solid State Research) to make the line profile accessible.

The SIMS analysis was performed by Tolga Acartürk (surface analysis group, MPI for Solid State Research) on a TOF-SIMS IV (ION-TOF, Germany). The surface of an area of $1000 \times 1000 \mu\text{m}^2$ was cleaned by sputtering for 30 min with a 2 keV Cs^+ source. An area of $500 \times 500 \mu\text{m}^2$ was measured in bunched mode (15 keV Ga^+) recording anions with an image resolution of $1024 \times 1024 \text{ pixel}^2$.

3.3 Dense thin-film microelectrodes

3.3.1 Sample preparation

Dense, SPS sintered and annealed pellets of BZY_x were cut into $5 \times 5 \times 0.5 \text{ mm}^3$ pieces and fine-polished (Plastic Polish HPA 10, Pieplow & Brandt, Germany) on one side (crystal preparation group). Dense, polycrystalline thin-film layers of BSFZ and BSCF (targets from classical sintered pellets) were applied by PLD with $\approx 100 \text{ nm}$ thickness (substrate temperature = $770 \text{ }^\circ\text{C}$, $p_{\text{O}_2} = 0.4 \text{ mbar}$, laser pulse frequency = 5 Hz , pulse energy = 660 mJ , 30 min annealing at $650 \text{ }^\circ\text{C}$ after deposition). Microelectrodes with 20, 40, 60, 80 and $100 \mu\text{m}$ diameter were created by photolithography (all Technology group). The resulting pattern is sketched in 3.6. The sample was glued on a $6 \times 6 \times 0.5 \text{ mm}^3$ sapphire plate (CrysTec, Germany) with silver foil ($25 \mu\text{m}$, Chempur, Germany) and silver paste (Demetron, Germany). The silver paste was dried in air at room temperature; the organic binder was burned during heating the sample in the microcontact chamber resulting in a porous silver counter-electrode.

3.3.2 Impedance spectroscopy

The microelectrodes were connected to the impedance analyzer (WE) by a new Pt/20% Ir needle (nominal tip radius = $2.5 \mu\text{m}$, Moser Jewel, USA) and the counter-electrode to the CE connection by an used PtIr needle. An Alpha High Resolution Dielectric Analyser with a POT/GAL 15V 10A Electrochemical Impedance Test Interface (Novocontrol, Germany) was used to record the impedance spectra from 1 MHz to 10 mHz at 20 mV amplitude. The impedance spectra were measured between 350 and $700 \text{ }^\circ\text{C}$, 100ppm and 100% oxygen content, 0.2 and 20 mbar water partial pressure and -200 and $+200 \text{ mV}$ DC bias.

A thermovoltage occurs between WE and CE for two reasons: Asymmetric heating of the sample and local cooling of the microelectrode through the PtIr tip. For partial pressure dependence measurements on microelectrodes with the same diameter the effect is constant and does, therefore, not change the result. For the temperature and diameter dependence analysis the cooling effect plays a role as for the T dependence the relative cooling effect is different at different temperatures and for the diameter dependence smaller microelectrodes are stronger affected than larger. The effect of the thermovoltage was checked by an additional external

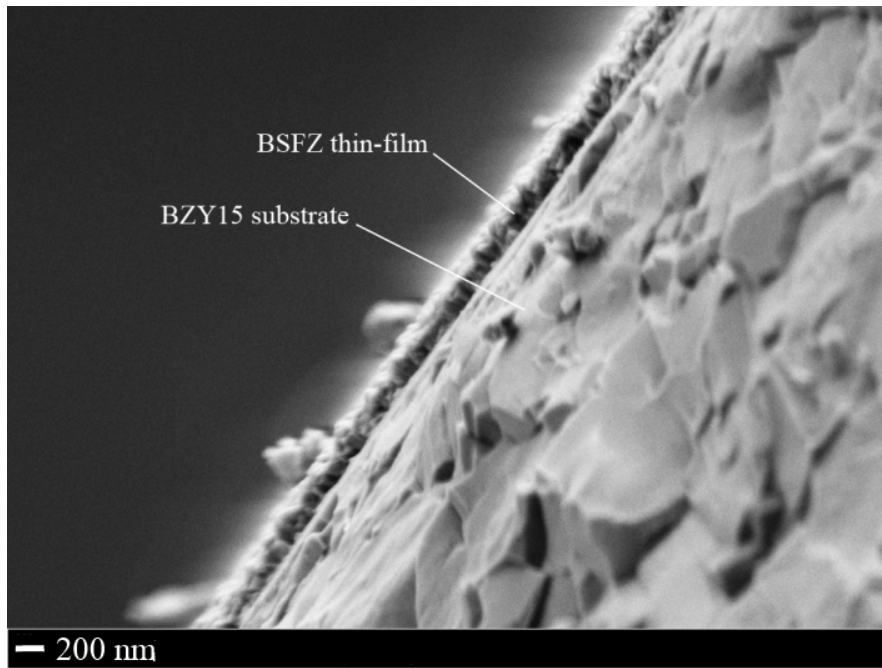


Figure 3.5: SEM image of a dense 100 nm BSFZ thin-film applied by PLD on a polished BZY15 substrate.

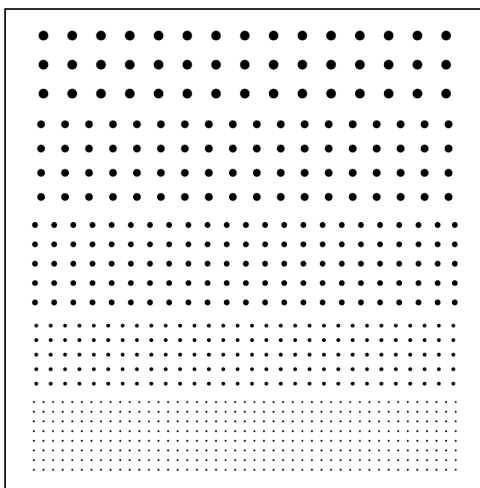


Figure 3.6: Schematic pattern of the microelectrodes applied on a $5 \times 5 \text{ mm}^2$ substrate.

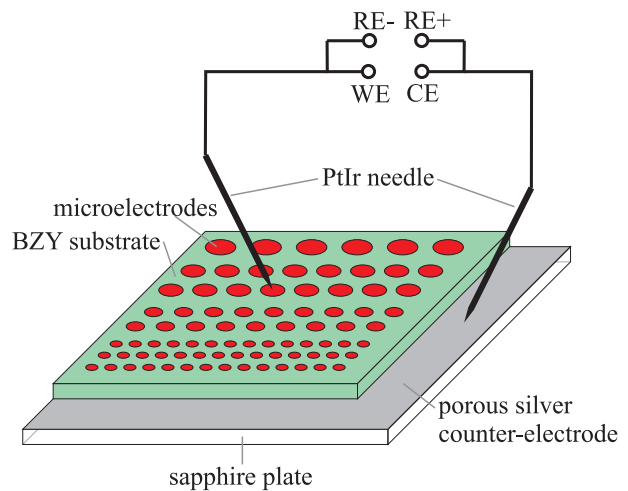


Figure 3.7: Schematic setup of the impedance measurements.

capacitor between WE connection and needle as suggested by Opitz et al. but its influence on the dependency parameters was found to be negligible compared to the disturbance by the electronic leakage in the BZY substrate (cf. chapter 4.5).^[87]

4 Results and Discussion

4.1 Sample characterization

After powder synthesis, the crystal structure and presence of a single phase is checked with XRD. In figure 4.1 one unit cell of the cubic perovskite structure ABO_3 (spacegroup $Pm\bar{3}m$) here with one oxygen vacancy δ is shown.^[88] The lattice oxygen forms corner sharing BO_6 octahedra with the small B cation in the center. The larger A site is located at the corners of the unit cell and coordinated by 12 oxide ions. The powder diffraction patterns from as-prepared powders of the four selected materials BSFZ, BSCF, BSCN and LSCF are shown in figure 4.2. All four crystallize single-phased, BSFZ, BSCF and BSCN in the cubic perovskite structure. In contrast, LSCF crystallizes in the rhombohedral form (spacegroup $R\bar{3}c$) which is more favorable for smaller A site cations (Goldschmidt tolerance factor $< 1^a$, cf. also the smaller pseudo-cubic lattice constant in table 4.1). The lattice parameters of the as-prepared powders are summarized in table 4.1. The lattice constant a of the electrode materials with cubic perovskite structure are comparable and smaller than of the BZY electrolytes (≈ 420 pm).

In figure 4.3 powder diffraction patterns of different BSFZ samples are collected. In black the same as-prepared sample as seen in figure 4.2 is shown as reference. In blue the powder was analyzed after fully hydration in 20 mbar p_{H_2O} cooling from 800 °C to room temperature to check that the hydrated form is stable. In red a pellet was measured after many heating/cooling, hydration/dehydration cycles to check phase stability. The average composition determined by ICP-OES (Analytical Chemistry, MPI for Intelligent Systems, Stuttgart) is $Ba_{0.50}Sr_{0.51}Fe_{0.80}Zn_{0.20}O_{3-\delta}$, i.e. a small but tolerable A site excess occurs. Occasionally, a

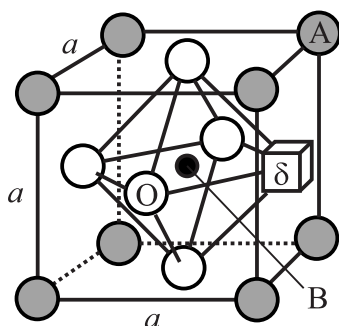


Figure 4.1: Unit cell of the cubic perovskite structure with one oxygen vacancy. Redrawn from Adler.^[88]

^aThe Goldschmidt tolerance factor is a parameter for the stability of the cubic perovskite structure (ideally 1) and is calculated to 0.98 for LSCF using the ionic radii r of A, B and O by $(r_A + r_O)/(\sqrt{2}(r_B + r_O))$, here, calculated for ionic radii taken from Shannon^[89] of La^{3+} , Sr^{2+} , Co^{3+} , Fe^{3+} and O^{2-} with their respective coordination.^[90]

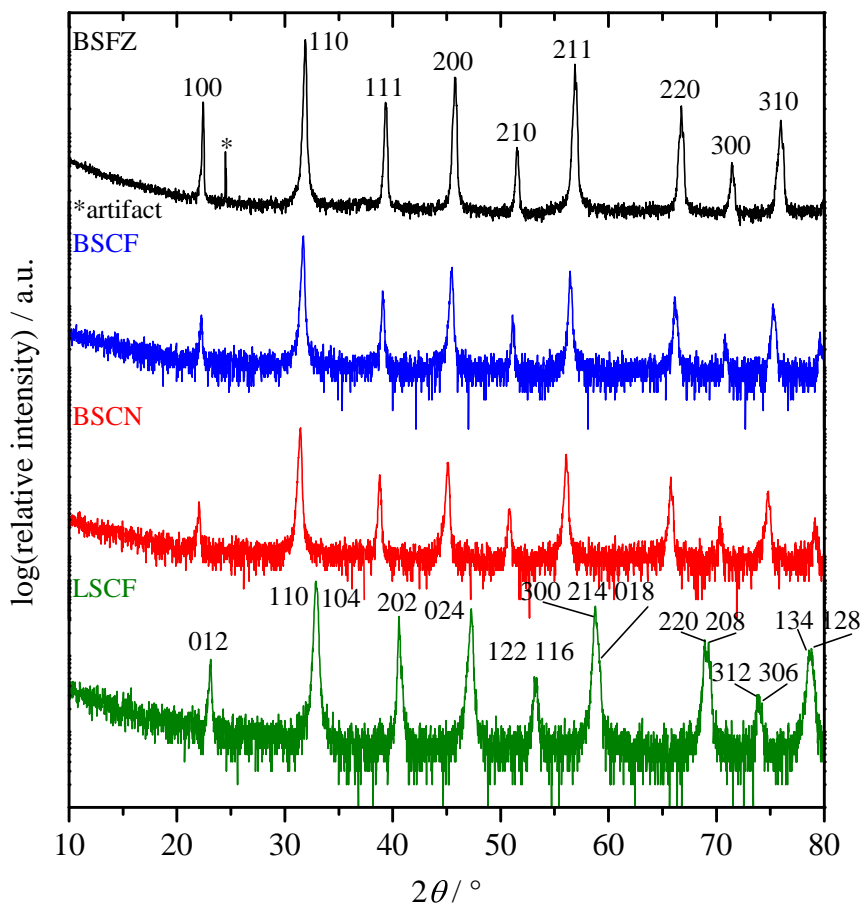


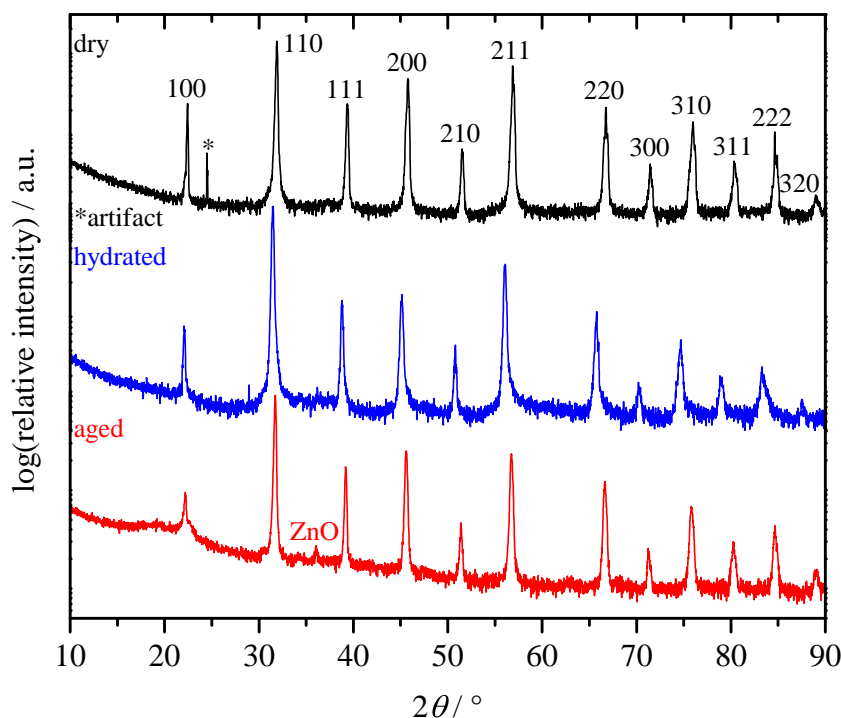
Figure 4.2: Powder diffraction patterns of as-prepared powder samples. The numbers indicate the miller indices hkl . For the rhombohedral structure of LSCF not all indices are shown. Ordinate scaled logarithmically to emphasize the presence or absence of secondary phases.

ZnO secondary phase was found, e.g. in the red pattern. However, the presence of the phase is not related to the aging of the material as it occurred in freshly prepared samples as well as disappeared after sintering or was not present in aged specimens. Owing to the small intensity in the diffraction pattern the amount is supposed to be less than 5% and was not taken into the defect chemistry analysis (the dopant concentrations are much higher than possible changes by formation of ZnO impurities).

Last but not least, the absence of the blocking character of grain-boundaries in samples of mixed-conducting perovskites (for proton-conducting perovskites they are highly blocking^[91–93]) was confirmed for BSFZ. In figure 4.4 an impedance spectrum ($T = 0^\circ\text{C}$ in dry N_2) of a SPS sintered pellet with 0.1 cm thickness, 0.16 cm^2 area and porous silver electrodes applied on both sides is shown. To shift the bulk contribution of the dielectric properties to an accessible frequency range ($\leq 10\text{ MHz}$) the pellet was equilibrated at 600°C in 1% p_{O_2} and quenched to room temperature to ensure a high resistance (low hole concentration) and, consequently, a low peak frequency $\omega = (RC)^{-1}$ of the semicircle. Only one semicircle is found in the impedance spectrum with a dielectric constant of $\epsilon_r \approx 75$ which is in the typical

Table 4.1: Perovskite structure and lattice parameters obtained from powder diffraction patterns by Topas software.

Composition	Structure	Lattice Parameters
BSFZ		$a = 396$ pm
BSCF	cubic ($Pm\bar{3}m$)	$a = 399$ pm
BSCN		$a = 401$ pm
LSCF	rhombohedral ($R\bar{3}c$)	$a = 545$ pm / $c = 1325$ pm (pseudo-cubic $a' = 384$ pm)

**Figure 4.3:** BSFZ diffraction patterns of as-prepared (black), hydrated (blue) powder and sintered pellet (red) after many heating/cooling and hydration/dehydration cycles. The variation of the lattice constant (shift of the signals) is caused by different $[OH_{\bullet O}^{\bullet}]$ and $[V_{\bullet O}^{\bullet}]$.

range for the bulk of mixed-conducting perovskites. As no further contribution is measured, the grain-boundaries are not blocking for holes^b and, hence, do not have to be taken into account in the analysis.^[95]

^bThe blocking character of grain boundaries arises from a non-negligible space charge layer forming a positively charged grain boundary core which is owing to repulsion (all point defects considered here are positive) blocking. Thus, the grain boundaries in BSFZ are expected to be not blocking for $V_{\bullet O}^{\bullet}$ and $OH_{\bullet O}^{\bullet}$, as well.^[94]

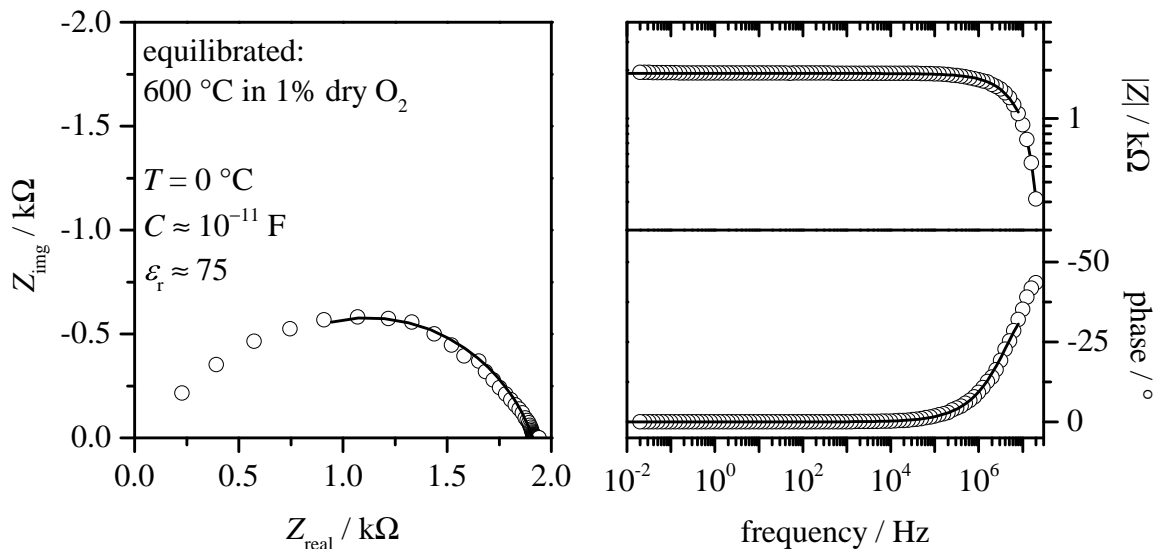


Figure 4.4: Impedance spectrum (complex and Bode plot) of a SPS sintered BSFZ pellet at 0 °C in dry N₂. The pellet was quenched in dry 1% p_{O₂} at 600 °C before.

4.2 Thermodynamic analysis

The defect chemistry of Ba_{0.5}Sr_{0.5}Fe_{0.8}Zn_{0.2}O_{3-δ} BSFZ was investigated by thermogravimetry, conductivity measurements and SIMS. Most qualitative and quantitative information was extracted from the thermogravimetric data. Conductivity and SIMS provide only qualitative information, yet, as their measurements are at the very beginning. Representative mass relaxations after p_{H₂O} change in 10 mbar and 1 bar p_{O₂} at 400 °C are shown in figure 4.5a and b. It is obvious that both the magnitude of the weight change as well as diffusion kinetics differ by roughly one order of magnitude each between both analyzed p_{O₂} values. In the next sections the defect concentrations of all charge carriers are analyzed for dry and humid conditions. The total conductivity is shown as well to check the suitability as electrode material and later to analyze the diffusion kinetics. As mentioned previously, the analysis of experimental data in dry atmosphere is straightforward as only two charge carriers are relevant and the thermodynamics can be reduced to equation 2.1. In the three charge carrier system the analysis is much more complex and side conditions have to be presumed.

For the analysis the following, general conditions are set: Ba²⁺, Sr²⁺ and Zn²⁺ have fixed valencies and the perovskite A³⁺B³⁺O₃ is taken as the undoped reference. Hence, the acceptor-dopant concentration in BSFZ is fixed to 1.2 ([Ba²⁺] + [Sr²⁺] + [Zn²⁺] = 0.5 + 0.5 + 0.2). Fe³⁺ is the regular lattice species Fe_{Fe}^x and Fe⁴⁺ is formally positive charged (Fe_{Fe}[•]), corresponding to localized electron holes h[•]. In oxidizing atmosphere, Fe_{Fe}['] (i.e. Fe²⁺) is very unfavorable, i.e. electrons e' as defect are neglected. The oxygen vacancy concentration varies between 0.2 (all Fe in 4+ oxidation state - BSFZ fully oxidized with maximum hole concentration) and 0.6 (all Fe³⁺ - hole concentration formally zero).

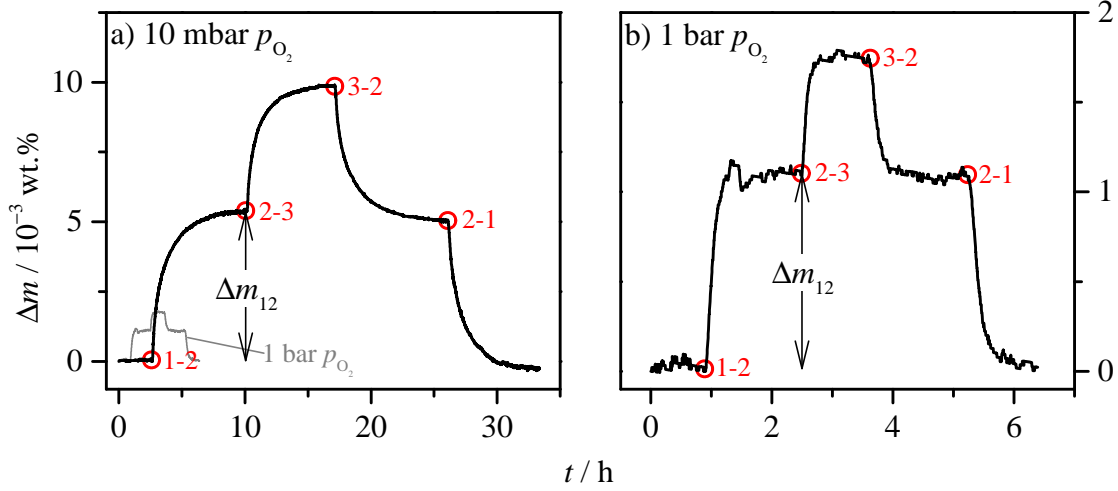


Figure 4.5: Representative mass relaxations of BSFZ pellets with 1.5 mm thickness in H_2O humid, oxidizing atmosphere at 400°C in a) 10 mbar and b) 1 bar p_{O_2} . At the red circles the $p_{\text{H}_2\text{O}}$ was abruptly changed from one value to another indicated by the red numbers with 1 = 5.70 mbar, 2 = 9.83 mbar and 3 = 14.5 mbar $p_{\text{H}_2\text{O}}$.

4.2.1 Dry atmosphere

In dry, oxidizing conditions protonic defects are absent and only oxygen vacancies and electronic holes have to be taken into account. Consequently, equation 2.1 with the respective equilibrium constant K_{ox} (eq. 2.4) is sufficient to describe the defect thermodynamics. The change in the oxygen vacancy concentration $\Delta\delta$ can directly calculated from the mass change Δm with changes in temperature and p_{O_2} as Δm is exclusively caused by the uptake or release of oxygen (M_{BSFZ} = molar weight of BSFZ ($\approx 212 \text{ gmol}^{-1}$) and M_{O} = molar weight of oxygen).

$$\Delta\delta = \frac{\Delta m \times M_{\text{BSFZ}}}{m_{\text{BSFZ}} \times M_{\text{O}}} \quad (4.1)$$

An absolute value for δ was measured for a quenched sample using iodometric titration and found to be 0.46 ± 0.02 at 350°C and 10 mbar p_{O_2} . From this reference all other, absolute δ values are calculated and the result for 10 mbar and 1 bar p_{O_2} in dependence of the temperature is shown in figure 4.6a. Data reported by Wei et al. are plotted in figure 4.6a and are in very good agreement.^[96] They lie in-between the values of this work which is expected as the p_{O_2} with 200 mbar (dry air) in the work of Wei et al. is in-between the p_{O_2} values of this work, as well. With the previously defined conditions the mean oxidation state of Fe can be calculated and is plotted as secondary ordinate on the right hand-side of figure 4.6a. At temperatures above 750°C the δ value reported by Wei et al. overshoots the value of 0.6 implying that Fe^{2+} occurs. In contrast, the data of this work confirm the unfavorable energetics of the 2+ oxidation state as δ approaches the $\delta = 0.6$ plateau at high temperatures (cf. 10 mbar data). Feldhoff et al. reported BSFZ non-stoichiometry data collected by TGA and iron oxidation states measured in-situ by Mössbauer spectroscopy in dry air.^[97] These $\Delta\delta$ are a bit lower but in principle in good agreement with data from Wei et al. and this work. In contrast, the absolute δ values and, consequently, the iron oxidation states are higher, i.e. at 950°C

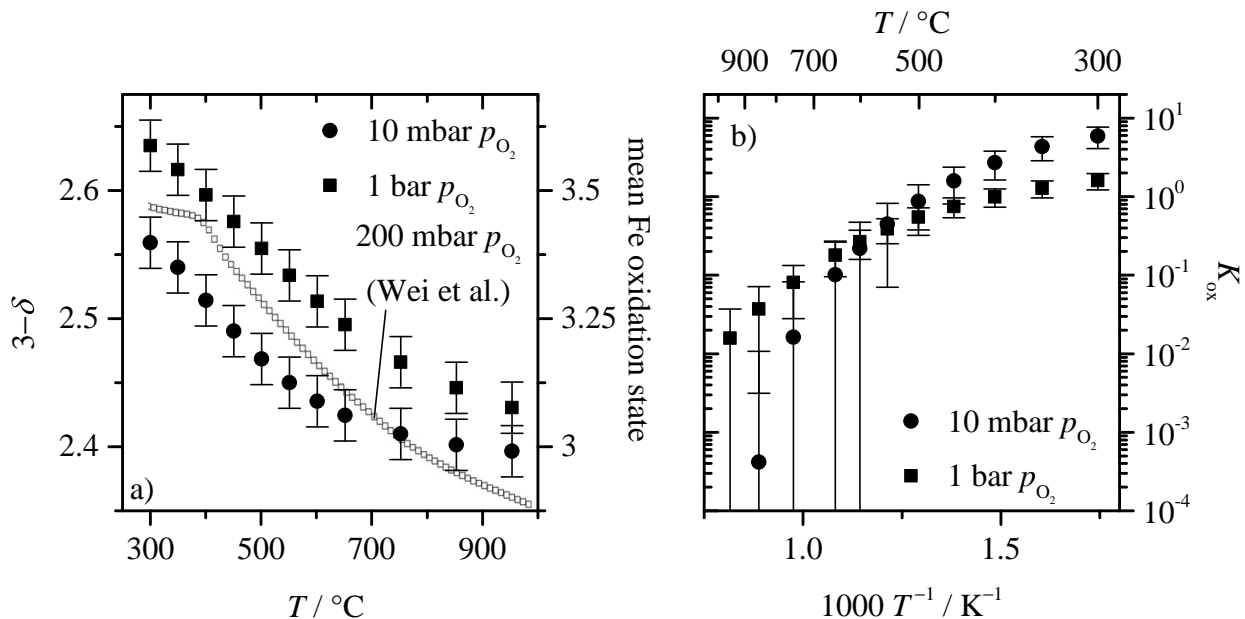


Figure 4.6: Thermodynamic data of BSFZ at 10 mbar and 1 bar p_{O_2} in dry conditions. a) Oxygen non-stoichiometry $3 - \delta$ and mean oxidation state of iron. Reported data by Wei et al. is put in the graph as open symbols.^[96] b) Calculated K_{ox} values using eq. 2.9 with $[A'] = 1.2$. The value at 950 $^\circ\text{C}$ and 10 mbar p_{O_2} is not reasonable as owing to the electroneutrality $[h^\bullet]$ is formally negative.

they reported a δ value of 2.5 and a mean oxidation state of 3.25+ instead of 2.4 and 3+ found in this work. At lower temperatures the mean oxidation states of Feldhoff et al. are in good agreement accommodating the lower $\Delta\delta$ values. Additionally, Feldhoff et al. supports the precondition of unfavorable Fe^{2+} as this species was not found. In contrast to the present work, both Wei and Feldhoff et al. discovered an inflection point in δ at 400 $^\circ\text{C}$. The difference in the measurement procedure is that Wei and Feldhoff et al. heated/cooled continuously with 5 Kmin^{-1} which might be too fast at lower temperatures even for powder samples. In the present work, the temperature was changed stepwise with $\Delta T = 50 \text{ K}$ and the mass change was recorded until full equilibration.

In figure 4.6b the K_{ox} values for 10 mbar and 1 bar p_{O_2} calculated through eq. 2.9 are shown ($[\text{OH}_\text{O}^\bullet]$ is zero). They coincide within one order of magnitude up to 750 $^\circ\text{C}$ (K_{ox} is p_{O_2} independent for ideal systems). The deviation might be related to the fact that calculating K from defect concentrations (the activity coefficients are assumed to be unity) fails at a certain point. As the oxygen vacancy concentration approaches its maximum value of 0.6 and, hence, the hole concentration formally reaches zero at high temperatures and low p_{O_2} K_{ox} rapidly decreases at 10 mbar p_{O_2} with increasing temperature. At the highest temperature δ slightly exceeds 0.6 (still valid within the error bar) resulting in a formally negative hole concentration. Therefore, this K_{ox} value has no physical meaning and the data point is skipped (the value is higher and not negative as the hole concentration is squared in eq. 2.4). From the van't Hoff plot of K_{ox} $\Delta_{\text{ox}}H^0$ and $\Delta_{\text{ox}}S^0$ can be calculated. This is analyzed together with

K_{hydrat} in the next section.

The total conductivity which equals the electronic hole bulk conductivity ($t_{h^\bullet} \approx 1$, no blocking grain-boundaries – cf. figure 4.4) was measured on bar shaped samples by four-point DC conductivity measurements in 10 mbar and 1 bar p_{O_2} (dry) between 300 and 700 °C.^[73] The results are plotted in figure 4.7a together with conductivity values reported by Wei et al.^[96] As expected, σ_{h^\bullet} is higher at higher p_{O_2} (higher h^\bullet concentration) with a maximum at 350 °C (10 mbar) and 400 °C (1 bar), respectively. Wei et al. reported values in the same order of magnitude but, however, with an maximum at 600 °C. In the publication of Wei et al. no experimental detail about the conductivity measurement is given. Owing to the high number of data points the question whether the sample was fully equilibrated to the environment arises. This might be the reason for the too low conductivity values at low temperatures (too low hole concentration) and the shift of the maximum (too high hole concentration). Nonetheless, this is pure speculation.

Figure 4.7b shows the mobility of the holes calculated from their conductivity and concentration (calculated from δ through the electroneutrality condition - cf. eq. 2.7) using

$$u_{h^\bullet} = \frac{\sigma_{h^\bullet} V_{\text{M,BSFZ}}}{e N_{\text{A}} [h^\bullet]} \quad (4.2)$$

(molar volume of BSFZ $V_{\text{M,BSFZ}} = 37.4 \text{ cm}^3 \text{ mol}^{-1}$, the defect concentration is given as molar fraction, $N_{\text{A}} = \text{Avogadro's number}$ and $e = \text{unit charge}$). The mobility of h^\bullet in BSFZ is slightly lower than reported for the zinc free related perovskite BSF by Jung et al.^[98] The reported mobility of BSF has a maximum at 400 °C. However, an explanation for the maximum in the

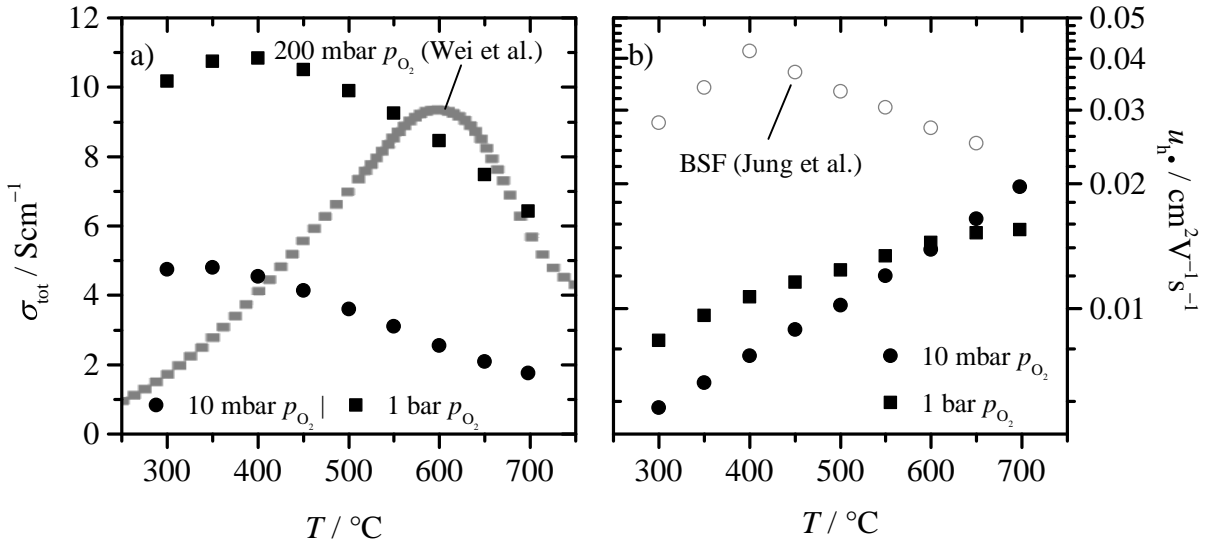


Figure 4.7: Electrical data for BSFZ in dry, oxidizing atmosphere with $p_{\text{O}_2} = 10 \text{ mbar}$ and 1 bar. a) Total (\approx electronic) conductivity. The gray symbols are copied from a work by Wei et al.^[96] b) Mobility of h^\bullet calculated from its concentration and conductivity. The open symbols are mobility values for BSF reported by Jung et al.^[98] All literature data were measured in dry air.

mobility as well as the negative slope above this maximum is not given. In contrast, the calculated mobility for BSFZ shows an increase with temperature as expected for small polaron hopping with an activation energy of 0.21 ± 0.01 eV for 10 mbar and 0.14 ± 0.01 eV for 1 bar p_{O_2} .

All in all, BSFZ has, in agreement with literature data, a high concentration of oxygen vacancies which is possibly a criterion for achieving a high proton concentration (uptake of water by acid-base reaction is easier than by redox reaction - cf. chapter 2.1). For a cathode material the electronic conductivity is rather small (cf. 40 Scm^{-1} for BSCF and $100 - 1000 \text{ Scm}^{-1}$ for LSCF^[39]). From an application point of view this will require higher demands with respect to the current collector.

4.2.2 Humid atmosphere

In humid atmosphere all three charge carriers $V_{\text{O}}^{\bullet\bullet}$, $\text{OH}_{\text{O}}^{\bullet}$ and h^{\bullet} have to be taken into account. The proton-concentration cannot ad hoc be calculated from the mass change upon $\Delta p_{\text{H}_2\text{O}}$ as have been done in dry atmosphere. Therefore, there is no simple, analytical solution anymore as the mass change can be caused by water and hydrogen uptake, and any mixed case. To have a first impression of the maximum proton concentration at room temperature particle sized samples of LSCF, BSCN, BSCF and BSFZ (in addition, also with 10 and 30 mol% Zn, denoted as BSFZ10 and BSFZ30) were hydrated down to room temperature in 20 mbar $p_{\text{H}_2\text{O}}$ and N_2 ($p_{\text{O}_2} \approx 10$ ppm). The proton concentrations measured by Karl-Fischer titration and thermogravimetric/mass spectrometric analysis are summarized in table 4.2 sorted through increasing concentration. The proton concentration seems qualitatively to increase with increasing $V_{\text{O}}^{\bullet\bullet}$ concentration which is, however, not the only criterion as e.g. BSCF has lower proton concentration as BSFZ but a comparable oxygen vacancy concentration. In contrast, for the series of BSFZ the proton concentration scales almost perfectly with the Zn concentration ($[\text{OH}_{\text{O}}^{\bullet}]_{\text{max}} \approx [\text{Zn}'_{\text{Fe}}]$). LSCF, BSCN and BSCF have exclusively redox-active transition metals on their B-site resulting in more covalent TM-O bonds and less negative $\Delta_{\text{hydrat}} H^0$.^[24]

Table 4.2: Measured proton concentrations of selected electrode materials with mixed conductivity by Karl-Fischer titration and thermogravimetry combined with mass spectra analysis. Particles (100 - 250 μm diameter) produced by crushing and sieving classically sintered pellets samples were hydrated at 20 mbar $p_{\text{H}_2\text{O}}$ in N_2 cooling stepwise from 800 °C to room temperature.

Composition	Abbreviation	$[\text{OH}_{\text{O}}^{\bullet}]$ at 20 °C / mol%	
		Karl-Fischer	TG-MS
$\text{La}_{0.6}\text{Sr}_{0.4}\text{Co}_{0.8}\text{Fe}_{0.2}\text{O}_{3-\delta}$	LSCF	0.04 ± 0.04	0.3 ± 0.2
$\text{Ba}_{0.5}\text{Sr}_{0.5}\text{Co}_{0.9}\text{Nb}_{0.1}\text{O}_{3-\delta}$	BSCN	1.0 ± 0.7	3 ± 1
$\text{Ba}_{0.5}\text{Sr}_{0.5}\text{Co}_{0.8}\text{Fe}_{0.2}\text{O}_{3-\delta}$	BSCF	10 ± 2	3 ± 1
$\text{Ba}_{0.5}\text{Sr}_{0.5}\text{Fe}_{0.9}\text{Zn}_{0.1}\text{O}_{3-\delta}$	BSFZ10	11 ± 5	not measured
$\text{Ba}_{0.5}\text{Sr}_{0.5}\text{Fe}_{0.8}\text{Zn}_{0.2}\text{O}_{3-\delta}$	BSFZ	21 ± 1	19 ± 1
$\text{Ba}_{0.5}\text{Sr}_{0.5}\text{Fe}_{0.7}\text{Zn}_{0.3}\text{O}_{3-\delta}$	BSFZ30	40 ± 10	not measured

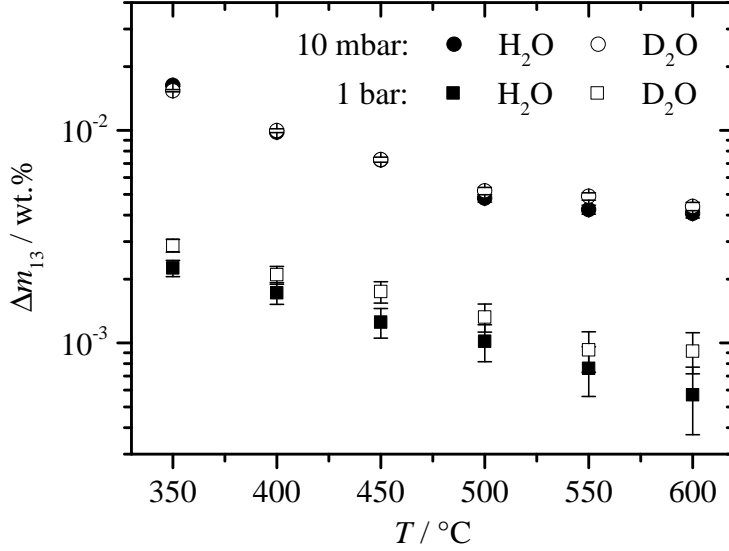


Figure 4.8: Mass change of BSFZ pellets upon changing $p_{\text{H}_2\text{O}}$ or $p_{\text{D}_2\text{O}}$ between 5.70 (5.95 for D_2O) and 14.5 mbar at 10 mbar and 1 bar p_{O_2} .

In contrast, Zn is redox-inactive fixed at 2+ oxidation state increasing the basicity of the oxide yielding more negative $\Delta_{\text{hydrat}}H^0$. This explains the almost direct proportional increase of the proton concentration with increasing Zn concentration from BSFZ10 to BSFZ30. BSCF and BSFZ seem to be promising candidates for mixed $\text{OH}^\bullet/\text{h}^\bullet$ conducting electrodes and are further investigated. BSFZ with the highest proton concentration and stability (BSFZ30 was at the border of stability as BSFZ40 could not be synthesized single-phased) is investigated in greatest detail to ensure a high signal to noise ratio in the TG in the first experiments.

In figure 4.8 the raw data for the mass change Δm of BSFZ dense pellets upon $p_{\text{H}_2\text{O}}$ change between 5.70 and 14.5 mbar (sum of both jumps in figure 4.5) are shown for H_2O and D_2O in both p_{O_2} . Two differences between both p_{O_2} are found: The mass change in 1 bar p_{O_2} is roughly one order of magnitude lower and the difference between H_2O and D_2O is more pronounced than in 10 mbar where the mass change is more or less independent on the water species.

For the analysis of this three charge carrier situation eq. 2.9 and 2.10 are used with $[A'] = 1.2$. For one single $p_{\text{H}_2\text{O}}$ jump both equations can be formulated for both $p_{\text{H}_2\text{O}}$ values where the sample is thermodynamically equilibrated (before the change and after full relaxation). This results in four equations (K_{ox} eq. 2.9 and K_{hydrat} eq. 2.10 formulated for both $p_{\text{H}_2\text{O}}$) and six unknowns ($[\text{OH}^\bullet]_1$, $[\text{OH}^\bullet]_2$, $[\text{V}^{\bullet\bullet}]_1$ and $[\text{V}^{\bullet\bullet}]_2$ at $p_{\text{H}_2\text{O}}$ 1 and 2, and the $p_{\text{H}_2\text{O}}$ independent K_{ox} and K_{hydrat} values). A fifth equation is obtained from the condition that the sum of the mass changes resulting from changes in $[\text{OH}^\bullet]$ and $[\text{V}^{\bullet\bullet}]$ have to equal the measured mass change (e.g. Δm_{12} in figure 4.5):

$$\Delta m_{12} = n_{\text{BSFZ}} [M_{\text{H}} ([\text{OH}^\bullet]_2 - [\text{OH}^\bullet]_1) + M_{\text{O}} ([\text{V}^{\bullet\bullet}]_1 - [\text{V}^{\bullet\bullet}]_2)] \quad (4.3)$$

(n_{BSFZ} = amount of BSFZ in mol, M_k = molar mass and $[k]_i$ = concentration of species k at $p_{\text{H}_2\text{O}}$ number i). As a system of five equations with six unknowns has an infinite amount

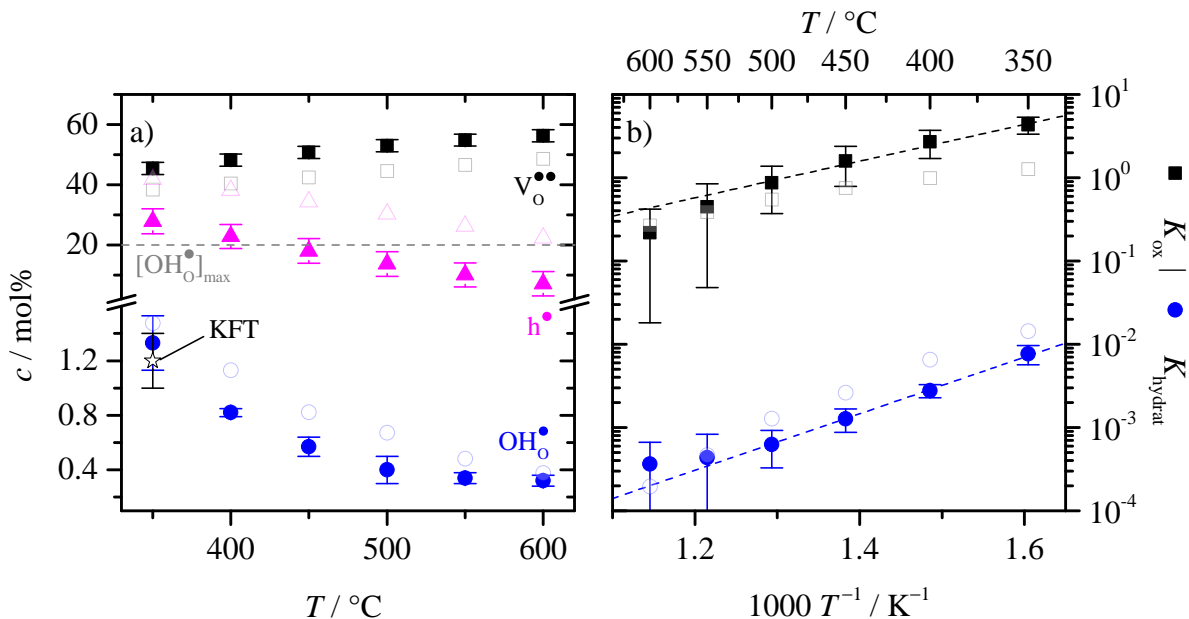


Figure 4.9: Thermodynamic results of the numerical solution for $p_{\text{O}_2} = 10$ mbar. The respective result for 1 bar p_{O_2} is shown in light open symbols. a) All three relevant defect concentrations. The value determined by Karl-Fischer titration of a hydrated, quenched pellet is shown as star. b) Calculated K values using eq. 2.9 and 2.10. The linear regressions to calculate ΔH^0 and ΔS^0 (eq. 2.11) are shown as dashed line.

of solutions, a further side conditions has to be set. As K_{ox} is only a function of the temperature and, hence, independent on the partial pressures, the values for K_{ox} calculated in dry atmosphere (previous section) are used for the calculations in humid atmosphere reducing the number of unknowns to five. Even for activity coefficients differing from unity this can be justified by the fact that the absolute concentration changes are small and that the activity coefficients, thus, remain unchanged. The set of five equations with five unknowns is numerically solved using MATLAB. The used MATLAB functions are given in appendix A.1. With the obtained K_{hydrat} and K_{ox} from dry conditions all three defect concentrations can be calculated for given $p_{\text{H}_2\text{O}}$.

In figure 4.9 the result of this procedure is shown for 10 mbar p_{O_2} and 20 mbar $p_{\text{H}_2\text{O}}$ (standard $p_{\text{H}_2\text{O}}$ used at $T_{\text{H}_2\text{O}} = 17$ °C of the humidifier (to avoid water condensation in the gas pipes without heating them the thermostat needs to be below room temperature)). It can be seen that $V_{\text{O}}^{\bullet\bullet}$ is the dominant species with respect to the concentration and is increasing with T (oxygen release). The concentration of h^{\bullet} is, however, lower and decreasing with increasing T and, finally, the $\text{OH}_{\text{O}}^{\bullet}$ concentration is roughly one order of magnitude lower and decreasing with increasing T (dehydration). From the slope and the intercept with the ordinate of van 't Hoff plot (figure 4.9b) ΔH^0 and ΔS^0 can be calculated from eq. 2.11. The linear regression is shown as dashed line in figure 4.9b, the resulting values are summarized in table 4.3 and discussed at the end of this section.

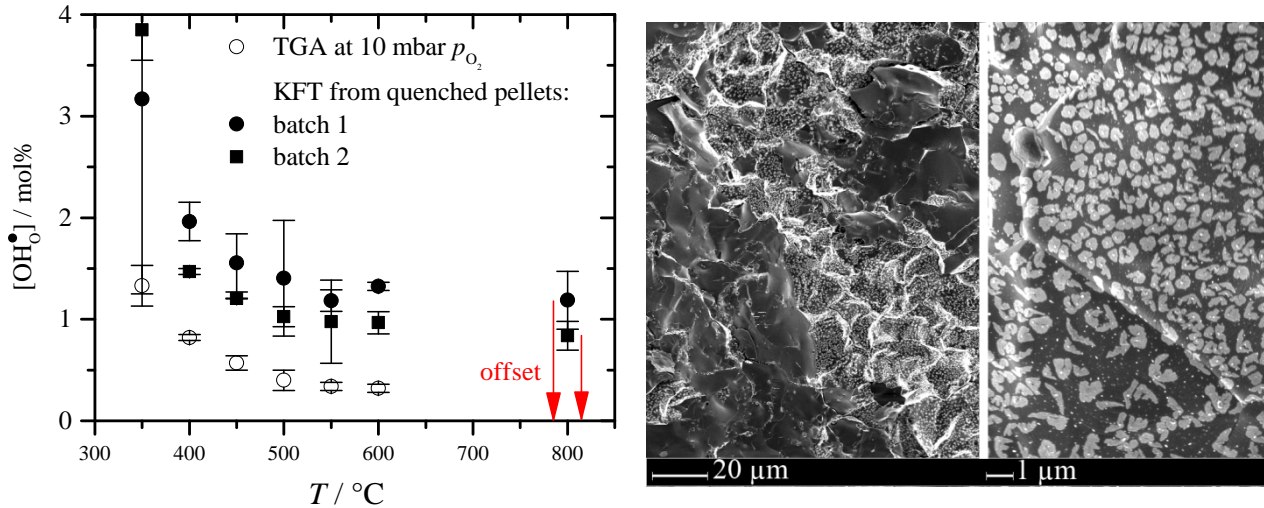


Figure 4.10: Left: Proton concentrations in 10 mbar p_{O_2} and 20 mbar $p_{\text{H}_2\text{O}}$ determined by Karl-Fischer titration of quenched pellets (closed symbols) compared to the results of the numerical calculation of the TG experiments (open symbols). Right: SEM images of one of these pellets.

To further check the stability of the numerical solution the water content was ex-situ determined by Karl-Fischer titration. After having finished the in-situ TG experiments their SPS sintered pellets were quenched between 350 and 600 °C at 10 mbar p_{O_2} and 20 mbar $p_{\text{H}_2\text{O}}$. In figure 4.9 the results of early measurements (“fresh”, i.e. less aged samples) at 350 °C are displayed by stars and agrees well with the TG experiment. Unfortunately, later measurements (aged samples) at other temperatures deviated from the TG results. In figure 4.10 left all results of two pellet batches are shown: batch 1 are the pellets used for the TG results in 10 mbar, batch 2 in 1 bar p_{O_2} . An additional point quenched from 800 °C was measured where the water concentration is supposed to be zero. It is obvious that there is an offset of the Karl-Fischer values as (i) the values at 800 °C are not zero, (ii) the deviation between the Karl-Fischer and the TG values is constant (constant offset) and (iii) this offset is different between both batches. Subtracting this offset the Karl-Fischer values agree quite well with the TG result. Reasons for the offset could be the quenching procedure, i.e. that during quenching the sample were partially hydrated in addition or surface adsorbed water fractions. The second reason is in agreement with the fact that this deviation occurred after several quenching and Karl-Fischer cycles. It has to be noted that these cycles mean harsh treatments to the sample as it is rapidly cooled (quenching), heated (water release for Karl-Fischer) and cooled (after KFT) during a short time period which might accelerate degradation effects of the surface. This is confirmed by SEM pictures shown in figure 4.10 right. The large dark areas without light spots are regions which were only exposed to air for a short time as the pellet was fractures just before entering it to the SEM. The areas with the light spots were exposed to air and the quenching/KFT conditions. The white spots might be some surface segregated clusters being responsible for the offset in the water content (e.g. (Ba,Sr) hydroxides or carbonates).

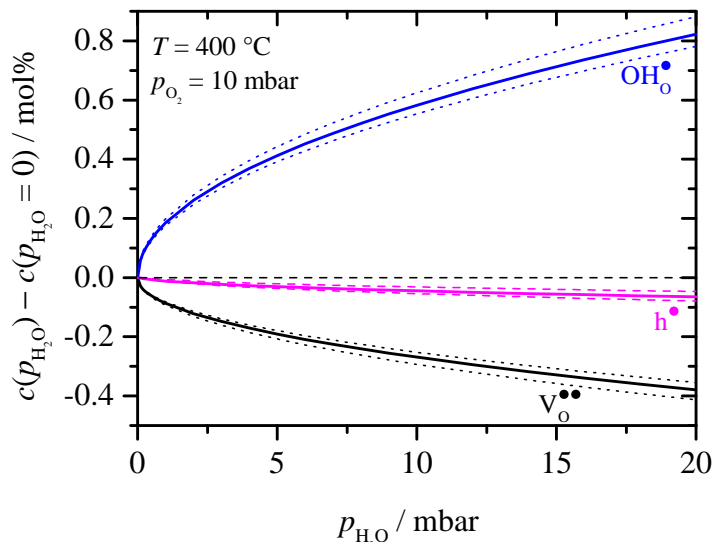


Figure 4.11: Change of the defect concentrations from the numerical solution at $T = 400\text{ °C}$ and $p_{\text{O}_2} = 10\text{ mbar}$ as function of $p_{\text{H}_2\text{O}}$. Errors are obtained from using the error ranges $K_{\text{ox}} \pm \Delta K_{\text{ox}}$ and $K_{\text{hydrat}} \pm \Delta K_{\text{hydrat}}$ in additional calculations.

Figure 4.11 shows the change of the defect concentrations as function of $p_{\text{H}_2\text{O}}$ at fixed $p_{\text{O}_2} = 10\text{ mbar}$ and $T = 400\text{ °C}$ as representative example. The concentrations follow a $\sqrt{p_{\text{H}_2\text{O}}}$ law as defined by the thermodynamic equations (2.5 and 2.6). The major fraction of protons is incorporated by acid-base equilibration, and the change in $\text{V}_{\text{O}}^{\bullet\bullet}$ is roughly half the change of $\text{OH}_{\text{O}}^{\bullet}$ (exactly half for pure acid-base reaction). Additionally, a minor fraction of protons is incorporated by redox reaction as also h^{\bullet} slightly decreases with increasing $p_{\text{H}_2\text{O}}$.

Applying this numerical procedure to the TG data in 1 bar p_{O_2} results in acid-base thermodynamics, as well. This can physically and mathematically be explained. The K_{ox} values derived from results in dry conditions (figure 4.6) do not change much between both examined p_{O_2} values (less than one order of magnitude in the relevant temperature range between 350 and 600 °C) which is physically reasonable as they are in fact supposed to be p_{O_2} independent. The $p_{\text{O}_2}^{1/2} K_{\text{ox}}$ values calculated from measurements in 1 bar p_{O_2} are less than 1.3. Having a look back at the thermodynamic defect model in chapter 2.1 (figures 2.1 and 2.2) at $p_{\text{O}_2}^{1/2} K_{\text{ox}}$ values up to unity predominantly water uptake upon $\Delta p_{\text{H}_2\text{O}}$ is expected. Therefore, using defect concentration instead of activities (which are not known) to calculate the thermodynamic constants, it is not a surprise that the numerical fit runs into the acid-base regime. Owing to the one order of magnitude smaller Δm values (cf. figure 4.8) also the protonic concentration would be one order of magnitude lower compared to 10 mbar p_{O_2} . In the following, three explanations are given that this cannot be the case for 1 bar p_{O_2} . Consequently, the proton concentrations are calculated through the assumption of pure hydrogen uptake.

(i) The Δm data not only differ in both p_{O_2} values, but also in H_2O compared D_2O . In 10 mbar the mass change is almost independent on the water species proving the incorporation of protons by acid-base reaction (a minor difference between uptake of H_2O ($M = 18\text{ gmol}^{-1}$) and D_2O ($M = 20\text{ gmol}^{-1}$) is hardly measurable). In contrast, in 1 bar O_2 the mass change in

D_2O is larger by roughly a factor two. In the case of pure acid-base water uptake, this would mean that the deuteron is twice the proton concentration which is from a thermodynamic point of view hard to believe. Of course, this statement is weakened owing to the overlapping error bars but, nevertheless, all Δm values in D_2O are larger without exception. On the contrary, assuming that in 1 bar p_{O_2} protons are incorporated by redox reaction (eq. 2.3) both differences to 10 mbar p_{O_2} are understood. The molar mass of H is smaller by a factor of 18 compared to H_2O resulting in a one order of magnitude smaller Δm (under the condition that the proton concentration is the same). The molar mass of D is twice the molar mass of H explaining the by a factor of two larger Δm (again under the condition of the same concentration).

(ii) Proton concentrations of pellet samples quenched from high temperatures between 350 and 600 °C determined by Karl-Fischer titration show that the concentration difference between both oxygen partial pressures is small. In figure 4.13 three values are added as star: For 350 and 500 °C measured at 1 bar p_{O_2} , for 350 °C additionally at 10 mbar p_{O_2} . It can be seen that the data points at 350 °C are close together and that all three shown results agree very well with the values calculated through the mass relaxation. Unfortunately, with increasing amount of hydrating/quenching/KFT cycles the results start to deviate which was discussed two pages before (figure 4.10).

(iii) The mass transients clearly show that the relaxation is up to two orders of magnitude faster in 1 bar than in 10 mbar p_{O_2} (cf. figure 4.26). If acid-base thermodynamics takes place in both p_{O_2} values the mobility of $V_{O}^{\bullet\bullet}$ has to be very different in both cases (the mass transient is dominated by motion of $V_{O}^{\bullet\bullet}$). This can physically be not the case as $D_{V_{O}^{\bullet\bullet}}$ is independent of p_{O_2} (of course, small variations are possible and the transient of the slow $V_{O}^{\bullet\bullet}$ motion is determined not only by $D_{V_{O}^{\bullet\bullet}}$ but this is discussed in detail in chapter 4.3). In contrast, the assumption that in 1 bar p_{O_2} the transient is largely caused only by the motion of hydrogen perfectly explains this very different behavior. Note that argument (iii) is probably the weakest as is can not ruled out that the faster transients result from cracks in the pellet. This is discussed in detail in chapter 4.4.1. However, (i) and (ii) alone certainly support the following statements.

How can this apparent contradiction be resolved? While the protons can easily be assumed as ideal dilute, it is obviously not the case for $V_{O}^{\bullet\bullet}$ and h^{\bullet} . For the measurements at 10 mbar p_{O_2} the deviation between concentrations and activities has no significant influence on the analysis as BSFZ is in the acid-base regime, anyway. For 1 bar p_{O_2} the difference in the activities between $V_{O}^{\bullet\bullet}$ and h^{\bullet} obviously causes a shift from acid-base to redox thermodynamics despite $[V_{O}^{\bullet\bullet}] > [h^{\bullet}]$ (i.e. for the activities a probably $a_{V_{O}^{\bullet\bullet}} < a_{h^{\bullet}}$), but the fit to the defect model in terms of concentrations yields acid-base water incorporation. On the one hand, calculated K_{ox} values using $[OH_O^{\bullet}]$ obtained from both limiting cases, i.e. pure acid-base (Δm only from water uptake, minimum proton concentration) and pure redox (Δm only from hydrogen uptake, maximum proton concentration) thermodynamics, are close to each other and close to the values in dry conditions; the deviation is smaller than the error. On the other hand from a mathematical point of view, the difference from K_{ox} calculated from dry conditions to K_{ox} calculated with proton concentrations derived from assumed acid-base thermodynamics is smaller than to K_{ox} calculated with proton concentrations obtained from

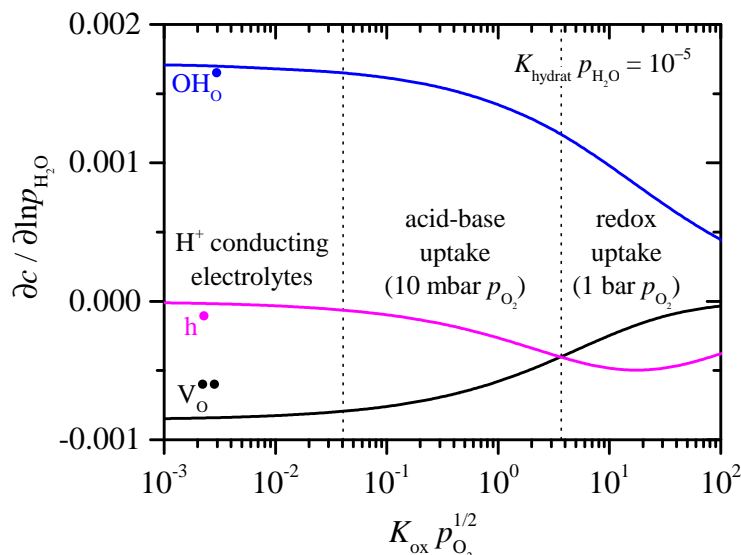


Figure 4.12: Finite change of the defect concentrations divided by a finite change of $p_{\text{H}_2\text{O}}$ using the thermodynamic defect model with an acceptor-dopant concentration of 1.2 (BSFZ) as function of $K_{\text{ox}} p_{\text{O}_2}^{1/2}$ for a representative constant value of $K_{\text{hydrat}} p_{\text{H}_2\text{O}} = 10^{-5}$.

redox thermodynamics. Thus, the mathematical minimum of errors (within the model of ideally dilute defects) is found in the acid-base regime.

To summarize, in 10 mbar p_{O_2} protons (i.e. water) are taken up predominantly by acid-base reaction resulting in a slower mass transient and larger mass change. In 1 bar p_{O_2} protons are incorporated mainly by redox reaction giving faster mass relaxations and smaller mass changes. It is exciting that the thermodynamic mechanism of proton uptake changes within only two orders of magnitude in p_{O_2} which corresponds to a factor of 10 on the $K_{\text{ox}} p_{\text{O}_2}^{1/2}$ scale which is, however, supported by the thermodynamic model presented in chapter 2.1. In figure 4.12 the change of the defect concentrations upon changing $p_{\text{H}_2\text{O}}$ for BSFZ at a representative $K_{\text{hydrat}} p_{\text{H}_2\text{O}}$ value of 10^{-5} is plotted for a $K_{\text{ox}} p_{\text{O}_2}^{1/2}$ range relevant for oxidizing conditions and BSFZ. For high $K_{\text{ox}} p_{\text{O}_2}^{1/2}$ values, i.e. representing the conditions in 1 bar, more protons are taken up by the loss of holes than by oxygen vacancies (redox uptake). The thermodynamics switches to the acid-base dominated range upon rather small changes in p_{O_2} representing the conditions in 10 mbar. The border where $[\text{V}_{\circ}^{\bullet\bullet}] = [\text{h}^{\bullet}]$ was identified as thermodynamic criterion distinguishing between predominantly acid-base and redox proton-uptake (cf. figure 2.1 and 2.2). The defect concentrations extracted from TG data for BSFZ show that $[\text{V}_{\circ}^{\bullet\bullet}]$ is always larger than $[\text{h}^{\bullet}]$ (figure 4.13) but, of course, the difference is less at 1 bar, respectively, at the lowest temperatures $[\text{h}^{\bullet}]$ equals $[\text{V}_{\circ}^{\bullet\bullet}]$. The difference between theory and experiment is owing to the fact that the defects obviously cannot be handled as ideally dilute, i.e. the activity coefficients differ. This shifts the “ $[\text{V}_{\circ}^{\bullet\bullet}] = [\text{h}^{\bullet}]$ criterion” and a change from acid-base to redox proton uptake can occur although $[\text{V}_{\circ}^{\bullet\bullet}] \geq [\text{h}^{\bullet}]$. Therefore, the criterion to a priori distinguish between acid-base and redox thermodynamics, namely the ratio between $[\text{V}_{\circ}^{\bullet\bullet}]$ and $[\text{h}^{\bullet}]$ derived in chapter 2.1, cannot directly be applied here. In addition, the changed defect concentration can lead to different hydration (less negative $\Delta_{\text{hydrat}} H^0$ for higher hole

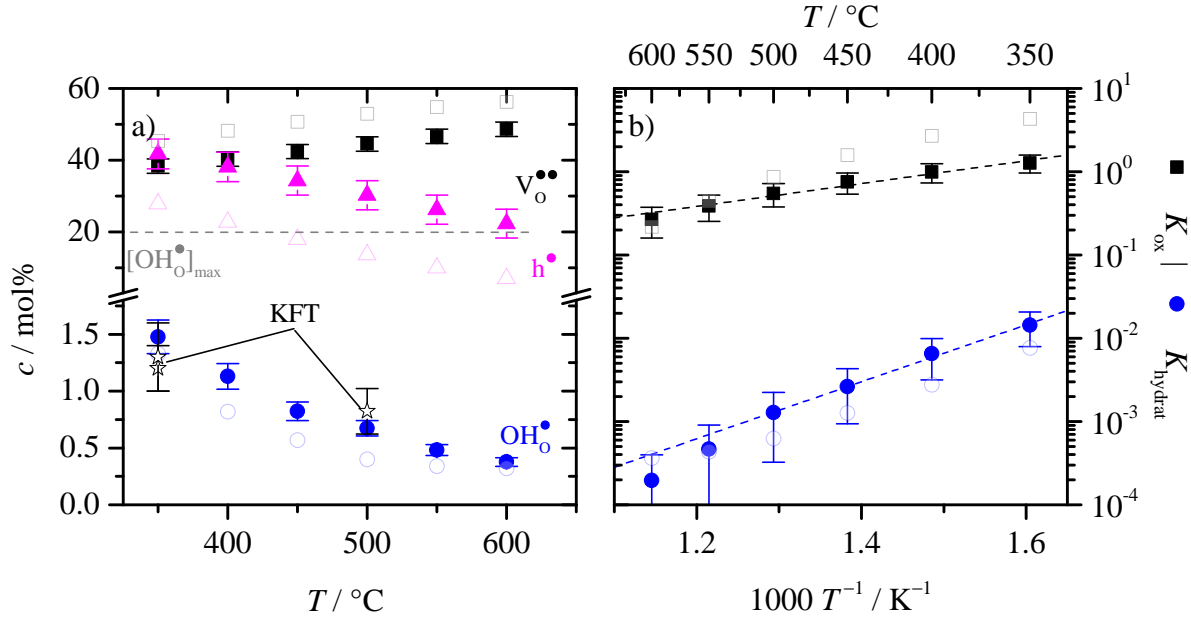


Figure 4.13: Thermodynamic results of the numerical solution for $p_{O_2} = 1$ bar assuming that $[V_O^{\bullet\bullet}]$ does not change with p_{H_2O} . The respective results for 10 mbar p_{O_2} (under different assumptions) are shown in light open symbols. a) All three relevant defect concentrations. Exemplary results from KFT determined proton concentrations from hydrated and quenched samples are shown as stars. b) Calculated K values using eq. 2.9 and 2.10. The linear regressions to calculate ΔH^0 and ΔS^0 (eq. 2.11) are shown as dotted line.

concentrations) and oxidation Gibbs free enthalpies ΔG^0 which can cause a higher change in $K_{ox} p_{O_2}^{1/2}$ and in $K_{hydrat} p_{H_2O}$. Hence, the experimental results behaving obviously non-ideal do not contradict with the ideal thermodynamic model.

The defect concentrations in 1 bar calculated under the condition that $[V_O^{\bullet\bullet}]$ does not change upon p_{H_2O} (only proton uptake by redox reaction eq. 2.3) are shown in figure 4.13a. The proton concentration change can, in principle, directly be calculated from the mass change which now refers only to a contribution of protons. To calculate absolute concentrations and K_{hydrat} MATLAB script A.4 is used where K_{ox} is implicitly included into the calculation by fixing $[V_O^{\bullet\bullet}]$ to its known value in dry atmosphere. For comparison, the respective values for 10 mbar p_{O_2} are drawn in light colors. The proton concentration in the higher p_{O_2} is slightly larger. With the three arguments for the redox thermodynamics at 1 bar it can be claimed without any doubt that the proton concentrations given here are not overestimated. Even a small fraction of acid-base activity (e.g. 10%) would be immediately visible in the thermogravimetric transient as the uptake of oxygen (as a part of the water uptake) strongly contributes to the total mass change and, hence, its slower diffusion must be visible. As this is not the case, the side condition made for the 1 bar analysis is valid. In contrast, the given proton concentrations for 10 mbar can be considered as a lower bound. Hence, a higher redox fraction at 10 mbar than resulting from the numerical solution cannot completely be ruled out. Nevertheless, this fraction must not be too high as it then would be visible in the thermogravimetric relaxation (cf. simulations section 4.3.5). With these statements, the final result is that the

Table 4.3: Standard reaction enthalpies ΔH^0 and entropies ΔS^0 for all three thermodynamic equilibria calculated from the linear regression of the respective $1/T$ plot of the K values (figure 4.9 and 4.13) using eq. 2.11.

p_{O_2}	oxidation		hydration		reduction	
	$\Delta_{ox}H^0 / \text{kJmol}^{-1}$	$\Delta_{ox}S^0 / \text{Jmol}^{-1}\text{K}^{-1}$	$\Delta_{hydrat}H^0 / \text{kJmol}^{-1}$	$\Delta_{hydrat}S^0 / \text{Jmol}^{-1}\text{K}^{-1}$	$\Delta_{red}H^0 / \text{kJmol}^{-1}$	$\Delta_{red}S^0 / \text{Jmol}^{-1}\text{K}^{-1}$
10 mbar	$-40(\pm 30)$	$-50(\pm 40)$	$-70(\pm 20)$	$-150(\pm 30)$	$-30(\pm 50)$	$-100(\pm 70)$
1 bar	$-30(\pm 10)$	$-40(\pm 20)$	$-70(\pm 30)$	$-140(\pm 50)$	$-40(\pm 40)$	$-100(\pm 70)$

proton concentration is within the analyzed range more or less independent on p_{O_2} . This is in agreement with results of Hashimoto et al. who measured the proton concentration of BSCF with varying cobalt content at 600 °C with Karl-Fischer titration. They hydrated the samples in humidified oxygen and argon and found that the proton concentration is within the error range the same.^[27]

From the defect concentrations K_{ox} and K_{hydrat} are calculated for 1 bar p_{O_2} - figure 4.13b. The results for 10 mbar are shown as light points as well as the linear regression to obtain ΔH^0 and ΔS^0 . Within the error bars and the knowledge that calculating K from concentrations is an approximation, the K values are independent on the gas composition which is a physically reasonable result.

All ΔH^0 and ΔS^0 values for the three equilibria 2.1, 2.2 and 2.3 are summarized in table 4.3. For the linear regression only the K values between 350 and 600 °C, i.e. the observed range,

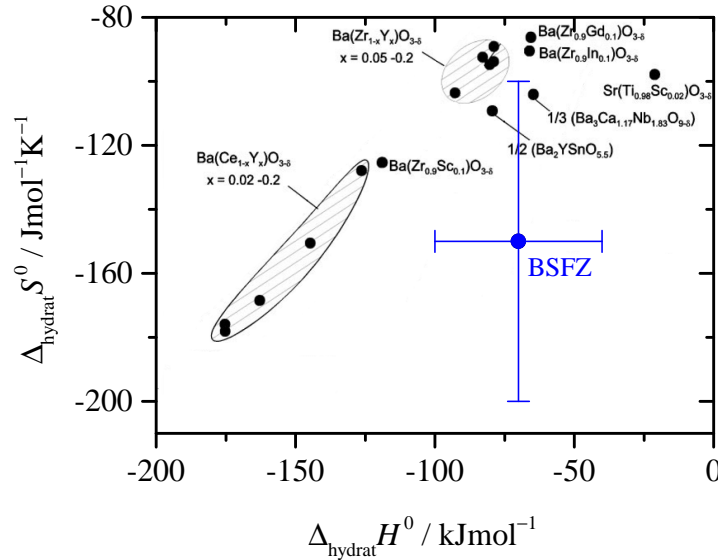


Figure 4.14: Hydration enthalpy vs. entropy of a variety of proton-conducting perovskite electrolytes published by Kreuer (figure taken from the paper).^[16] The results of BSFZ presented in this work is added with its error bars.

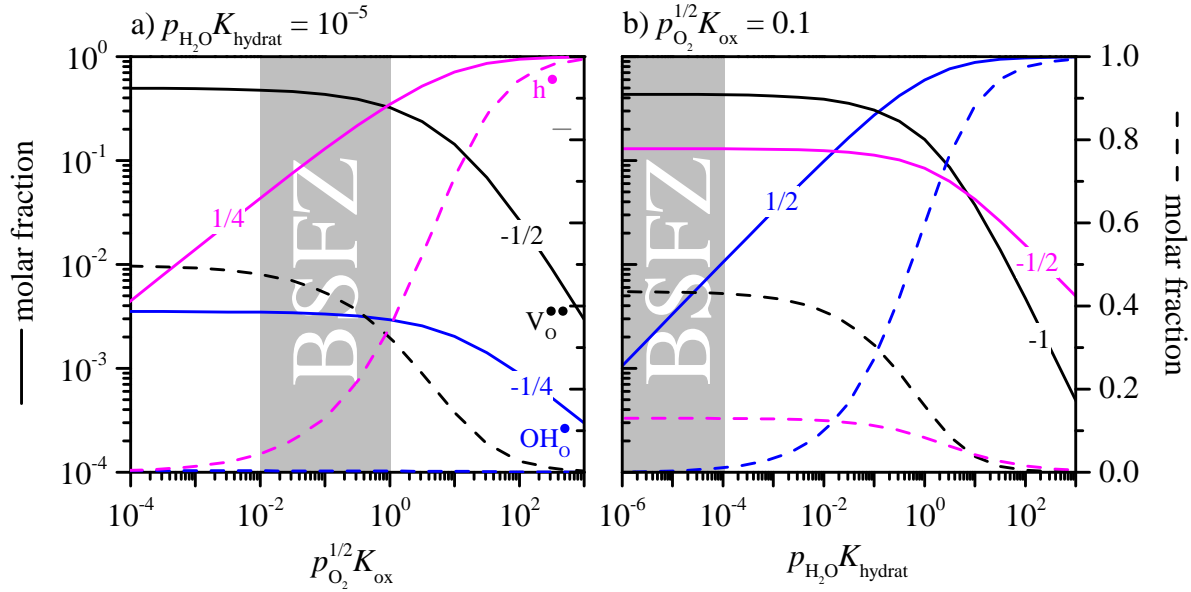


Figure 4.15: Partial pressure dependencies of the three mobile charge carrier bulk concentrations for a) p_{O_2} and b) $p_{\text{H}_2\text{O}}$ in logarithmic (solid lines, left scale bar) and linear (dashed lines, right scale bar) scale. The experimental $p_{\text{O}_2}^{1/2} K_{\text{ox}}$ and $p_{\text{H}_2\text{O}} K_{\text{hydrat}}$ ranges for BSFZ are indicated in gray.

were taken as the calculated K values generally not follow an ideal linearity. This results in the high error margins given for ΔH^0 and ΔS^0 . All in all, the standard reaction enthalpies and entropies are the same at both p_{O_2} values which is again physically reasonable and in very good agreement with the fact that the proton concentration is also independent on p_{O_2} . All three reactions (from left to right) are exothermic. $\Delta_{\text{hydrat}} G^0$ and $\Delta_{\text{red}} G^0$ are endergonic in the analyzed temperature range. $\Delta_{\text{ox}} G^0$ is slightly exergonic up to 500 °C and then becomes slightly endergonic. Last but not least, the values are in the same range as reported for mixed-conducting perovskite electrodes and proton-conducting electrolytes. The hydration enthalpy and entropy values for BSFZ are added to figure 4.14 of $\Delta_{\text{hydrat}} H^0$ vs. $\Delta_{\text{hydrat}} S^0$ for a variety of proton-conducting electrolyte materials reported by Kreuer.^[16] $\Delta_{\text{hydrat}} H^0$ for BSFZ agrees with values for $\text{Ba}(\text{Zr}, (\text{Y}, \text{Gd}, \text{In}))\text{O}_{3-\delta}$, $\Delta_{\text{hydrat}} S^0$ with $\text{Ba}(\text{Ce}, \text{Y})\text{O}_{3-\delta}$ (owing to the large error bar also with $\text{Ba}(\text{Zr}, \text{Y})\text{O}_{3-\delta}$). However, $\Delta_{\text{hydrat}} G^0$ is smaller for BSFZ resulting in lower proton concentrations than for the typical proton-conducting electrolytes. The oxidation enthalpy $\Delta_{\text{ox}} H^0$ is in the same range as values reported by Wang et al. for BSF (-68 to -58 kJmol^{-1}) and BSCF (-47 to -100 kJmol^{-1}).^[83]

Finally, the partial pressure dependencies of the bulk defect concentrations relevant for BSFZ are shown in figure 4.15a and b. They are two-dimensional cuts of the three-dimensional plots in figure 2.1. For the p_{O_2} dependence average values of $p_{\text{H}_2\text{O}} K_{\text{hydrat}} = 10^{-5}$ and of $p_{\text{O}_2}^{1/2} K_{\text{ox}} = 0.1$ for the $p_{\text{H}_2\text{O}}$ dependence experimentally found for BSFZ are taken. The experimental $p_{\text{O}_2}^{1/2} K_{\text{ox}}$ and $p_{\text{H}_2\text{O}} K_{\text{hydrat}}$ ranges relevant for BSFZ are highlighted in gray. To obtain the exponent of the partial pressure dependencies the concentrations are plotted logarithmically (left scale bar). The given numbers on top of the lines indicate the limiting slopes

which can easily be extracted from the mass action constants. In addition, the concentrations are shown on a linear scale (dashed lines) to visualize that although the concentrations seem to be constant in the logarithmic scale they change with p_{O_2} , respectively, $p_{\text{H}_2\text{O}}$. However, the absolute change is small and seems, therefore, to be constant in the logarithmic scale.

p_{O_2} dependence: For the experimentally relevant BSFZ range the holes exhibit a clear 1/4 dependency expected for the p-conducting regime. The exponents for $[\text{OH}_{\text{O}}^{\bullet}]$ and $[\text{V}_{\text{O}}^{\bullet\bullet}]$ are near zero or slightly negative, whereas $[\text{V}_{\text{O}}^{\bullet\bullet}]$ responds more strongly to a change in p_{O_2} than $[\text{OH}_{\text{O}}^{\bullet}]$. This is fine agreement with the experimental results where the proton concentration was found to be p_{O_2} independent.

$p_{\text{H}_2\text{O}}$ dependence: The exponent for the $p_{\text{H}_2\text{O}}$ dependence of $[\text{OH}_{\text{O}}^{\bullet}]$ is 1/2 as expected from the mass action law in agreement with the TG experiments (the sample responds to a change in $p_{\text{H}_2\text{O}}$). The absolute $[\text{V}_{\text{O}}^{\bullet\bullet}]$ and $[\text{h}^{\bullet}]$ are very weakly $p_{\text{H}_2\text{O}}$ dependent owing to the fact that their concentration is one to two orders of magnitude larger than $[\text{OH}_{\text{O}}^{\bullet}]$. Even the small redox fraction in the acid-base dominated regime at 10 mbar p_{O_2} is hardly visible.

4.3 Simulation of the diffusion model

In this chapter numerically simulated time-resolved concentration profiles of $\text{V}_{\text{O}}^{\bullet\bullet}$, h^{\bullet} and $\text{OH}_{\text{O}}^{\bullet}$ upon change in the chemical potential μ_{O} and μ_{H} based on the flux equations derived in chapter 2.2.2 are given. These simulations are related to experiments where $p_{\text{H}_2\text{O}}$ and/or p_{O_2} in the gas phase are changed. Typically, only one component is changed to not make the analysis more complex than it is. Here, only changes in $p_{\text{H}_2\text{O}}$ are treated as this is performed in thermogravimetric and DC conductivity relaxation experiments. The defect diffusivities are fixed to conditions where $D_{\text{h}^{\bullet}} > D_{\text{OH}_{\text{O}}^{\bullet}} > D_{\text{V}_{\text{O}}^{\bullet\bullet}}$ which is the typical case for perovskites.^[99]

To understand the influence of parameters such as hole concentration, degree of protonation, defect diffusivity ratio, fraction between water and hydrogen uptake to the total proton incorporation on the time development of the concentration profiles individually, only one of these parameters is changed keeping all other constant (the acceptor dopant concentration is fixed to unity in all simulations). After computational details in the next section, the following individual parameter changes are examined in the succeeding sections:

(i) Changing the hole concentration. Of course, this changes also the $\text{V}_{\text{O}}^{\bullet\bullet}$ and $\text{OH}_{\text{O}}^{\bullet}$ concentration, but the degree of hydration X is fixed and only acid-base thermodynamics are considered. In addition, two different degrees of hydration are analyzed. The scope is to examine the influence of the hole concentration (experimentally related to increasing p_{O_2}) and the degree of hydration on the strength of decoupling between fast hydrogen and slow oxygen diffusion.

(ii) Changing the ratio between proton and oxygen vacancy diffusivity ($D_{\text{OH}_{\text{O}}^{\bullet}}$ to $D_{\text{V}_{\text{O}}^{\bullet\bullet}}$). The defect concentrations, degree of hydration and $D_{\text{OH}_{\text{O}}^{\bullet}}$ to $D_{\text{h}^{\bullet}}$ ratio are fixed to values related to BSFZ. Acid-base thermodynamics are still assumed and the influence on the strength of

decoupling is of interest. This is experimentally related to changing the temperature as $D_{\text{OH}\bullet}$ and $D_{\text{V}\bullet\bullet}$ have typically very different activation energies, hence, their ratio changes.^[16:70]

(iii) Changing the fraction between water and hydrogen uptake. Now, protons are allowed to be incorporated by both acid-base and redox thermodynamics and the ratio between both is varied keeping the diffusivities, initial concentrations and degree of protonation constant. This is experimentally related to changing the p_{O_2} as well as in (i), but more related to the defect model. It has been shown that with increasing p_{O_2} (or increasing concentration of redox-active cations, thus, increasing K_{ox}) the redox fraction (fraction of protons taken up by hydration-deoxygenation equilibration (eq. 2.3) compared to the total proton uptake) increases as well.

Treatment (i) and (ii) are to some point artificial as in an experiment with changing the temperature (most common procedure) or gas composition all above examined parameters change simultaneously (e.g. with changing the temperature defect concentrations, degree of protonation, redox fraction and diffusivity ratio are changed). Nevertheless, this procedure is performed to check under which conditions the expected two-fold relaxation (decoupled diffusion of hydrogen and oxygen) can be observed in the mass relaxation where both contributions of the two-fold kinetics result in a mass increase. This is done in section 4.3.5 where the mass transients are calculated from the simulated time-resolved $\text{V}_{\text{O}}^{\bullet\bullet}$ and $\text{OH}_{\text{O}}^{\bullet}$ profiles (h^{\bullet} does not contribute to the mass) in (i) to (iii).

(iv) To finally analyze the development of the decoupling for a realistic system, defect concentrations were taken from the thermodynamic model derived in chapter 2.1. $p_{\text{H}_2\text{O}}K_{\text{hydrat}}$ is fixed to 10^{-2} which is a compromise between being close to conditions found for BSFZ (here, the maximum $p_{\text{H}_2\text{O}}K_{\text{hydrat}}$ is about 2×10^{-4}) and still having a high enough degree of protonation to make relevant results visible (the degree of protonation in BSFZ is small resulting in some effects to disappear). The varied quantity is $p_{\text{O}_2}^{1/2}K_{\text{ox}}$, being related to changes in p_{O_2} (for fixed material composition). The initial defect concentrations are calculated through given $p_{\text{O}_2}^{1/2}K_{\text{ox}}$ and $p_{\text{H}_2\text{O}}K_{\text{hydrat}}$ values, the initial concentration changes upon $\Delta p_{\text{H}_2\text{O}}$ are calculated through a change of 10% in $p_{\text{H}_2\text{O}}$ recalculating the new defect concentrations. The values used for all simulations (i) to (iv) are summarized in appendix B.

4.3.1 Simulation details

All simulations are performed for one-dimensional diffusion into a plane sheet with thickness $2l$, sketched in figure 4.16 for the migration of a neutral species. The thickness of the plane sheet sample is divided into a finite number of layers with height Δl . The length l is arbitrary chosen as 10^{-3} cm and Δl as 10^{-5} cm, hence, the sample is cut into 100 slices. Before changing the defect concentrations the sample is fully equilibrated, i.e. all defect concentrations are set to their initial value in all parts of the sample (in figure 4.16 they are set to zero). At the initial time $t = 0$ all defect concentrations are changed to their thermodynamic final values in the first layer being in direct contact to the gas phase (in figure 4.16 the first box reaches the final concentration of four particles, the assumption of fast surface reaction makes the diffusion length l arbitrary), i.e. fast surface reaction and diffusion control is presumed (therefore, the

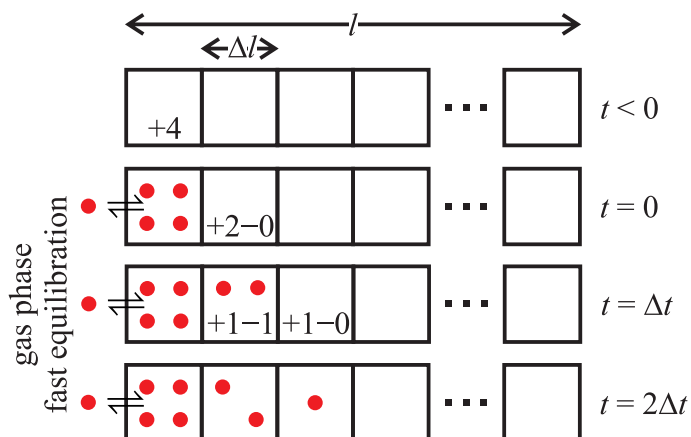


Figure 4.16: Outline of the simulation procedure. For the sake of simplicity, the migration of a neutral species (red dot) is shown. The numbers in the boxes (representing the slices mentioned in the text) indicate the particles entering or leaving the box according to the gradient and chemical diffusivity to update the numbers of particles in each box in the row below.

chosen length l is arbitrary). Experimentally this corresponds to a change of $p_{\text{H}_2\text{O}}$ and/or p_{O_2} for a sample thicker than the critical thickness (cf. section 2.2.1). As a consequence, a concentration gradient between the first and second slice is introduced. For a small time interval Δt (commonly set to 7×10^{-9} s, depends on the magnitude of the defect diffusivities) the flux between both slices is calculated based on the flux equations in chapter 2.2.2 and the new concentrations are updated according to this flux (in figure 4.16 the gradient causes a flux of two particles during Δt , hence, two particles are in the second slice after Δt , the first slice still has four particles owing to the fast surface equilibration). Now, new concentration gradients have developed, the fluxes during Δt are calculated and the new concentrations updated (in the sketch owing to the gradient one particle leaves slice 2 to slice 3 but also one particle is entering slice 2 from slice 1). This iterative procedure is performed until all slices have obtained the final concentrations.

To calculate the fluxes of $\text{V}_{\text{O}}^{\bullet\bullet}$ and H_1^{\bullet} , one of the three equations for each flux derived in section 2.2.2 – eqs. 2.38 to 2.40 – has to be used; which one is irrelevant for the result. For the set of eq. 2.38 the fluxes between slice i and $i + 1$ are calculated through

$$J_{\text{V}_{\text{O}}^{\bullet\bullet}}^{i \rightarrow i+1} = -D_{\nabla \text{V}(\text{H})}^{\text{V}} \frac{[\text{V}_{\text{O}}^{\bullet\bullet}]_{i+1} - [\text{V}_{\text{O}}^{\bullet\bullet}]_i}{\Delta l} - D_{\nabla \text{H}(\text{V})}^{\text{V}} \frac{[\text{OH}_{\text{O}}^{\bullet}]_{i+1} - [\text{OH}_{\text{O}}^{\bullet}]_i}{\Delta l} \quad (4.4)$$

and

$$J_{\text{H}_1^{\bullet}}^{i \rightarrow i+1} = -D_{\nabla \text{H}(\text{V})}^{\text{H}} \frac{[\text{OH}_{\text{O}}^{\bullet}]_{i+1} - [\text{OH}_{\text{O}}^{\bullet}]_i}{\Delta l} - D_{\nabla \text{V}(\text{H})}^{\text{H}} \frac{[\text{V}_{\text{O}}^{\bullet\bullet}]_{i+1} - [\text{V}_{\text{O}}^{\bullet\bullet}]_i}{\Delta l} \quad (4.5)$$

The defect concentrations in slice i are updated according to the fluxes of this defect entering or leaving from the neighboring slices.

$$[\text{V}_{\text{O}}^{\bullet\bullet}]_i = [\text{V}_{\text{O}}^{\bullet\bullet}]_i + \left(\frac{\Delta t}{\Delta l} \left(J_{\text{V}_{\text{O}}^{\bullet\bullet}}^{i-1 \rightarrow i} - J_{\text{V}_{\text{O}}^{\bullet\bullet}}^{i \rightarrow i+1} \right) \right) \quad (4.6)$$

and

$$[\text{OH}_{\text{O}}^{\bullet}]_i = [\text{OH}_{\text{O}}^{\bullet}]_i + \left(\frac{\Delta t}{\Delta l} \left(J_{\text{H}_1^{\bullet}}^{i-1 \rightarrow i} - J_{\text{H}_1^{\bullet}}^{i \rightarrow i+1} \right) \right) \quad (4.7)$$

The hole concentration is obtained from the local electroneutrality condition.

$$[\text{h}^\bullet]_i = [A'] - 2[\text{V}_\text{O}^{\bullet\bullet}]_i - [\text{OH}_\text{O}^\bullet]_i \quad (4.8)$$

The time steps Δt need to be small to ensure that the fluxes are smaller than the respective absolute concentration (otherwise more particles than allowed through electroneutrality would formally enter or more particles than present would formally leave the slice). As the concentration gradients decrease with time, Δt is increased in a step-wise manner to keep the simulation time at an acceptable level (generally, one simulation takes ≈ 90 min). Furthermore, the four chemical diffusion coefficients (e.g. 2.38) are set to be time and space independent, i.e. they are calculated from the initial defect concentrations and predefined defect diffusivities. This is a reasonable approximation as exemplary simulations showed that the chemical diffusivities are only weakly concentration dependent (for small concentration changes) and that the influence on the simulation results can be qualitatively as well as quantitatively neglected (cf. appendix 1 in Merkle et al.^[100]). The output of the simulation script contains space- and time-resolved normalized, integrated concentration profiles for the three charge carriers.

4.3.2 Varying the hole concentrations

The presence of holes h^\bullet can lead to a decoupled migration of hydrogen and oxygen upon increased $p_{\text{H}_2\text{O}}$ (instead of ambipolar water diffusion).^[30;31;33] The proton flux can then be coupled to the typically much faster holes (ambipolar diffusion of hydrogen decreasing the hole concentration), followed by the slower oxygen vacancy flux also coupling to the holes (ambipolar diffusion of oxygen, restoring the initial hole concentration). Note that these fluxes are not independent of each other as proposed by Yoo et al.^[33] making the physical analysis more complex as derived in chapter 2.2.2. So firstly, the influence of the hole concentration on the decoupling in water uptake is analyzed. The defect diffusivities are chosen to be 10^{-6} , 10^{-5} and $10^{-4} \text{ cm}^2\text{s}^{-1}$ for $D_{\text{V}_\text{O}^{\bullet\bullet}}$, $D_{\text{OH}_\text{O}^\bullet}$ and D_{h^\bullet} , respectively (the result depends on the ratio, not on the absolute values). Only acid-base thermodynamics is presumed ($\Delta[\text{OH}_\text{O}^\bullet] = -2\Delta[\text{V}_\text{O}^{\bullet\bullet}]$) and two different degrees of hydration ($X = 0.1$ and 0.5) are chosen to analyze its influence. From these side-conditions, all defect concentrations are calculated varying $[\text{h}^\bullet]$ between 10^{-4} (electrolyte, hind left corner in figure 2.1) and 0.99 (electronic conductor with very low $\text{OH}_\text{O}^\bullet$ and $\text{V}_\text{O}^{\bullet\bullet}$ concentration, hind right corner). All used input data are given in table B.1. With respect to an experiment, these conditions cover changing the p_{O_2} for a given material with constant dopant concentration and certain redox activity. Nonetheless, it has to be considered that this approach is rather artificial as the thermodynamic defect model prescribes that with increasing $[\text{h}^\bullet]$ the redox fraction has to increase, too. These conditions lead to changes of several parameters (concentrations, degree of hydration, redox fraction) as shown in section 4.3.6. Here, qualitative trends upon changes in only one parameter are to be demonstrated.

The time-resolved, integrated, normalized concentration profiles for three exemplary $[\text{h}^\bullet]$ values for $X = 0.5$ are given in figure 4.17. In the three top figures the concentrations are plotted against the square root of the time t to visualize the short term behavior. Vice versa, in the bottom figures the difference $1 - \text{normalized concentration}$ is semi-logarithmically drawn versus the linear time to highlight the long term evolution. If the processes can be described by one diffusivity, the concentration profile shows only one linear regime in both types of

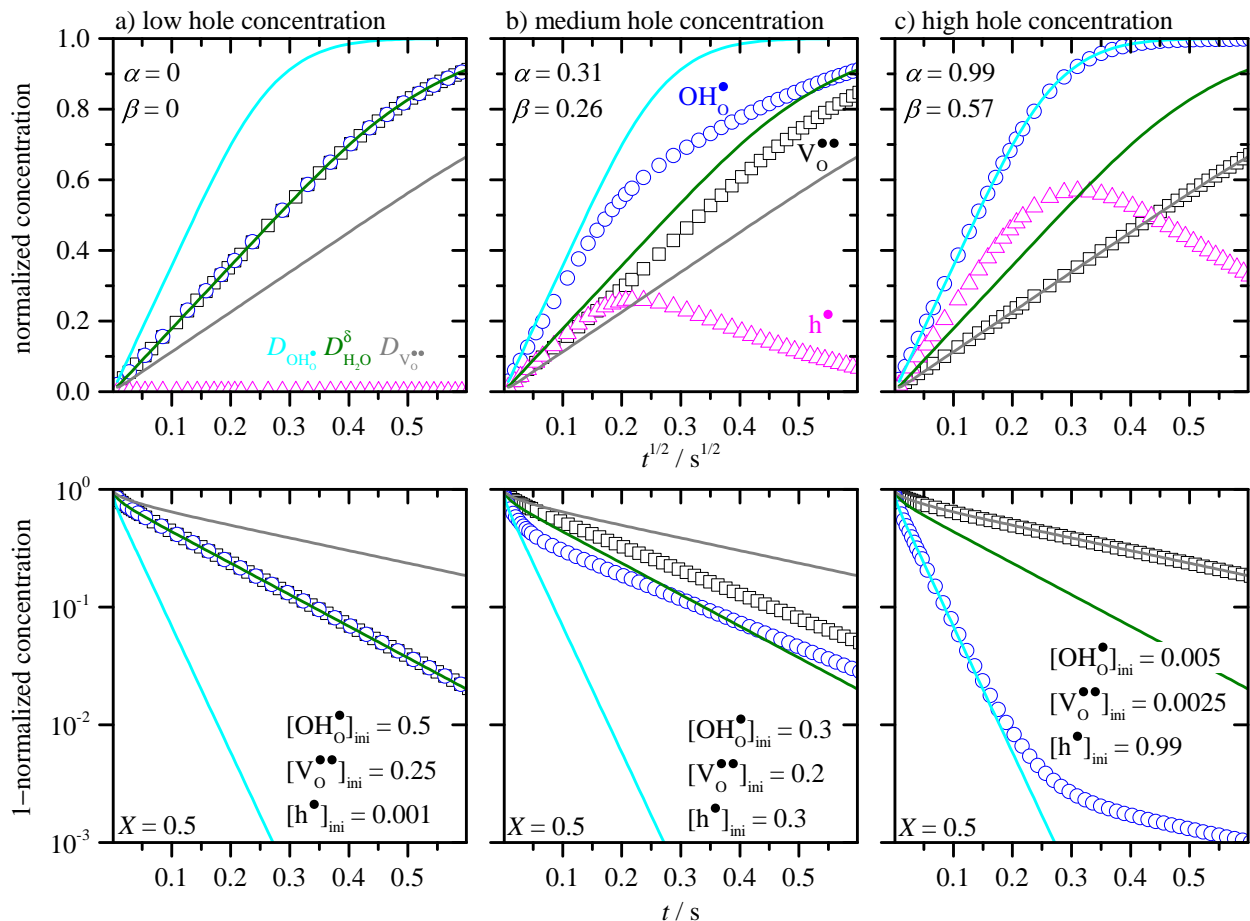


Figure 4.17: Integrated, normalized defect concentrations for different hole concentrations. $[V_O^{\bullet\bullet}]$ (black squares) and $[OH_O^\bullet]$ (blue circles) are normalized to their initial and final values. $[h^\bullet]$ (magenta triangles) is normalized to $-\Delta[OH_O^\bullet]$. Note that although the normalized values for $[V_O^{\bullet\bullet}]$ and $[h^\bullet]$ are positive, their change with respect to their initial values is negative. The given, initial concentrations are rounded values (exact values in table B.1, appendix B). The colored lines represent the profiles for the indicated diffusivities $D_{OH_O^\bullet}$ (cyan), $D_{V_O^{\bullet\bullet}}$ (gray) and $D_{H_2O^\delta}$ (green). Top: Normalized concentration versus time^{1/2} to highlight the short term behavior. Bottom: 1-normalized concentration in logarithmic scale versus time to show the long term relaxation. The values α and β are introduced later in this section.

plotting, and the diffusion coefficient can be either extracted from the slope m of the short time behavior using eq. 4.9^[64] or the solution of Fick's second law eq. 4.12^[101]. This is obvious from the solid lines in figure 4.17 which show the hypothetical concentration profiles if they are determined by only one diffusivity $D_{OH_O^\bullet}$ (blue), $D_{V_O^{\bullet\bullet}}$ (gray) or $D_{H_2O^\delta}$ (green) for the coupled diffusion of water calculated from eq. 2.43. The parameters α and β in the figure are related to the strength of decoupling between hydrogen and oxygen migration. They are introduced and defined soon.

$$D^{\text{eff}} = \frac{\pi l^2 m^2}{4} \quad (4.9)$$

Figure 4.17a corresponding to $[h^\bullet] \ll [V_{\text{O}}^{\bullet\bullet}] \approx [\text{OH}_{\text{O}}^\bullet]$ represents the proton-conducting electrolyte case at very low p_{O_2} (reducing conditions). It is very clear that the holes do not contribute to the migration as their integrated concentration is constant. Consequently, the oxygen vacancy and proton diffusion are directly coupled and their profiles behave as predicted by the chemical diffusion of water eq. 2.43. The simulated profiles (squares for $V_{\text{O}}^{\bullet\bullet}$ and circles for $\text{OH}_{\text{O}}^\bullet$) converge with the analytical solution for $D_{\text{H}_2\text{O}}^\delta$ (green line) which proves that the simulation works correctly.

Figure 4.17b shows the situation for an increased hole concentration with $[h^\bullet] \approx [V_{\text{O}}^{\bullet\bullet}] \approx [\text{OH}_{\text{O}}^\bullet]$, representing a mixed oxygen vacancy/proton/hole conductor. Five interesting aspects are found. (i) A transient hole flux occurs although the initial gradient in the hole concentration $\nabla[h^\bullet]$ is zero (of course, as soon as the hole flux begins, a gradient is generated). This is an example where a flux of a species can occur in a medium with three mobile charge carriers without having an own concentration gradient. (ii) The fast proton can migrate in a decoupled way from the slow $V_{\text{O}}^{\bullet\bullet}$ as it couples to the holes. Hence, the proton diffuses faster than with $D_{\text{H}_2\text{O}}^\delta$ but still slower than with $D_{\text{OH}_{\text{O}}^\bullet}$. (iii) Vice versa, the oxygen vacancy is not dragged by the fast proton and, therefore, migrates slower than with $D_{\text{H}_2\text{O}}^\delta$ but faster than with $D_{V_{\text{O}}^{\bullet\bullet}}$ coupled to holes as well. (iv) Consequently, the sample is partly reduced via fast motion of hydrogen (coupled $\text{OH}_{\text{O}}^\bullet/h^\bullet$) and slowly reoxidized via motion of oxygen (coupled $V_{\text{O}}^{\bullet\bullet}/h^\bullet$). This is seen in the concentration profile of the holes which are decreased for short times (note that the normalization results in positive values) and relax back to their initial value for longer times. (v) Looking closer at the proton profile, e.g. figure 4.17b top, it is recognized that it cannot be described by a single diffusion coefficient anymore as it shows two linear regimes. From the long term plot in the bottom figure the proton and oxygen vacancy profile are approximately parallel, hence, they migrate with the same diffusivity.

For the short time behavior the diffusivities are directly extracted from the slope m of the linear regime in the $t^{1/2}$ plot using eq. 4.9. These diffusivities describe the effective evolution of the concentration profiles (for “short” times) and are, therefore, called effective diffusion coefficients $D_{\text{H}}^{\text{eff}}$ for the proton (chemical diffusion of hydrogen) and $D_{\text{O}}^{\text{eff}}$ for the oxygen vacancy (chemical diffusion of oxygen). The results for both analyzed degrees of hydration are summarized in the bottom part of figure 4.18 as function of the hole concentration. From the plot it appears that the decoupling (both D^{eff} start to deviate) starts already at rather low hole concentrations (two orders of magnitude smaller than the ionic defect concentrations) and is quite pronounced where h^\bullet is still the minor defect (e.g. 10^{-1}). The deviation between $D_{\text{H}}^{\text{eff}}$ and $D_{\text{O}}^{\text{eff}}$ seems to follow the hole transference number, plotted in magenta in the top part of figure 4.18 (together with the proton (blue) and oxygen vacancy (gray) transference numbers). However, this behavior depends on the proton uptake mechanism (acid-base or redox, cf. section 4.3.4) and the ratio of the defect diffusivities (cf. Merkle et al.^[100]). Consequently, the hole concentration and conductivity alone are not good parameters for the degree of decoupling. To quantify and compare the ratio between $D_{\text{H}}^{\text{eff}}$ and $D_{\text{O}}^{\text{eff}}$ the normalized ratio between both is defined as α and calculated through

$$\alpha = \frac{(D_{\text{H}}^{\text{eff}} - D_{\text{O}}^{\text{eff}})D_{V_{\text{O}}^{\bullet\bullet}}}{(D_{\text{OH}_{\text{O}}^\bullet} - D_{V_{\text{O}}^{\bullet\bullet}})D_{\text{O}}^{\text{eff}}} \quad (4.10)$$

This ratio is zero for single-fold water diffusion and unity for the case that $D_{\text{H}}^{\text{eff}}$ and $D_{\text{O}}^{\text{eff}}$ obtain the values of $D_{\text{OH}_o^\bullet}$ and $D_{\text{V}_o^{\bullet\bullet}}$. Later, it will be seen that this is strictly speaking only valid for the pure acid-base thermodynamics and that both effective diffusivities can over-, respectively, undershoot these limits yielding α values larger than unity. Furthermore, α does not include the relative contribution of $D_{\text{H}}^{\text{eff}}$ and $D_{\text{O}}^{\text{eff}}$ to the total stoichiometry change, which also varies with $[\text{h}^\bullet]$, respectively, with the ability to allow proton uptake by redox reaction (cf. section 4.3.4).

Before continuing the discussion for α , an alternative parameter to quantify the decoupling can be defined. The transient change of hole concentration normalized to the change in proton concentration (triangles in figure 4.17) shows how strong the sample is reduced before being reoxidized. In the extreme limit, the sample is homogeneously reduced by hydrogen uptake, i.e. the normalized change in hole concentration is unity at its maximum. Then, the hydrogen and oxygen migration can be treated to be independent. In the case of ambipolar water diffusion, $[\text{h}^\bullet]$ does not change and the normalized values are zero. The fraction of transient sample reduction indicates the strength of the decoupling of hydrogen and oxygen migration and, furthermore, includes the contribution of the fast hydrogen uptake determined by $D_{\text{H}}^{\text{eff}}$. Therefore, the maximum of the integrated, normalized, transient hole concentration covers these cases and, in principle, all parameters which influence the degree of decoupling (defect diffusivities, degree of hydration, degree of redox fraction (see section 4.3.4)). To distinguish

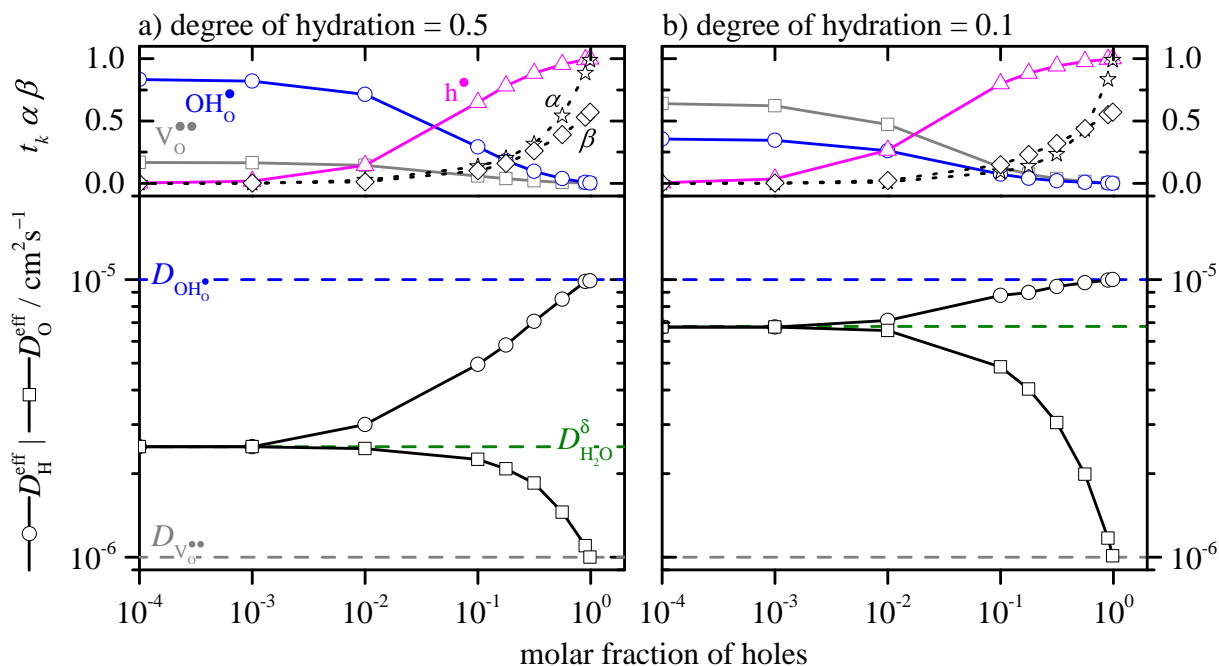


Figure 4.18: Effective diffusivities $D_{\text{H}}^{\text{eff}}$ (circles) and $D_{\text{O}}^{\text{eff}}$ (squares), transference numbers for OH_o^\bullet (blue), $\text{V}_o^{\bullet\bullet}$ (gray) and h^\bullet (magenta), normalized ratio α between both D^{eff} values (stars) and normalized transient reduction β (diamonds) with increasing $[\text{h}^\bullet]$ for two different degrees of hydration.

this parameter from α it is called normalized transient reduction β , defined as

$$\beta = \frac{[h^\bullet]_{\max} - [h^\bullet]_{t=0}}{[OH_O^\bullet]_{t=\infty} - [OH_O^\bullet]_{t=0}} \quad (4.11)$$

where $[h^\bullet]_{\max}$ is the maximum concentration in the time-dependent normalized hole concentration profile.

Finally, figure 4.17c is to be discussed and will give a hint whether α or β is a suitable parameter for the strength of decoupling. Here, the hole concentration has almost its maximum value, hence, the ionic concentrations and the water uptake are small. These conditions are found in the right corner of figure 2.1 and 2.2. Now, the short term migration of OH_O^\bullet and $V_O^{\bullet\bullet}$ converge with their respective defect diffusivities, i.e. α reaches its maximum value 1 suggesting a maximum in decoupling. Nonetheless, the proton profile still has to be described by in fact two effective diffusivities, but the contribution of the slow long term process can be neglected as it is very small. Looking at the transient hole concentration it is clear that the sample is not fully reduced, the value of β reads 0.57 in contrast to α . Consequently, β is a good parameter to check the strength of decoupling whereas α is less intuitive at this stage but might be useful in some cases. Therefore, both parameters are given and discussed when necessary.

The quantities α (stars) and β (diamonds) are additionally plotted in the top part of figure 4.18. Comparing both different degrees of hydration, the decoupling starts at lower hole concentrations for higher X but ends up in the same final values. All in all, the main decoupling process occurs within one to two orders of magnitude in $[h^\bullet]$, while the main change of t_{h^\bullet} occurs within three orders of magnitude. This is in very good agreement with experimental results of Kim and Yoo where the main decoupling in water uptake in BZY20 at high temperatures and p_{O_2} (moderate concentration of h^\bullet) takes place within four to eight orders of magnitude in p_{O_2} ($[h^\bullet] \propto p_{O_2}^{-1/4}$).^[33]

4.3.3 Varying the ratio of $D_{OH_O^\bullet}$ to $D_{V_O^{\bullet\bullet}}$

In the next two sections defect concentrations are fixed and the influence of the mobility ratio (this section) and thermodynamic uptake mechanism (next section) is investigated. The defect concentrations and degree of hydration are set to values relevant for mixed-conducting electrodes, i.e. $[OH_O^\bullet] \approx [V_O^{\bullet\bullet}] \approx [h^\bullet]$ and $X \approx 0.1$ (still assuming pure acid-base thermodynamics to ensure the change of only one parameter). The normalized, integrated defect profiles together with α and β for the short and long term range are plotted in figure 4.19. The ratio between $D_{OH_O^\bullet}$ and $D_{V_O^{\bullet\bullet}}$ is set in the way that $D_{OH_O^\bullet}$ is fixed to 10^{-5} and $D_{V_O^{\bullet\bullet}}$ is varied (it is worth to mention here again that it is the ratio what is important, not the absolute values). These simulations cover the experiment of changing the temperature owing to different activation energies for $D_{OH_O^\bullet}$ and $D_{V_O^{\bullet\bullet}}$.^[16;70] Of course, a change in temperature also changes the concentrations but for these theoretical considerations only one parameter should be changed at a time. Furthermore, it is important to mention that for low degrees of hydration the influence of the actual D_{h^\bullet} on the decoupling process can be neglected.^[100]

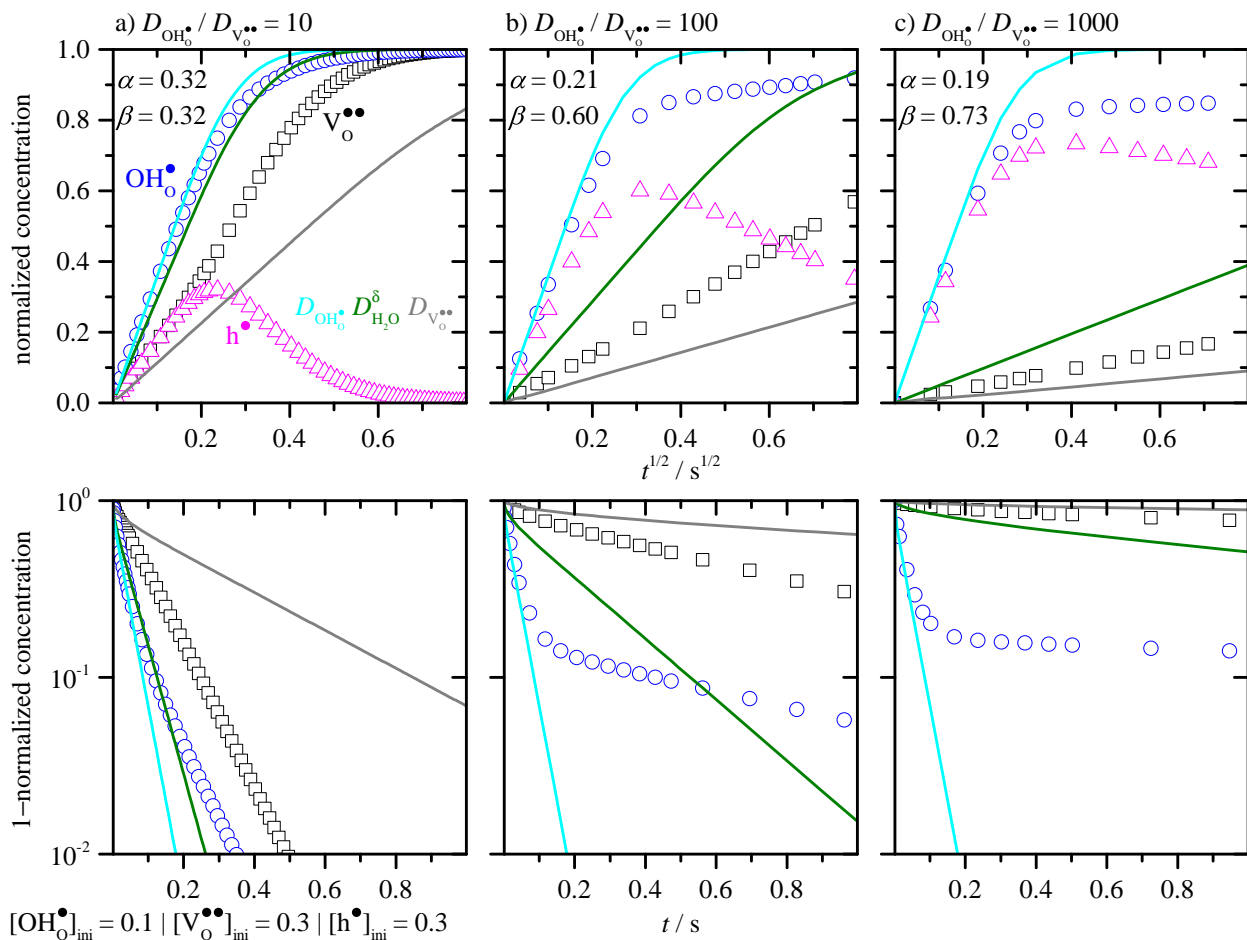


Figure 4.19: Integrated, normalized concentration profiles for different $D_{\text{OH}\bullet}$ to $D_{\text{V}\bullet\bullet}$ ratios. $\text{V}_{\text{O}}^{\bullet\bullet}$ (black squares) and $\text{OH}\bullet$ (blue circles) are normalized to their initial and final values. $\text{h}\bullet$ (magenta triangles) is normalized to $-\Delta[\text{OH}\bullet]$. Note that although the values for $\text{V}_{\text{O}}^{\bullet\bullet}$ and $\text{h}\bullet$ are positive, their change with respect to their initial values is negative. The given, initial concentrations are rounded values (exact values in table B.3, appendix B). The colored lines represent the profiles for the indicated diffusivities $D_{\text{OH}\bullet}$ (cyan), $D_{\text{V}\bullet\bullet}$ (gray) and $D_{\text{H}_2\text{O}}^\delta$ (green). Top: Normalized concentration versus time^{1/2} to highlight the short term behavior. Bottom: 1-normalized concentration in logarithmic scale versus time to show the long term relaxation.

As expected from eq. 2.44 $D_{\text{H}_2\text{O}}^\delta$ decreases with decreasing $D_{\text{V}\bullet\bullet}$ for fixed X . For the proton profile analogous to the previous section two linear regimes are found where the first one for short times is defined by $D_{\text{H}}^{\text{eff}}$ and the second one approximately by $D_{\text{O}}^{\text{eff}}$. The $[\text{V}_{\text{O}}^{\bullet\bullet}]$ profile can still be described by this one diffusion coefficient. With increasing deviation between both relevant defect diffusivities the contribution of the fast hydrogen incorporation increases which is in very good agreement with the degree of transient reduction β . Moreover, β reaches not unity although both defect diffusivities are three orders of magnitude apart, and, seems to run into a maximum. Another simulation with $D_{\text{V}\bullet\bullet} = 10^{-12}$ gives a β of 0.81. Thus, although the oxygen migration is orders of magnitude slower, the sample is not homogeneously reduced before being reoxidized as proposed by Yoo et al.^[33] The increase of α is also not a surprise

as the reoxidation is slower and the sample is stronger reduced. In contrast, the degree of decoupling α behaves on the first sight counter-intuitive at it decreases with increasing ratio. This owes to the normalization of α as the absolute decoupling between $D_{\text{H}}^{\text{eff}}$ and $D_{\text{O}}^{\text{eff}}$ is increased, but the relative decoupling compared to the limit values $D_{\text{OH}\bullet}$ and $D_{\text{V}\bullet\bullet}$ is decreased.

4.3.4 Varying the contribution of hydrogen uptake to the total proton uptake

In this section the protons are allowed to be thermodynamically incorporated by mixed acid-base (eq. 2.2) and redox (eq. 2.3) equilibration. The defect conditions are fixed to $[\text{OH}\bullet] \approx [\text{V}\bullet\bullet] \approx [\text{h}\bullet]$ and the degree of protonation to $X'' \approx 0.07$, i.e. the initial concentrations and $\Delta[\text{OH}\bullet]$ are kept constant, $\Delta[\text{V}\bullet\bullet]$ and $\Delta[\text{h}\bullet]$ are changed with respect to their contributions (cf. table B.4).

In figure 4.20 the normalized, integrated concentrations are shown for three exemplary redox fractions. The proton profile hardly changes but approaches the $D_{\text{OH}\bullet}$ related profile, i.e. $D_{\text{H}}^{\text{eff}} \approx D_{\text{OH}\bullet}$ (for higher degrees of hydration the change is stronger and $D_{\text{H}}^{\text{eff}} > D_{\text{OH}\bullet}$ is possible, cf. section 4.3.6 and Merkle et al.^[100]). Nonetheless, still two linear regimes are found. A new effect owing to the redox fraction is the different behavior of the $\text{V}\bullet\bullet$ profile compared to the previous results. Now, two linear regimes are observed which becomes more pronounced with increasing redox fraction. According to the former made definitions $D_{\text{O}}^{\text{eff}}$ is calculated from the slope of the linear part for the short time regime. Comparing all three redox fractions $D_{\text{O}}^{\text{eff}}$ not only approaches $D_{\text{V}\bullet\bullet}$ which is the expected behavior, it even under-shoots the gray line in figure 4.20c, i.e. $D_{\text{O}}^{\text{eff}} < D_{\text{V}\bullet\bullet}$. This observation can be explained from the flux equations. For this purpose flux equation 2.39 ($J_{\text{V}\bullet\bullet} = -D_{\nabla\text{V}(\text{h})}^{\text{V}} \nabla c_{\text{V}\bullet\bullet} - D_{\nabla\text{h}(\text{V})}^{\text{V}} \nabla c_{\text{h}\bullet}$) is taken. $D_{\nabla\text{V}(\text{h})}^{\text{V}}$ is positive, $\nabla c_{\text{V}\bullet\bullet}$ is negative and $D_{\nabla\text{h}(\text{V})}^{\text{V}}$ and $\nabla c_{\text{h}\bullet}$ (for short times until the maximum in the hole transient) are negative. Hence, including the minus signs the first term of the equation $-D_{\nabla\text{V}(\text{h})}^{\text{V}} \nabla c_{\text{V}\bullet\bullet}$ is positive and the second $-D_{\nabla\text{h}(\text{V})}^{\text{V}} \nabla c_{\text{h}\bullet}$ negative, i.e. two contributions – the first accelerating, the second decelerating the $\text{V}\bullet\bullet$ flux – compete. With increasing redox fraction the accelerating part decreases as the initial $\nabla c_{\text{V}\bullet\bullet}$ is decreased (less protons are compensated by oxygen vacancies). Simultaneously, $\nabla c_{\text{h}\bullet}$ increases and the flux is stronger decelerated. This is the reason for the low $D_{\text{O}}^{\text{eff}}$ for short times. Owing to the fast diffusion of hydrogen, $\nabla c_{\text{h}\bullet}$ depletes fast and its decelerating character decreases. Finally, as the slow oxygen flux dominates of the hydrogen flux the flux direction of holes changes switching the sign of $\nabla c_{\text{h}\bullet}$ to positive. That is the point where $J_{\text{V}\bullet\bullet}$ is accelerated by $\nabla c_{\text{h}\bullet}$ and becomes faster than $D_{\text{V}\bullet\bullet}$, the slope of the $\text{V}\bullet\bullet$ profile is larger than the gray line and even crosses it e.g. for 60% redox fraction.

As a result of the small slope used to calculate $D_{\text{O}}^{\text{eff}}$, α not only increases with increasing redox fraction, it also becomes larger than unity. With higher redox fraction the $\text{V}\bullet\bullet$ flux becomes less important, its contribution to the decoupling can be more and more safely neglected until chemical diffusion of hydrogen is reached (100% redox fraction). Here, α is less suited as it pretends a high degree of decoupling but neglects that the contribution of the oxygen flux decreases to zero in the limit case. β intuitively increases and will reach

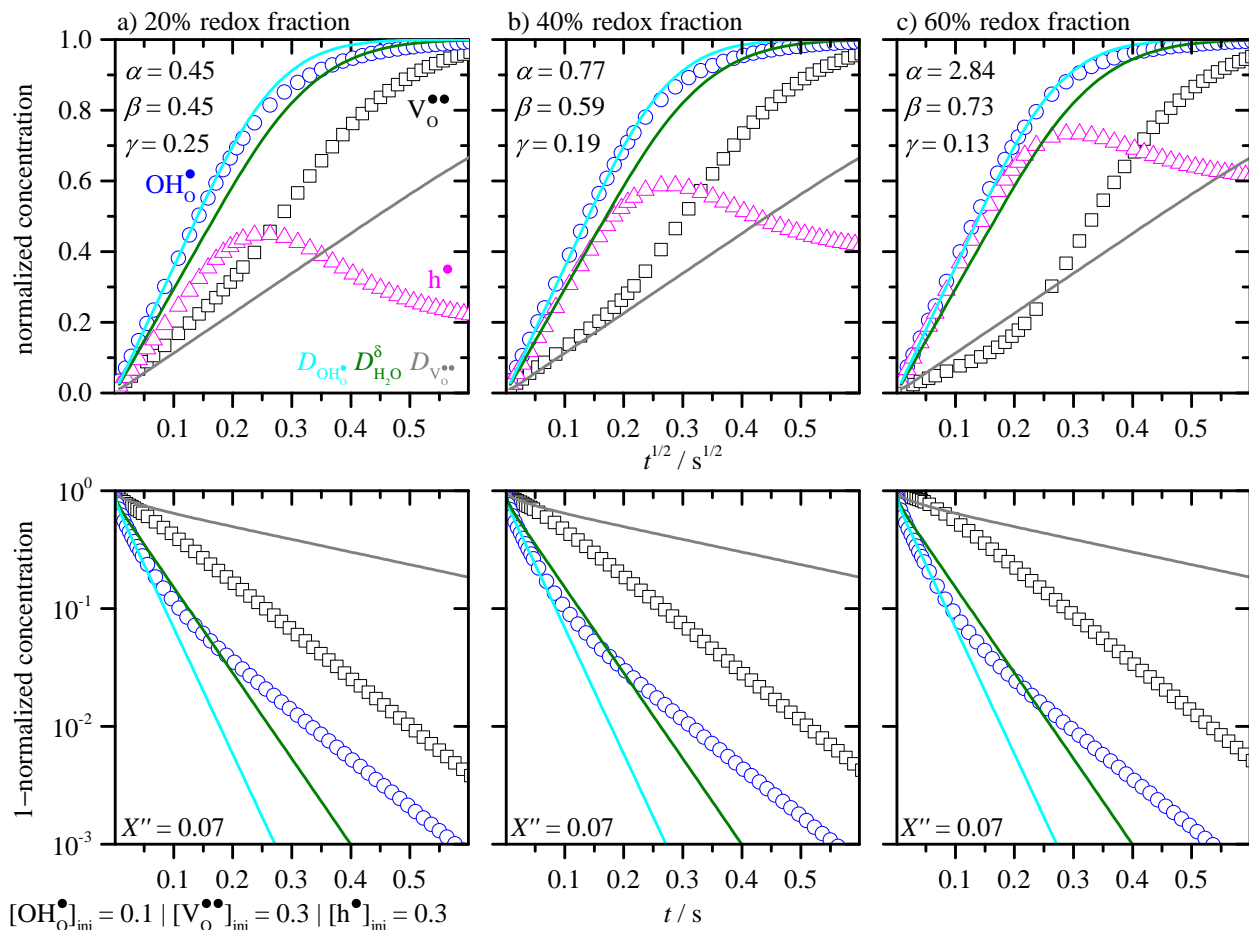


Figure 4.20: Integrated, normalized concentration profiles for different redox fractions $-\Delta[h^{\bullet}]/\Delta[OH_O^{\bullet}]$. $V_O^{\bullet\bullet}$ (black squares) and OH_O^{\bullet} (blue circles) are normalized to their initial and final values. h^{\bullet} (magenta triangles) is normalized to $-\Delta[OH_O^{\bullet}]$. Note that although the values for $V_O^{\bullet\bullet}$ and h^{\bullet} are positive, their change with respect to their initial values is negative. The given, initial concentrations are rounded values (exact values in table B.4, appendix B). The colored lines represent the profiles for the indicated diffusivities $D_{OH_O^{\bullet}}$ (cyan), $D_{V_O^{\bullet\bullet}}$ (gray) and $D_{H_2O}^{\delta}$ (green). Top: Normalized concentration versus $time^{1/2}$ to highlight the short term behavior. Bottom: 1-normalized concentration in logarithmic scale versus time to show the long term relaxation.

unity for 100% redox fraction but the decoupling would be zero, i.e. single-fold diffusion of hydrogen is observed. Hence, also β is less suited for this case. Therefore, a third parameter γ is defined which is the difference between β and the redox fraction. For pure acid-base thermodynamics (section 4.3.2 and 4.3.3) $\gamma = \beta$. γ reaches its maximum for a large transient reduction (large β) and low redox fraction. Therefore, γ is probably the best parameter to quantify the observable (measurable) degree of decoupling including all influencing effects. γ is additionally shown in figure 4.20 and decreases with increasing redox fraction.

4.3.5 Effect on mass and conductivity relaxations

One intention of the previous simulations is to check under which conditions the two-fold relaxation is experimentally observable. In a DC conductivity relaxation experiment the decoupling is theoretically supposed to be easily measurable as the flux of electron holes changes its direction between reduction (fast H flux) and reoxidation (slow O flux). Hence, a DC transient versus time would qualitatively follow the h^\bullet profile plotted in the respective figures. Nonetheless, for materials with very high hole conductivity (i.e. high mobility at medium concentration) a low relative change in $[h^\bullet]$ is hardly measurable (resolution limit of the DC device).

Most experimental data for BSFZ were collected using TG mass relaxation upon $\Delta p_{\text{H}_2\text{O}}$. Therefore, the influence of the previous parameters on the mass transient is discussed. Despite the already made experiments, this is not as trivial as for the conductivity relaxation as now both fluxes have the same direction and, moreover, the flux of O contributes 8 times stronger to the total weight change as the flux of H (in case of pure acid-base thermodynamics) which makes it very difficult to observe the decoupling. In figure 4.21 the normalized mass transients versus $t^{1/2}$ are shown for each analyzed set of changed parameters.

In figure 4.21a the change of mass relaxation with increasing hole concentration, i.e. increasing degree of decoupling is shown. For low hole concentrations (black) a two-fold relaxation is not observed and not expected as ambipolar diffusion of water takes place. At medium hole concentration (red) the decoupling is still weak ($\beta = 0.26$) but not clearly visible.^c Even at maximum possible decoupling ($\alpha = 1$ and $\beta = 0.57$) it might for an ideal experiment be visible, but the effect is still weak and can be overlaid by other experimental uncertainties (resolution of the TG, gas switching times). It has to be noted here again that the last case is very hypothetical and that for a real system water uptake by redox reaction would take place.

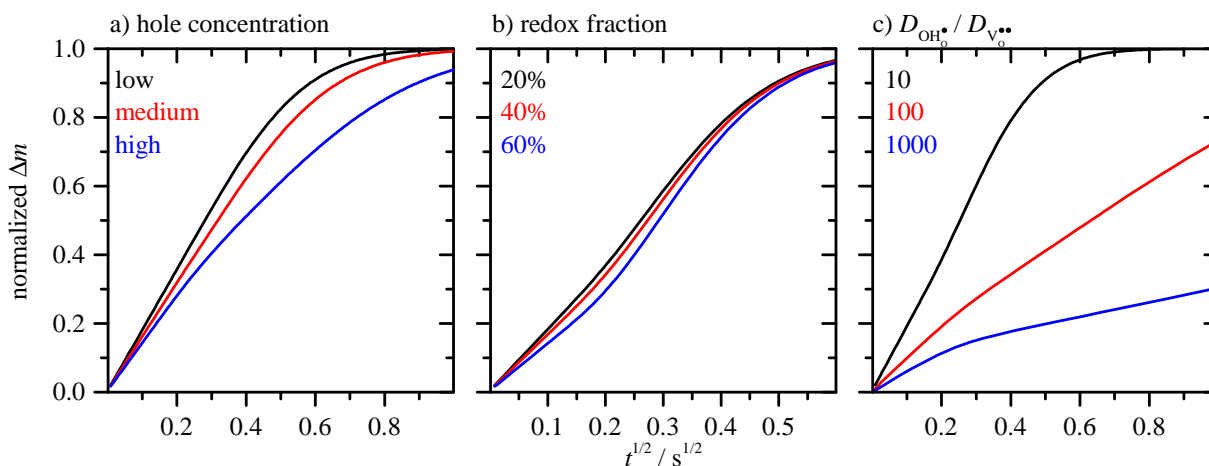


Figure 4.21: Normalized mass transients for the different, analyzed changes of one parameter.

^cThe change in $D_{\text{O}}^{\text{eff}}$ between all three curves is of course visible but in praxis this can also be owing to different D_{V^\bullet} values.

Figure 4.21b shows the change of the mass transient with change of the redox fraction. Before the simulations I expected an increased slope for short times (concave inflection) accommodating the increased contribution of the fast H flux. Interestingly, the opposite is the case and the slope is smaller at the beginning resulting in a convex inflection – cf. blue line. The reason is, that the increased slope by the increased H contribution is overcompensated by the decelerated O flux for short times as discussed in section 4.3.4. All in all, the difference between the transients is small and the decoupling effect is hardly observed.

Last but not least, the mass transients for different diffusivity ratios are shown in figure 4.21c. For one order of magnitude difference (black line) the decoupling is weak ($\beta = 0.32$) and not visible. At two orders of magnitude difference (red line) the expected concave inflection starts to become observable but from an experimental point of view it will be seen in section 4.4.1 that the still weak effect will be compensated by technical difficulties. At least, for three (and more) orders of magnitude difference in $D_{V_{\bullet\bullet}^{\circ}}$ and $D_{OH_{\bullet}^{\circ}}$ where β almost reaches its maximum (0.73 for three orders, maximum at ≈ 0.8) the two-fold relaxation is clearly visible and probably measurable.

4.3.6 Increasing the hole concentration with $p_{O_2}^{1/2} K_{ox}$ at fixed $p_{H_2O} K_{hydrat}$

In the last section of this chapter a combined examination is performed. It was mentioned several times that the previous discussions are more of conceptional intention to analyze the separated influence of single parameters on the decoupling process. Now, simulations are analyzed based on concentrations and concentration changes according to the thermodynamic defect model described in section 2.1. To visualize the increasing decoupling effect with increasing hole concentration $p_{H_2O} K_{hydrat}$ is fixed to an arbitrary but representative^d value of 10^{-2} . $[h^{\bullet}]$ is increased by increasing $p_{O_2}^{1/2} K_{ox}$ from 10^{-6} (electrolyte) to 10^3 (electrode material).

In figure 4.22 concentration profiles for three different $p_{O_2}^{1/2} K_{ox}$ values are shown which cover the cases a) electrolyte with low hole concentration, b) transition from electrolyte at high p_{O_2} and T to mixed-conducting electrode and c) electrode material. Already at hole concentration $[h^{\bullet}] < [V_{\bullet\bullet}^{\circ}]$ the decoupling starts slightly but overall almost only water is incorporated (a). At moderate hole concentration $J_{H^{\bullet}}$ and $J_{V_{\bullet\bullet}^{\circ}}$ decouple stronger and the redox fraction is increased. Consequently, both fluxes cannot be described by a single, effective diffusion coefficient as both profiles show two pronounced linear regimes each. For hole concentrations reaching almost the acceptor-dopant concentration protons are incorporated almost exclusively by redox reaction, i.e. the redox fraction is nearly unity and the proton and hole profiles converge (ambipolar diffusion of hydrogen, $D_H^{\delta} \approx D_{OH_{\bullet}^{\circ}}$ owing to the low degree of hydration). Moreover, the small remaining oxygen vacancy flux falls below the gray profile, hence, $D_O^{eff} < D_{V_{\bullet\bullet}^{\circ}}$. This was also observed by exclusively changing the redox fraction in section 4.3.4.

^dRepresentative in a way to cover conditions found for BSFZ, i.e. moderate proton concentration, but still sufficiently high degree of hydration, here 0.1, to make the effects visible.

All results, i.e. effective diffusivities for short times $D_{\text{H}}^{\text{eff}}$ and $D_{\text{O}}^{\text{eff}}$, their normalized ratio α , normalized transient reduction β , the combined parameter γ as well as the transference numbers for the three charge carriers, are summarized in figure 4.23 as function of $[\text{h}^\bullet]$ (a) and $p_{\text{O}_2}^{1/2} K_{\text{ox}}$ (b) for a low degree of hydration $p_{\text{H}_2\text{O}} K_{\text{hydrat}} = 10^{-2}$. In contrast to figure 4.18 where only $[\text{h}^\bullet]$ is changed, both effective diffusivities not only decouple with increasing $p_{\text{O}_2}^{1/2} K_{\text{ox}}$, $D_{\text{H}}^{\text{eff}}$ reaches a maximum by even slightly overshooting $D_{\text{OH}_\bullet\text{O}}$ and $D_{\text{O}}^{\text{eff}}$ undershoots $D_{\text{V}_\bullet\bullet\text{O}}$. The cases where $D_{\text{O}}^{\text{eff}} < D_{\text{V}_\bullet\bullet\text{O}}$ are of less physical relevance as the oxygen vacancy concentration and, consequently, its flux approaches zero. Furthermore, it still has to be kept in mind that the D^{eff} values cover only the short term relaxation. These aspects are the reason why the

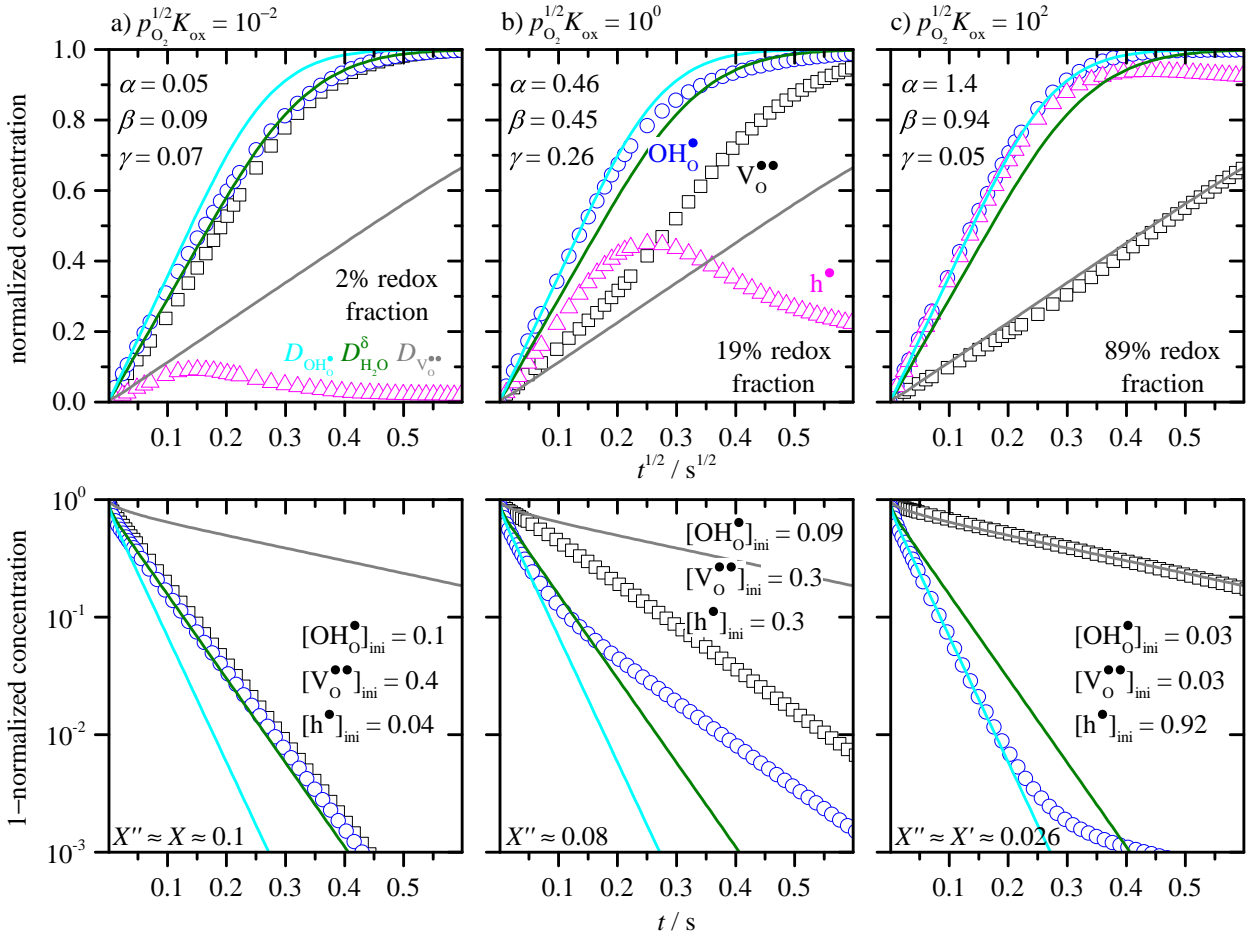


Figure 4.22: Integrated, normalized concentration profiles for different $p_{\text{O}_2}^{1/2} K_{\text{ox}}$ values at $p_{\text{H}_2\text{O}} K_{\text{hydrat}} = 10^{-2}$ ($X \approx 0.1$). $\text{V}_{\text{O}}^{\bullet\bullet}$ (black squares) and $\text{OH}_{\text{O}}^{\bullet}$ (blue circles) are normalized to their initial and final values. h^\bullet (magenta triangles) is normalized to $-\Delta[\text{OH}_{\text{O}}^{\bullet}]$. Note that although the values for $\text{V}_{\text{O}}^{\bullet\bullet}$ and h^\bullet are positive, their change with respect to their initial values is negative. The given, initial concentrations are rounded values (exact values in table B.5, appendix B). The colored lines represent the profiles for the indicated diffusivities $D_{\text{OH}_{\text{O}}^{\bullet}}$ (cyan), $D_{\text{V}_{\text{O}}^{\bullet\bullet}}$ (gray) and $D_{\text{H}_2\text{O}}^{\delta}$ (green). Top: Normalized concentration versus time^{1/2} to highlight the short term behavior. Bottom: 1 – normalized concentration in logarithmic scale versus time to show the long term relaxation.

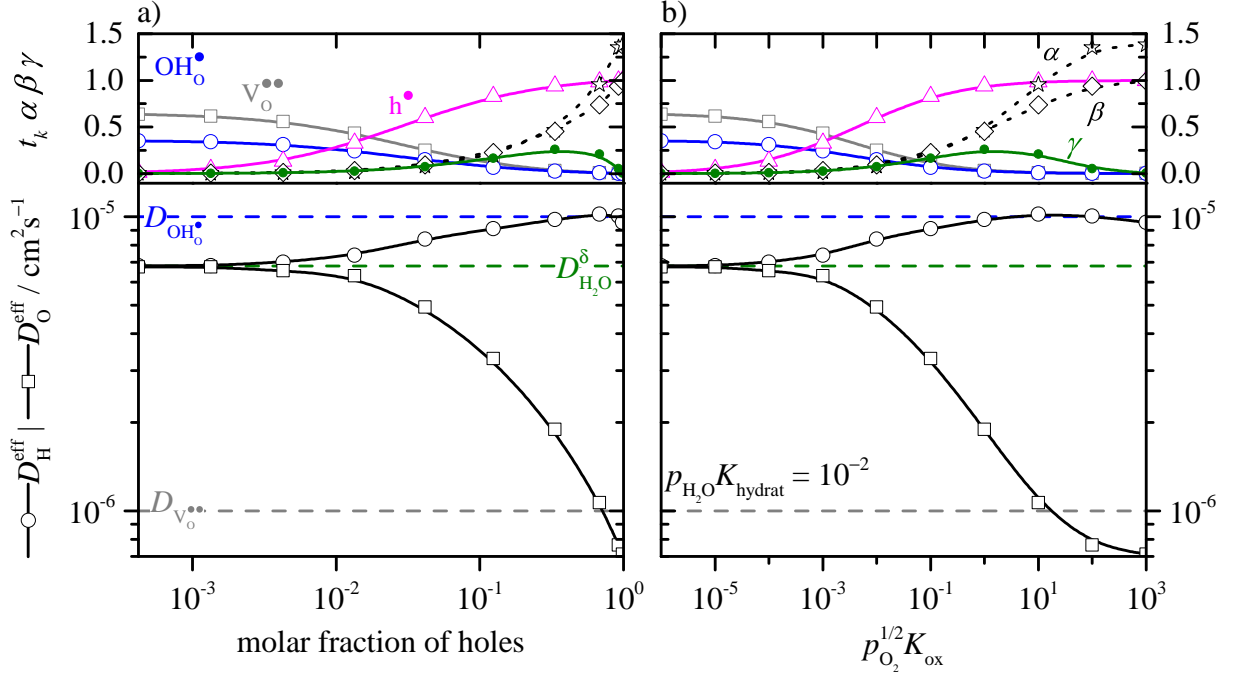


Figure 4.23: Effective diffusivities $D_{\text{H}}^{\text{eff}}$ (circles) and $D_{\text{O}}^{\text{eff}}$ (squares), transference numbers for OH_0^\bullet (blue), $\text{V}_0^{\bullet\bullet}$ (gray) and h^\bullet (magenta), normalized ratio α (stars), normalized transient reduction β (diamonds) and γ (green dots) with increasing $[\text{h}^\bullet]$ for $p_{\text{O}_2}^{1/2} K_{\text{ox}} = 10^{-6}$ to 10^3 at $p_{\text{H}_2\text{O}} K_{\text{hydrat}} = 10^{-2}$. a) Plotted against $[\text{h}^\bullet]$ in comparison to figure 4.18 and b) against $p_{\text{O}_2}^{1/2} K_{\text{ox}}$ in comparison to the three-dimensional plots in section 2.1.

degree of decoupling α increases faster than β even to values above unity. Interestingly and in contrast to the previous simulations, β now reaches its final value of 1 for the case of pure hydrogen uptake, i.e. ambipolar diffusion of hydrogen. Thus, although $\beta = 1$, only single-fold diffusion takes place which is the reason that in the presence of partial hydrogen uptake by redox reaction β is less suited as parameter for the decoupling and, hence, γ was introduced in section 4.3.4. This parameter γ is plotted as green bullets and reaches as expected a maximum for the combination of high degree of decoupling and moderate redox fraction. Approaching single-fold diffusion of H_2O or H , γ decreases to zero.

Finally, the effective diffusivities, β and γ are shown for the total analyzed Kp range in figure 4.24 (in figure 4.23b a two-dimensional section of figure 4.24 is plotted). In the left plot the defect diffusion coefficients are drawn as dashed lines and the chemical diffusivity of water $D_{\text{H}_2\text{O}}^{\delta}$ as red line, calculated from eq. 2.43. Three different cases are highlighted as bold blue and black lines: (A) For low degrees of protonation $D_{\text{H}}^{\text{eff}} \approx D_{\text{OH}_0^\bullet}$ and the decoupling mainly occurs by a decrease in $D_{\text{O}}^{\text{eff}}$ reaching and slightly overshooting $D_{\text{V}_0^{\bullet\bullet}}$. But as mentioned for high $p_{\text{O}_2}^{1/2} K_{\text{ox}}$ values protons are incorporated by hydrogen uptake, i.e. $D_{\text{O}}^{\text{eff}}$ does not contribute to the relaxation process. This is additionally visualized by the three-dimensional plot of β and γ in the right figure. With increasing $p_{\text{O}_2}^{1/2} K_{\text{ox}}$ the normalized redox fraction β reaches unity whereas γ runs through a maximum being zero for low $p_{\text{O}_2}^{1/2} K_{\text{ox}}$ values

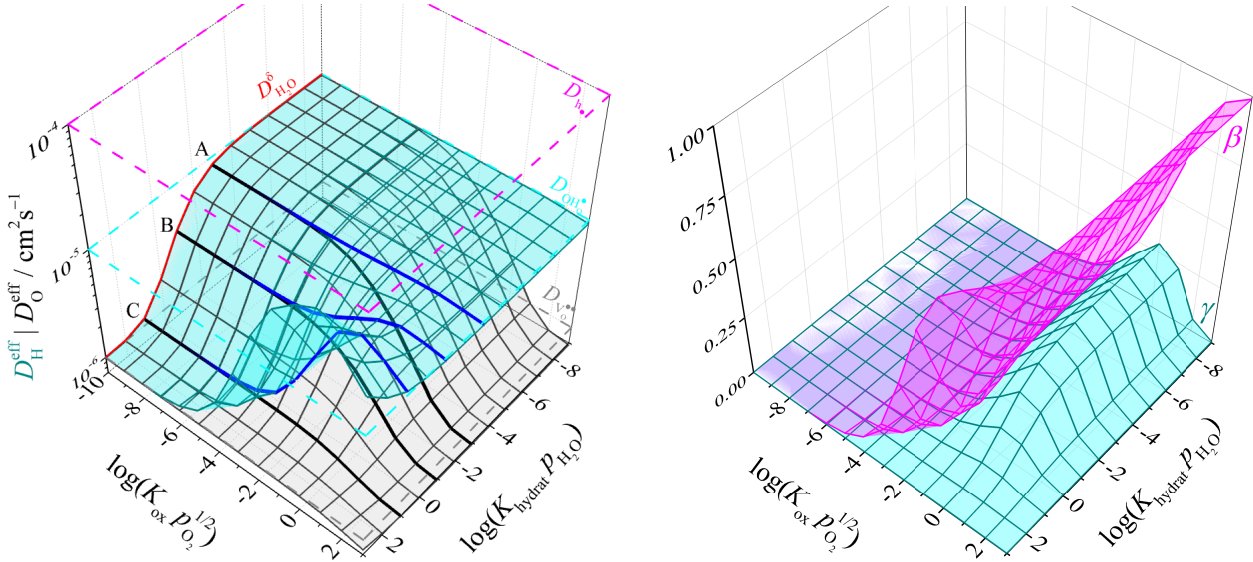


Figure 4.24: Effective diffusivities $D_{\text{H}}^{\text{eff}}$ (blue) and $D_{\text{O}}^{\text{eff}}$ (gray), normalized transient reduction β (magenta) and $\gamma = \beta - \text{redox fraction}$ (blue) for the total Kp range. The defect diffusivities, the chemical diffusivity of water $D_{\text{H}_2\text{O}}^{\delta}$ (red) and three exemplary degree of hydrations (A, B, C) are highlighted.

(ambipolar diffusion of water, no decoupling) and high $p_{\text{O}_2}^{1/2} K_{\text{ox}}$ values (ambipolar diffusion of hydrogen, no decoupling). (B) For intermediate degrees of protonation the decoupling of the effective diffusivities is roughly symmetrical as qualitatively shown by Kim and Yoo.^[33] As already found in figure 4.23 $D_{\text{H}}^{\text{eff}}$ increases to $D_{\text{OH}\cdot}$ slightly overshooting it. The behavior is qualitatively not changed compared to case (A). For high degrees of protonation (C) $D_{\text{O}}^{\text{eff}}$ does not change much as it is already close to $D_{\text{V}\cdot\cdot}$ and the main decoupling occurs through $D_{\text{H}}^{\text{eff}}$ (opposite to case (A)). Now, $D_{\text{H}}^{\text{eff}}$ strongly overtakes $D_{\text{OH}\cdot}$ with increasing $p_{\text{O}_2}^{1/2} K_{\text{ox}}$ still running into its final value of $D_{\text{OH}\cdot}$. This overshooting is explained by the fact that here the redox fraction starts to increase at lower $p_{\text{O}_2}^{1/2} K_{\text{ox}}$ values than for intermediate and low degrees of hydration. This is seen in the right plot of figure 4.24 where the magenta surface of the redox fraction β bends towards lower $p_{\text{O}_2}^{1/2} K_{\text{ox}}$ values with increasing $p_{\text{H}_2\text{O}} K_{\text{hydrat}}$. The chemical diffusion coefficient of hydrogen representing this redox contribution is allowed to range between $D_{\text{h}\cdot}$ (low $[\text{h}\cdot]$) and $D_{\text{OH}\cdot}$ (high $[\text{h}\cdot]$) – cf. eq. 2.45. For high degrees of hydration this contribution becomes dominant at early decoupling stages which is visible in the overshoot of $D_{\text{H}}^{\text{eff}}$. For lower degrees of hydration $D_{\text{H}}^{\text{eff}}$ adopts values of D_{H}^{δ} at higher $p_{\text{O}_2}^{1/2} K_{\text{ox}}$ values where the latter is already decreased to $D_{\text{OH}\cdot}$. Therefore, no overshooting is observed. The overshooting phenomenon results also in the behavior of γ the maximum of which decreases along the $p_{\text{H}_2\text{O}} K_{\text{hydrat}}$ axis with increasing degree of hydration.

All the results from the simulations will help in the next sections to analyze, discuss and understand the thermodynamic and diffusion behavior of BSFZ.

4.4 Diffusion - Single-fold vs. two-fold

In this chapter the relaxation characteristics of BSFZ upon $p_{\text{H}_2\text{O}}$ change is discussed based on the defect thermodynamic results in the previous section and the diffusion model of a three charge carrier system in section 2.2.2. A few results were already touched in the thermodynamic analysis section 4.2 to understand the reversible defect chemistry.

4.4.1 Thermogravimetric relaxation

As already recognized in the beginning of chapter 4.2 there is a severe difference between the mass transients of BSFZ in 10 mbar and 1 bar p_{O_2} . In figure 4.25 the first jump of the example in figure 4.5 at 400 °C from $p_{\text{H}_2\text{O}} = 5.70$ mbar to 9.83 mbar at constant $p_{\text{O}_2} = 10$ mbar (a) and 1 bar (b) is shown. The extended diffusion model – chapter 2.2.2 – predicts that in a system with three mobile charge carriers contributing to the relaxation upon stepwise change of the respective gas-phase activities the resulting transient, here mass transient, in principle cannot simply be described by one chemical diffusion coefficient.

Nonetheless, for predominant acid-base thermodynamics present at 10 mbar p_{O_2} the mass relaxation is dominated by the uptake of oxygen, i.e. as a first approximation the transient in figure 4.25a is fitted with a single diffusion coefficient using the well-known solution for Fick's second law for one-dimensional diffusion into a plane sheet with fast surface equilibration, eq. 4.12 and 4.13.^[101] As the fit neglects the small contribution of the hydrogen migration and assumes that the oxygen migration can be described by a single chemical diffusion coefficient (which was shown not necessarily to be the case) it is not exactly $D_{\text{O}}^{\text{eff}}$ (introduced in chapter 2.2.2) that is obtained. Therefore, the fitted D value is called $D_{1\text{param}}$ to highlight that is

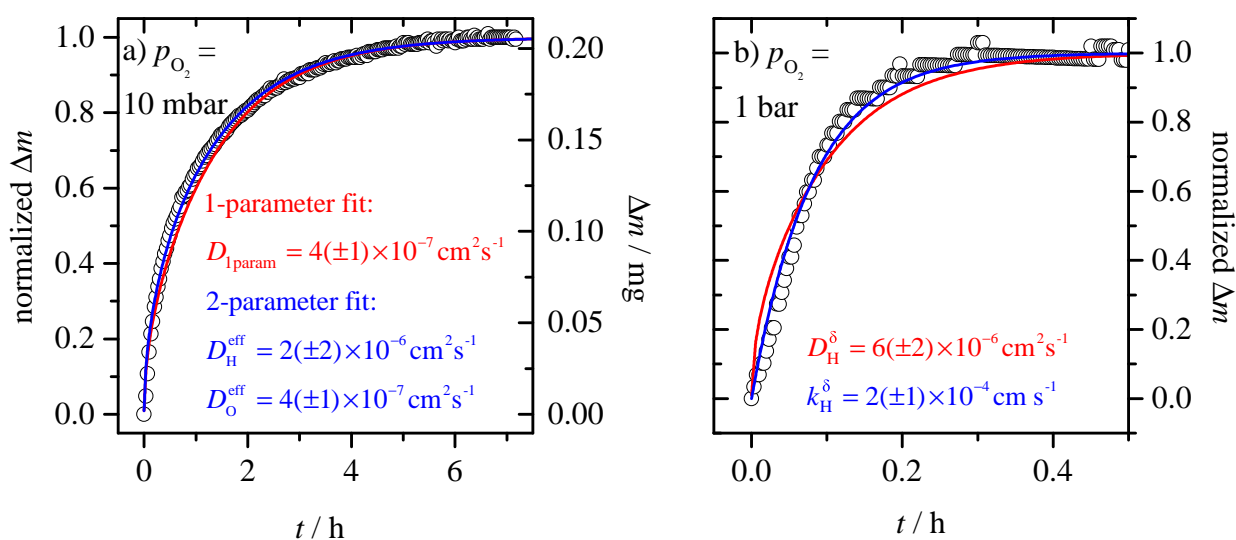


Figure 4.25: Exemplary mass relaxation for the first jump at constant p_{O_2} from $p_{\text{H}_2\text{O}} = 5.70$ mbar to 9.83 mbar at 400 °C. a) $p_{\text{O}_2} = 10$ mbar b) $p_{\text{O}_2} = 1$ bar. The respective fitting results are shown as solid lines and values, see text for interpretation.

the solution from the one-parameter fit.

$$\frac{\Delta m}{\Delta m_\infty} = 1 - f(D, t) \quad (4.12)$$

$$f(D, t) = \frac{8}{\pi^2} \sum_{n=0}^{\infty} (2n+1)^{-2} e^{-\frac{(2n+1)^2 \pi^2 D t}{4l^2}} \quad (4.13)$$

Alternatively, the fitting procedure corresponding to the two-fold relaxation can be applied.^[31] For this purpose the migration of H and O is assumed to be independent of each other, which is also a simplification of the diffusion model (full decoupling into first homogeneous reduction by hydrogen diffusion and second homogeneous reoxidation by oxygen migration is only present in an extreme case). The corresponding diffusion in homogeneous medium is mathematically expressed by eq. 4.14 where two single-fold solutions from Fick's second law are weighted with a factor Δm_k expressing their final contribution to the total mass change.

$$\Delta m = (\Delta m_{\text{H}} + \Delta m_{\text{O}}) - \Delta m_{\text{H}} f(D_{\text{H}}^{\text{eff}}, t) - \Delta m_{\text{O}} f(D_{\text{O}}^{\text{eff}}, t) \quad (4.14)$$

Here, both diffusion coefficients are denoted as effective diffusivities D^{eff} , although the simulation of the model showed that in many cases the proton profile and in some cases even the oxygen profile cannot be described by a single, effective diffusivity. In figure 4.25a all fit results are shown as solid lines and values. Owing to the fact that a strong decoupling is not observed in the transient both fits match the measured data very well (that the two-fold fit matches better is not a surprise simply from the mathematical fact of having more fit parameters). Hence, $D_{1\text{param}}$ and $D_{\text{O}}^{\text{eff}}$ are identical. $D_{\text{H}}^{\text{eff}}$ is larger than $D_{\text{O}}^{\text{eff}}$ but owing to the low contribution to Δm_∞ the error is very large, hence, this result is not relevant. Thus, for the behavior of the transients in 10 mbar p_{O_2} only the one-parameter fit $D_{1\text{param}}$ is discussed further.

Before continuing, the relaxation in 1 bar p_{O_2} needs to be understood. In section 4.2 three arguments were given supporting that at this oxygen partial pressure protons are incorporated more or less exclusively by redox-thermodynamics, i.e. oxygen vacancies do not contribute to the transient and the migration can analytically be described as both driving forces are now coupled: $\nabla c_{\text{OH}_\bullet} = -\nabla c_{\text{h}\bullet}$. Inserting this coupling into eq. 2.40 yields

$$J_{\text{H}_i^\bullet} = -((1 - t_{\text{OH}_\bullet})D_{\text{OH}_\bullet} + t_{\text{OH}_\bullet}D_{\text{h}\bullet})\nabla c_{\text{OH}_\bullet} \neq -(t_{\text{h}\bullet}D_{\text{OH}_\bullet} + t_{\text{OH}_\bullet}D_{\text{h}\bullet})\nabla c_{\text{OH}_\bullet} \quad (4.15)$$

Note that as $t_{\text{V}\bullet\bullet} \neq 0$, i.e. $1 - t_{\text{OH}_\bullet} \neq t_{\text{h}\bullet}$, this chemical diffusion coefficient for hydrogen diffusion D_{H}^{δ} differs from the analogous value for the two charge carrier case derived in eq. 2.45. Nevertheless, equal to the latter the flux of the protons can be described by a single diffusivity. The above expression can also simply be obtained from eqs. 2.38 and 2.39 setting $\nabla c_{\text{V}\bullet\bullet} = 0$.

In figure 4.25b the result of the one-parameter fit using eq. 4.12 is shown as red line. It is obvious that the fit is quite poor and that the shape of the measured data rather shows a linear increase for the short-term behavior. For this observation three explanations have to be considered.

(i) Owing to the fact that the diffusion of hydrogen is supposed to be much faster than of oxygen, the transient at 1 bar p_{O_2} is possibly now determined by the surface exchange

reaction (characterized by the effective rate constant k^δ). This shift from D - to k - control can further be enhanced as k_{H}^δ (characterizing the redox-reaction) is supposed to differ from k_{hydrat}^δ (characterizing the acid-base hydration), i.e. two effects – clearly faster diffusion and probably slower surface exchange reaction – are identified.^e A k -determined transient is fitted through eq. 4.16.^[72] Both fitting results are added in figure 4.25b – the obtained diffusion coefficient can without any doubt be denoted as chemical diffusivity of hydrogen D_{H}^δ and the effective rate constant as k_{H}^δ . It is clear that the latter (blue line) fits the measured data better.

$$\frac{\Delta m}{\Delta m_\infty} = 1 - e^{-\frac{kt}{l}} \quad (4.16)$$

(ii) The linear regime for short times can also be seen as a flattening of the D -controlled relaxation. As the relaxation is very fast ($\tau_{1/2} \approx 4$ min) the beginning might be decelerated by the gas switching time (it takes about 5 min until the new $p_{\text{H}_2\text{O}}$ is reached). This also explains that the relaxation is more or less independent on the temperature as the gas switching time is, of course, independent on the temperature as well.

(iii) Unfortunately, it cannot totally be ruled out that the short transients in 1 bar p_{O_2} result from cracks which possibly were formed during heating/cooling and equilibration with the gas phase at changed conditions which causes volume changes of the pellet (it is rather the stoichiometric gradient during equilibration than the temperature gradient which can cause strains in the pellet leading to cracks). These cracks lead to shorter diffusion length shifting the transient probably to the k -controlled case (explanation (i)).

Nonetheless, for the next discussions $D_{1\text{param}}$ and D_{H}^δ are used. Under the condition that the relaxation in 1 bar p_{O_2} is k -determined, the latter quantity is a lower bound for the “real” D_{H}^δ which is even faster (otherwise it would be D -determined).

All fitting results in H_2O and D_2O humidified atmospheres are summarized in an Arrhenius plot in figure 4.26a for $D_{1\text{param}}$ (10 mbar p_{O_2}) and b for D_{H}^δ (1 bar p_{O_2}). To further prove the correct assignment of the diffusion coefficients defect diffusivities for $\text{V}_{\text{O}}^{\bullet\bullet}$ and $\text{OH}_{\text{O}}^\bullet$ for similiar materials extracted from literature data are drawn as dashed lines. For $D_{\text{OH}_{\text{O}}^\bullet}$ (blue lines) data for BZY10 from Kreuer are extrapolated from lower temperatures, and for BZY20 from Yamazaki et al.^f [16;102] For $D_{\text{V}_{\text{O}}^{\bullet\bullet}}$ (gray lines) three materials are given. The oxygen vacancy diffusivity of related perovskites BSF and BSCF are also extrapolated from high temperature data from Wang et al.^[70] $D_{\text{V}_{\text{O}}^{\bullet\bullet}}$ values for BSFZ are not found in the literature. To estimate these values, oxygen flux data j_{O_2} from Martynyczuk et al. using BSFZ as permeation membrane are converted to $D_{\text{V}_{\text{O}}^{\bullet\bullet}}$ by eq. 4.17 and extrapolated to lower temperatures.^[42;103]

^eThis fact complicates the two-fold relaxation in 10 mbar p_{O_2} even more as one or both processes can be k -determined instead of the claimed D -determination. Nevertheless, this has no consequences for the interpretation as the oxygen migration characterized by $D_{1\text{param}}$ clearly is D or at least Dk -determined and the probably k -determined hydrogen migration is hardly measurable.

^fThe Yamazaki et al. data are not extrapolated but fitted through their trapping model. The data is extracted from figure 1a in their publication.^[102]

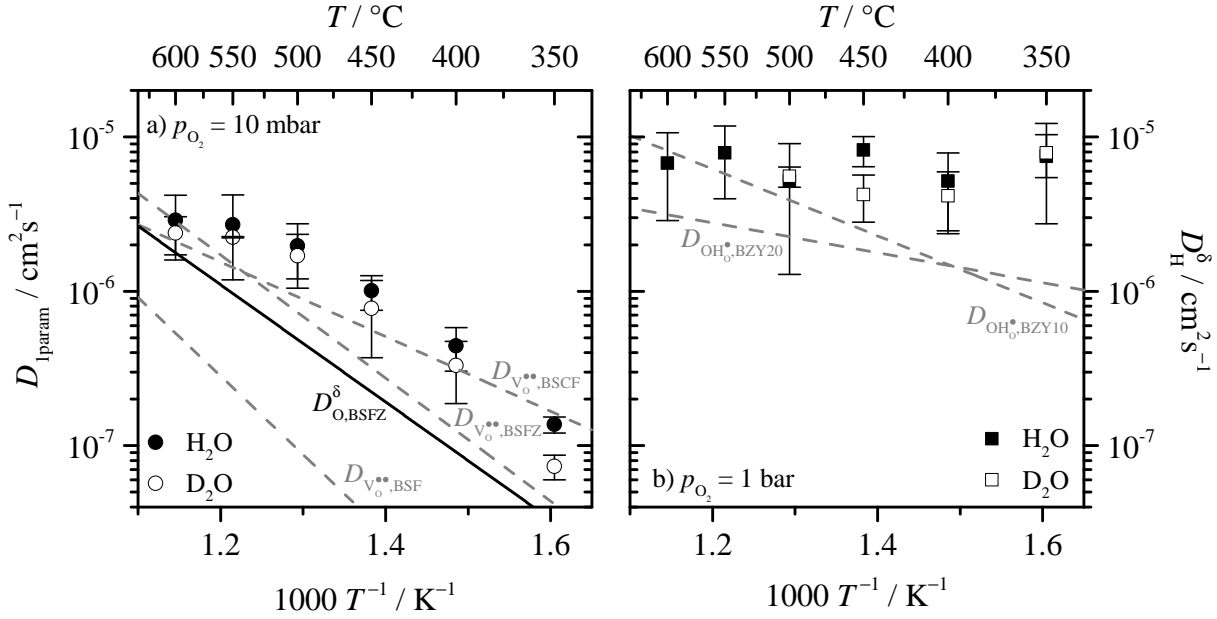


Figure 4.26: Diffusivities obtained from TG relaxation upon $\Delta p_{\text{H}_2\text{O}}$ through single-fold fit for a) $p_{\text{O}_2} = 10$ mbar ($D_{1\text{param}}$) and b) $p_{\text{O}_2} = 1$ bar (D_{H}^{δ}) for H_2O (closed symbols) and D_2O (open symbols). Several defect diffusivities extracted from literature data are shown as dashed lines for $\text{V}_{\text{O}}^{\bullet\bullet}$ (gray) and $\text{OH}_{\text{O}}^{\bullet}$ (blue). Chemical diffusivities for oxygen in BSFZ $D_{\text{O}, \text{BSFZ}}^{\delta}$ (black line) are extracted from the relaxation of the temperature steps.

$$j_{\text{O}_2} = -\frac{RT}{16F^2L} \int_{\ln p'_{\text{O}_2}}^{\ln p''_{\text{O}_2}} t_{\text{eon}} \sigma_{\text{ion}} d \ln p_{\text{O}_2} \quad (4.17)$$

For mixed-conducting electrodes with perceptible electronic conductivity $t_{\text{eon}} \approx 1$ and σ_{ion} being to first approximation p_{O_2} independent, eq. 4.17 is rewritten to eq. 4.18 using Nernst-Einstein relation eq. 2.19.

$$D_{\text{V}_{\text{O}}^{\bullet\bullet}} = -\frac{4V_{\text{M}}Lj_{\text{O}_2}}{[\text{V}_{\text{O}}^{\bullet\bullet}]} \ln \frac{p'_{\text{O}_2}}{p''_{\text{O}_2}} \quad (4.18)$$

p'_{O_2} and p''_{O_2} are the oxygen partial pressures of the feed (high p_{O_2}) and sweep (low p_{O_2}) side of the membrane, respectively, L the thickness of the membrane and V_{M} the molar volume of the ceramic, here BSFZ with $37.4 \text{ cm}^3 \text{ mol}^{-1}$. The extracted $D_{\text{V}_{\text{O}}^{\bullet\bullet}, \text{BSFZ}}$ lies between $D_{\text{V}_{\text{O}}^{\bullet\bullet}}$ for BSF and BSCF. All extracted defect D values need to be taken with care as they are extrapolated from experimental data outside the temperature range shown here, i.e. the intersection between $D_{\text{V}_{\text{O}}^{\bullet\bullet}}$ for BSCF and BSFZ should not be taken too seriously. Nevertheless, the data supply a framework into which the BSFZ results fit reasonable well.

$D_{1\text{param}}$ does not show an ideal linear behavior in the T^{-1} plot but a curvature. Two explanations can be given. (i) Trapping of the protons (defect association of mobile protons to immobile acceptors) can occur with decreasing temperature which leads to a stronger decrease of the diffusivity with decreasing temperature owing to the additional contribution of

the trapping energy. This was experimentally found and discussed for protons in Y-doped BaZrO₃ by Yamazaki et al.^[102] (ii) From the extended diffusion model an ideal linearity in the Arrhenius plot is not necessarily expected for these chemical diffusivities. This is explained for the example of chemical, single-fold diffusion of water (the results can qualitatively be transferred to the three-charge-carrier case but is easier understood for two-charge carriers). For high temperatures the degree of hydration is low, i.e. $D_{\text{H}_2\text{O}}^\delta \approx D_{\text{OH}\bullet}$. With decreasing temperature the degree of hydration is increased and $D_{\text{H}_2\text{O}}^\delta$ decreases more strongly than given by $D_{\text{OH}\bullet}$ approaching $D_{\text{V}\bullet\bullet}$ for a high degree of hydration. This transition of $D_{\text{H}_2\text{O}}^\delta$ from high to low temperature is not necessarily linear in an Arrhenius plot as the temperature dependence of the four contributions to $D_{\text{H}_2\text{O}}^\delta$ ($D_{\text{OH}\bullet}$, $D_{\text{V}\bullet\bullet}$, $[\text{OH}\bullet]$ and $[\text{V}\bullet\bullet]$) is not the same. In figure 4.27 discussed below the equivalent behavior for a system with three mobile charge carriers is given. The isotope effect found for $D_{1\text{param}}$ in H₂O and D₂O (latter values are lower, cf. open circles in figure 4.26a) proves that the proton/deuteron defects have an influence of the chemical diffusion of oxygen (i.e. $D_{1\text{param}} \approx D_{\text{O}}^{\text{eff}} > D_{\text{V}\bullet\bullet}$) otherwise the migration of oxygen is supposed to be independent on the nature of the water species. In addition, roughly estimated D_{O}^δ values for BSFZ are shown in figure 4.26a as solid black line. They are extracted from the mass transient of the temperature steps between two $\Delta p_{\text{H}_2\text{O}}$ relaxation experiments[§]. $D_{1\text{param}} \approx D_{\text{O}}^{\text{eff}}$ is larger than D_{O}^δ which is in agreement with the physical model. However, D_{O}^δ is lower than the extracted $D_{\text{V}\bullet\bullet, \text{BSFZ}}$ which is in contrast to the physical model (cf. eq. 2.21) but is still reasonable close within the uncertainty.

D_{H}^δ is larger than $D_{1\text{param}}$ which is in agreement with all explanations given for the large D_{H}^δ values. They show a very weak temperature dependence. In addition, a strong isotope effect is not measured – except the data at 450 °C – supporting only explanation (ii). However, D_{H}^δ and k_{red}^δ are known to have lower activation energies than respective values for oxygen exchange (D_{H}^δ for low degrees of hydration is close to $D_{\text{OH}\bullet}$ having typically lower E_a values than $D_{\text{V}\bullet\bullet}$).^[16;70;104] However, the small slope of D_{H}^δ experimentally found in the Arrhenius plot can also arise from the relaxation being gas diffusion controlled which is supposed to be temperature independent. Nevertheless, Kreuer found that in perovskites with tetravalent B-site cations the activation energies for proton hopping is lower than for pentavalent B cations, and claimed that perovskites with trivalent B-site cations show even higher proton mobilities with less activation energy than the tetravalent.^[105] Leaving out the results at 350 °C which appear to be too high, the slope of the other data points is not much smaller than for BZY20, in agreement with Kreuer’s statement. Hence, although not excluding the presence of cracks explicitly, the shown values are within a reasonable range and do not obviously conflict with literature data. D_{H}^δ corresponds to the chemical diffusion coefficient, because at high p_{O_2} protons are exclusively incorporated by redox thermodynamics. Owing to the low degree of hydrogenation and based on the simulation results D_{H}^δ is then very close to $D_{\text{OH}\bullet}$ in BSFZ (cf. eq. 4.15 – for $t_{\text{h}\bullet} \approx 1$ $J_{\text{H}_i^\bullet} \approx D_{\text{OH}\bullet} \nabla c_{\text{OH}\bullet}$).

The previous observations are further supported by simulations using the three charge carrier diffusion model. For this purpose, $D_{\text{V}\bullet\bullet}$ is taken from eq. 4.18 using data by Martynczuk et al.^[42], $D_{\text{OH}\bullet}$ is set equal to be D_{H}^δ from the measurements in 1 bar p_{O_2} and $D_{\text{h}\bullet}$.

[§]Upon ΔT oxygen and water are equilibrated simultaneously. However, the oxygen uptake/release is much larger (higher $\Delta[\text{V}\bullet\bullet]$, cf. figure 4.6) than for water.

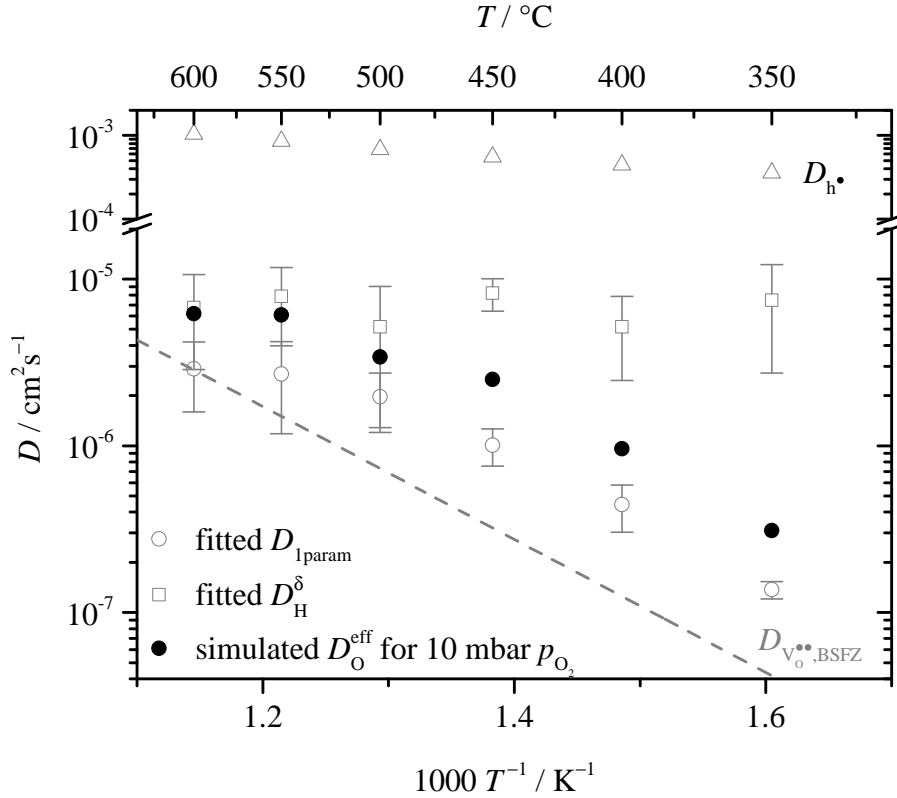


Figure 4.27: Measured $D_{1\text{param}}$ (open circles, 10 mbar p_{O_2}), $D_{\text{H}}^{\delta} \approx D_{\text{OH}\bullet}$ (open squares, 1 bar p_{O_2}), $D_{\text{h}\bullet}$ (open triangles, from conductivity and concentration data) and $D_{\text{V}\bullet\bullet}$ (dashed line) extracted from oxygen flux data of Martynczuk^[42] are shown and used to simulate $D_{\text{O}}^{\text{eff}}$ (closed circles).

is calculated from the conductivity values at 10 mbar p_{O_2} in figure 4.7 using Nernst-Einstein relation eq. 2.19. For the initial and final defect concentrations results from the first $p_{\text{H}_2\text{O}}$ jump of the thermodynamic analysis in chapter 4.2 are used. All numerical values are given in table B.6. In figure 4.27 the simulated $D_{\text{O}}^{\text{eff}}$ values are plotted together with the used diffusivities. The measured concave curvature of $D_{1\text{param}}$ in 10 mbar p_{O_2} is nicely reproduced by the simulations, although the absolute values are higher for which two reasons can be given. (i) The input $D_{\text{V}\bullet\bullet}$ values are extracted and extrapolated from oxygen flux literature data, hence, the “real” $\text{V}\bullet\bullet$ diffusivity can deviate (in agreement with the fact that these extracted $D_{\text{V}\bullet\bullet, \text{BSFZ}} > \text{measured } D_{\text{O}, \text{BSFZ}}^{\delta}$). (ii) Trapping effects are neglected in the diffusion model which can lead to a non-negligible deviation from the trapping-free situation, as discussed by Yamazaki et al. for BZY20.^[102] The simulations further show that the measured $D_{1\text{param}}$ is larger than the defect diffusivity for $\text{V}\bullet\bullet$, a result already found in chapter 4.3 for conditions where $[\text{V}\bullet\bullet] \approx [\text{h}\bullet]$ which is exactly the case for BSFZ at 10 mbar p_{O_2} . Simulations for 1 bar p_{O_2} under the condition of redox thermodynamics are needless as this situation can analytically be described by D_{H}^{δ} (eq. 4.15).

Finally, the proton-conductivity $\sigma_{\text{OH}\bullet}$ is calculated from defect diffusivity and concentration using Nernst-Einstein relation eq. 2.19. As argued previously D_{H}^{δ} obtained from the single-fold fit of the mass relaxation at 1 bar p_{O_2} can be equaled to $D_{\text{OH}\bullet}$ which is used to calculate $\sigma_{\text{OH}\bullet}$.

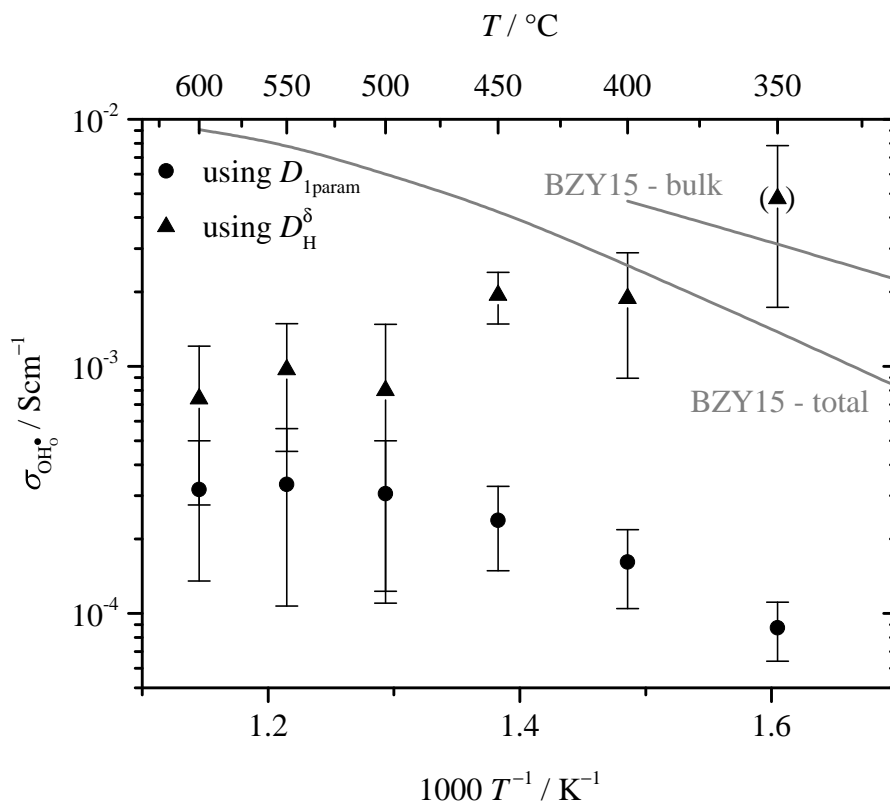


Figure 4.28: Calculated estimates for $\sigma_{\text{OH}_\bullet}$ of BSFZ through $D_{1\text{param}}$ (circles, pessimistic approach) and D_{H}^δ (triangles) together with bulk and total (bulk + grainboundary) proton conductivity of BZY15 directly measured by impedance spectroscopy ($p_{\text{H}_2\text{O}} \approx 20$ mbar, $p_{\text{O}_2} \approx 10$ ppm).

Nevertheless, to safely decide whether or not the proton-conductivity is sufficient to enable the bulk path in the oxygen reduction mechanism (keeping possibly cracking of the pellet in mind), $\sigma_{\text{OH}_\bullet}$ is additionally calculated with $D_{1\text{param}}$. This value is a (pessimistic) lower bound for the proton diffusivity as TG relaxation and simulations show that $D_{1\text{param}} > D_{\text{V}\bullet\bullet}$, and that $D_{\text{V}\bullet\bullet}$ can be supposed to be not much more than two orders of magnitude less than D_{OH_\bullet} (otherwise the two-fold relaxation would be measurable in the TG transient). The calculated $\sigma_{\text{OH}_\bullet}$ values are plotted in figure 4.28. The gray, solid lines show bulk and total (bulk + grain boundary) proton conductivity obtained from own impedance measurements at BZY15 pellets (at > 400 °C the high frequency bulk semicircle cannot be extracted from the spectra). The pessimistic estimate for $\sigma_{\text{OH}_\bullet}$ has a maximum at 550 °C and the same curvature as $D_{1\text{param}}$. The $\sigma_{\text{OH}_\bullet}$ calculated through D_{H}^δ shows an apparent negative activation energy. Both effects can be described by the competition between increasing D_{OH_\bullet} and decreasing hydration with increasing temperature, as also observed for proton-conducting electrolytes.^[16] All values except the highest at 350 °C (outlier, high error bar) are below the total conductivity of BZY15, hence, the higher D_{OH_\bullet} for BSFZ discussed in figure 4.26 is compensated by the lower $[\text{OH}_\bullet]$. Even if the $\sigma_{\text{OH}_\bullet}$ calculated through D_{H}^δ are overestimated by the presence of cracks in the pellets, the exact proton-conductivity in BSFZ ranges between the two given borders. Hence, this is the first work where values for $\sigma_{\text{OH}_\bullet}$ in a mixed-conducting perovskite are given, at

least within an error range of one order of magnitude.

Coming to the final question, even the pessimistic estimation of $\sigma_{\text{OH}\bullet}$ for BSFZ is orders of magnitude above the required minimum for the bulk path estimated from diameter dependent impedance spectroscopy data for (La,Sr)MnO_{3±δ} (LSM). LSM, known to have a very low ionic conductivity of $3 \times 10^{-8} \text{ Scm}^{-1}$ at 800 °C, exhibits oxygen reduction via bulk path for dense 100 nm thin-film microelectrodes on YSZ.^[12] Thus, the bulk path for the oxygen reduction at BSFZ on BZY is definitely expected, and will be proved by impedance spectroscopy in section 4.6.

4.4.2 SIMS and DC relaxation

The two-fold relaxation is expected to be more easily observable by DC conductivity (non-monotonic behavior of hole concentration) and the proton concentration and mobility can directly be measured by tracer-diffusion and SIMS analysis. However, both experiments are at an early stage for BSFZ, especially the tracer experiments are very time consuming (technique destroys the sample). Thus, only very few data is collected so far and are shown here for the sake of a qualitative rather than quantitative interpretation.

In figure 4.29a the space-resolved depth profiles of the counts of the deuterium signal (negative D⁻ are recorded) for both p_{O_2} values are shown. The counts are normalized to the sum of representative signals for each cation (⁵⁶Fe, ⁶⁴ZnO, ⁸⁸SrO₂ and ¹³⁸BaO) to relatively compare the signal, i.e. to check whether the deuterium concentration is equal for both oxygen partial pressures.^h The normalized counts for $p_{\text{O}_2} = 1 \text{ bar}$ are slightly less than for 10 mbar, in contrast to the thermodynamic TG analysis in chapter 4.2. As mentioned there, the redox fraction at 10 mbar might be underestimated which then explains the difference. Furthermore, the deviation in the normalized counts might arise from the different oxygen non-stoichiometry. The SIMS signal intensity depends on the matrix of the material and a calibration is mandatory to quantitatively compare the concentrations. Nevertheless, with the deuterium signal intensities being not orders of magnitude apart, the deuterium concentration is roughly independent of p_{O_2} , similar to the TG results.

To extract the tracer diffusion coefficient $D_{\text{OD}\bullet}^*$ the space-resolved profiles are fitted to eq. 4.19, the analytical solution for one-dimensional diffusion through Fick's second law where c_x^* is the tracer concentration at point x , $c_{x=0}^*$ at the sample surface $x = 0$ and c_{bg}^* the deuterium concentration of the background, and t is the tracer exchange time (here: 1 h). The data points from $x = 0$ to 0.005 cm are not considered in the fit. As visible from the shape of the profiles (for tracer diffusion a linear slope is expected for low x values, cf. fit result in figure 4.29b) there is a bending in the approximately linear graph around 50 μm depth. This is due to the fact that the samples were equilibrated and exchanged in the TG setup where the samples had to cool down to $\approx 100 \text{ °C}$ before the sample could be removed. During this

^hThe counts are proportional to the absolute concentration. The proportionally differs between different material compositions, i.e. also the $\text{V}_{\text{O}}^{\bullet\bullet}$ concentration. Hence, to obtain the deuterium concentration from the D⁻ signal intensity deuterium implanted samples of same composition with known deuterium concentration are necessary for calibration.

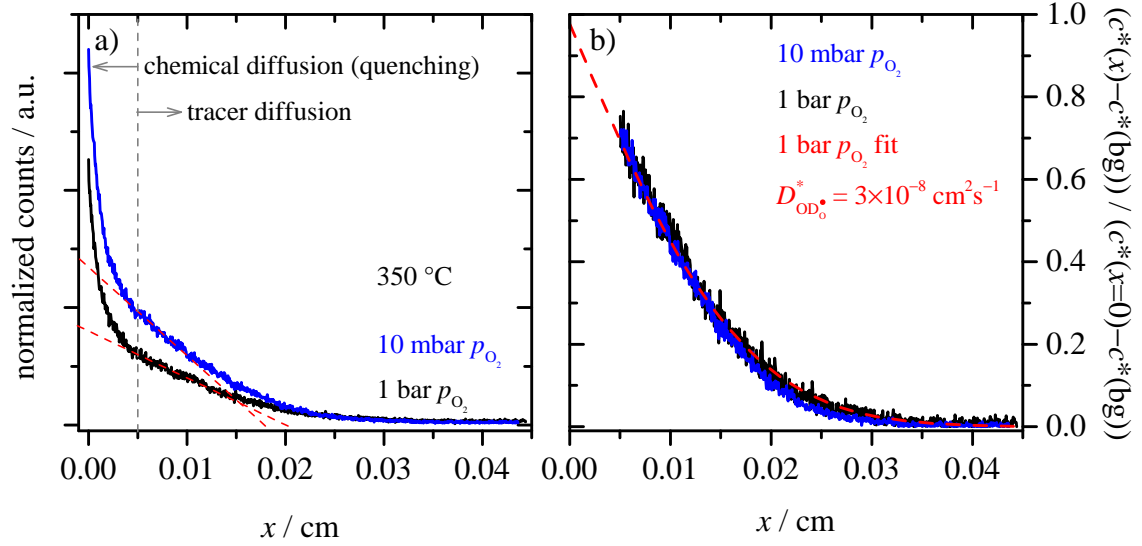


Figure 4.29: Space-resolved deuterium SIMS signal (counts of D^- , line scan) a) normalized to the sum of representative cation counts and b) normalized to range between zero and unity for 10 mbar (blue) and 1 bar (black) p_{O_2} . In b) the first 50 μm are not taken into the fit (red dashed line) to exclude the chemical diffusion in this region owing to the too slow quenching of the sample. The red dashed lines in a) give the linear extrapolation to estimate the counts at the surface in the absence of chemical diffusion.

rather long quenching (about 20 min) additional chemical diffusion took place which explains the shape of the profile. The linear regime of the deeper profile is then extrapolated to $x = 0$ (red dashed straight lines in figure 4.29a) and the intersection with the ordinate there is taken as $c_{x=0}^*$. In principle, the tracer diffusivity and tracer surface exchange coefficient k^* can be fitted simultaneously. However, for the latter the absolute concentrations need to be known, especially at the surface. The counts in figure 4.29a are further normalized according to the left side of eq. 4.19 to range between 1 at $x = 0$ and 0 at $x = L/2$ where L is the sample thickness, i.e. infinitely fast surface reaction and, consequently, only D -control is presumed.

$$\frac{c_x^* - c_{\text{bg}}^*}{c_{x=0}^* - c_{\text{bg}}^*} = \text{erfc}\left(\frac{x}{2\sqrt{D^*t}}\right) - \left(\exp\left(\frac{k^*x + k^{*2}t}{D^*}\right) \times \text{erfc}\left(\frac{x}{2\sqrt{D^*t}} + k^*\sqrt{\frac{t}{D^*}}\right)\right) \quad (4.19)$$

In figure 4.29b the normalized data points together with the fit (red dashed line) are shown. It is seen immediately that D^* is independent of p_{O_2} which is a reasonable result (a slight deviation might occur owing to different $[V_{\text{O}}^{\bullet\bullet}]$ - cf. simulations and diffusion equations). As tracer diffusion of protons in perovskites takes place by interstitial hopping, $D_{\text{OD}_\bullet}^* = D_{\text{OD}_\bullet} \approx D_{\text{OH}_\bullet}$, i.e. $D^* - \text{OD}_\bullet$ could directly be used to calculate the proton conductivity. Unfortunately, comparing the value for $D_{\text{OD}_\bullet}^* = 3 \times 10^{-8} \text{ cm}^2 \text{ s}^{-1}$ with $D_{\text{H}}^\delta = 7 \times 10^{-6} \text{ cm}^2 \text{ s}^{-1} \approx D_{\text{OH}_\bullet}$ of the TG relaxation, there is a deviation by two orders of magnitude, for which I do not have a reasonable explanation at the moment. The presumption of infinitely fast surface reaction (k^* is, therefore, not discussed) does not have such a huge effect on the value of D^* . Even the lack of knowing the background does not result in this large deviation. Nevertheless, one has to keep in mind that all TG extracted diffusivities lie within a reasonable framework of defect

diffusivities for $V_{\text{O}}^{\bullet\bullet}$ and $\text{OH}_{\text{O}}^{\bullet}$, cf. figure 4.26, i.e. at the moment the doubt is rather about the single value of $D_{\text{OD}_{\text{O}}}^*$ from SIMS, not vice versa. Nevertheless, the SIMS profile shows in agreement with the TG results that BSFZ takes up a perceptible amounts of protons and their concentration is more or less p_{O_2} independent.

Last but not least, figure 4.30 shows the total conductivity relaxation $\Delta\sigma$ upon $\Delta p_{\text{H}_2\text{O}}$ (7.06 to 19.4 mbar) at 10 mbar (a) and 1 bar (b) p_{O_2} for a 300 nm thick and 2 mm wide and long thin-film at 400 °C. Firstly, the total conductivity being equal to the hole conductivity ($t_{\text{h}\bullet} \approx 1$) responds to a change in $p_{\text{H}_2\text{O}}$ which proves that a $p_{\text{H}_2\text{O}}$ change also affects the hole concentration although the relative changes are small. The relaxation at 10 mbar p_{O_2} shows a two-fold behavior supporting the expected decoupled migration of protons and oxygen vacancies. The conductivity relaxing back but not to its initial value further agrees with the TG result that mainly water is incorporated (acid-base), but that a minor fraction of protons is taken up by hydrogenation (difference between initial and final value, i.e. $\Delta\sigma_{\text{H}} - \Delta\sigma_{\text{O}}$, corresponds to the redox fraction, cf. next paragraph). Nevertheless, these data need to be taken with great care. The diffusion length of 1 mm is very large resulting in very long measurement times (here 10 days, but on the other hand a large diffusion length is required to be D -controlled). The long-term stability of the thin-film has to be questioned which is seen e.g. by the fluctuations during the back relaxation. Therefore, the resulting fit parameters are ambiguous expressed by the large errors in $\Delta\sigma_{\text{O}}$ and $D_{\text{O}}^{\text{eff}}$.

The non-monotonic signal is fitted to eq. 4.14 where $\Delta\sigma$ instead of Δm is used, i.e. $\Delta\sigma_{\text{H}}$ is the transient reduction through hydrogen diffusion and $\Delta\sigma_{\text{O}}$ transient reoxidation through oxygen diffusion.¹ Unfortunately, taking all data points into the fit leads to a $\Delta\sigma_{\text{O}}$ value being larger than $\Delta\sigma_{\text{H}}$ which would mean that the sample is further reoxidized than reduced before which is, however, physically not reasonable and disagrees with the thermodynamic model. Therefore, keeping e.g. degradation effects in mind, the data range needs to be cut off to obtain a meaningful fit result. The data was cut at $t \approx 165$ h and the result is shown as red dashed line in figure 4.30a together with the four fit parameters. Taking too small a data range results in a high redox fraction in contrast to the TG result at 10 mbar p_{O_2} . Of course, this cut is somehow arbitrary, but was selected guided by the eye (the signal seemed to run into a final value there) and to yield reasonable fit results. However, this cut is reflected by the very high error bars for $D_{\text{O}}^{\text{eff}}$ (plus minus one order of magnitude) and $\Delta\sigma_{\text{O}}$ (zero (100% redox fraction) to values larger than $\Delta\sigma_{\text{H}}$). The transient $\Delta\sigma$ contributions suggest a redox fraction of about 30% which is higher than TG data suggest. But within the high error bar and the fact that the TG analysis might underestimate the redox fraction, these results are not contradicting. The values contributing to the fast diffusivity $D_{\text{H}}^{\text{eff}}$ and $\Delta\sigma_{\text{H}}$ are more stable with respect to the input data (smaller error bars); however, $D_{\text{H}}^{\text{eff}}$ is roughly one order of magnitude lower than D_{H}^{s} from the TG result (both fitted diffusivities are $\approx D_{\text{OH}_{\text{O}}^{\bullet}}$). $D_{\text{O}}^{\text{eff}}$ is lower than D_{Iparam} , as well, but the value is to be taken not too seriously as it strongly changes with the input data range. The deviation in the results between both techniques

¹Note that this solution can only be directly transferred to conductivity relaxation where the applied DC voltage (i.e. the direction of measurement) is perpendicular to the diffusion direction. In appendix C it is shown mathematically that for small concentration changes this solution can also be applied to setups where the applied DC voltage and diffusion direction are parallel. In addition, it was confirmed by using a hole profile of one of the simulations.

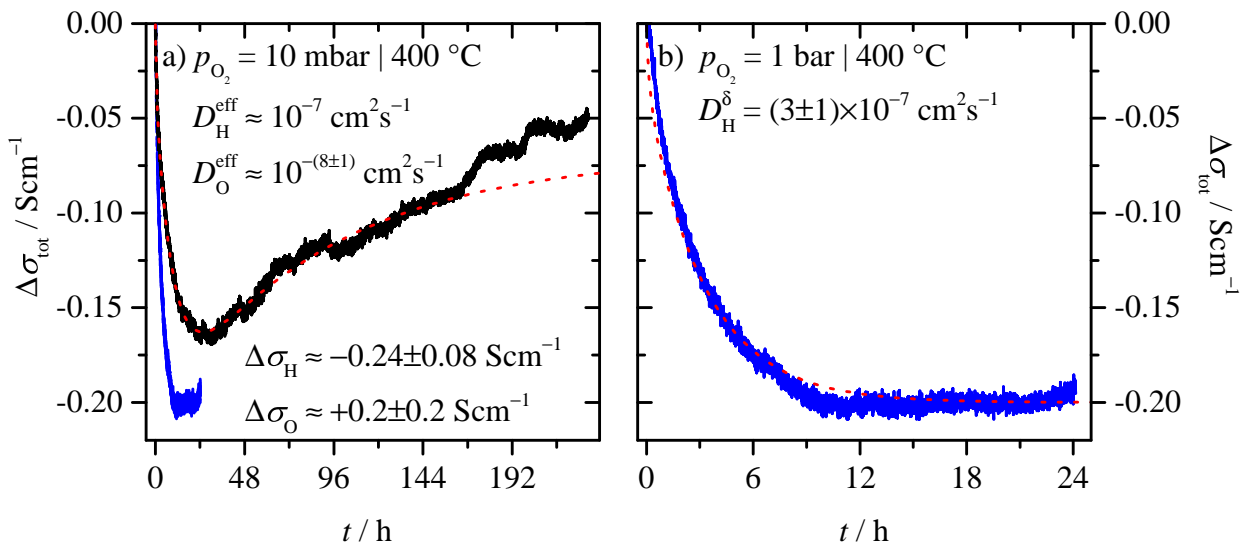


Figure 4.30: Transient conductivity relaxation upon $\Delta p_{\text{H}_2\text{O}}$ from 7.06 to 19.4 mbar at $T = 400\text{ °C}$ in a) 10 mbar and b) 1 bar p_{O_2} . In a) the transient in 1 bar (blue curve) is additionally shown for comparison.

can be related to the fact that fundamentally different samples have been used, i.e. a bulk sample in the TG and a thin-film in the conductivity relaxation. Note that in the latter even the cation composition can differ owing to losses in the PLD process. Hence, the thin-film might have different electrochemical properties (activity coefficients) than the respective bulk.

The DC conductivity relaxation in 1 bar p_{O_2} (figure 4.30b) shows a monotonic, single-fold behavior in agreement with the TG results. This proves the previously made assumptions that protons are exclusively incorporated by redox thermodynamics, hence, by reducing the sample. The obtained chemical diffusivity D_{H}^{δ} is slightly larger than $D_{\text{H}}^{\text{eff}}$ at 10 mbar but, nonetheless, they are in good agreement. Using Nernst-Einstein relation eq. 2.19 together with the diffusivity of holes in bulk BSFZ (figure 4.7b) the final change $\Delta\sigma = -0.2\text{ Scm}^{-1}$ corresponds to a final change of -7×10^{-3} in $\Delta[\text{h}^{\bullet}] = -\Delta[\text{OH}_{\text{O}}^{\bullet}]$. The respective result of the bulk TG sample gives $\Delta[\text{OH}_{\text{O}}^{\bullet}] = 4\times 10^{-3}$. The difference of a factor two can be explained by thin-film having different properties (concentration or hole diffusivity) than bulk, thus, they are in a reasonable agreement.

All in all, SIMS and DC analysis generally agree with the TG results on a qualitative and in some parts on a quantitative scale. However, the quantitative results deviate partially quite strong. Too less data is collected for now to give definite explanations, which at present have to be taken with care and, hence, are not further discussed.

4.5 Effect of electronic conductivity in BZY on the impedance

The impedance measurements for the analysis of the oxygen reduction reaction are performed with BZY as electrolyte in oxidizing atmospheres ($p_{\text{O}_2} = 10^{-4}$ to 1) and at elevated temperatures (400 to 700 °C). In the three-dimensional defect concentration plot figure 2.1 it is visible that with increasing p_{O_2} (oxidation) as well as increasing temperature/decreasing $p_{\text{H}_2\text{O}}$ (decreasing hydration) the concentration of h^\bullet even in a proton-conducting perovskite such as $\text{Ba}(\text{Zr,Ce,Y})\text{O}_{3-\delta}$ is increased providing an electronic conductivity. This can lead to perceptible electronic transference numbers t_{h^\bullet} . Grimaud et al. reported values for t_{h^\bullet} up to 0.2 for $\text{Ba}(\text{Ce,Yb})\text{O}_3$ and Ji et al. calculated t_{h^\bullet} to be even unity for $\text{BaZr}_{0.85}\text{Y}_{0.15}\text{O}_{3-\delta}$ at 800 °C and $p_{\text{O}_2} = 1$.^[106;107]

A more generalized behavior of the transference numbers is visualized in figure 4.31. For the sake of clarity only representative 2D cuts out of the 3D surface for reasonable $p_{\text{H}_2\text{O}}K_{\text{hydrat}} = 1$ (high $\Delta_{\text{hydrat}}G^0$ in humid atmosphere) and $p_{\text{O}_2}^{1/2}K_{\text{ox}} = 10^{-6}$ (nominally redox-inactive material) are shown. Physically reasonable defect diffusivity ratios^[99] characterized by $D_{\text{h}^\bullet} = 10^2 D_{\text{OH}_\bullet^\circ} = 10^4 D_{\text{V}_\bullet^\circ}$ are used to calculate the respective conductivities σ_k and transference numbers t_k for defect species k using Nernst-Einstein relation eq. 2.19. It is obvious that in the used measurement conditions, i.e. humid, oxidizing atmosphere at moderate temperatures (highlighted in yellow), t_{h^\bullet} can reach rather high values with $t_{\text{OH}_\bullet^\circ}$ still remaining the dominant contribution.

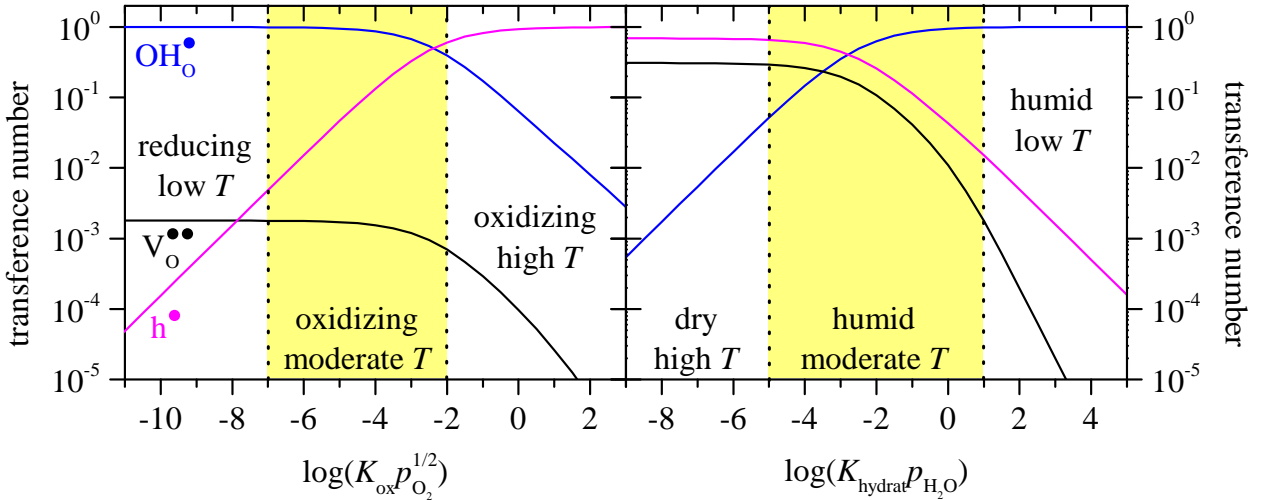


Figure 4.31: Change of the transference numbers with variation in temperature and gas composition (variation in the respective Kp values) for a representative diffusivity ratio ($D_{\text{h}^\bullet} = 10^2 D_{\text{OH}_\bullet^\circ} = 10^4 D_{\text{V}_\bullet^\circ}$) at fixed $p_{\text{H}_2\text{O}}K_{\text{hydrat}} = 1$ (left) and fixed $p_{\text{O}_2}^{1/2}K_{\text{ox}} = 10^{-6}$ (right). The range relevant for the impedance measurements in this work is highlighted in yellow.

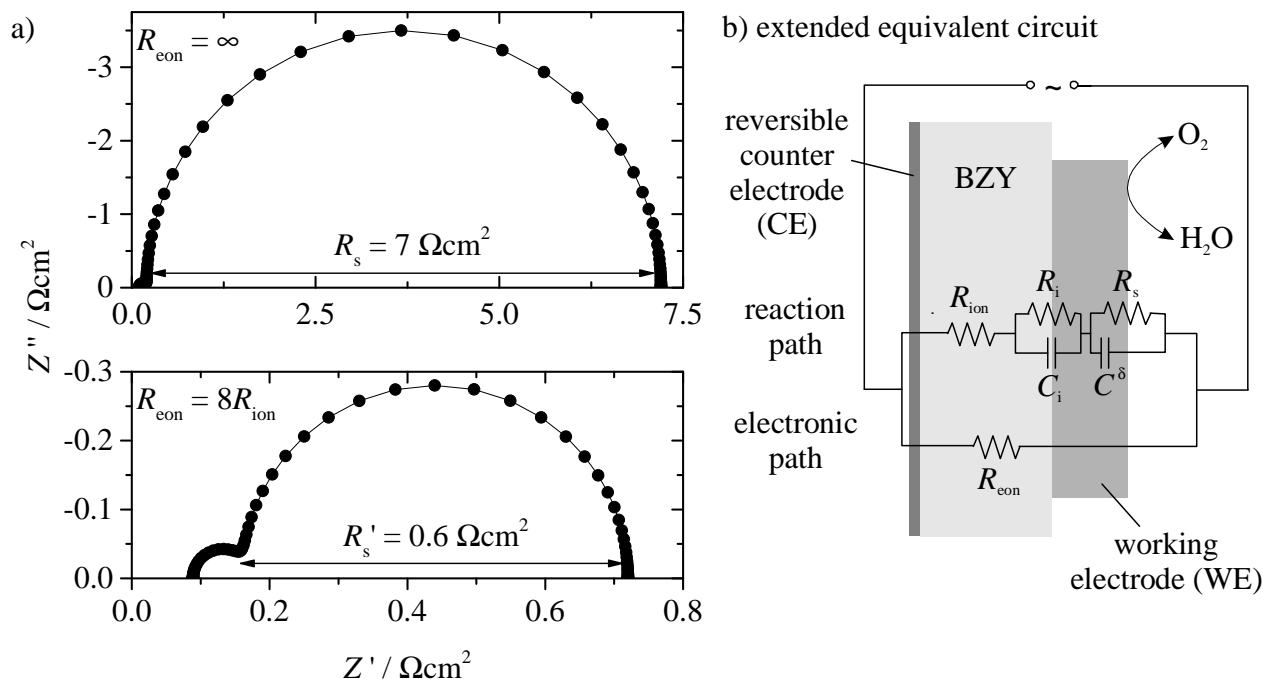


Figure 4.32: a) Simulated impedance spectra based on the phenomenological equivalent circuit (b) using ZView. The area normalized values used in the simulation are typical values for dense, thin-film microelectrodes on well-conducting protonic electrolytes ($t_{\text{h}\bullet} = 0.1$) and are $R_{\text{ion}} = 0.1 \Omega\text{cm}^2$, $R_{\text{eon}} = 0.8 \Omega\text{cm}^2$, $R_i = 0.1 \Omega\text{cm}^2$, $R_s = 7 \Omega\text{cm}^2$, $C_i = 2 \times 10^{-3} \text{Fcm}^{-2}$ and $C^\delta = 2 \times 10^{-2} \text{Fcm}^{-2}$. b) Phenomenological equivalent circuit (figure 2.6) extended by an electronic short-circuit path in parallel to the reaction path. The background image sketches the electrochemical cell of the microelectrode setup with an reversible counter electrode.

Though $t_{\text{OH}\bullet}$ is still dominant, the resulting electronic conductivity can not be neglected. Typically, impedance spectroscopy studies on oxygen reduction reaction are performed on symmetrical or here (different electrodes) at least in gas-symmetrical cells where both electrodes are exposed to the same oxidizing, humid atmosphere. Then, the undesired electronic conductivity leads to a measurable electronic resistance. For microelectrodes the respective $R_{\text{h}\bullet}$ reads analogous to R_{ion} (spreading resistance of a small circular contact)

$$R_{\text{h}\bullet} = (2d_{\text{ME}}\sigma_{\text{h}\bullet})^{-1} \quad (4.20)$$

(d_{ME} : diameter of microelectrode).^[15] To be more general, $R_{\text{h}\bullet}$ is called R_{eon} in the following.^j The phenomenological equivalent circuit (cf. chapter 2.3.1) with its ionic reaction path needs to be extended by an electronic short-circuit path in parallel - cf. figure 4.32b. For the sake of simplicity, capacitive contributions from the electrolyte are neglected as they typically lie within stray capacitances ($< 10^{-12} \text{F}$). Now, it is obvious that this short-circuit will influence the impedance measurement. Furthermore, it is clear that the strength of this influence does not depend on $t_{\text{h}\bullet}$ alone but on the ratio between R_{eon} and $(R_{\text{ion}} + R_i + R_s)$. The consequence is that even for small $t_{\text{h}\bullet}$ values R_{eon} can severely dominate the total impedance if

^jThe statement is independent of the defect nature ($\text{h}\bullet$ or e') of the electronic resistance.

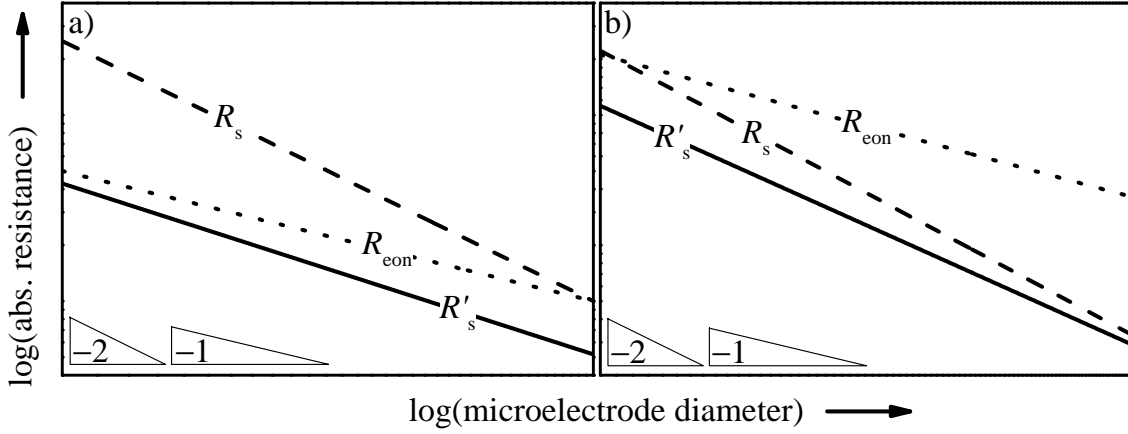


Figure 4.33: Effect of R_{eon} on the diameter dependence of the measured resistance R'_s compared to the real surface reaction resistance R_s . a) $R_{\text{eon}} < R_s$: measured diameter dependence closer to -1 . b) $R_{\text{eon}} > R_s$: measured diameter dependence closer to -2 (in case of bulk path).

$(R_{\text{ion}} + R_i + R_s)$ is higher.

Unfortunately, this is exactly the case for dense, thin-film (micro-)electrodes on highly doped BZY (and any other, proton-conducting electrolyte). Owing to the small (compared to porous single-phase and composite electrodes) surface area and triple-phase-boundary length of the microelectrode R_s is very large compared to R_i and R_{ion} and, therefore, dominates the reaction path (upper branch in the equivalent circuit figure 4.32b). For BZY with 15% and even 6% Y – typical dopant concentration with rather good protonic bulk conductivities – R_{eon} is much smaller compared to R_s ; hence, the total impedance is dominated by the short-circuit formed by the low R_{eon} . In figure 4.32a the effect of R_{eon} is simulated for exemplary, typical resistances and capacitances (both are area normalized) for mixed-conducting microelectrodes on BZY15. The upper spectrum where $R_{\text{eon}} = \infty$ looks as expected with the three contributions from the reaction path. Turning on the electronic short-circuit path the consequences are severe. The total impedance as well as the resistance of the low frequency semicircle are decreased by one order of magnitude and approach R_{eon} . Furthermore, the interface resistance R_i appears to be more dominant. The influence on the capacitances is less severe (and neglected here) as the disturbing capacitance of the respective R_{eon} process is very small.

In the rest of the thesis, measured resistances of the reaction path R_{ion} , R_i and R_s disturbed by R_{eon} are called apparent resistances denoted with a prime. As R_s is of greatest interest (contains information about the oxygen reduction reaction) and R_{ion} and R_i are small, we will only focus on R_s . The R_{eon} influenced R'_s can be calculated through eq. 4.21.

$$R'_s = \frac{R_s R_{\text{eon}}^2}{(R_{\text{ion}} + R_{\text{eon}} + R_i + R_s)(R_{\text{ion}} + R_{\text{eon}} + R_i)} \quad (4.21)$$

Three, general cases are discussed: For $R_s \gg R_{\text{eon}}$ (dense, thin-film electrodes on well-conducting electrolyte) $R'_s \approx R_{\text{eon}}$, for $R_s \ll R_{\text{eon}}$ (electrolyte with negligible electronic short-circuit) $R'_s \approx R_s$ and finally, for $R_s \approx R_{\text{eon}}$ (\approx means within one order of magnitude) $R'_s < R_{\text{eon}}$ and R_s . The last case is supposed to occur using porous electrodes with a

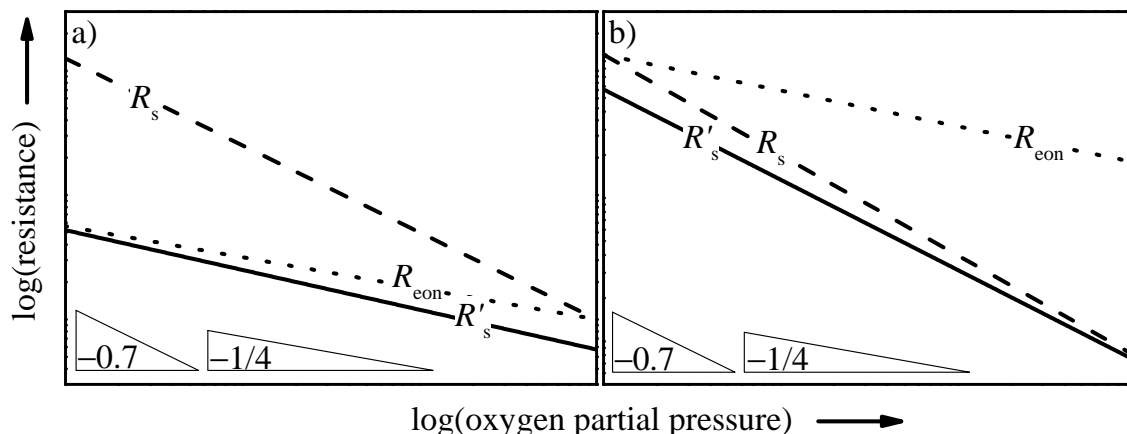


Figure 4.34: Effect of R_{eon} on the p_{O_2} dependence of the measured resistance R'_s compared to the real surface reaction resistance R_s . a) $R_{\text{eon}} < R_s$: exponent of the measured p_{O_2} dependence closer to $-1/4$. b) $R_{\text{eon}} > R_s$: exponent of the measured p_{O_2} dependence closer to e.g. -0.7 (or whatever value the exponent for R_s is).

high surface area and therefore lower R_s values. This case is beyond the scope of this thesis and part of a paper.^[48] The general consequence is that in the presence of a non-negligible electronic short-circuit the measured impedances are always lower than the pure contributions from the reaction path. It is clear that this can lead to wrong conclusions and makes it even more difficult to compare different measurements and materials as R_{eon} can strongly scatter between different batches of BZY of same composition (because it is also affected by the blocking character of grain boundaries).^[92] Moreover, this disturbance can have drastically consequences in the mechanistic interpretation using R'_s but implicitly assuming $R'_s = R_s$. This is schematically shown in the following pictures where R'_s is calculated through eq. 4.21.

In figure 4.33 the influence on the diameter dependence - a strong criterion for bulk or surface path - is sketched assuming that the bulk path takes place for the oxygen reduction, i.e. R_s scales with the inverse area of the microelectrode, hence with the inverse square of the diameter (slope -2). In contrast, R_{eon} as a spreading resistance scales with the inverse diameter (cf. eq. 4.20).^[15] If R_{eon} is dominating the overall impedance (left case) the diameter dependence of R'_s is larger than but close to -1 possibly leading to the false conclusion that the surface path takes place. If R_{eon} is larger than R_s the slope of R'_s is close to but smaller than -2 . Consequently, in the case of disturbing R_{eon} and oxygen reduction via bulk path the measured diameter dependencies lie between -1 and -2 .

For the p_{O_2} dependence shown in figure 4.34 and temperature dependence (not shown) analogous behaviors are found. R_{eon} scales with $p_{\text{O}_2}^{-0.25}$ in the p-type conducting regime. The p_{O_2} dependence of R_s is not known a priori for mixed-conducting electrodes on proton-conducting electrolytes; therefore, similar values as on YSZ are assumed - in this example -0.7 (molecular oxygen involved in rds, cf. chapter 2.3.1). Again, in the R_{eon} dominated regime (left case) R'_s scales with p_{O_2} via an exponent close to but larger than -0.25 . This could lead to the wrong conclusion that only atomic oxygen is involved in the rds. For R_s being dominant the slope is close to but smaller than -0.7 . All in all, for the exponent of the p_{O_2} dependence of R'_s

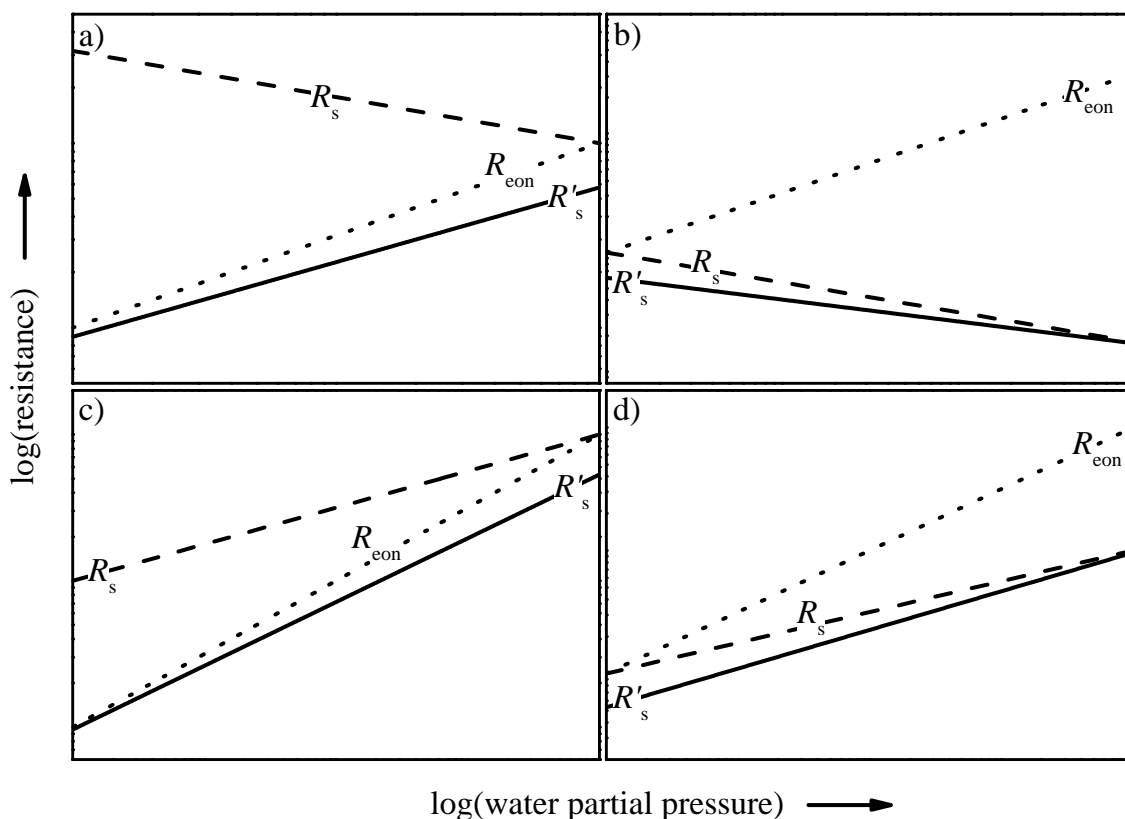


Figure 4.35: Effect of R_{eon} on the $p_{\text{H}_2\text{O}}$ dependence of the measured resistance R'_s compared to the real surface reaction resistance R_s . a) $R_{\text{eon}} < R_s$: exponent of the measured $p_{\text{H}_2\text{O}}$ dependence of R'_s closer to that of R_{eon} and even the sign is switched (positive instead of negative slope). b) and d) $R_{\text{eon}} > R_s$: exponent of the measured p_{O_2} dependence closer to that of R_s . c) $R_{\text{eon}} < R_s$: exponent of the measured $p_{\text{H}_2\text{O}}$ dependence closer to that of R_{eon} .

values between -0.25 and the actual exponent for R_s can be observed making it difficult to conclude which oxygen species is involved in the rds. To be more general, p_{O_2} dependencies of R_s smaller than -0.25 - even zero - are possible. For an analogous schematic plot of the temperature dependence the activation energies for R_{eon} and R_s can arbitrarily be chosen (both values for $R_{\text{eon}}^{\text{k}}$ and R_s are not known a priori). For now, this parameter is less important to understand the oxygen reduction mechanism. Hence, this behavior is not shown explicitly but behaves, in principle, in similar way (the apparent activation energy of R'_s is supposed to lie in-between the activation energies of R_s and R_{eon}).

Last but not least, the influence on the $p_{\text{H}_2\text{O}}$ dependence is to be discussed. In the literature positive and negative values for the $p_{\text{H}_2\text{O}}$ dependencies of the low frequency semicircle are reported. Measurements for LSC thin-films on YSZ in dry and humid oxidizing atmosphere show that R_s is lower in humid atmosphere than in dry proposing a negative $p_{\text{H}_2\text{O}}$

^kFor R_{eon} the slope of the Arrhenius plot not only depends on the activation energy of the mobility of h^\bullet but also on temperature dependence of their concentration (cf. chapter 2.1). Hence, predicting the apparent T dependence of R_{eon} is difficult.

dependence.^[108] In contrast, Grimaud et al. published a small negative dependence for BSCF but a slightly positive for LSFC on $\text{Ba}(\text{Ce},\text{Y})\text{O}_{3-\delta}$.^[26] Also $p_{\text{H}_2\text{O}}$ independent low frequency contributions are found.^[79;82] Consequently, four different limit cases have to be considered: R_{eon} , respectively R_{s} dominating, both for positive and negative $p_{\text{H}_2\text{O}}$ dependencies of R_{s} - figure 4.35. From the thermodynamic view (chapter 2.1) R_{eon} is expected to have a positive $p_{\text{H}_2\text{O}}$ dependence as holes are consumed upon increasing $p_{\text{H}_2\text{O}}$ (cf. eq. 2.3).

If R_{s} dominates the impedance, the slope of R'_{s} is close to the one of R_{s} (case b) and d) in figure 4.35), as before, but can now be smaller (b) *or* larger (d). This is, of course, because R_{s} has a smaller slope than R_{eon} . In the diameter and p_{O_2} dependence case the slope of R_{s} was always larger than that of R_{eon} . Secondly, if R_{eon} is dominant, the slope of R'_{s} is determined by R_{eon} as well. The most severe consequence is shown in case a): The influence of R_{eon} can even switch the sign of the slope leading to a drastic misinterpretation of the oxygen reduction mechanism.

The following general conclusions can be drawn. Measured R'_{s} values are always smaller or equal to R_{s} and R_{eon} ; hence, the electrode appears to be more active. Measured exponents (slopes in the double-logarithmic plots) of dependencies on the electrode morphology (e.g. electrode surface), temperature, oxygen and water partial pressure lie between the exponents for R_{s} (being related to kinetic properties of the electrode) and R_{eon} (being related to thermodynamic properties of the electrolyte). Consequently, analyzing impedance data for electrodes on proton-conducting perovskite electrolytes the electronic short-circuit has to be taken into account. Otherwise the interpretation of the data can lead to wrong conclusions.

4.5.1 Influence on the impedance spectra

Before discussing the mechanism of the oxygen reduction reaction based on impedance data of microelectrodes the strength of the influence of R_{eon} needs to be checked. As proposed in chapter 4.5 the real surface reaction resistance R_{s} can be much larger by more than one order of magnitude than R_{eon} for highly doped BZY caused by the electronic short-circuit (equivalent circuit figure 4.32b). In figure 4.36 impedance spectra of microelectrodes of mixed conductors BSCF and BSFZ on different electrolytes under almost the same (temperature difference of 50 K between YSZ and BZY) conditions are shown. For YSZ the electronic transference number t_{eon} is smaller than approximately 10^{-7} .^[109] Here, the electronic short-circuit can be neglected as the resulting R_{eon} is orders of magnitude larger than R_{s} . The measured impedance spectrum (figure 4.36 a) looks exactly like the simulated one with $R_{\text{eon}} = \infty$ in figure 4.32: The total impedance is dominated by the large surface reaction resistance of the small microelectrode. A small contribution from the electrode/electrolyte interface is found in the medium frequency range (inset) and a high frequency intercept from the ionic resistance of the electrolyte. As the capacitance C_{ion} (dielectric contribution) of YSZ single crystal is small the semicircle of the $R_{\text{ion}}C_{\text{ion}}$ element is out of the measured range.

Measuring the same microelectrodes on the proton-conducting electrolyte BZY15 the impedance spectra look qualitatively the same, but are quantitatively different. There are still three contributions suggesting that they originate from the same processes as on YSZ - HF: electrolyte, MF: electrolyte/electrode interface, LF: electrode. The big difference is that for

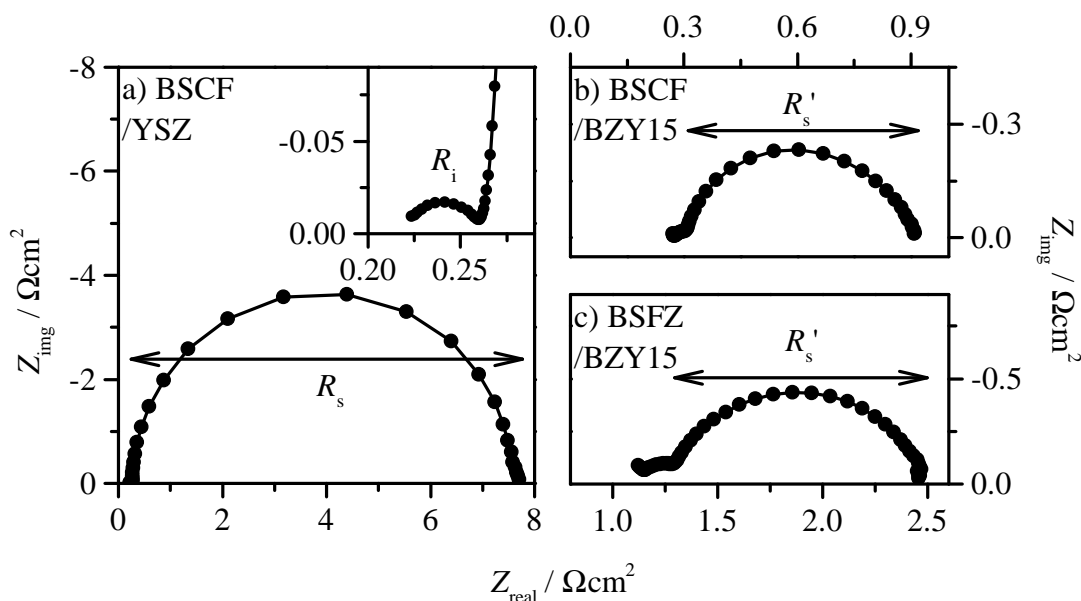


Figure 4.36: Exemplary, measured impedance spectra of mixed-conducting BSCF and BSFZ microelectrodes of 60 μm diameter. a) BSCF on YSZ (750 $^{\circ}\text{C}$, 1.1 mbar p_{O_2} , dry). b) BSCF on BZY15 (700 $^{\circ}\text{C}$, 1.1 mbar p_{O_2} , 20 mbar $p_{\text{H}_2\text{O}}$). c) BSFZ on BZY15 (700 $^{\circ}\text{C}$, 1.1 mbar p_{O_2} , 20 mbar $p_{\text{H}_2\text{O}}$) – Note that the abscissa does not start at zero.

BSCF the total and LF impedance is about one order of magnitude smaller, although a higher resistance would be expected as the temperature is 50 K lower. The HF and MF contributions are of similar magnitude but this is supposed to be by chance as different materials and interfaces are investigated. Also the surface reaction resistances are not strictly comparable as different mechanisms or different rate determining steps can be expected for YSZ (requiring incorporation of oxygen) and BZY (not necessarily requiring incorporation of oxygen), respectively. Nonetheless, it is not very likely that the reaction rate of BSCF is more than one order of magnitude faster on BZY than on YSZ.

For BSFZ on BZY15 the total as well as the LF resistance is about a factor four, respectively, eight smaller than for BSCF on YSZ. BSFZ being a Co-free electrode is supposed to be catalytically less active for the oxygen reduction than BSCF (cf. lower activity of BSF vs. BSCF on YSZ in Wang et al.^[70]). In contrast, it is also visible that the contribution of the electrolyte BZY is six times larger for BSFZ than BSCF. The reason for this is the high variation in the conductivity of BZY ceramics (largely determined by the blocking grain boundaries) also observed in literature data.^[92]

Generally, the measured difference between mixed-conducting microelectrodes on YSZ and BZY15 is exactly the same as proposed by the simulation (figure 4.32). Hence, the electronic short-circuit caused by R_{eon} in the BZY electrolyte is identified as the reason. With this phenomenon in mind all on the first sight contradicting impedance measurements can be explained without any doubt (cf. next sections¹). However, the influence of R_{eon} can also

¹For example: The exponent of the dependence on the microelectrode diameter suggested the rds to occur at the TPB, but, in contrast, the electrode appeared to be more active by one order of magnitude compared

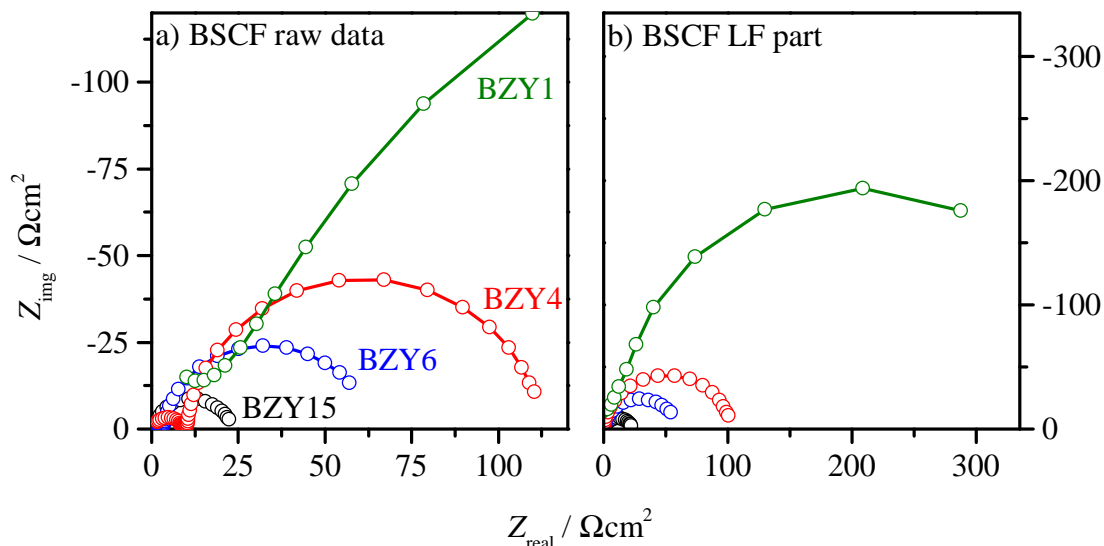


Figure 4.37: Dependence of the impedance spectra on Y dopant concentration x in BZY x . All spectra measured at 500 °C, 1 mbar p_{O_2} and 20 mbar $p_{\text{H}_2\text{O}}$, except on BZY1 taken at 550 °C. a) Raw, area normalized spectra. The semicircle visible for BZY1 is the high frequency contribution of R'_{ion} . b) High frequency part subtracted to compare the R'_s dependence.

lead to ambiguities in the interpretation, seen e.g. in figure 4.36. R'_s is larger for BSFZ than for BSCF which can on the one hand be explained by the lower catalytic activity of BSFZ. However, also the high frequency intercept is more than three times larger though the same electrolyte is used (scattering of BZY conductivity data). Thus on the other hand, as R_{eon} is dominating R'_s a difference in the electronic hole conductivity between the individual substrates of BZY15 also explains the higher R'_s for BSFZ than BSCF. In short, there is a correlation between the magnitude of the HF intercept (contribution only from BZY, i.e. R'_{ion} and R_{eon}) and the LF semicircle (contribution from electrode R_s and electrolyte R_{eon} - for BZY15 mainly from R_{eon}) which makes the comparison between both materials difficult. To summarize, taking R_{eon} into account leaves no contradicting results anymore, but one has to keep in mind that in some cases it impedes an unambiguous interpretation of measured values.

This correlation which is the strongest proof for the effect of R_{eon} is clearly visible in figure 4.37. Here, impedance spectra for BSCF microelectrodes on BZY with different Y-content at the same conditions (except for BZY1 where T is 50 K higher, explanation see later in the text) are shown. In the left plot the raw, area normalized impedance spectra are shown, in the right plot the HF+MF contribution is subtracted to directly compare the LF contribution. With decreasing doping concentration the conductivity of BZY decreases and the respective resistance increases. In contrast, it is remarkable that also the LF semicircle scales with the dopant concentration of the electrolyte as this contribution is directly related to the oxygen reaction rate which is supposed to be independent on the Y content in the electrolyte. Taking

to YSZ where the whole electrode surface is active. This is contradicting as the TPB length is much smaller than the surface of the electrode, i.e. even if the electrode on BZY is more active (area (of the TPB length!) specific resistance is then smaller than for YSZ) the absolute value is supposed to be higher.

R_{eon} into account everything becomes clear.

Table 4.4: Dependency of R'_{ion} , R'_s and $C^{\delta'}$ on acceptor dopant Y concentration in BZYx extracted from spectra in figure 4.37. R_{eon} is estimated by calculating t_{eon} from the BZY15 measurement where $R'_s \approx R_{\text{eon}}$ and assuming that t_{eon} is identical for all Y contents.

Y / mol%	$R'_{\text{ion}}/\Omega\text{cm}^2$	$R'_s/\Omega\text{cm}^2$	$\approx R_{\text{eon}}$	$C^{\delta'}/\text{Fcm}^{-2}$
15	0.519	21.3	$2 - 3 \times 10^1$	1.6×10^{-2}
6	1.90	57.5	10^2	1.5×10^{-2}
4	9.61	104	5×10^2	1.4×10^{-2}
1	459	481	2×10^4	2.5×10^{-2}

The reported literature data for bulk and total conductivity collected by Shirpour et al.^[92] show that published total conductivities vary by up to four orders of magnitude between present BZY15 and BZY5. This is confirmed by the measurements. In table 4.4 the fitted and normalized values R'_{ion} , R'_s and $C^{\delta'}$ are summarized. R'_{ion} for BZY1 is three orders of magnitude larger than for BZY15. The ratio between R_{ion} and R_{eon} is assumed to be fixed by a constant t_{eon} under the same conditions (of course some variations can occur but will be small^m); hence, also R_{eon} is about three orders of magnitude different between BZY1 and BZY15 shifting the system from the R_{eon} dominated (BZY15) to the R_s dominated regime (BZY1). Thus, the measured value of $21.3 \Omega\text{cm}^2$ for R'_s on BZY15 is $\sim R_{\text{eon}}$ and t_{eon} can be approximated to be $0.02 - R_{\text{eon}}$ is roughly fifty times larger than R_{ion} . For BZY1 R_{eon} is calculated to be about $2 \times 10^4 \Omega\text{cm}^2$ and R'_s is approximately equal to R_s . The estimated R_{eon} values are also shown in table 4.4. Furthermore, the fitted data show that the chemical capacitance of the electrode $C^{\delta'}$ is independent on the electrolyte, i.e. it is not affected by R_{eon} .

4.5.2 Influence on the exponents of the parameter dependencies

Last but not least, the influence of R_{eon} on the exponents of the parameter dependencies of R'_s on microelectrode diameter d , temperature and p_{O_2} is discussed. Here, some points of the discussion regarding the oxygen reduction mechanism (chapter 4.6) have to be anticipated. In figure 4.38 the diameter dependence of R'_s and the chemical capacitance $C^{\delta'}$ on the Y content in BZY is shown. Expecting the bulk path for the oxygen reduction R_s is supposed to scale with the area of the microelectrode, hence, with the square of its diameter. In contrast, R_{eon} scales inversely proportional with the diameter (spreading resistance behavior).^[15] The measured diameter dependence for R'_s on BZY15 is around -1 – i.e. equal to the expected dependence for R_{eon} – and increases with decreasing Y-content finally reaching values around -2 – the expected value for the surface reaction via bulk path. Another explanation could be that for BZY15 the surface path and for BZY1 the bulk path takes place and for Y-contents in between a mixture of both. On the one hand, this is very unlikely as there is no reasonable explanation why the oxygen reduction reaction should change its mechanism when

^mThe blocking character of the grain boundaries is comparable for $\text{OH}_\text{O}^\bullet$ and h^\bullet and the mass action constants K_{hydrat} and K_{ox} will not depend strongly on the Y concentration.

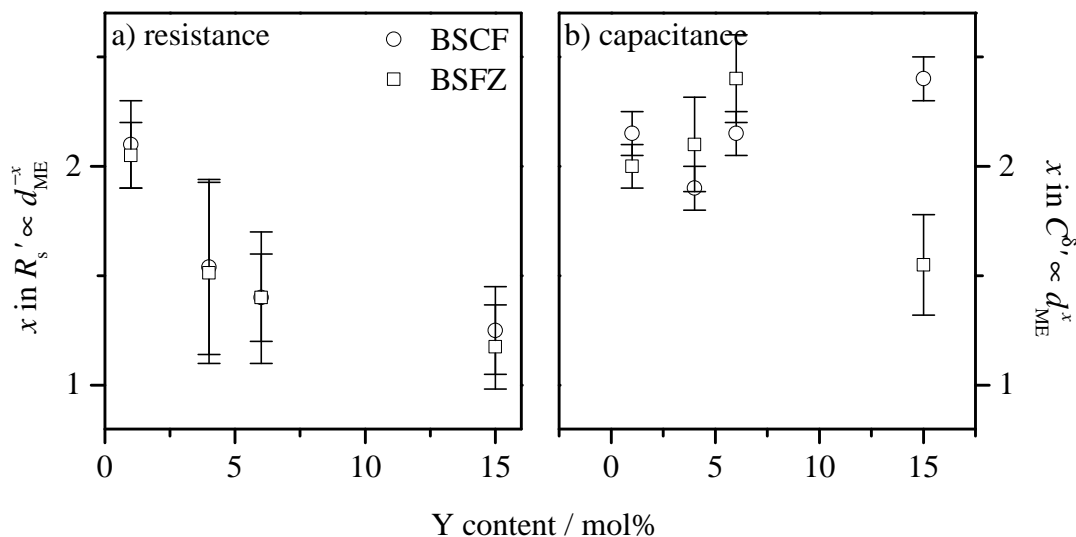


Figure 4.38: Measured microelectrode diameter dependencies of R'_s and the respective chemical capacitance $C^{\delta'}$ on BZY substrates with different Y content.

only the dopant content of the substrate is modified. If this was the case then a larger LF resistance in the impedance is expected for BZY15 than for BZY1 but, in fact, the opposite is observed. Furthermore, the diameter dependence of the chemical capacitance is more or less independent of the Y-content proving that C^{δ} is not influenced by R_{con} . All in all, this is the second very obvious finding that R_{con} strongly influences the result of the impedance data.

In figure 4.39 the same Y-dependence is plotted for the activation energy. Again, the values increase with decreasing Y-content whereas the trend is not as clear as for the diameter dependence. This is owing to the fact that the $1/T$ slopes of R_{con} and R_s are closer together

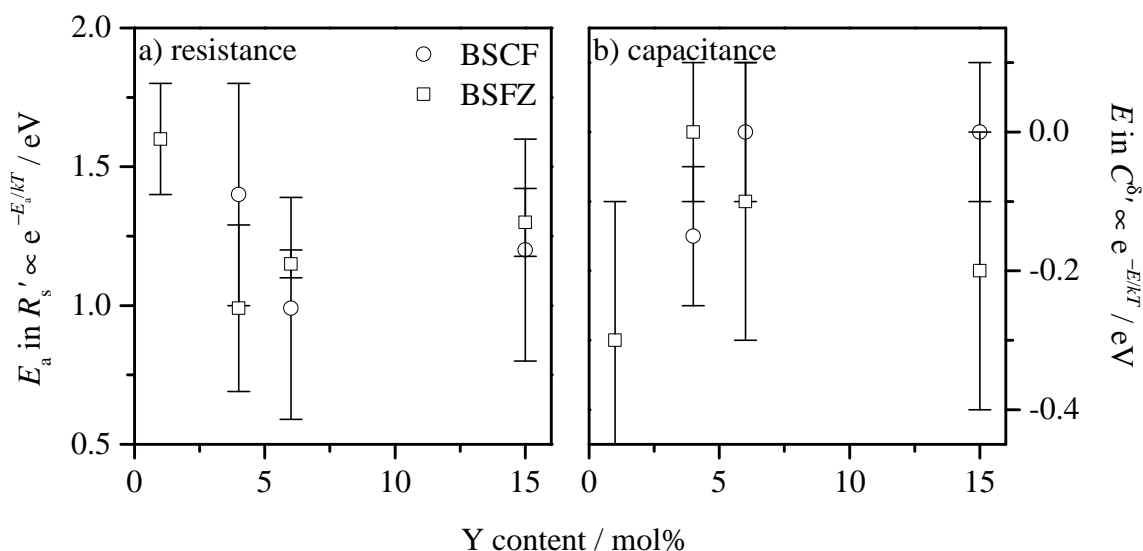


Figure 4.39: Measured activation energies of R'_s and the temperature dependence of the chemical capacitance $C^{\delta'}$ at substrates with different Y content.

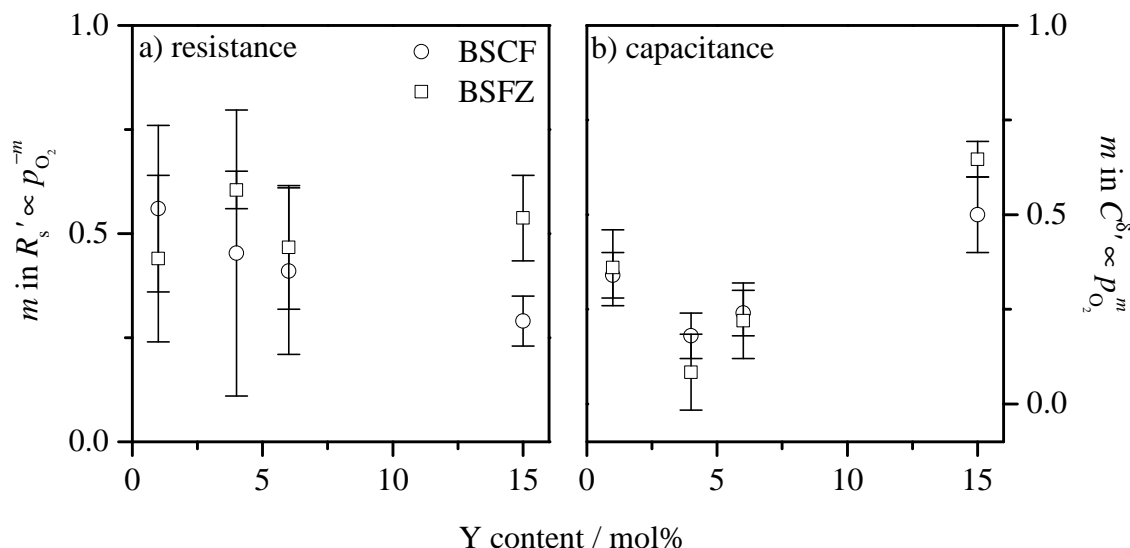


Figure 4.40: Measured p_{O_2} dependencies of R'_s and the respective, chemical capacitance $C^{\delta'}$ for BZY substrates with different Y content.

than for the diameter dependence where a strong difference results in a clear result. Hence, the variation of R_{ion} and R_{eon} in different BZYx batches gains even more importance resulting in stronger scattering of the data. Nevertheless, the tendency for the activation energy of R'_s is still visible. The temperature dependencies for $C^{\delta'}$ are only shown for the sake of completeness.

Finally, the Y-content dependence of the p_{O_2} dependence is shown in figure 4.40. For BSCF the trend of decreasing exponent with increasing Y content is clearly visible. For BZY15 the p_{O_2} dependence of R'_s even falls below 0.5 indicating that possibly only atomic oxygen is involved in the rds. With decreasing Y concentration the p_{O_2} dependence is increasing above 0.5 seemingly suggesting that now molecular oxygen is involved (details see chapter 4.6). As argued earlier a change in oxygen reduction mechanism at the electrode with the Y-content in the electrolyte is very unlikely. For BZY15 the p_{O_2} dependence of $-1/4$ (p-type conductivity) makes a large contribution to the overall p_{O_2} dependence of R'_s , while for BZY1 probably the real p_{O_2} dependence of R_s is measured. Unfortunately, for BSFZ the p_{O_2} dependence of R'_s does not follow this rule. A general explanation is given in the next paragraph. The chemical capacitance shows no trend with Y-content as expected. Interestingly the values are the same for BSCF and BSFZ which is further discussed in chapter 4.6.

A last remark has to be made about the scattering and the not always clear tendency of the Y-content dependencies. The explicit influence of R_{eon} on the dependency parameters of R'_s outlined in chapter 4.5 is only valid when the total system is in thermodynamic equilibrium. The equilibration of the electrode thin-film with the gas phase after changing temperature or partial pressure is very fast (very short diffusion length and high diffusivities), in contrast, the equilibration of the dense, polycrystalline BZY substrate with its blocking nature of the grain boundaries is slow, especially, at lower temperatures and Y-dopant concentration. Changing one parameter during the series of the measurements, it is not feasible to wait until BZY is fully equilibrated (which can take many hours), simply to avoid too much degradation of

the microelectrode which would lead to a even more complex analysis. Consequently, the measured T , p_{O_2} and $p_{\text{H}_2\text{O}}$ dependencies of R_{eon} follow not necessarily the thermodynamic rules. Their measured dependencies depend to some degree on the direction in which T , p_{O_2} and $p_{\text{H}_2\text{O}}$ are changed, i.e. increasing or decreasing, which can both weaken or strengthen the dependency parameter of R_{eon} . Therefore, the change of the parameters needs to be standardized. For the diameter dependence measurements T , p_{O_2} and $p_{\text{H}_2\text{O}}$ are constant leading to less scattering and a clear trend, as shown in figure 4.38.

4.5.3 Influence on the DC bias dependence

For mixed-conducting electrodes on YSZ the oxygen reduction reaction is accelerated both on cathodic (working electrode as minus pole) and anodic (working electrode as plus pole) DC bias, i.e. R_s decreases with negative and positive applied DC biases (not necessarily with identical slopes^[110]) having its maximum at zero bias.^[13] In contrast, on BZY this maximum is shifted to cathodic bias values. In figure 4.41a the bias dependencies of R'_s for BSCF and BSFZ are shown together with the bias dependence of R_{eon} measured on the same sample. R_{eon} is measured using pore-free gold microelectrodes deposited besides the BSCF microelectrodes on the same BZY substrate where the ionic path is blocked (very high R_s for gold) and R_{eon} is measured as DC value.

The shift of the maximum to cathodic bias can be explained by the bias dependence of R_{eon} with the help of figure 4.41b. Owing to its much larger size the extended counter electrode (CE) is assumed to be reversible (its contributing resistance is much smaller than of the microelectrode making a reference electrode needless^[14]), i.e. the electrochemical potential of

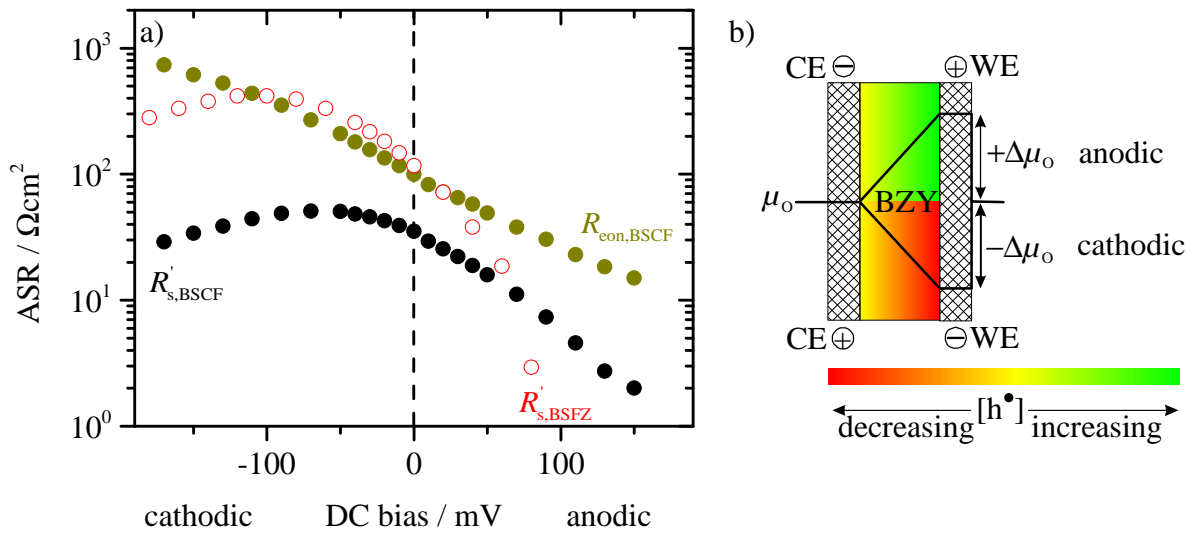


Figure 4.41: a) DC bias dependencies of R'_s and R_{eon} . The solid symbols belong to measurements on the same sample at the same conditions. BSCF on BZY4: $T = 500^\circ\text{C}$, $p_{\text{O}_2} = 100\text{ mbar}$, $p_{\text{H}_2\text{O}} = 20\text{ mbar}$. BSFZ on BZY1: $T = 600^\circ\text{C}$, $p_{\text{O}_2} = 11\text{ mbar}$, $p_{\text{H}_2\text{O}} = 20\text{ mbar}$. b) Effect of applied DC bias on μ_{O} .^[110;111] The color gradient indicates the decreased (red) and increased (green) hole concentration compared to the bias free value (yellow) resulting in a concentration gradient across the electrolyte.

oxygen μ_{O} does not change upon bias and is fixed by the p_{O_2} in the gas phase. On applying a cathodic bias η (reducing conditions) μ_{O} drops by $\Delta\mu_{\text{O}} = 2F\eta$. Under the condition that R_{s} drops at the surface of the electrode (surface reaction slow compared to ion transport through the electrode film) μ_{O} drops at the surface, as well. The gradient in μ_{O} between CE and WE generates a gradient in the concentration of holes, i.e. for cathodic bias the electrolyte is reduced in the area close to the electrode. This causes an electronically less conducting zone increasing R_{eon} . In contrast, at anodic bias μ_{O} is increased oxidizing the area of BZY close to the electrode, and increasing both the concentration of holes and the electronic conductivity (For microelectrodes as WE and much larger CE, most of the voltage across the electrolyte drops in the hemisphere close the microelectrode.^[15]). Consequently, R_{eon} increases with cathodic and decreases with anodic bias, confirmed by the measurements at gold microelectrodes (cf. 4.41a). The bias response of R'_{s} is now understood as follows: With anodic bias, both R_{s} and R_{eon} are decreased; thus, the decrease of R'_{s} is accelerated (stronger slope for anodic than for cathodic bias). For cathodic bias R_{s} is decreased as well, but R_{eon} increases. This means with increasing cathodic bias R_{s} and R_{eon} diverge (for the case that $R_{\text{s}} < R_{\text{eon}}$), R'_{s} becomes more and more R_{s} dominated running through a maximum. From zero cathodic bias to this maximum R'_{s} is still R_{eon} dominated, i.e. the bias behavior of R_{eon} is observed (increasing slope). At higher bias values than at this maximum the R_{s} behavior dominates R'_{s} which is then increasing with increasing cathodic bias.

4.5.4 Strategies to diminish the influence of R_{eon}

After identifying the problem, four approaches to solve it are suggested based on quantifying, blocking or increasing R_{eon} .

(i) The first approach is a mathematically one. If one knows the exact value for R_{eon} one can use the extended equivalent circuit (figure 4.32b) to fit the ionic path values fixing R_{eon} to the known value. In practice, R_{eon} is determined experimentally by impedance or DC measurements on gold microelectrodes (cf. also section 4.5.3). Gold is blocking for the oxygen reduction, hence, for the complete ionic path. Consequently, R_{eon} is measured as total impedance or DC resistance. Unfortunately, to use this method it is necessary to quantify R_{eon} extremely precisely. Otherwise, small errors in R_{eon} can lead to very large errors in the fit result of R_{s} . This is the reason why the method does not work sufficiently well for BZY with high Y concentrations. Here, R'_{s} is very close to R_{eon} and the fit taking quantified R_{eon} values into account mostly runs into infinite R_{s} values or even does not work at all (when the measured R_{eon} value is smaller than R'_{s} the fit cannot be solved). For lower doped BZY where both R_{s} and R_{eon} or even R_{s} alone determine the impedance, another problem appears. The equilibration with the gas phase of these lower doped BZY is very slow (blocking grain boundaries). As the area of BZY below a microelectrode can equilibrate via the whole electrode surface for the mixed conductors (conductive for all charge carriers) but only through the triple phase boundary length for the gold contacts (ionically insulating) the respective BZY parts differ in their defect concentrations, consequently, also in their R_{eon} values. One would have to wait until BZY is fully equilibrated which takes too long for lower doped BZY and degradation effects of the mixed-conducting microelectrodes gain in importance. More generally, it was reported repeatedly that measured conductivity data scatter much for BZY. Even if the electrolyte is equilibrated, R_{eon} values for different areas on an individual substrate

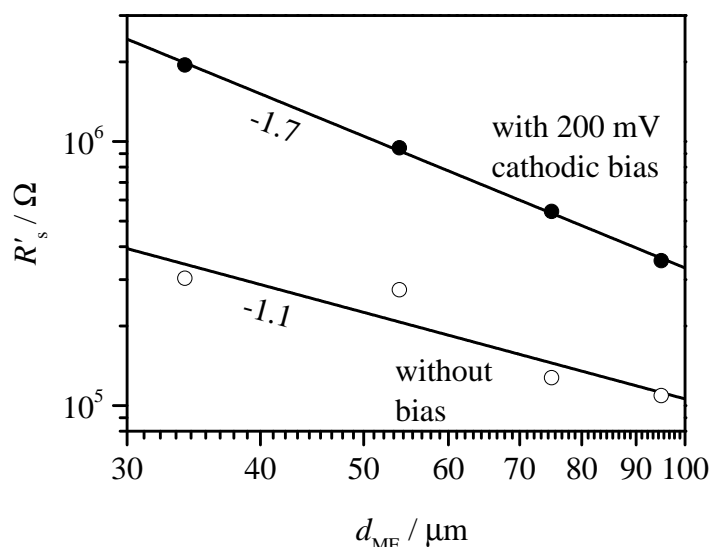


Figure 4.42: Microelectrode diameter dependence of R'_s for BSCF on BZY6 without (open symbols) and with applied 200 mV cathodic DC bias at 600 °C, 0.86 mbar p_{O_2} and 20 mbar $p_{\text{H}_2\text{O}}$.

can still differ owing to different grain sizes and distributions of the grain boundary properties. All in all, this method works for some individual measurements but owing to the scattering of the fit and the fact that it does not always work the dependency parameters could not be determined more accurately.

(ii) Blocking the electronic conductivity is the next possibility. Here, trials with potassium hydroxide (melting point 400 °C) sandwiched between two BZY substrates (the top with microelectrodes on top, the bottom to avoid KOH contact with the silver counter-electrode) were performed. While this in principle worked for some single measurements, it was not possible to keep the sample and, consequently, the measurements stable as the KOH melt started to creep on the microelectrodes.

(iii) Another way to block or at least diminish the effect of R_{eon} is measuring with applied cathodic DC bias which decreases the concentration of holes in the area close to the working electrode (cf. figure 4.41 and chapter 4.5.3) increasing R_{eon} to either the mixed or even R_s dominating regime. This works quite well for the diameter dependence exemplary shown in figure 4.42. Without bias the measurements are R_{eon} dominated and the diameter dependence of -1 expected for the spreading resistance is measured. Applying a cathodic DC bias of 200 mV shifts the measurements to the mixed regime increasing the diameter dependence to -1.7 which is rather close to the value of -2 expected for the bulk path. Too high bias values cannot be applied to ensure that the reduction mechanism does not change and to avoid irreversible changes of the electrode surface by cation migration.^[112] Unfortunately, for the T , p_{O_2} and $p_{\text{H}_2\text{O}}$ dependent measurements this method cannot be applied as the quantitative influence of the DC bias changes with these parameters and is different for R_s and R_{eon} . I.e. the quantitative behavior of both R_s and R_{eon} on DC bias needs to be known which makes

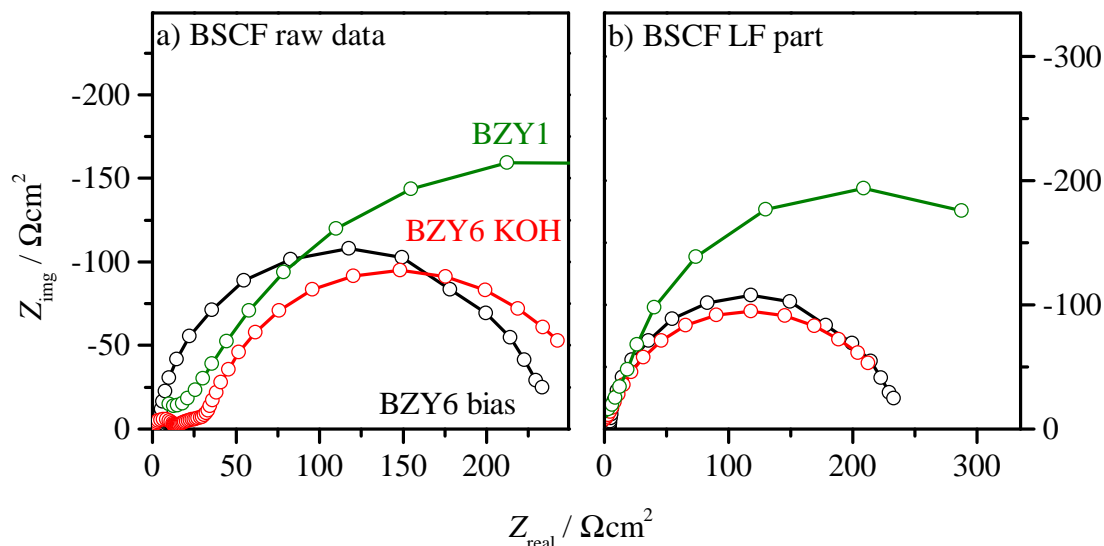


Figure 4.43: Comparison of three different methods to diminish the influence of R_{eon} BZY on the impedance spectra of BSCF microelectrodes ($p_{\text{O}_2} \approx 1$ mbar, $p_{\text{H}_2\text{O}} \approx 20$ mbar and $T = 500^\circ\text{C}$, respectively 550°C for BZY1).

the analysis more complex and uncertain.

(iv) Last but not least, the last approach is to increase R_{eon} by decreasing the Y dopant concentration. In figure 4.37 the increase of the LF semicircle with the decrease of the Y content was already shown to shift the system towards the R_s dominated regime. It is also obvious that comparably low Y concentrations are necessary to succeed with this strategy. In table 4.4 the ratio between R'_s and approximated values for R_{eon} are compared. Even at BZY1 and moderate conditions (550°C and 1 mbar p_{O_2}) R_{eon} is less than two orders of magnitude larger; for higher T and p_{O_2} even less. Though this is not the ultimate solution, this approach works best, the samples are stable and the measurements are reproducible. The only disadvantage is that R_{ion} can dominate the total impedance, i.e. the LF semicircle is then hardly visible. Hence, for each experiment suitable measurement conditions have to be found. This is the reason why the spectra on BZY1 in figure 4.37 was measured at 550°C instead of 500°C used in the other examples. This limits the utilizability as with lower Y concentrations the R_s contribution is not well resolved anymore.

A comparison of method (ii) to (iv) is shown in figure 4.43. Coincidentally, the KOH layer in this single measurement and the bias had the same quantitative effect on R'_s . It is visible that R_{eon} still influences the impedance as the LF semicircle using BZY1 as substrate is two times large at 50 K higher temperature. Even here, a disturbance by R_{eon} cannot be fully excluded. Altogether, measuring the dependency parameters on BZY1 works best and is the strategy of choice, except for the diameter dependence, where measuring with applied cathodic DC bias also succeeded. The mechanistic conclusions which can now be drawn are summarized in the next chapter.

4.6 Oxygen reduction mechanism

In this section the results of the dependencies for BSFZ and BSCF on BZY1 on microelectrode diameter, oxygen and water partial pressure (here on BZY6) are discussed. The oxygen reduction surface resistance R_s (actually R'_s – cf. previous chapter) and C^δ are analyzed. In the equivalent circuit used for the fit a more general constant phase element Q instead of a capacitor was used as the semicircles are non-ideal. This is typically related to slightly inhomogeneous resistive or capacitive contributions. The capacitance is calculated through eq. 4.22 where z indicates the degree of depression of the semicircle.^[94]

$$C = (R^{1-z}Q)^{1/z} \quad (4.22)$$

4.6.1 Diameter dependence

In figure 4.44 the dependencies on the microelectrode diameter are shown. From the estimated proton-conductivity of BSFZ in chapter 4.4.1 the bulk path is highly expected. The surface resistances for BSFZ and BSCF scale inversely with the square of the diameter, i.e. the area of the microelectrode, indicating that the whole electrode (area or volume) is involved in the ORR, i.e. the bulk path is confirmed, even for BSCF with a probably lower proton concentration (cf. room temperature values in table 4.2). The chemical capacitance C^δ being related to the volume of the electrode scales with the area of the microelectrode as well (for constant film thickness, the volume scales with the square of the diameter). The data points for BSCF on BZY1 at $d_{ME} = 100 \mu\text{m}$ deviated systematically from the linear behavior of the other data points for all four samples of this batch (four specimens were produced simultaneously in the PLD and photolithography process). Therefore, these data are not included in the linear regression. Although R_{con} is probably still affecting the impedance (even on BZY1 R_{con} is estimated to be less than one to two orders of magnitude larger than R_s , cf. table 4.4) the diameter dependence of R'_s fits the expected value of 2.

In fact, there is another effect which influences the diameter dependences, namely the local temperature decrease of the microelectrode through the PtIr tip which influences the ideal behavior. Smaller electrodes are more strongly cooled than larger ones, i.e. R_s values are not only increasing with decreasing microelectrode diameter (with slope 2) they are additionally increased by the lower local temperature. Consequently, too high diameter dependencies are observed, e.g. my colleagues Anja Wedig and Sebastian Stämmeler investigating the ORR using YSZ electrolytes obtained exponents of about 2.4.^[113;114] For BZY1, the influence of the thermal effect increasing and R_{con} decreasing the diameter dependence are compensating by chance. The presence of the bulk path was additionally confirmed by investigating the influence of cathodic bias on the dependency parameters as discussed in figure 4.42. The last remark here is that $C^{\delta'}$ scatters less, also indicating that it is less or not influenced by R_{con} (thus, the $'$ is actually not necessary).

4.6.2 Partial pressure dependencies of R'_s

The exponents of the partial pressure dependencies of R_s are important parameters to conclude on the rate determining step in the oxygen reduction mechanism as they provide information about involved species. However, expected values for m and n in $R_s \propto p_{\text{O}_2}^m p_{\text{H}_2\text{O}}^n$ cannot a priori

be given as not only the reaction order with respect to the oxygen/water plays a role. Also the reaction order of the point defects being themselves p_{O_2} and $p_{\text{H}_2\text{O}}$ dependent influence the measured partial pressure dependencies. I.e. the combination of reaction order and partial pressure dependence of the defects results in overall exponents of p_{O_2} and $p_{\text{H}_2\text{O}}$ dependence m and n . To provide expectable signs and value ranges for the exponents and to understand the influences of the point defects (Do they decrease or increase the “ideal” exponents?) two possible rate determining steps are assumed, given in table 4.5 and 4.6. These hypothetical mechanisms do not cover all cases, rather they are representative in terms of reaction orders and partial pressure dependencies. Therefore, in the first example in table 4.5 a rds involving atomic oxygen species (2O_{ad}^-) and in the second one in table 4.6 involving molecular water species ($\text{H}_2\text{O}_{\text{ads}}$) are selected as candidates whose reaction orders are examined.

The first assumed rds in table 4.5 is the incorporation of a reduced oxide anion adsorbed at the cathode surface into the surface of the cathode material. This is related to the rds for mixed-conducting perovskite thin-films on YSZ, although there the incorporation of an adsorbed superoxide ($\text{O}_{2,\text{ads}}^-$) takes place. The situation here is more simplified as the molecular oxygen from the gas phase is considered as already dissociated at the surface. These multiple reactions being not rate determining can be summarized in one preceding (pre) quasi-equilibrium.

The concentration of empty adsorption sites at the surface (limit of low coverage) and regular oxygen sites ($\text{O}_{\text{O}}^\times$) are constant and are included in the prefactors. The rates of the forward $\overrightarrow{\mathfrak{R}}_1$ and backward $\overleftarrow{\mathfrak{R}}_1$ reaction are given in table 4.5. The point defects at the surface are assumed to equilibrate fast with the bulk defects. In contrast, $[\text{O}_{\text{ad}}^-]$ being not contained in a bulk defect equilibrium is substituted from the preceding quasi-equilibrium. In the following, only the forward reaction rate will be considered as it is more intuitive for the argumentation. However, because of microscopic reversibility the final results, i.e. the overall effective reaction

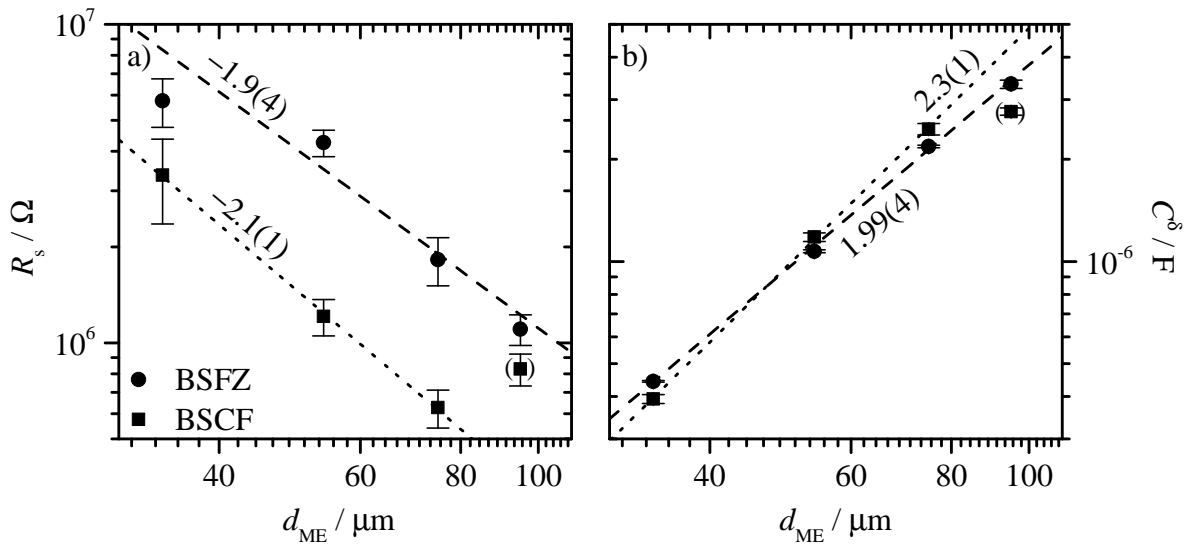


Figure 4.44: Microelectrode diameter dependence of R'_s (a) and $C^{\delta'}$ (b) on BZY1. $T = 600^\circ\text{C}$ for BSFZ and 550°C for BSCF, $p_{\text{O}_2} = 11\text{ mbar}$, $p_{\text{H}_2\text{O}} = 20\text{ mbar}$ and film thickness $\approx 100\text{ nm}$.

Table 4.5: Hypothetical mechanism with adsorbed atomic oxygen incorporated into an oxygen vacancy at the surface being the rate determining step (rds, 1 indicates that this is the first example). The preceding (pre) steps are summarized in one quasi-equilibrium.

	preceding equilibrium and rate determining step	equilibrium constant and reaction rates
pre	$O_{2(\text{gas})} \rightleftharpoons 2 O_{\text{ad}}^- + 2 h^\bullet$	$K_{\text{pre}} = [O_{\text{ad}}^-]^2 [h^\bullet]^2 p_{O_2}^{-1}$
rds	$O_{\text{ad}}^- + V_{\text{O}}^{\bullet\bullet} \longrightarrow O_{\text{O}}^\times + h^\bullet$	$\begin{aligned} \vec{\mathfrak{R}}_1 &= \vec{k}_1 [O_{\text{ad}}^-] [V_{\text{O}}^{\bullet\bullet}] \\ \overleftarrow{\mathfrak{R}}_1 &= \overleftarrow{k}_1 [h^\bullet] \end{aligned}$

rate and partial pressure dependencies are with respect to $R_s \propto (k^a)^{-1} \propto \mathfrak{R}_0$ (cf. eq. 2.47) independent of this choice. The equilibrium exchange rate \mathfrak{R}_0 is then calculated to

$$\mathfrak{R}_0 = \vec{\mathfrak{R}}_1 = \vec{k}_1 K_{\text{pre}}^{1/2} [V_{\text{O}}^{\bullet\bullet}] [h^\bullet]^{-1} p_{O_2}^{1/2} \propto p_{O_2}^{1/2+a} p_{H_2O}^{0+b} \quad (4.23)$$

The reaction orders in the forward rate are 0.5 for oxygen, zero for water, -1 for h^\bullet and $+1$ for $V_{\text{O}}^{\bullet\bullet}$. The latter two itself are p_{O_2} and p_{H_2O} dependent yielding the overall exponents $1/2 + a$ and $0 + b$ of the partial pressure dependencies of \mathfrak{R}_0 . a and b are the exponents of the effective oxygen and water partial pressure dependencies of the involved point defects, in this case $V_{\text{O}}^{\bullet\bullet}$ and h^\bullet .ⁿ As surface defects are involved, these exponents may differ from the exponents of the bulk defects, but fast equilibration between surface and bulk defects can be assumed and only tendencies (signs of a and b) are to be discussed here. For a more detailed overview of possible oxygen incorporation steps in mixed $V_{\text{O}}^{\bullet\bullet}/h^\bullet$ conducting perovskites see Merkle and Maier.^[75]

Next, the same procedure is performed for another rds having water species involved to derive their and the protons reaction orders and effective partial pressure dependencies.

Surface adsorbed molecular water species are substituted by the succeeding equilibrium. Regular lattice oxygen and surface adsorption sites are constant. Now for intuitive reasons the forward and backward rate are used yielding analogous to the first example

$$\mathfrak{R}_0 = \vec{\mathfrak{R}}_2 = \overleftarrow{\mathfrak{R}}_2 = \vec{k}_2 [OH_{\text{O}}^\bullet]^2 = \overleftarrow{k}_2 K_{\text{suc}}^{-1} [V_{\text{O}}^{\bullet\bullet}] p_{H_2O} \propto p_{O_2}^{0+a} p_{H_2O}^{1+b} \quad (4.24)$$

The reaction order for the water and $V_{\text{O}}^{\bullet\bullet}$ in the backward reaction are 1 and zero for oxygen, h^\bullet and OH_{O}^\bullet . In the forward rate the reaction order for OH_{O}^\bullet is 2 and zero for all other species, thus, the overall effective reaction orders of forward and backward rate are positive or zero for all species.

The overall results derived from both examples for reaction orders and expectable effective partial pressures of the defects are summarized in table 4.7. In general, the reaction orders for

ⁿMathematically this effective exponents originate from the product of reaction order and partial pressure dependence of the respective defect. This can generally expressed as follows: $\mathfrak{R}_0 \propto [k]^o$ where o is the reaction order of defect species k . $[k] \propto p_{O_2}^p p_{H_2O}^q$ where p and q are the exponents of the gas partial pressure dependencies of defect k . Thus, $\mathfrak{R}_0 \propto (p_{O_2}^p p_{H_2O}^q)^o = p_{O_2}^{op} p_{H_2O}^{oq}$ and the products $op = a$ and $oq = b$ are the exponents of the effective partial pressure dependencies of k .

Table 4.6: Hypothetical mechanism with ex-corporation of protonic defects at the surface to yield surface adsorbed water being the rate determining step (rds, 2 indicates that this is the second example). The succeeding (suc) step is given as quasi-equilibrium.

	rate determining step and preceding/succeeding equilibrium	reaction rates and equilibrium constant
rds	$2\text{OH}_\text{O}^\bullet \longrightarrow \text{H}_2\text{O}_\text{ads} + \text{V}_\text{O}^{\bullet\bullet} + \text{O}_\text{O}^\times$	$\overrightarrow{\mathfrak{R}}_2 = \overrightarrow{k}_2[\text{OH}_\text{O}^\bullet]^2$ $\overleftarrow{\mathfrak{R}}_2 = \overleftarrow{k}_2[\text{H}_2\text{O}_\text{ads}][\text{V}_\text{O}^{\bullet\bullet}][\text{O}_\text{O}^\times]$
suc	$\text{H}_2\text{O}_\text{ads} \rightleftharpoons \text{H}_2\text{O}_\text{gas}$	$K_\text{suc} = p_{\text{H}_2\text{O}}[\text{H}_2\text{O}_\text{ads}]^{-1}$

O_2 , H_2O , $\text{V}_\text{O}^{\bullet\bullet}$ and $\text{OH}_\text{O}^\bullet$ are positive or zero, and for h^\bullet negative or zero. More specifically, for molecular oxygen and water species involved in the rds the reaction orders are +1, for atomic ones they are +0.5 and if not involved they are zero. The exponents of the effective oxygen and water partial pressure dependencies result from the product of the bulk exponents^o (cf. figure 4.15, values given in the table) and the respective reaction order. For p_{O_2} they are negative or zero for all defects, i.e. if being involved in the rds they all decrease the exponent of the oxygen partial pressure dependence – in other words a in eqs. 4.23 and 4.24 is negative or zero. In contrast, the exponents of the effective water partial pressure dependencies for the defects differ in sign, b is negative for $\text{V}_\text{O}^{\bullet\bullet}$ and positive for $\text{OH}_\text{O}^\bullet$ and h^\bullet . Consequently, even if the reaction order is zero for O_2 and/or H_2O , R_s can be p_{O_2} and/or $p_{\text{H}_2\text{O}}$ dependent through the effective partial pressure dependencies of point defects being involved in the rds. This aspect is not considered in the mechanisms proposed in the literature, and can lead to grossly wrong conclusions.

Table 4.7: Exponents of the partial pressure dependencies of the bulk defects derived from the thermodynamic model, overall reaction orders derived from the kinetic considerations in this chapter and resulting effective partial pressure dependency exponents of the three charge carriers with respect to $\mathfrak{R}_0 \propto R_\text{s}^{-1}$.

	bulk exponents		overall reaction order	effective exponents	
	p_{O_2}	$p_{\text{H}_2\text{O}}$		$p_{\text{O}_2}^a$	$p_{\text{H}_2\text{O}}^b$
$\text{V}_\text{O}^{\bullet\bullet}$	−0.5 to 0	−1 to 0	≥ 0	≤ 0	≤ 0
$\text{OH}_\text{O}^\bullet$	−0.25 to 0	0 to 0.5	≥ 0	≤ 0	≥ 0
h^\bullet	0 to 0.25	−0.5 to 0	≤ 0	≤ 0	≥ 0

The partial pressure dependencies of area normalized R'_s (closed symbols) and R'_{ion} (open symbols) for BSFZ and BSCF are shown in figure 4.45a for p_{O_2} and b for $p_{\text{H}_2\text{O}}$. The p_{O_2} dependencies of R'_s slightly differ, i.e. for BSCF it is little below and for BSFZ little above −0.5.

^oEven if the surface defects equilibrate fast with the bulk defects, the numerical values of the exponents may differ, but the sign will be the same. However, this has no influence on the discussion as exact values are not given, anyway.

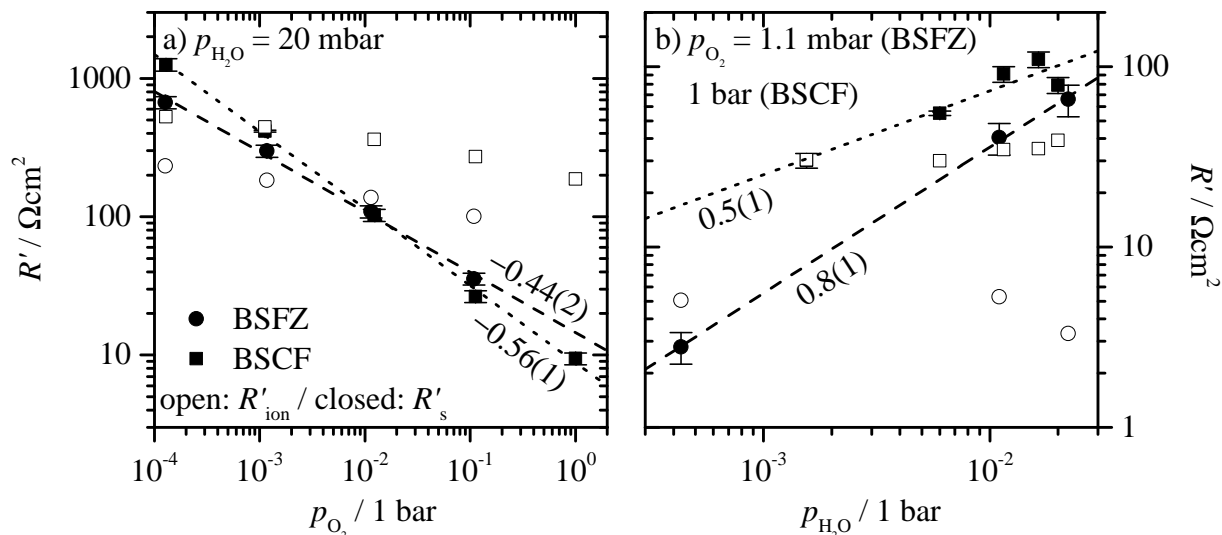


Figure 4.45: Oxygen (on BZY1) (a) and water (on BZY6) (b) partial pressure dependence of R'_s . $T = 600\text{ }^\circ\text{C}$ for BSFZ and $550\text{ }^\circ\text{C}$ for BSCF, $p_{\text{H}_2\text{O}} = 20\text{ mbar}$, $d_{\text{ME}} = 100\text{ }\mu\text{m}$ for BSFZ and $80\text{ }\mu\text{m}$ for BSCF and film thickness $\approx 100\text{ nm}$.

Based on the previous kinetic considerations, this might suggest that for BSCF (dependency < -0.5) molecular and for BSFZ (dependency > -0.5) atomic oxygen species are involved in the rds. However, some influence of R_{eon} can still not be ruled out. The presence of R_{eon} is visible as a small p_{O_2} dependence of -0.1 for R'_{ion} (R_{ion} is p_{O_2} independent, $R_{\text{eon}} \propto p_{\text{O}_2}^{-1/4}$). R'_{ion} is on the same order of magnitude as R'_s for low p_{O_2} and one order of magnitude above for high p_{O_2} values. Hence, R_{eon} is roughly one to two orders of magnitude larger than R'_s ($t_{\text{eon}} \geq 0.1$), thus, still influencing $R_s \geq R'_s$. In general, BSFZ as Cobalt-free cathode material is less catalytically active, i.e. it is supposed to have a higher R_s under the same conditions than BSCF (cf. BSCF vs. BSF on YSZ^[70]). R'_{ion} is about half an order of magnitude smaller for the BSFZ than for the BSCF sample. Consequently, the influence of R_{eon} on the impedance is more severe for BSFZ (R'_s is stronger R_{eon} dominated) than for BSCF (R'_s less R_{eon} dominated). I.e. the measured p_{O_2} dependence is more strongly decreased for BSFZ towards $-1/4$ of R_{eon} leading to values above -0.5 although the dependence of R_s itself is higher. Note that the values in figure 4.45a are accidentally identical as they are measured at different temperatures and R_{eon} can vary. Furthermore, it has been shown through the first example being rds that the effective oxygen partial pressure dependence of the point defects would decrease the p_{O_2} dependence exponent to values much above -0.25 . Consequently, it is highly plausible that for both BSFZ and BSCF the undisturbed p_{O_2} dependencies of R_s are below -0.5 and that molecular oxygen is involved in the rds for both cathode materials.

The $p_{\text{H}_2\text{O}}$ dependencies of R'_s , figure 4.45b, are both strongly positive. They are on the one hand in agreement with results for $\text{La}_{0.6}\text{Sr}_{0.4}\text{Co}_{0.2}\text{Fe}_{0.8}\text{O}_{3-\delta}$ (k^δ decreases from dry to humid atmosphere^[115]), but on the other hand in contrast to results for thin-film LSC electrodes on YSZ (R_s decreases from dry to humid atmosphere^[108]) and porous BSCF electrodes on BCY (cf. table 2.1^[25]). Unfortunately, the $p_{\text{H}_2\text{O}}$ dependence of R_{eon} is positive as well (eq. 2.3). Although the $p_{\text{H}_2\text{O}}$ dependency was measured using a BZY6 substrate with stronger influence of R_{eon} , the positive dependency was qualitatively confirmed for BSFZ on BZY1 (exponent

≈ 0.7 but the measured $p_{\text{H}_2\text{O}}$ was very small). Furthermore, analogously to the p_{O_2} dependence measurements (figure 4.45a) where BZY1 was used R'_{ion} is in the same range or, at least, one order of magnitude smaller than R'_s . Thus, using BZY6 R_{eon} disturbs the measurements slightly stronger than using BZY1, but the positive measured slope is real (meaning also caused by R'_s) and gives important information about the rds. R'_{ion} itself is more or less $p_{\text{H}_2\text{O}}$ independent, i.e. the negative slope expected for R_{ion} (increasing $[\text{OH}^\bullet_{\text{O}}] \propto \sigma_{\text{OH}^\bullet_{\text{O}}} \propto R_{\text{ion}}^{-1}$ with increasing $p_{\text{H}_2\text{O}}$) and the positive slope expected for R_{eon} (decreasing $[\text{h}^\bullet] \propto \sigma_{\text{h}^\bullet} \propto R_{\text{eon}}^{-1}$ with increasing $p_{\text{H}_2\text{O}}$) compensate each other. It has been shown at both examples in the kinetic considerations above that if the reaction order of one species (oxygen or water) is non-zero the reaction order of the other species (water or oxygen) is zero (a rds where an oxygen species is involved in the forward and a water species in the backward reaction is very unlikely). As the reaction order for oxygen was found to be non-zero the reaction order for water must be zero, the positive slope of R'_s vs. $p_{\text{H}_2\text{O}}$ arises from the effective water partial pressure dependence of the point defects. Otherwise, if the reaction order for water is non-zero as well, a negative slope would then highly be expected. $\text{V}^\bullet_{\text{O}}$ is the most plausible defect which has a negative effective water partial pressure dependence. Thus, it can further be concluded that oxygen vacancies must be involved in the rds which is in agreement with the p_{O_2} dependence.

Finally, the partial pressure dependencies of R_s suggest that obviously it is mandatory to incorporate molecular oxygen into an oxygen vacancy at the electrode surface to dissociate it. This is the same result as for mixed-conducting perovskites on YSZ. The influence of the water on the reduction kinetics is somehow conflicting as on the one hand protons are necessary to exhibit a high enough proton-conductivity to enable the bulk path, but on the other hand the surface exchange rate k is decreased with increasing $p_{\text{H}_2\text{O}}$ owing to its negative influence on $[\text{V}^\bullet_{\text{O}}]$. This is in contrast to results for LSC on YSZ where k^q is accelerated by the presence of H_2O , suggesting that the oxygen reduction mechanism or at the least the rds is different on proton-conducting electrolytes.

4.6.3 Partial pressure dependencies of $C^{\delta'}$

The partial pressure dependencies of area normalized $C^{\delta'}$ are given in figure 4.46a (p_{O_2}) and b ($p_{\text{H}_2\text{O}}$). Interestingly, the p_{O_2} dependencies as well as the absolute values are the same for BSCF and BSFZ. Additionally, the p_{O_2} dependence is much higher than for BSCF on YSZ (0.04 ± 0.02 , in agreement with 0.05 ± 0.01 at 700°C measured by Lei Wang^[73]), the absolute values are equal or larger (related to the lower temperature and the known increase of C^δ with decreasing T ^[73] – cf. figure 4.39). For the three charge carrier system not only the chemical capacitance for oxygen C^δ_{O} as for the two charge carrier system on YSZ (here, protons are not present) but also the chemical capacitance for hydrogen C^δ_{H} has to be considered. Referring to eq. 2.15 their area normalized expressions are

$$\begin{aligned} C^\delta_{\text{O}} &= 2^2 F^2 L \frac{\partial c_{\text{O}}}{\partial \mu_{\text{O}}} \\ C^\delta_{\text{H}} &= 1^2 F^2 L \frac{\partial c_{\text{H}}}{\partial \mu_{\text{H}}} \end{aligned} \quad (4.25)$$

To calculate numerical values for C^δ the response of the chemical potentials on a small applied

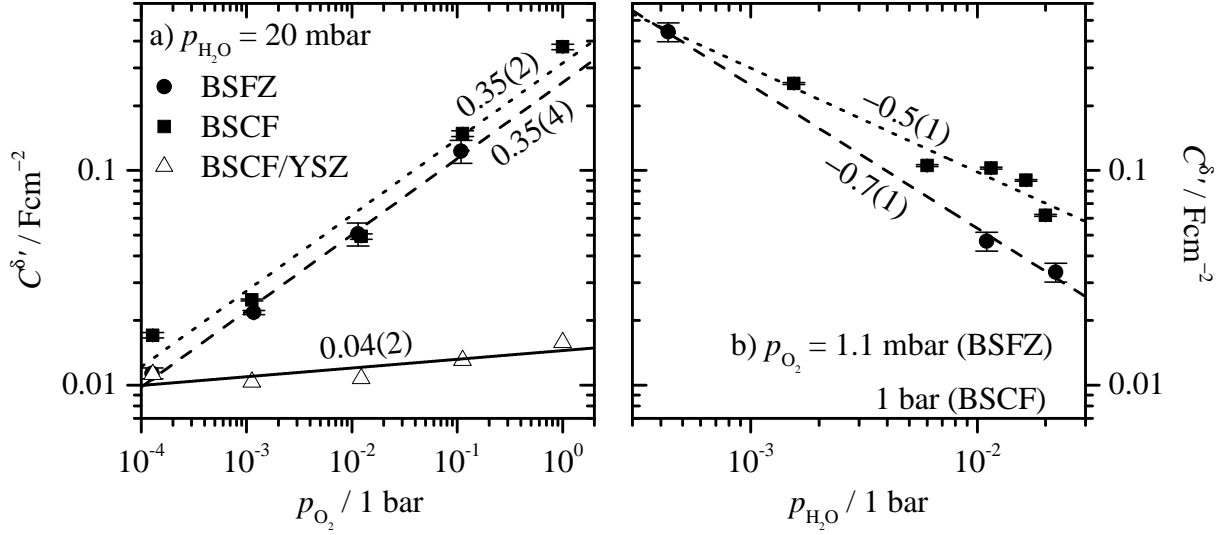


Figure 4.46: Oxygen (on BZY1) (a) and water (on BZY6) (b) partial pressure dependence of $C^{\delta'}$. $T = 600^\circ\text{C}$ for BSFZ and 550°C for BSCF, $p_{\text{H}_2\text{O}} = 20\text{ mbar}$, $d_{\text{ME}} = 100\ \mu\text{m}$ for BSFZ and $80\ \mu\text{m}$ for BSCF and film thickness $\approx 100\ \text{nm}$. The triangles are measured chemical capacitances for BSCF on YSZ at $T = 750^\circ\text{C}$, $p_{\text{H}_2\text{O}} < 0.7\text{ mbar}$ (nominally dry) and $d_{\text{ME}} = 80\ \mu\text{m}$.

AC (or DC) voltage η needs to be understood. This is sketched in figure 4.47a for the cathodic part (with respect to the working electrode, the extended counter electrode is reversible) of the AC signal (the sign of $F\eta$ is switched for the anodic case).^[110] The partial changes in μ_{O} (red) and μ_{H} (light blue) are

$$\begin{aligned}\partial\mu_{\text{O}} &= -\partial\tilde{\mu}_{\text{V}\bullet\bullet} + 2\partial\tilde{\mu}_{\text{h}\bullet} \\ \partial\mu_{\text{H}} &= \partial\tilde{\mu}_{\text{OH}\bullet} - \partial\tilde{\mu}_{\text{h}\bullet}\end{aligned}\quad (4.26)$$

$\partial\tilde{\mu}_{\text{V}\bullet\bullet}$ (gray) and $\partial\tilde{\mu}_{\text{OH}\bullet}$ (black) are zero (constant between CE and WE) as their relaxation with the electrolyte on a small disturbance through η is fast. $\tilde{\mu}_{\text{h}\bullet}$ (magenta) develops a gradient across the electrolyte (which is in the ideal case insulating for electronic charge carriers), hence,

$$\begin{aligned}\partial\mu_{\text{O}} &= 2\partial\tilde{\mu}_{\text{h}\bullet} = 2F\eta \\ \partial\mu_{\text{H}} &= -\partial\tilde{\mu}_{\text{h}\bullet} = -F\eta = -0.5\partial\mu_{\text{O}}\end{aligned}\quad (4.27)$$

Therefore, the chemical potential of water, $\partial\mu_{\text{H}_2\text{O}} = \partial\mu_{\text{O}} + 2\partial\mu_{\text{H}} = 0$ (dark blue), is constant over the total sample and $\partial\mu_{\text{H}}$ in eq. 4.25 is $-0.5\partial\mu_{\text{O}}$. The concentration change of oxygen is $\partial c_{\text{O}} = -\partial c_{\text{V}\bullet\bullet}$ and $\partial c_{\text{H}} = \partial c_{\text{OH}\bullet}$ for hydrogen. The change of the chemical potential of oxygen in the mixed-conducting electrode can be expressed as the change of an effective oxygen partial pressure $\partial\mu_{\text{O}} \approx RT\partial\ln p_{\text{O}_2}$ (activity coefficient unity). Inserting these relations and eq. 4.27 into 4.25 finally gives

$$\begin{aligned}C_{\text{O}}^{\delta} &\approx -\frac{4F^2L}{RT} \frac{\partial c_{\text{V}\bullet\bullet}}{\partial\ln p_{\text{O}_2}} \\ C_{\text{H}}^{\delta} &\approx -\frac{2F^2L}{RT} \frac{\partial c_{\text{OH}\bullet}}{\partial\ln p_{\text{O}_2}}\end{aligned}\quad (4.28)$$

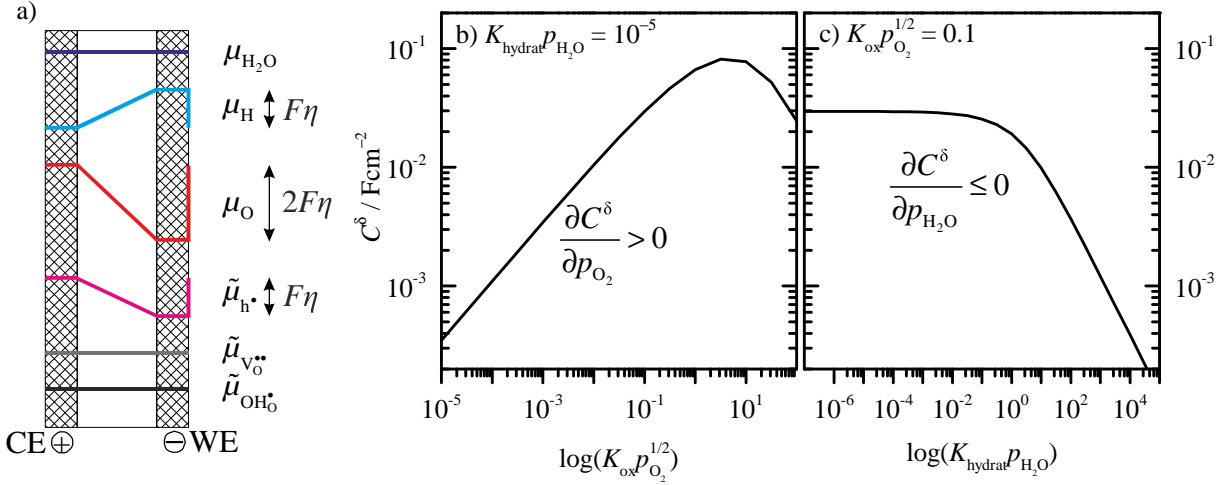


Figure 4.47: a) Response of the electrochemical potentials for all relevant species in mixed-conducting electrodes to a small change in the electrical potential through an applied voltage (AC or DC, here shown for cathodic DC). The counter-electrode is reversible owing to its large surface area compared to the working electrode.^[110] b) p_{O_2} dependence of the chemical capacitance calculated through eq. 4.29 ($L = 100 \text{ nm}$, $T = 600 \text{ K}$) and c) the respective $p_{\text{H}_2\text{O}}$ dependence for experimentally reasonable Kp values and ranges.

The partial derivatives for a system with three mobile charge carriers have been numerically calculated (thermodynamic introduction chapter 2.1 – cf. figure 2.3). Both chemical capacitances are connected in parallel, hence, they add up to a total, measured capacitance

$$C^\delta \approx \frac{2F^2L}{RTV_m} \left(-\frac{\partial c_{\text{V}_\text{O}^{\bullet\bullet}}}{\partial \ln p_{\text{O}_2}} - \frac{\partial c_{\text{OH}_\text{O}}}{\partial \ln p_{\text{O}_2}} \right) = \frac{2F^2L}{RTV_m} \left(\frac{\partial c_{\text{h}\cdot}}{\partial \ln p_{\text{O}_2}} \right) \quad (4.29)$$

Owing to the electroneutrality condition the first term in brackets equals to $\partial c_{\text{h}\cdot} / \partial \ln p_{\text{O}_2}$ (magenta surface plot in figure 2.3). The molar volume V_m has to be introduced as the partial derivatives were calculated for molar fractions.

The calculated values for C^δ ($T = 600 \text{ K}$) are plotted in figure 4.47b for a experimentally reasonable $K_{\text{hydrat}} p_{\text{H}_2\text{O}} = 10^{-5}$ (cf. figure 4.9) and c for $K_{\text{ox}} p_{\text{O}_2}^{1/2} = 0.1$ (cf. figure 4.13). For the range of $K_{\text{ox}} p_{\text{O}_2}^{1/2} = 10^{-3}$ to 1 relevant for the measured conditions for BSFZ (and similar for BSCF) the calculated C^δ increases with increasing p_{O_2} which is in agreement with the measured data. For the range of $K_{\text{hydrat}} p_{\text{H}_2\text{O}} 10^{-6}$ to 10^{-4} the calculated C^δ is, however, $p_{\text{H}_2\text{O}}$ independent which disagrees with the strong negative $p_{\text{H}_2\text{O}}$ dependence found in figure 4.46b. At least, for high $K_{\text{hydrat}} p_{\text{H}_2\text{O}}$ values above 1 the calculated C^δ starts to decrease. Obviously, the defects and/or the activity of oxygen in the electrode do not behave ideally which might shift the negative slope of $\partial C^\delta / \partial p_{\text{H}_2\text{O}}$ to lower $K_{\text{hydrat}} p_{\text{H}_2\text{O}}$ values. Thus, the calculated behavior of C^δ does not totally disagree with the measured data as the slope is, at least, zero or negative, but definitely not positive.

4.6.4 Temperature dependence and comparison of the catalytic activities

The temperature dependence, i.e. the activation energy for R_s , scatters most along the different samples and BZY substrates as seen in figure 4.39a in section 4.5.2. Nonetheless, with values around 1.5 eV the activation energy is comparable to data on YSZ and does, hence, not contradict the previously made conclusions. However, the mechanistic information of this parameter is poor as the enthalpies of all processes, i.e. reaction rate constant k of the rds and equilibrium constants K of the preceding and succeeding equilibria (cf. examples in eq. 4.23 and 4.24), contribute to the measured activation energy which can, in principle, obtain any reasonable value.

Owing to R_{con} decreasing the absolute impedance but scattering between individual BZY substrates, a comparison of the absolute surface reaction resistances is difficult. In addition, the surface properties alone vary typically more than bulk properties. In general, the resistance is higher for BSFZ than for BSCF on BZY under similar conditions in agreement with cobalt containing and free (La,Ba,Sr)(Co,Fe)O_{3-δ} on YSZ.^[39] R_s values for BSCF on BZY and on YSZ (BSFZ on YSZ not available) additionally requires extrapolation from different measurement ranges to be comparable. Within all errors and uncertainties (\approx one order of magnitude) there is no significant difference, i.e. a conclusion whether the oxygen reduction reaction is faster in H⁺-SOFCs than in O²⁻-SOFCs cannot be made at the moment.

5 Summary and Conclusions

This thesis is concerned with mixed-conducting perovskites as electrode material in solid oxide fuel cells using proton-conducting electrolytes (H^+ -SOFC). In particular, it is the thermodynamic and transport behavior, and the oxygen exchange reaction mechanism at the electrode surface that are inspected. All of these properties are highly determined by the physics and electrochemistry of the mobile charge carriers (point defects of zero dimension). Under fuel cell conditions where the oxygen exchange electrode (cathode) is exposed to oxidizing, humid (water formation at the cathode) atmosphere, three charge carriers are of interest: The ionic defects oxygen vacancies $V_O^{\bullet\bullet}$ and interstitial protons associated to a regular lattice oxygen OH_O^\bullet , and the electronic defect holes h^\bullet . These defects provide the mixed-conducting characteristics which is necessary to enhance the catalytically active zone beyond the typically limited triple-phase-boundary (electrode, electrolyte and gas phase in direct contact) to the whole electrode surface. With respect to H^+ -SOFCs, electrode materials with mixed proton/hole conductivity are highly desired so that the proton from the electrolyte can migrate through the electrode to its surface where then the water formation takes place.

In the thermodynamic and transport behavior treatment the three mobile charge carriers are not independent of each other as they are coupled via local electroneutrality. This is, of course, also the case in a system with “only” two mobile charge carriers. However, in the latter the coupling is unambiguous as the defect concentration of one species can directly be calculated from the other through this electroneutrality condition. In contrast, having three charge carriers only the sum of the concentration of two carriers can be calculated through the third one, i.e. the correlation between the three defects is a priori ambiguous. Thus, the mathematical description and the physical interpretation are more complex. Usually numerical analysis is necessary to solve the equations. For the diffusion treatment it was found that four (instead of one for a situation with two mobile charge carriers) chemical diffusion coefficients are needed to fully describe the flux of the three defects.

Thermodynamics – The first important goal was to quantify the proton concentration which is one of the criteria for a material to be suited as electrode in a H^+ -SOFC. The complexity arises from the fact that protons can be incorporated by water uptake (a water molecule splits up into proton and hydroxide ion where latter occupies an oxygen vacancy and the proton is attached to a regular oxygen site, forming two protonic defects) and hydrogen uptake (incorporation of water by simultaneous release of oxygen, i.e. a combined hydration-deoxygenation). From the big zoo of possible electrode materials with perovskite structure four different candidates were selected. To compare in a first step their capability in taking up protons the maximum proton concentration was measured ex-situ for samples hydrated down to room temperature and was found to increase from ≈ 0.1 to 20 mol% in the series LSCF ($La_{0.6}Sr_{0.4}Co_{0.8}Fe_{0.2}O_{3-\delta}$), BSCN ($Ba_{0.6}Sr_{0.4}Co_{0.9}Nb_{0.1}O_{3-\delta}$), BSCF ($Ba_{0.5}Sr_{0.5}Co_{0.8}Fe_{0.2}O_{3-\delta}$) and BSFZ ($Ba_{0.5}Sr_{0.5}Fe_{0.8}Zn_{0.2}O_{3-\delta}$). Therefore, the latter one being a promising candidate

for mixed protonic/electronic conductors was selected for detailed investigations. The proton concentration under fuel cell conditions ($350 - 600\text{ }^\circ\text{C}$, $p_{\text{O}_2} = 10\text{ mbar}$ and 1 bar and $p_{\text{H}_2\text{O}} = 20\text{ mbar}$) was determined ex-situ with Karl-Fischer titration of hydrated and quenched pellets, and in-situ by analyzing the thermogravimetric relaxation upon step-wise changes in $p_{\text{H}_2\text{O}}$ and $p_{\text{D}_2\text{O}}$. For this analysis, the fundamental understanding of the thermodynamic and diffusive behavior of a defect system with three mobile charge carriers is mandatory. The mass change upon $\Delta p_{\text{H}_2\text{O}}$ in the in-situ experiments cannot simply be assigned to water or hydrogen as any combination is thermodynamically possible. It was found for BSFZ that the mode of proton incorporation changes from predominantly acid-base thermodynamics at 10 mbar (mass increase mainly by water uptake) to almost exclusively redox thermodynamics (mass increase by hydrogen uptake) at $1\text{ bar } p_{\text{O}_2}$. The proton concentration in $20\text{ mbar } p_{\text{H}_2\text{O}}$ ranges from 0.32 to $1.5\text{ mol}\%$ between 600 and $350\text{ }^\circ\text{C}$, and was, in addition, found to be less p_{O_2} dependent which is in agreement with the thermodynamic defect chemistry model and literature data for BSCF.^[27]

Diffusion kinetics – For the water uptake in a medium with two ionic and one electronic mobile defect two limiting cases are identified in the literature.^[30–33] In a material without electronic charge carriers water migrates via coupled, ambipolar diffusion of $\text{V}_{\text{O}}^{\bullet\bullet}$ and $\text{OH}_{\text{O}}^{\bullet}$ yielding a single chemical diffusivity of water. Redox thermodynamics where only hydrogen is taken up leads to ambipolar diffusion of protons and holes yielding a single chemical diffusivity, as well. Mixed-conducting perovskites having a sufficiently high mobility and concentration of electronic charge carriers exhibit a so called two-fold relaxation upon water uptake, i.e. for the short time behavior hydrogen (ambipolar diffusion of protons and holes, typically being fast) is taken up reducing the sample (decrease of hole concentration), followed by oxygen (ambipolar diffusion of oxygen vacancies and holes, typically slower) for longer times reoxidizing the sample. These three regimes and their dependence on various parameters such as hole concentration, mobilities of the three defects and degree of protonation were theoretically analyzed in the present thesis by numerical simulations based on the derived flux equations. The main purpose was to check under which conditions the two-fold relaxation is observable in a mass relaxation experiment where both contributions (hydrogen and oxygen uptake) lead to a mass increase.

The two limiting situations in terms of thermodynamics – protonation via water or hydrogen uptake – are found in BSFZ for different p_{O_2} , and strongly affect the relaxation kinetics. For $1\text{ bar } p_{\text{O}_2}$ hydrogen is taken up upon $\Delta p_{\text{H}_2\text{O}}$ resulting in fast mass transient and small mass changes. For $10\text{ mbar } p_{\text{O}_2}$ water is predominantly incorporated yielding slower mass relaxations and larger mass changes. The difference between water uptake at low and hydrogen uptake at high p_{O_2} was confirmed by SIMS analysis of D_2O tracer exchanged samples (more or less same relative deuterium concentration) and conductivity relaxation experiments upon $\Delta p_{\text{H}_2\text{O}}$ for thin-film samples on MgO which shows a non-monotonic two-fold relaxation for 10 mbar and a monotonic single-fold relaxation for $1\text{ bar } p_{\text{O}_2}$.

Proton conductivity – From the mass relaxation transients diffusion coefficients could be extracted. The measured thermogravimetric transients in $10\text{ mbar } p_{\text{O}_2}$ (acid-base thermodynamics) could not reliably be fitted by the two-fold relaxation model expected from the simulations as the contribution of the fast hydrogen migration to the overall weight gain was

too small. Instead, they were fitted with one effective diffusivity. However, the numerical simulations showed that these values are a lower bound for the proton diffusivity. Therefore, they are used for a conservative estimation as to whether or not the proton conductivity in BSFZ is sufficiently high to enable the whole electrode surface to be catalytically active. In contrast, the fitted diffusivity of the mass relaxation in 1 bar p_{O_2} is assigned to the chemical diffusion of hydrogen and can be fitted well. Simulations showed that for low degrees of hydrogenation as found in BSFZ the chemical diffusivity of hydrogen is within the errors equal to the defect diffusivity of protons. Thus, its fit results were directly used to calculate the proton conductivity. All fitted chemical diffusivities lie in a reasonable range compared to defect diffusivities for $\text{V}_{\text{O}}^{\bullet\bullet}$ and $\text{OH}_{\text{O}}^{\bullet}$ taken from literature of comparable materials. The proton conductivities calculated from proton concentrations obtained in the thermodynamic analysis and effective diffusivities obtained from the transients range from $\approx 9 \times 10^{-5}$ in the most conservative to $2 \times 10^{-3} \text{ Scm}^{-1}$ in the realistic estimation. Comparing these values with the proton-conductivity of BZY15 which is known to be one of the best high temperature proton conductors, they are up to one and a half orders of magnitude smaller. However, even the most pessimistic estimation is orders of magnitude above a required minimum of about $3 \times 10^{-8} \text{ Scm}^{-1}$ (found as border between surface and bulk path for $(\text{La,Sr})\text{MnO}_{3\pm\delta}$ on YSZ^[12]) to enable the whole electrode surface to be catalytically active.

Electronic leakage in the electrolyte – The proton-conducting electrolyte chosen as substrate for the BSFZ and BSCF electrodes was Y-doped BaZrO_3 . In the literature it is known that holes in proton-conducting electrolytes with perovskite structure appearing in oxidizing atmosphere at elevated temperature lead to a non-negligible electronic conductivity in the electrolyte. In the present thesis it is demonstrated that the electronic resistance in the electrolyte leads to an electronic leakage which severely affects the impedance spectra, in particular the low frequency contribution which is related to the oxygen reduction kinetics. The electronic leakage not only decreases the absolute measured impedance values (making it in fact impossible to compare different materials and conditions), it changes the exponents of the dependencies on the microelectrode diameter, oxygen and water partial pressure which provide important information about the oxygen reduction mechanism. This disturbance, not considered by any investigations in the literature, possibly leads to severe misinterpretation with respect to the oxygen reduction reaction. For now, the best and most reproducible strategy to diminish this influence is to decrease the Y-dopant concentration to 1% , i.e. to sufficiently increase the electronic leakage resistance. It has to be emphasized that in a real fuel cell this electronic conductivity in the electrolyte is suppressed at the anodic side (reducing atmosphere with very low p_{O_2} decreasing the hole concentration) and, thus, does not impair the fuel cell operation.

Oxygen reduction mechanism – The whole electrode surface being catalytically active was confirmed by impedance spectroscopy on dense, thin-film microelectrodes. The low frequency contribution to the total impedance, assigned to the surface reaction resistance, is inversely proportional to the oxygen reduction rate of the rate determining step (slowest elementary reaction). The surface reaction resistance inversely scales with the microelectrode area, indicating that the rate determining step occurs at the whole electrode surface. This result was found for BSFZ and BSCF – proving that both electrode materials are sufficiently conductive for protons. The exponent of the p_{O_2} dependence of the surface reaction resistance

being smaller than -0.5 but larger than -1 indicates that molecular oxygen (reaction order of unity) is involved in the rate determining step. In addition, a point defect contributing a positive effective p_{O_2} dependence to the surface reaction resistance must participate in the rate determining step increasing the exponent from -1 to less negative values. The exponent of the water partial pressure dependence of the surface reaction resistance was found to be positive. As the reaction order of oxygen was found to be non-zero the reaction order of water is supposed to be zero and the measured $p_{\text{H}_2\text{O}}$ dependence must originate from the positive effective $p_{\text{H}_2\text{O}}$ contribution of a participating defect. The oxygen vacancy is the only defect with a positive effective $p_{\text{H}_2\text{O}}$ contribution to the surface reaction resistance. Thus, it was identified as the only possible defect participating in the rate determining step. To summarize, molecular oxygen and an oxygen vacancy are involved in the rate determining step. It is obviously mandatory for the oxygen dissociation to have oxygen vacancies involved at the surface, although the incorporation of oxygen is, in principle, not necessary for the formation of water at the cathode. For further detailed mechanistic investigations the influence of the electronic leakage in the electrolyte needs to be reproducibly suppressed.

To finally summarize the key results of this work: It was shown that mixed-conducting cathode materials with perovskite structure take up perceptible amounts of protons to enable the whole electrode surface to be catalytically active for the water formation, at least for thin-film electrodes with small diffusion length. It is to the best of my knowledge the first work which quantified both the proton concentration and a plausible estimate of the proton conductivity over a wide range of oxygen partial pressure and temperature relevant for fuel cell operation. For BSFZ the proton incorporation mechanism upon water partial pressure increase was found to change from predominantly acid-base water to predominantly redox hydrogen uptake within only two orders of magnitude in p_{O_2} . The kinetics of the stoichiometric relaxation is understood with the help of numerical simulations for simultaneous diffusion of protons, oxygen vacancies and holes. The electronic conductivity in the electrolyte used for the impedance measurements causes a non-negligible electronic leakage disturbing the analysis. After having sufficiently eliminated this disturbance, the whole electrode surface was confirmed to be catalytically active. Furthermore, it was found that molecular oxygen species and oxygen vacancies are participating in the rate determining step of the oxygen reduction mechanism. These results now serve a starting point for a knowledge-based improvement of the cathode performance in proton-conducting solid oxide fuel cells.

A MATLAB scripts

A.1 Defect concentrations from $p_{O_2}^{1/2} K_{ox}$ and $p_{H_2O} K_{hydrat}$

MATLAB file A.1: get_TDDData.m

```
function [H,v,h,H2,v2,h2,dHdlnpH2O,dvdlnpH2O,dhdlnpH2O,dHdlnpO2,dvdlnpO2,dhdlnpO2] = get_TDDData(pKhy,pKox,p,A,v0)

%The first values of pKhy and pKox decide in which corner the iteration starts;
%v0(1,2,3) are the starting guesses for the vac. in this corner;
%unfortunately quality of the results highly depends on the starting corner;
%you have to try; recommendation is to start pKhy = highest and pKox =
%lowest value
%p(1) and p(2) are both partial pressures to calculate dc/dlnp, same dlnp used
%for H2O and O2
%A = acceptor dopand concentration;

options = optimset('Display','off','TolFun',1E-16,'MaxFunEvals',1000,'MaxIter',
    ,4000,'TolX',1E-16,'Algorithm','levenberg-marquardt','ScaleProblem','',
    'Jacobian');
f = 0.9; %factor for "wrong starting value on purpose"

p2Khy = (p(2)/p(1)).*pKhy;
p2Kox = sqrt(p(2)/p(1)).*pKox;
n = length(pKhy);
m = length(pKox);
[H,v,h,H2,v2,h2,dHdlnpH2O,dvdlnpH2O,dhdlnpH2O,dHdlnpO2,dvdlnpO2,dhdlnpO2] =
    deal(zeros(n,m));

for i = 1:n
    for j = 1:m
        if (i == 1 && j == 1)
            v(i,j) = fsolve(@(x) get_v(x,[pKhy(i),pKox(j),A]),v0(1),options);
            v2(i,j) = fsolve(@(x) get_v(x,[p2Khy(i),pKox(j),A]),v0(2),options);
            v3(i,j) = fsolve(@(x) get_v(x,[pKhy(i),p2Kox(j),A]),v0(3),options);
        elseif (i == 1 && j > 1)
            v(i,j) = fsolve(@(x) get_v(x,[pKhy(i),pKox(j),A]),f*v(i,j-1),options);
            v2(i,j) = fsolve(@(x) get_v(x,[p2Khy(i),pKox(j),A]),f*v2(i,j-1),options);
            v3(i,j) = fsolve(@(x) get_v(x,[pKhy(i),p2Kox(j),A]),f*v3(i,j-1),options);
        elseif (i > 1 && j == 1)
            v(i,j) = fsolve(@(x) get_v(x,[pKhy(i),pKox(j),A]),f*v(i-1,j),options);
            v2(i,j) = fsolve(@(x) get_v(x,[p2Khy(i),pKox(j),A]),f*v2(i-1,j),options);
        else
            v(i,j) = fsolve(@(x) get_v(x,[pKhy(i),pKox(j),A]),f*v(i-1,j-1),options);
            v2(i,j) = fsolve(@(x) get_v(x,[p2Khy(i),pKox(j),A]),f*v2(i-1,j-1),options);
            v3(i,j) = fsolve(@(x) get_v(x,[pKhy(i),p2Kox(j),A]),f*v3(i-1,j-1),options);
        end
    end
end
```

```

        v3(i,j) = fsolve(@(x) get_v(x,[pKhy(i),p2Kox(j),A]), f*v3(i-1,j),
            options);
    else
        v(i,j) = fsolve(@(x) get_v(x,[pKhy(i),pKox(j),A]), f*v(i-1,j-1),
            options);
        v2(i,j) = fsolve(@(x) get_v(x,[p2Khy(i),pKox(j),A]), f*v2(i-1,j-1),
            options);
        v3(i,j) = fsolve(@(x) get_v(x,[pKhy(i),p2Kox(j),A]), f*v3(i-1,j-1),
            options);
    end

    H(i,j) = (-1*v(i,j)*pKhy(i)+sqrt(v(i,j)^2*pKhy(i)^2-4*pKhy(i)*(v(i,j)
        ^2-3*v(i,j))))/2;
    H2(i,j) = (-1*v2(i,j)*p2Khy(i)+sqrt(v2(i,j)^2*p2Khy(i)^2-4*p2Khy(i)*(v2
        (i,j)^2-3*v2(i,j))))/2;
    H3(i,j) = (-1*v3(i,j)*pKhy(i)+sqrt(v3(i,j)^2*pKhy(i)^2-4*pKhy(i)*(v3(i,
        j)^2-3*v3(i,j))))/2;

    h(i,j) = sqrt(pKox(j)*v(i,j)/(3-v(i,j)-H(i,j)));
    h2(i,j) = sqrt(pKox(j)*v2(i,j)/(3-v2(i,j)-H2(i,j)));
    h3(i,j) = sqrt(p2Kox(j)*v3(i,j)/(3-v3(i,j)-H3(i,j)));

    dHdlnpH2O(i,j) = (H(i,j)-H2(i,j))/(log(p(1))-log(p(2)));
    dvdlnpH2O(i,j) = (v(i,j)-v2(i,j))/(log(p(1))-log(p(2)));
    dhdlnpH2O(i,j) = (h(i,j)-h2(i,j))/(log(p(1))-log(p(2)));

    dHdlnpO2(i,j) = (H(i,j)-H3(i,j))/(log(p(1))-log(p(2)));
    dvdlnpO2(i,j) = (v(i,j)-v3(i,j))/(log(p(1))-log(p(2)));
    dhdlnpO2(i,j) = (h(i,j)-h3(i,j))/(log(p(1))-log(p(2)));
end
end
end

```

MATLAB file A.2: get_v.m

```

function F = get_v(x,k)

pKhy = k(1);
pKox = k(2);
A = k(3);
H = (-1*x*pKhy+sqrt(x^2*pKhy^2-4*pKhy*(x^2-3*x)))/2;
F = ((3-x-H)*(A-2*x-H)^2/x)-pKox;

end

```

A.2 Defect concentrations from Δm upon $\Delta p_{\text{H}_2\text{O}}$ for BSFZ

MATLAB file A.3: TGA_fixKox.m

```

function F = TGA_fixKox(x,k)

MHD = 1; %ATTENTION: Set MHD either to 1 (H) or 2 (D)
pO2 = k(1)/1000;
pH2O1 = k(2)/1000;
pH2O2 = k(3)/1000; %all p in mbar
Kox = k(4);
nBSFZ = k(5); %mmol
dm = k(6); %mg
c1 = x(1);
c2 = x(2);
d1 = x(3);
d2 = x(4);
Khy = x(5);

F = [(c1^2)/(pH2O1*d1*(3-d1-c1))-Khy; %eq. 1
      (c2^2)/(pH2O2*d2*(3-d2-c2))-Khy; %eq. 2
      ((3-d1-c1)*(1.2-2*d1-c1)^2)/(sqrt(pO2)*d1)-Kox; %eq. 3
      ((3-d2-c2)*(1.2-2*d2-c2)^2)/(sqrt(pO2)*d2)-Kox; %eq. 4
      (nBSFZ*((c2-c1)*MHD+(d1-d2)*16))-dm]; %eq. 5

end

```

MATLAB file A.4: TGA_redox.m

```

function F = TGA_redox(x,k)

MHD = 1; %ATTENTION: Set MHD either to 1 (H) or 2 (D)
pH2O1 = k(1)/1000;
pH2O2 = k(2)/1000;
d = k(3);
nBSFZ = k(4); %mmol
dm = k(5); %mg
c1 = x(1);
c2 = x(2);
Khy = x(3);

F = [(c1^2)/(pH2O1*d*(3-d-c1))-Khy;
      (c2^2)/(pH2O2*d*(3-d-c2))-Khy;
      (nBSFZ*(c2-c1)*MHD)-dm];

end

```


B Input data for diffusion simulations

Table B.1: Acid-base thermodynamics, high degree of hydration, increasing hole concentration: $X = 0.5$ / $\Delta[h^\bullet] = 0$ / $D_{V_{\bullet\bullet}} = 10^{-6} \text{ cm}^2\text{s}^{-1}$ / $D_{OH_{\bullet}} = 10^{-5} \text{ cm}^2\text{s}^{-1}$ / $D_{h^\bullet} = 10^{-4} \text{ cm}^2\text{s}^{-1}$

$[V_{\bullet\bullet}]$	$\Delta[V_{\bullet\bullet}]$	$[OH_{\bullet}]$	$\Delta[OH_{\bullet}]$	$[h^\bullet]$
0.25	-0.025	0.5	0.05	0.0001
0.2498	-0.02498	0.4995	0.04995	0.001
0.2475	-0.02475	0.495	0.0495	0.01
0.225	-0.0225	0.45	0.045	0.1
0.2056	-0.02056	0.4111	0.04111	0.1778
0.171	-0.0171	0.3419	0.03419	0.3162
0.1094	-0.01094	0.2189	0.02189	0.5623
0.025	-0.0025	0.05	0.005	0.9
0.0025	-0.00025	0.005	0.0005	0.99

Table B.2: Acid-base thermodynamics, low degree of hydration, increasing hole concentration: $X = 0.1$ / $\Delta[h^\bullet] = 0$ / $D_{V_{\bullet\bullet}} = 10^{-6} \text{ cm}^2\text{s}^{-1}$ / $D_{OH_{\bullet}} = 10^{-5} \text{ cm}^2\text{s}^{-1}$ / $D_{h^\bullet} = 10^{-4} \text{ cm}^2\text{s}^{-1}$

$[V_{\bullet\bullet}]$	$\Delta[V_{\bullet\bullet}]$	$[OH_{\bullet}]$	$\Delta[OH_{\bullet}]$	$[h^\bullet]$
0.4499	-0.004999	0.09999	0.009999	0.0001
0.4495	-0.004995	0.0999	0.00999	0.001
0.4455	-0.00495	0.099	0.0099	0.01
0.405	-0.0045	0.09	0.009	0.1
0.37	-0.004111	0.08222	0.008222	0.1778
0.3077	-0.003419	0.06838	0.006838	0.3162
0.197	-0.002189	0.04377	0.004377	0.5623
0.045	-0.0005	0.01	0.001	0.9
0.0045	-0.00005	0.001	0.0001	0.99

Table B.3: Acid-base thermodynamics, low degree of hydration, decreasing oxygen vacancy diffusivity: $X = 0.1 / \Delta[\text{h}^\bullet] = 0 / D_{\text{OH}_\bullet} = 10^{-5} \text{ cm}^2\text{s}^{-1} / D_{\text{h}^\bullet} = 10^{-4} \text{ cm}^2\text{s}^{-1}$

$D_{\text{V}_\bullet\bullet}/\text{cm}^2\text{s}^{-1}$	$[\text{V}_\bullet\bullet]$	$\Delta[\text{V}_\bullet\bullet]$	$[\text{OH}_\bullet]$	$\Delta[\text{OH}_\bullet]$	$[\text{h}^\bullet]$
10^{-6}	0.3103	-0.003448	0.06896	0.006896	0.3103
10^{-7}	0.3103	-0.003448	0.06896	0.006896	0.3103
10^{-8}	0.3103	-0.003448	0.06896	0.006896	0.3103

Table B.4: Low degree of hydration, increasing redox thermodynamics: $X \approx 0.07 / D_{\text{V}_\bullet\bullet} = 10^{-6} \text{ cm}^2\text{s}^{-1} / D_{\text{OH}_\bullet} = 10^{-5} \text{ cm}^2\text{s}^{-1} / D_{\text{h}^\bullet} = 10^{-4} \text{ cm}^2\text{s}^{-1}$

$[\text{V}_\bullet\bullet]$	$\Delta[\text{V}_\bullet\bullet]$	$[\text{OH}_\bullet]$	$\Delta[\text{OH}_\bullet]$	$[\text{h}^\bullet]$	$\Delta[\text{h}^\bullet]$
0.3103	-0.002759	0.06896	0.006896	0.3103	-0.001379
0.3103	-0.002069	0.06896	0.006896	0.3103	-0.002759
0.3103	-0.001379	0.06896	0.006896	0.3103	-0.004138

Table B.5: Low degree of hydration for representative, fixed $p_{\text{H}_2\text{O}}K_{\text{hydrat}}$ with increasing $p_{\text{O}_2}^{1/2}K_{\text{ox}}$: $p_{\text{H}_2\text{O}}K_{\text{hydrat}} = 10^{-2} / D_{\text{V}_\bullet\bullet} = 10^{-6} \text{ cm}^2\text{s}^{-1} / D_{\text{OH}_\bullet} = 10^{-5} \text{ cm}^2\text{s}^{-1} / D_{\text{h}^\bullet} = 10^{-4} \text{ cm}^2\text{s}^{-1}$

$p_{\text{O}_2}^{1/2}K_{\text{ox}}$	$[\text{V}_\bullet\bullet]$	$\Delta[\text{V}_\bullet\bullet]$	$[\text{OH}_\bullet]$	$\Delta[\text{OH}_\bullet]$	$[\text{h}^\bullet]$	$\Delta[\text{h}^\bullet]$
10^{-6}	4.500×10^{-1}	-2.520×10^{-3}	9.962×10^{-2}	5.040×10^{-3}	4.285×10^{-4}	-9.815×10^{-7}
10^{-5}	4.495×10^{-1}	-2.518×10^{-3}	9.958×10^{-2}	5.038×10^{-3}	1.354×10^{-3}	-3.103×10^{-6}
10^{-4}	4.481×10^{-1}	-2.511×10^{-3}	9.945×10^{-2}	5.032×10^{-3}	4.275×10^{-3}	-9.801×10^{-6}
10^{-3}	4.438×10^{-1}	-2.490×10^{-3}	9.906×10^{-2}	5.012×10^{-3}	1.344×10^{-2}	-3.088×10^{-5}
10^{-2}	4.302×10^{-1}	-2.426×10^{-3}	9.783×10^{-2}	4.948×10^{-3}	4.172×10^{-2}	-9.655×10^{-5}
10^{-1}	3.907×10^{-1}	-2.230×10^{-3}	9.404×10^{-2}	4.754×10^{-3}	1.246×10^{-1}	-2.938×10^{-4}
10^0	2.918×10^{-1}	-1.693×10^{-3}	8.303×10^{-2}	4.196×10^{-3}	3.334×10^{-1}	-8.099×10^{-4}
10^1	1.306×10^{-1}	-6.925×10^{-4}	5.748×10^{-2}	2.925×10^{-3}	6.814×10^{-1}	-1.540×10^{-3}
10^2	2.517×10^{-2}	-7.612×10^{-5}	2.585×10^{-2}	1.351×10^{-3}	9.238×10^{-1}	-1.199×10^{-3}
10^3	2.901×10^{-3}	-3.196×10^{-6}	8.834×10^{-3}	4.720×10^{-4}	9.854×10^{-1}	-4.656×10^{-4}

Table B.6: Simulation of TG transients of BSFZ in 10 mbar p_{O_2}

$T/^\circ\text{C}$	$D_{V_{\bullet\bullet}}/\text{cm}^2\text{s}^{-1}$	$D_{OH_{\bullet}}/\text{cm}^2\text{s}^{-1}$	$D_{h_{\bullet}}/\text{cm}^2\text{s}^{-1}$	$[V_{\bullet\bullet}]$	$\Delta[V_{\bullet\bullet}]$	$[OH_{\bullet}]$	$\Delta[OH_{\bullet}]$	$[h_{\bullet}]$	$\Delta[h_{\bullet}]$
350	4.200×10^{-8}	7.475×10^{-6}	3.570×10^{-4}	0.4570	-9.460×10^{-4}	6.792×10^{-3}	2.116×10^{-3}	0.2793	-2.244×10^{-4}
400	1.200×10^{-7}	5.177×10^{-6}	4.475×10^{-4}	0.4838	-5.855×10^{-4}	4.092×10^{-3}	1.278×10^{-3}	0.2283	-1.067×10^{-4}
450	3.200×10^{-7}	8.235×10^{-6}	5.547×10^{-4}	0.5084	-4.515×10^{-4}	3.086×10^{-3}	9.645×10^{-4}	0.1802	-6.146×10^{-5}
500	7.300×10^{-7}	5.167×10^{-6}	6.800×10^{-4}	0.5305	-3.069×10^{-4}	2.060×10^{-3}	6.441×10^{-4}	0.1369	-3.025×10^{-5}
550	1.500×10^{-6}	7.856×10^{-6}	8.529×10^{-4}	0.5490	-2.670×10^{-4}	1.766×10^{-3}	5.525×10^{-4}	0.1002	-1.853×10^{-5}
600	2.800×10^{-6}	6.750×10^{-6}	1.040×10^{-3}	0.5636	-2.529×10^{-4}	1.655×10^{-3}	5.179×10^{-4}	0.0711	-1.208×10^{-5}

C Conductivity measurements vertical & parallel to diffusion direction

In this chapter it is mathematical shown that for small concentration changes the solution of Fick's second law of one-dimensional diffusion through a plane sheet can be used for fitting conductivity relaxation data measured in parallel to the diffusion direction. Measuring vertical against the diffusion direction the average conductivity σ_t at time t is simply the algebraic mean of the partial conductivities which are then expressed by the Nernst-Einstein relation 2.19:

$$\sigma_t = \frac{1}{l} \int_0^l \sigma_{x,t} dx = \frac{k}{l} \int_0^l (c_0 + \Delta c_{x,t}) dx \quad (\text{C.1})$$

with $k = (F^2 D)/(RT)$ and $c_{x,t} = c_0 + \Delta c_{x,t}$ where c_0 is the initial concentration and $\Delta c_{x,t}$ the time and space dependent change of the concentration (owing to the $p_{\text{H}_2\text{O}}$ jump e.g.). This equation is simply rewritten to

$$\sigma_t = kc_0 + \frac{k}{l} \int_0^l \Delta c_{x,t} dx \quad (\text{C.2})$$

Measuring parallel with the diffusion direction the inverse time dependent, average conductivity is the algebraic mean of the inverse partial conductivities:

$$\frac{1}{\sigma_t} = \frac{1}{l} \int_0^l \frac{1}{\sigma_{x,t}} dx = \frac{1}{lk} \int_0^l \left(\frac{1}{c_0 + \Delta c_{x,t}} \right) dx \quad (\text{C.3})$$

Using the third binomial series $a^2 - b^2 = (a + b)(a - b)$ the fraction in brackets is extended by $(c_0 - \Delta c_{x,t})$ and reads

$$\frac{1}{\sigma_t} = \frac{1}{lk} \int_0^l \left(\frac{c_0 - \Delta c_{x,t}}{c_0^2 - \Delta c_{x,t}^2} \right) dx \quad (\text{C.4})$$

For small $\Delta c_{x,t}$ its square in the denominator is negligible compared to c_0^2 (e.g. for a final Δc of 10% the created error decreases to 1%) resulting in

$$\frac{1}{\sigma_t} \approx \frac{1}{lk} \int_0^l \left(\frac{c_0 - \Delta c_{x,t}}{c_0^2} \right) dx = \frac{1}{kc_0} - \frac{1}{klc_0^2} \int_0^l \Delta c_{x,t} dx \quad (\text{C.5})$$

The difference of the fractions is summarized by using a common denominator and the whole equation is inverted giving the final

$$\sigma_t \approx \frac{klc_0^2}{lc_0 - \int_0^l \Delta c_{x,t} dx} \quad (\text{C.6})$$

Again, the fraction is extended using the third binomial series:

$$\sigma_t \approx \frac{klc_0^2 \left(lc_0 + \int_0^l \Delta c_{x,t} dx \right)}{l^2 c_0^2 - \left(\int_0^l \Delta c_{x,t} dx \right)^2} \quad (\text{C.7})$$

As an approximation the square of the integrated $\Delta c_{x,t}$ is neglected compared to $l^2 c_0^2$ and the final equation reads

$$\sigma_t \approx kc_0 + \frac{k}{l} \int_0^l \Delta c_{x,t} dx \quad (\text{C.8})$$

This is the same equation as for the case of measuring vertical against the diffusion.

Bibliography

- [1] U.S. Department of Energy, Comparison of fuel cell technologies, http://www1.eere.energy.gov/hydrogenandfuelcells/fuelcells/pdfs/fc_comparison_chart.pdf, 2011.
- [2] Z. P. Shao and S. M. Haile, *Nature*, 2004, **431**(7005), 170.
- [3] C. Peters, A. Weber, and E. Ivers-Tiffée, *J. Electrochem. Soc.*, 2008, **155**(7), B730.
- [4] I. M. Hung and C.-Y. Laing, *ECS Trans.*, 2009, **25**(2, Solid Oxide Fuel Cells 11 (SOFC-XI)), 2645.
- [5] L. Zhao, B. B. He, X. Z. Zhang, R. R. Peng, G. Y. Meng, and X. Q. Liu, *J. Power Sources*, 2010, **195**(7), 1859.
- [6] C. Huang, D. J. Chen, Y. Lin, R. Ran, and Z. P. Shao, *J. Power Sources*, 2010, **195**(16), 5176.
- [7] H. Iwahara, *Solid State Ionics*, 1995, **77**, 289.
- [8] F. S. Baumann, J. Fleig, G. Cristiani, B. Stuhlhofer, H. U. Habermeier, and J. Maier, *J. Electrochem. Soc.*, 2007, **154**(9), B931.
- [9] H. Iwahara, T. Yajima, T. Hibino, K. Ozaki, and H. Suzuki, *Solid State Ionics*, 1993, **61**(1-3), 65.
- [10] K. D. Kreuer, *Solid State Ionics*, 1999, **125**(1-4), 285.
- [11] V. Brichzin, J. Fleig, H. U. Habermeier, G. Cristiani, and J. Maier, *Solid State Ionics*, 2002, **152**, 499.
- [12] J. Fleig, H. R. Kim, J. Jamnik, and J. Maier, *Fuel Cells*, 2008, **8**(5), 330.
- [13] F. S. Baumann, J. Fleig, H. U. Habermeier, and J. Maier, *Solid State Ionics*, 2006, **177**(11-12), 1071.
- [14] V. Brichzin, J. Fleig, H. U. Habermeier, and J. Maier, *Electrochem Solid St*, 2000, **3**(9), 403.
- [15] J. Fleig, *Solid State Ionics*, 2003, **161**(3-4), 279.
- [16] K. D. Kreuer, *Ann. Rev. Mater. Res.*, 2003, **33**, 333.
- [17] E. Fabbri, T. K. Oh, S. Licoccia, E. Traversa, and E. D. Wachsman, *J. Electrochem. Soc.*, 2009, **156**(1), B38.

- [18] E. Fabbri, S. Licoccia, E. Traversa, and E. D. Wachsman, *Fuel Cells (Weinheim, Germany)*, 2009, **9**(2), 128.
- [19] E. Fabbri, S. Licoccia, E. Traversa, and E. D. Wachsman, *Materials Research Society Symposium Proceedings*, 2009, **1126**, No pp given.
- [20] C. Solis, V. B. Vert, M. Fabuel, and J. M. Serra, *J. Power Sources*, 2011, **196**(22), 9220.
- [21] K. V. Kravchyk, E. Quarez, C. Solis, J. M. Serra, and O. Joubert, *Int. J. Hydrog. Energy*, 2011, **36**(20), 13059.
- [22] C. Solis, L. Navarrete, and J. M. Serra, *J. Power Sources*, 2013, **240**, 691.
- [23] J. M. Serra, *Private Communication*.
- [24] D. L. Han, Y. Okumura, Y. Nose, and T. Uda, *Solid State Ionics*, 2010, **181**(35-36), 1601.
- [25] A. Grimaud, F. Mauvy, J. M. Bassat, S. Fourcade, M. Marrony, and J. C. Grenier, *J. Mater. Chem.*, 2012, **22**(31), 16017.
- [26] A. Grimaud, F. Mauvy, J. M. Bassat, S. Fourcade, L. Rocheron, M. Marrony, and J. C. Grenier, *J. Electrochem. Soc.*, 2012, **159**(6), B683.
- [27] D. Hashimoto, D. Han, and T. Uda, *Solid State Ionics*, 2014, (0).
- [28] J. Maier, *J. Am. Ceram. Soc.*, 1993, **76**(5), 1218.
- [29] J. Maier in *Festkörper - Fehler und Funktion*; B.G. Teubner, Stuttgart, 2000; pp. 440–455.
- [30] J. H. Yu, J. S. Lee, and J. Maier, *Angew. Chem.-Int. Edit.*, 2007, **46**(47), 8992.
- [31] H. I. Yoo, J. Y. Yoon, J. S. Ha, and C. E. Lee, *Phys Chem Chem Phys*, 2008, **10**(7), 974.
- [32] J. H. Yu, J. S. Lee, and J. Maier, *Solid State Ionics*, 2010, **181**(3-4), 154.
- [33] E. Kim and H. I. Yoo, *Solid State Ionics*, 2013, **252**, 132.
- [34] Z. P. Shao, W. S. Yang, Y. Cong, H. Dong, J. H. Tong, and G. X. Xiong, *J Membrane Sci*, 2000, **172**(1-2), 177.
- [35] B. Lin, S. Q. Zhang, L. C. Zhang, L. Bi, H. P. Ding, X. Q. Liu, H. F. Gao, and G. Y. Meng, *J. Power Sources*, 2008, **177**(2), 330.
- [36] L. Wang, R. Merkle, and J. Maier, *ECS Transactions*, 2009.
- [37] B. Lin, H. P. Ding, Y. C. Dong, S. L. Wang, X. Z. Zhang, D. Fang, and G. Y. Meng, *J. Power Sources*, 2009, **186**(1), 58.
- [38] Y. Lin, R. Ran, and Z. P. Shao, *Int. J. Hydrog. Energy*, 2010, **35**(15), 8281.

- [39] L. Wang, R. Merkle, Y. A. Mastrikov, E. A. Kotomin, and J. Maier, *J. Mater. Res.*, 2012, **27**(15), 2000.
- [40] H. H. Wang, C. Tablet, A. Feldhoff, and J. Caro, *Adv. Mater.*, 2005, **17**(14), 1785.
- [41] H. P. Ding, B. Lin, X. Q. Liu, and G. Y. Meng, *Electrochem. Commun.*, 2008, **10**(9), 1388.
- [42] J. Martynczuk, K. Efimov, L. Robben, and A. Feldhoff, *J Membrane Sci*, 2009, **344**(1-2), 62.
- [43] Y. Lin, R. Ran, D. J. Chen, and Z. P. Shao, *J. Power Sources*, 2010, **195**(15), 4700.
- [44] S. J. Skinner, *Int J Inorg Mater*, 2001, **3**(2), 113.
- [45] L. Yang, Z. Liu, S. Wang, Y. Choi, C. Zuo, and M. Liu, *J. Power Sources*, 2010, **195**(2), 471.
- [46] J. Dailly, S. Fourcade, A. Largeteau, F. Mauvy, J. C. Grenier, and M. Marrony, *Electrochim. Acta*, 2010, **55**(20), 5847.
- [47] J. Dailly, F. Mauvy, M. Marrony, M. Pouchard, and J. C. Grenier, *J. Solid State Electrochem.*, 2011, **15**(2), 245.
- [48] D. Poetsch, R. Merkle, and J. Maier, *J. Power Sources*, 2013, **242**, 784.
- [49] F. A. Kröger, *Chemistry of Imperfect Crystals*, 1964.
- [50] D. Baskar and S. B. Adler, *Solid Oxide Fuel Cells 10 (Sofc-X), Pts 1 and 2*, 2007, **7**(1), 1279.
- [51] W. Münch, G. Seifert, K. D. Kreuer, and J. Maier, *Solid State Ionics*, 1996, **86-88**, 647.
- [52] W. Münch, K. D. Kreuer, G. Seifertli, and J. Majer, *Solid State Ionics*, 1999, **125**(1-4), 39.
- [53] J. Maier in *Festkörper - Fehler und Funktion*; B.G. Teubner, Stuttgart, 2000; pp. 109–202.
- [54] R. Waser, *Ber Bunsen Phys Chem*, 1986, **90**(12), 1223.
- [55] H. Uchida, H. Yoshikawa, and H. Iwahara, *Solid State Ionics*, 1989, **35**(3-4), 229.
- [56] H. Uchida, H. Yoshikawa, T. Esaka, S. Ohtsu, and H. Iwahara, *Solid State Ionics*, 1989, **36**(1-2), 89.
- [57] T. Horita, K. Yamaji, N. Sakai, H. Yokokawa, A. Weber, and E. Ivers-Tiffée, *Electrochim. Acta*, 2001, **46**(12), 1837.
- [58] M. Sanders and R. O’Hayre, *J. Mater. Chem.*, 2010, **20**(30), 6271.
- [59] T. Norby, *Solid State Ionics*, 1999, **125**(1-4), 1.

- [60] A. Rothschild, W. Menesklou, H. L. Tuller, and E. Ivers-Tiffée, *Chem Mater*, 2006, **18**(16), 3651.
- [61] R. Merkle and J. Maier, *Angew. Chem.-Int. Edit.*, 2008, **47**(21), 3874.
- [62] H. J. M. Bouwmeester and A. J. Burggraaf in *CRC handbook of solid state electrochemistry*; WILEY-VCH Verlag, 1997; pp. 481–553.
- [63] R. Hancke, Z. A. Li, and R. Haugrud, *Int. J. Hydrog. Energy*, 2012, **37**(9), 8043.
- [64] J. Maier in *Festkörper - Fehler und Funktion*; B.G. Teubner, Stuttgart, 2000; pp. 290–315.
- [65] R. Merkle, J. Maier, and J. Fleig in *Handbook of Fuel Cells - Fundamentals, Technology and Applications*, ed. W. Vielstich, H. Yokokawa, and H. A. Gasteiger, Vol. 5; "John Wiley & Sons", New York, 2009; pp. 425–440.
- [66] Y. Y. Liu, X. Y. Tan, and K. Li, *Catal Rev*, 2006, **48**(2), 145.
- [67] A. V. Virkar, *Solid State Ionics*, 2001, **140**(3-4), 275.
- [68] M. D. Sanders and R. P. O'Hayre, *J Membrane Sci*, 2011, **376**(1-2), 96.
- [69] K. D. Kreuer, E. Schönherr, and J. Maier, *Solid State Ionics*, 1994, **70**, 278.
- [70] L. Wang, R. Merkle, and J. Maier, *J. Electrochem. Soc.*, 2010, **157**(12), B1802.
- [71] Y. A. Mastrikov, R. Merkle, E. Heifets, E. A. Kotomin, and J. Maier, *J Phys Chem C*, 2010, **114**(7), 3017.
- [72] J. Maier, *Solid State Ionics*, 1998, **112**(3-4), 197.
- [73] L. Wang, *PhD Thesis*, 2009.
- [74] J. Jamnik and J. Maier, *Phys Chem Chem Phys*, 2001, **3**(9), 1668.
- [75] R. Merkle and J. Maier, *Phys Chem Chem Phys*, 2002, **4**(17), 4140.
- [76] R. Merkle and J. Maier, *Top Catal*, 2006, **38**(1-3), 141.
- [77] W. Jung and H. L. Tuller, *Adv Energy Mater*, 2011, **1**(6), 1184.
- [78] G. J. la O', S. J. Ahn, E. Crumlin, Y. Oriksa, M. D. Biegalski, H. M. Christen, and Y. Shao-Horn, *Angew. Chem.-Int. Edit.*, 2010, **49**(31), 5344.
- [79] F. He, T. Z. Wu, R. R. Peng, and C. R. Xia, *J. Power Sources*, 2009, **194**(1), 263.
- [80] R. R. Peng, T. Z. Wu, W. Liu, X. Q. Liu, and G. Y. Meng, *J. Mater. Chem.*, 2010, **20**(30), 6218.
- [81] S. Ricote, N. Bonanos, F. Lenrick, and R. Wallenberg, *J. Power Sources*, 2012, **218**(0), 313.

- [82] L. Zhao, B. B. He, Y. H. Ling, Z. Q. Xun, R. R. Peng, G. Y. Meng, and X. Q. Liu, *Int. J. Hydrog. Energy*, 2010, **35**(8), 3769.
- [83] L. Wang, R. Merkle, G. Cristiani, B. Stuhlhofer, H.-U. Habermeier, and J. Maier, *ECS Transactions*, 2008, **13**(26), 85.
- [84] L. Besley and G. Bottomley, *J Chem Thermodyn*, 1973, **5**(3), 397.
- [85] D. Poetzsch, R. Merkle, and J. Maier, *Phys Chem Chem Phys*, 2014, **in revision**.
- [86] H. I. Ji, J. Hwang, K. J. Yoon, J. W. Son, B. K. Kim, H. W. Lee, and J. H. Lee, *Energ Environ Sci*, 2013, **6**(1), 116.
- [87] A. K. Opitz, A. Lutz, M. Kubicek, F. Kubel, H. Hutter, and J. Fleig, *Electrochim. Acta*, 2011, **56**(27), 9727.
- [88] S. B. Adler, *Chem Rev*, 2004, **104**(10), 4791.
- [89] R. D. Shannon, *Acta Crystallogr A*, 1976, **32**(Sep1), 751.
- [90] M. Johnsson and P. Lemmens, *J Phys-Condens Mat*, 2008, **20**(26).
- [91] M. Shirpour, R. Merkle, and J. Maier, *Solid State Ionics*, 2012, **216**, 1.
- [92] M. Shirpour, R. Merkle, and J. Maier, *Solid State Ionics*, 2012, **225**, 304.
- [93] M. Shirpour, R. Merkle, C. T. Lin, and J. Maier, *Phys Chem Chem Phys*, 2012, **14**(2), 730.
- [94] J. Fleig, *Solid State Ionics*, 2002, **150**(1&2), 181.
- [95] J. R. Jurado, M. T. Colomer, and J. R. Frade, *Solid State Ionics*, 2001, **143**(2), 251.
- [96] B. Wei, Z. Lu, X. Q. Huang, M. L. Liu, N. Li, and W. H. Su, *J. Power Sources*, 2008, **176**(1), 1.
- [97] A. Feldhoff, J. Martynczuk, M. Arnold, M. Myndyk, I. Bergmann, V. Sepelak, W. Gruner, U. Vogt, A. Hahnel, and J. Woltersdorf, *J Solid State Chem*, 2009, **182**(11), 2961.
- [98] J. I. Jung, S. T. Mixture, and D. D. Edwards, *Solid State Ionics*, 2010, **181**(27-28), 1287.
- [99] M. D. Sanders, H. Y. Zhu, R. J. Kee, and R. P. O'Hayre, *Solid State Ionics*, 2013, **249**, 6.
- [100] R. Merkle, D. Poetzsch, and J. Maier, *in preparation*, 2014.
- [101] J. Crank, in *The Mathematics of Diffusion*, Oxford University Press, New York, 1975; p. 48; 2 ed.
- [102] Y. Yamazaki, F. Blanc, Y. Okuyama, L. Buannic, J. C. Lucio-Vega, C. P. Grey, and S. M. Haile, *Nat. Mater.*, 2013, **12**, 647.

- [103] C. H. Chen, H. J. M. Bouwmeester, R. H. E. vanDoorn, H. Kruidhof, and A. J. Burggraaf, *Solid State Ionics*, 1997, **98**(1-2), 7.
- [104] R. Hancke, Z. A. Li, and R. Haugrud, *J. Electrochem. Soc.*, 2013, **160**(8), F757.
- [105] K. D. Kreuer, *Solid State Ionics*, 2000, **136**, 149.
- [106] A. Grimaud, J. M. Bassat, F. Mauvy, P. Simon, A. Canizares, B. Rousseau, M. Marrony, and J. C. Grenier, *Solid State Ionics*, 2011, **191**(1), 24.
- [107] H. I. Ji, B. K. Kim, J. H. Yu, S. M. Choi, H. R. Kim, J. W. Son, H. W. Lee, and J. H. Lee, *Solid State Ionics*, 2011, **203**(1), 9.
- [108] J. H. Joo, R. Merkle, and J. Maier, *J. Power Sources*, 2011, **196**(18), 7495.
- [109] K. L. Scholl and E. A. Fletcher, *Energy*, 1993, **18**(1), 69.
- [110] J. Fleig, *Phys Chem Chem Phys*, 2005, **7**(9), 2027.
- [111] J. H. Joo, R. Merkle, J. H. Kim, and J. Maier, *Adv. Mater.*, 2012, **24**(48), 6507.
- [112] F. S. Baumann, J. Fleig, M. Konuma, U. Starke, H. U. Habermeier, and J. Maier, *J. Electrochem. Soc.*, 2005, **152**(10), A2074.
- [113] A. Wedig, R. Merkle, B. Stuhlhofer, H. U. Habermeier, J. Maier, and E. Heifets, *Phys Chem Chem Phys*, 2011, **13**(37), 16530.
- [114] A. Wedig and S. Staemmler, *Private Communication*.
- [115] E. Bucher, W. Sitte, F. Klauser, and E. Bertel, *Solid State Ionics*, 2011, **191**(1), 61.

Acknowledgments

Zuerst möchte ich mich bei meinem Doktorvater Herrn Prof. Dr. Joachim Maier dafür danken, mir die unschätzbar wertvolle Möglichkeit gegeben zu haben am Max-Planck-Institut für Festkörperforschung wissenschaftlich zu arbeiten. Mein Dank gilt der großen Vielfalt an Möglichkeiten ein komplexes Thema, welches mich täglich aufs Neue faszinierte, zu bearbeiten, wofür mir alle nötigen Freiheiten gelassen wurden.

Ich bedanke mich bei Herrn Prof. Dr. Joris van Slageren für die Übernahme des Mitberichts und bei Herrn Prof. Dr. Rainer Niewa für die Übernahme des Prüfungsvorsitzes.

Mein tiefster Dank gilt Dr. Rotraut Merkle als interne Betreuerin. Ihr unendliches Wissen und ihre unerschöpfliche Geduld bewundere ich sehr. Ich bedanke mich sehr dafür, dass sie jederzeit für wissenschaftliche Diskussionen zur Verfügung stand, die den Prozess die komplexe Materie zu verstehen beschleunigt haben. Die Zusammenarbeit mit Rotraut hat sehr viel Spaß gemacht.

Mein weiterer Dank gilt Sofia Weiglein. Ihre Hilfe sich im Dschungel deutscher Bürokratie zurecht zu finden ist sehr wertvoll und hat mir selbst viel Zeit und Nerven erspart.

Ich möchte mich bei folgenden ehemaligen und aktuellen Kollegen für die experimentelle Unterstützung und wissenschaftlichen und natürlich auch nicht wissenschaftlichen Diskussionen bedanken, die ein entspanntes Arbeiten ermöglicht haben. Dr. Mona Shirpour (experimentelle Einführung in BaZrO_3), Dr. Anja Wedig (Mikrokontakte), Dr. Giuliano Gregori, Dr. Piero Lupetin und Michael Weissmayer (SPS), Dr. Marcus Göbel (C#), Andreas Wohlfarth (Karl-Fischer) und Oliver Gerbig (Versuchsaufbauten). Insbesondere bedanke ich mich bei Michael für die konstruktive Unterstützung bei der Optimierung der Sinterbedingungen, sofortigen Hilfe bei Problemen und interessanten Gespräche. Ich danke Dr. Dominik Samuelis für sein unerschöpfliches Wissen in allen Bereichen des wissenschaftlichen und nicht wissenschaftlichen Lebens, welches für sehr interessante und auch hilfreiche Diskussionen gesorgt hat. Bei Anja und Mona möchte ich mich auch für die vielen, teils tiefsinnigen Gespräche bedanken, durch die man den Kopf wieder frei bekommen hat für neue Gedanken.

Bei allen technischen Mitarbeitern der Abteilung bedanke ich mich für die experimentelle Unterstützung: Annette Fuchs (BaZrO_3 Pulver, Karl-Fischer, BET, REM), Udo Klock (Flussreglern, Feuchtesensoren und technischen Hilfe bei Problemen), Uwe Traub (IT-Unterstützung und lückenlosen Versorgung mit Software), Gaby Götz und Helga Hoier (gefühlte unendliche Anzahl an Pulverdiffrakogrammen und das Lösen von teils kniffligen Problemen rund um deren Auswertung), Peter Senk (Öfen und Gasleitungen) und Ewald Schmitt (Laborumräumung). Insbesondere danke ich Gaby für die vielen Gespräche und ihre Herzlichkeit. Bei Herrn Schmitt bedanke ich mich für die vielen, interessanten Gespräche im 92er Bus während der Fahrt zum

und vom Institut, die v.a. die relativen Wartezeiten bei Verspätungen deutlich verkürzt haben.

Bei der Technologiegruppe, insbesondere Ben Stuhlhofer, Stephan Schmidt und Yvonne Link bedanke ich mich für die Anfertigung sehr vieler Dünnfilmproben und bei der fachlichen Unterstützung Lösungen für auftauchende Probleme zu finden. Des Weiteren bedanke ich mich bei der Gruppe Analytische Chemie am Max-Planck-Institut für Intelligente Systeme für die chemische ICP-OES-Analyse vieler Oxide, deren Aufschluss nicht immer trivial war. Ich bedanke mich bei der Kristallpräparation für das Sägen, Formen und Polieren sehr vieler Proben. Insbesondere bedanke ich mich bei Barbara (Babs) Baum für ihre sehr präzise, sorgfältige und perfekte Arbeit und für die vielen, wenn auch nicht immer einfachen Gespräche, bei denen mich Frank Falkenberg aber gut unterstützt hat. Ein weiterer Dank gilt den Glasbläsern, der Werkstatt und dem Forscherbedarfslager, insbesondere Herrn Mathias Konrad für die fachliche Unterstützung. Ich danke Tolga Acartürk für die SIMS-Messungen und die detaillierte Hilfe bei der Auswertung.

Bei meiner Praktikantin Juliane Heitkämper bedanke ich mich für die Unterstützung bei den Karl-Fischer-Messungen, vor allem für das geduldige Sieben der vielen Pellets, und für die sehr angenehmen vier Wochen, die sie mit mir gearbeitet hat.

Bei Dr. Kay Potzger vom Helmholtz-Zentrum Dresden-Rossendorf bedanke ich mich für die Implantation von Deuterium in mehrere Proben.

Mein herzlichster und tiefster Dank gilt meinen Eltern. Ohne deren menschliche und natürlich auch finanzielle Unterstützung und unendlichen Verständnisses für meinen eigenen Weg wäre ich heute nicht an diesem Punkt angekommen. Leider ist es meinem Vater verwehrt, das Ende dieses akademischen Weges zumindest im Diesseits mitzuerleben. Er verlor am 04. Februar 2014 viel zu früh den unfairen Kampf gegen den Lungenkrebs. Möge er seine Ruhe finden, wo auch immer er gerade ist.

Mein abschließender, herzlichster und unendlicher Dank gehört Oliver Kikillus. Er bereichert, erfüllt und ergänzt mein Leben in allen nur denkbaren Bereichen, wofür ich ihn nicht mehr missen möchte. Vor allem muss ich ihn für die bedingungslose Unterstützung in den letzten Monaten danken. Ohne ihn wäre ich in dieser unendlich schweren Zeit in einem tiefen Loch versunken, von dem aus es nicht möglich gewesen wäre, diese Arbeit anzufertigen. Er hat mir und meiner Mutter in der unendlich komplizierten, deutschen Bürokratie im Erbrecht stets den Rücken frei gehalten, sodass ich mich weiter auf das Schreiben konzentrieren konnte.

Curriculum Vitae

Persönliche Informationen

Name: Daniel Pötzsch
Geburtsdatum: 24. März 1985
Geburtsort: Dresden
E-Mail: daniel@dpoetzsch.de

Akademische Ausbildung

Oktober 2010 – **Doktorand**
Juli 2014 Max-Planck-Institut für Festkörperforschung

Oktober 2005 – Studium **Diplom-Chemie**
September 2010 Universität Stuttgart
Titel der Diplomarbeit:
*“Untersuchung eines mit Methanol betriebenen
Superkondensator-Wasserstoffspeichers”*

September 1996 – **Allgemeine Hochschulreife**
Juli 2005 Gymnasium Gröbenzell